

# Università degli Studi di Milano-Bicocca

*Facoltà di Scienze Matematiche, Fisiche, Naturali  
Dipartimento di Scienze Geologiche e Geotecnologie*

**Doctor of Philosophy**  
*in*  
**Earth Sciences**



## **PHYSICAL AND MECHANICAL CHARACTERIZATION OF ALTERED VOLCANIC ROCKS FOR THE STABILITY OF VOLCANIC EDIFICES**

Antonio Pola Villaseñor

**Supervisor**  
Prof. Giovanni Battista Crosta

Academic year 2009/2010



---

## CONTENTS

LIST OF FIGURES.....	v
LIST OF TABLES.....	x
ACKNOWLEDGEMENTS.....	xi
ABSTRACT.....	xii
1. INTRODUCTION .....	1
1.1 Goals.....	2
2. STATE OF THE ART .....	4
2.1 Instability in volcanic edifice.....	4
2.1.1 Volcano instability induced by magma-intrusion.....	5
2.1.2 Volcano instability induced by regional and local tectonics .....	6
2.1.3 Volcano instability induced by hydrothermal alteration .....	8
2.1.4 Volcano instability induced by deformation of dipping substrata.....	10
2.2 Debris-avalanche.....	11
2.2.1 Geomorphic characteristics .....	11
2.3 Geotechnical properties of weathered/altered volcanic rocks.....	14
3. SAMPLING SITES .....	18
3.1 Brief geological description of Solfatara.....	18
3.2 Brief geological f description of Ischia .....	20
3.3 Brief geological description of Bolsena volcanic zone.....	21
3.4 Sampling.....	22
3.5 Petrographical study .....	23
3.5.1 Lava from Solfatara (SL).....	24
Fresh lava SLA1 .....	25
Slightly weathered lava SLA2 .....	25
Moderately weathered lava SLA3 .....	25
Highly weathered lava SLA4.....	26
Totally weathered lava SLA5 .....	26
3.5.2 Pyroclastic rocks from Solfatara (SP).....	28
Highly weathered pyroclastic SPRA1 .....	29
Highly weathered pyroclastic SPRA2 .....	29
Highly weathered pyroclastic SPRA3 .....	29
3.5.3 Green-Tuff deposit from Ischia (IGT).....	30
Fresh Ischia Green-Tuff IGTF.....	31
Highly weathered Ischia Green-Tuff IGTA .....	32
3.5.4 Pyroclastic rock from Bolsena (BoPRA).....	33
Slightly weathered Bolsena Pyroclastic rock (BoPRA) .....	34
3.6 Geochemistry.....	38
4. LABORATORY ANALYSIS .....	42
4.1 Experimental methodology .....	42
4.1.1 Ultrasonic pulse velocity measurements .....	43
4.1.2 Effective porosity by different techniques.....	44

---

4.1.3	Total porosity by different techniques .....	45
4.1.4	Uniaxial compressive strength and P-waves measurements .....	48
4.1.5	Tensile strength.....	49
4.1.6	Triaxial compressive strength.....	50
4.1.7	Oedometric test.....	52
4.2	Results of laboratory investigations .....	53
4.2.1	Characterization of Porosity .....	56
4.2.2	Evaluation of P and S waves velocity.....	60
4.2.3	Evaluation of uniaxial compressive strength.....	62
4.2.4	Evaluation of uniaxial compressive strength under stress-cycling experiments.....	66
4.2.5	Evaluation of tensile strength .....	68
4.2.6	Multiple linear regression .....	70
4.2.7	Triaxial strength.....	72
4.2.8	Failure patterns in triaxial test .....	76
4.2.9	Results of oedometric test.....	82
4.3	Conclusions of laboratory analyses.....	83
5.	STABILITY ANALYSIS .....	92
5.1	Numerical model .....	93
5.2	Material properties .....	93
5.3	Model elements and boundary conditions.....	95
5.4	Model analysis.....	97
6.	CONCLUSIONS .....	99
7.	REFERENCE.....	101
	APPENDIX.....	112

---

## LIST OF FIGURES

Figure 2.1 Factors contributing the development of structural instability at active volcanoes (McGuire, 1996).....	4
Figure 2.2 a) model relates flank failure perpendicular to the regional maximum horizontal stress direction ( $\sigma_{hmax}$ ), the cone elongation and alignment of dikes (Lagmay et al., 2000). b) model that relates vertical faults underneath a volcanic cone to the flank failure. c) model that relates strike slip faulting underneath volcano cones to the flank failure (Concha-Dimas et al., 2005). .....	6
Figure 2.3 Summary of model results for cones overlying strike-slip faulting zones. a) Right-lateral strike-slip fault. b) Left-lateral strike-slip fault. $\sigma_1$ and $\sigma_3$ are respectively, the maximum and minimum horizontal stress. $P$ and $R$ are synthetic faults generated at acute angles to the main strike-slip shear. From Lagmay et al., (2000).....	7
Figure 2.4 a) Formation of a normal fault sector collapse creating a typical horseshoe-shaped caldera. b) Schematic drawing of the deformation of the flank by the vertical faulting beneath a stratified heterogeneous cone. From Vidal and Merle, (2000).....	8
Figure 2.5 Analogue models. a) Sketches of an inclusion centred model and an off-centred inclusion model, with the different important geometrical parameters. b) The different sets of experiments (Cecchi et al., 2005). .....	9
Figure 2.6 A: Three-dimensional perspective with cutaway showing best estimate interpretation of internal edifice geology from detailed geologic mapping and geophysics. Dashed line shows western limit of intense alteration that extends to basement in Sunset Amphitheater north of line of section. B: Three-dimensional perspective showing simplified internal geology if widespread intense subsurface alteration is assumed. ....	10
Figure 2.7 Debris Avalanche Schematic Section. a) Longitudinal section stretching from the source amphitheater to the distal end; A' transverse section of the medial region; B' transverse section for the distal region (Ballard et al., 2000). b) Hummocks types. Type a, block facies with no matrix facies. Type b, predominantly matrix facies, debris-avalanche blocks scattered throughout. Type c, debris-avalanche block suspended in matrix facies; matrix facies probably carried debris-avalanche block. (Glicken 1996).....	12
Figure 2.8 a) map of hummock distribution and hummock trains, hummocks are generally large and concentrated in distal zones and, b) at crater, hummocks are smaller and cover a larger area (Shea et al., 2008).....	13
Figure 2.9 a) surface structures, b) longitudinal section, and c) transversal section of analogue model of lateral spreading with $\alpha=\pi/3$ and $d/R_{Model}=0$ , at $t_{Model}=60$ min (Andrade and van Wyk de vries 2010).....	14
Figure 2.10 Experimental results of analogue modelling: The asymmetric deformation type. Preferential spreading occurs with normal faults developing at the cone summit, sometimes grabens, and thrusts at the front slump. A bulge appears and leads to frequent landslides (Cecchi et al., 2005) 14	

---

Figure 3.1 Localization map of Solfatara. Some structural features are included in the map. Modified from Isaia et al., 2004. ....	19
Figure 3.2 Location map of field study area (Solfatara). a) Outcrop of Pyroclastic sequence. b) Outcrop of lava sequence. The solid circles indicate the sampling points. ....	20
Figure 3.3 Active fumaroles inside Solfatara caldera. Contact between pyroclastic and lava sequence is also visible. ....	20
Figure 3.4 Localization map of field study area (Ischia). The solid circles indicates the position of field study where samples were collected. ....	21
Figure 3.5 Localization map of field study area of Bolsena. The star indicates the position where samples were collected (After, Nappi et al., 1998). ....	22
Figure 3.6 TAS diagrams (Total Alkali vs. Silica) for volcanic rocks from Solfatara, Ischia and Bolsena. ....	24
Figure 3.7 Heavy fractured lava sequence from Solfatara; lava varies significantly on a short distance especially approaching to fumarolic activity. ....	24
Figure 3.8 Polarized light microscope images of the lava rocks from Solfatara, Plg Plagioclase, Snd Sanidine, Prx Pyroxene, Bio Biotite, P pores, Ar-Pry Argilized pyroxene, Si-am Silica-amorphous, Li-la lithic fragments of lava, Arg Argilization, Gl-fr Glass fragment, Mi-QZ micro-Quartz. ....	27
Figure 3.9 X-ray diffractograms of fresh and weathered varieties of lavas from Solfatara. ....	28
Figure 3.10 a) Fresh pyroclastic sequence from Solfatara. b) Chaotic Weathered/altered pyroclastic sequence from Solfatara. Fumarolic activity is observed. ....	29
Figure 3.11 Polarized light microscope images of the pyroclastic rocks from Solfatara, Plg Plagioclase, Snd Sanidine, Prx Pyroxene, Bio Biotite, P pores, Ar-Pry Argilized pyroxene, Si-am Silica-amorphous, Li-la Lithic fragments of lava, Arg Argilization, Gl-fr Glass fragment, Mi-QZ micro-Quartz. ....	30
Figure 3.12 X-ray diffractograms of weathered varieties of pyroclastic rocks from Solfatara. ....	30
Figure 3.13 a) hydrothermal alteration of Green Tuff (active intense fumaroles are visible). b) Outcrop of the Green tuff (faults and cracks are easy identified). ....	31
Figure 3.14 Polarized light microscope image of the volcanic rocks from Ischia. Plg Plagioclase, Snd Sanidine, Prx Pyroxene, Bio Biotite, P pores, Ar-Pry Argilized pyroxene, Si-am Silica-amorphous, Li-la Lithic fragments of lava, Arg Argilization, Gl-fr Glass fragment, Mi-QZ micro-Quartz. ....	32
Figure 3.15 X-ray diffractograms of fresh and weathered varieties of Green Tuff from Ischia and weathered pyroclastic rocks from Bolsena area. ....	33
Figure 3.16 The unaltered rock-normalized diagram for volcanic altered rocks from Solfatara, Ischia and Bolsena. ....	40
Figure 4.1 Illustration of total Porosity (n) in black colour extracted from two-dimensional digital image analysis. The matrix and minerals are shown in white. a-f) total porosity for Solfatara lava	

---

sequence (12.8, 16.9, 18.4, 15, 9.5 %, respectively); g-h) total porosity for Solfatara pyroclastic rock (24.8, 17.8 %, respectively); i) total porosity for Ischia pyroclastic rock (15.3 %). .....	46
Figure 4.2 (a) X-ray micro CT original images (b) Example of a filtered image reconstructed from a tomographic slice through sample SL4. (c) pore distribution obtained from thresholding of image b (d) 3D pore-system reconstruction.....	47
Figure 4.3 An example of a bi-logarithmic diagram used to examine fractal dimension (D). The Power law fitting relationship is shown, its exponent corresponds to the fractal dimension. ....	48
Figure 4.4 Sketch of uniaxial test arrangement. P-wave transducers and strain gauges are shown. b) Sketch of tensile test arrangement. c) Sketch of the general shape of the stress-strain curve illustrating mechanical parameters. Methods for calculating Young's Modulus and Poisson's ratio are also illustrated (from Brady and Brown 2004) .....	50
Figure 4.5 Mohr-Coulomb failure criterion in terms of stress parameters and corresponding Mohr stress circles ( $t-s$ ) and shear and normal stresses ( $\tau-\sigma$ ). .....	52
Figure 4.6 a) Circular cutter; sample 18 mm high. b) Soft oedometer ring; strain controlled Oedometer (WTD). .....	53
Figure 4.7 Compressive strength as a function of effective porosity. From Lumb (1983). ....	56
Figure 4.8 a) Total porosity as a function of lithotype obtained from pycnometer test, thin section analysis (3D) and X-ray tomography (Micro CT). b) Effective porosity as a function of lithotype obtained from bulk specific weight measurements, water immersion and mercury porosimeter. ....	58
Figure 4.9 a) Fractal dimension calculated from pores size distributions obtained by different techniques (see legend); b) Pore volume distribution of SLA sequence from thin-section image reconstruction; c) Pore volume distribution of SPRA and IGTF sequence from thin-section image reconstruction. The lack of information corresponds to the difficulty in preparing thin-sections in very soft samples. d) Pore volume distribution of SLA sequence from x-ray tomography image reconstruction; e) Pore volume distribution of SPRA sequence from x-ray tomography image reconstruction;. f) Pore volume distribution of IGT sequence and BoBRA from x-ray tomography image reconstruction. g) Pore volume distribution of SLA sequence from mercury porosimetry; h) Pore volume distribution of SPRA sequence from mercury porosimetry;. i) Pore volume distribution of IGT sequence and BoBRA from mercury porosimetry.....	60
Figure 4.10 P-S wave velocity a) propagation velocity of P-wave as a function of effective porosity. b) propagation velocity of S-wave as a function of effective porosity. c) propagation velocity of P-wave as a function of lithotype and grade of alteration. d) propagation velocity of S-wave as a function of lithotype and grade of alteration.....	62
Figure 4.11 a) Lithotype vs uniaxial compressive strength. b) Young's Modulus vs uniaxial compressive strength. c) Stress-strain behaviour for lava rock ( $\varnothing$ 18 mm in diameter). d) Stress-strain behaviour for pyroclastic rocks ( $\varnothing$ 18 mm in diameter). ....	64
Figure 4.12 a) Uniaxial compressive strength as a function of: a) $V_p$ , b) $V_s$ , c) $\eta_T$ , d) $\eta_e$ , e) dynamic Young's Modulus, f) Young's Modulus vs Uniaxial strength. ....	66
Figure 4.13 a) Evolution of Young's modulus as a function of lithotype, during increasing-amplitude cyclic stressing experiments. Stress-strain behaviour during increasing-amplitude cyclic stress	

---

experiments for: b) lavas series (SLA). c) pyroclastic rocks series (SPRA) d) pyroclastic rocks series (IGT and BoPRA). .....	68
Figure 4.14 Tensile strength (Brazilian test) as a function of: a) Lithotype b) Bulk density. Tensile stress-strain behaviour for: c) lava rock (disks of $\phi$ 54 mm in diameter). d) pyroclastic rocks (disks of $\phi$ 54 mm in diameter). .....	69
Figure 4.15 a) Tensile strength vs $\eta_e$ , b) $E_{T150}$ vs $\eta_e$ , c) Tensile strength vs $\eta_T$ , d) $E_{T150}$ vs $\eta_T$ .....	70
Figure 4.16 relationships between observed and quantified (predicted from Multiple Linear Regression). a) UCS eq. 13 b) Young's modulus eq.14.....	72
Figure 4.17 a) a) Mohr-Coulomb criterion in terms of maximum shear and mean normal effective stress(t-s). t-s points are interpolated by means of a linear relation. As shown in Figure 4.5, the b value is located where interpolation line crosses the x axis; the slope of this line corresponds to the angle $\beta$ (see also Table 4.3). b,c) Stress-strain behaviour for lava rock from multi-stage triaxial test. d) Stress-strain behaviour for pyroclastic rocks from multi-stage triaxial test. Confining pressure values are shown for all curves. ....	73
Figure 4.18 a) Stress-strain behaviour for pyroclastic rock in triaxial test (BoPRA sample of 54 mm in diameter) (confining stress = 5 MPa). b) 3D pore reconstruction from intact sample. c) 3D reconstruction after triaxial test. It shows four set of compaction bands and several conjugate shear planes.....	76
Figure 4.19 a) 3D Schematic illustration of structures resulting from failure modes in SLA1 sample. b) Post-failure photo of the specimen.....	76
Figure 4.20 a) 3D Schematic illustration of structures resulting from failure modes in SLA2 sample. b) Post-failure photo of the specimen.....	77
Figure 4.21 a) 3D Schematic illustration of structures resulting from failure modes in SLA3 and SLA4 samples. b) Illustration is reconstructed with series of x-ray tomography images.....	78
Figure 4.22 a) 3D Schematic illustration of structures resulting from failure modes in SLA5 samples. b) Illustration is reconstructed with series of x-ray tomography images .....	78
Figure 4.23 a) 3D Schematic illustration of structures resulting from failure modes in SPRA1 and SPRA3 samples. b) Illustration is reconstructed with series of x-ray tomography images.....	79
Figure 4.24 a) 3D Schematic illustration of structures resulting from failure modes in SPRA2 sample. b) Illustration is reconstructed with series of x-ray tomography images .....	80
Figure 4.25 a) 3D Schematic illustration of structures resulting from failure modes in IGTF sample. b) Illustration is reconstructed with series of x-ray tomography images.....	80
Figure 4.26 a) 3D Schematic illustration of structures resulting from failure modes in IGTA sample. b) Illustration is reconstructed with series of x-ray tomography images.....	81
Figure 4.27 2D Schematic illustration of structures resulting from various failure modes in weathered/altered volcanic rocks. Fracture mode is represented by four different profiles. Base of each sample has 54 mm of diameter. Fracture pattern in IGTF is highlighted by a dash line.....	82



---

Figure 4.28 Results of oedometric test. a) axial and radial stress vs axial strain; b) stress ratio vs axial strain; c) void ratio vs log axial stress; d) deviatoric stress vs mean effective stress. ....	83
Figure 4.29 schematic view of: a) $\eta_T$ obtained from X-ray tomography images analysis as a function of lithotype and grade of alteration. b) $\eta_e$ obtained from bulk specific weight measurements as a function of lithotype and grade of alteration .....	84
Figure 4.30 schematic view of the principal characteristics of the fractal dimension.....	85
Figure 4.31 schematic view of: a) P wave; and b) S wave as a function of Lithotype and grade of alteration.....	86
Figure 4.32 schematic view of: a) P wave; and b) S wave as a function of $\eta_e$ obtained from bulk specific weight measurements.....	86
Figure 4.33 schematic view of: a) uniaxial compressive strength as a function of alteration grade. b) Young's modulus evolution; compressive stress as a function of axial strain. ....	87
Figure 4.34 schematic view of UCS as a function of $\eta_i$ . ....	87
Figure 4.35 schematic view of Young's modulus evolution during Uniaxial compressive stress cycle test. ....	88
Figure 4.36 schematic view of tensile strength as a function of grade of alteration. ....	88
Figure 4.37 Intrinsic properties of: a) lava series (SLA), b) green tuff series (IGT), c) pyroclastic rock series (SPRA). ....	89
Figure 4.38 Schematic behaviour of tensile stress-strain curves.....	89
Figure 4.39 Schematic behaviour of stress-strain curves in triaxial tests.....	90
Figure 5.1 The model domain includes five units representing different components of the volcanic system.....	95
Figure 5.3 Distribution of stresses during volcano construction and layers degradation. From left to right: construction of layer 8; construction of layer 9; construction of layer 10 and degradation of layer 6.....	97
Figure 5.4 Maximum shear strain increment distribution at final step of the model (construction of layer 10 and degradation of layer 6).....	98
Figure 5.5 Distribution of total displacements at the final phase of the model.....	98
Figure 5.6 Distribution of horizontal displacements. From left to right: construction of layer 8; construction of layer 9; construction of layer 10 and degradation of layer 6.....	99

---

## LIST OF TABLES

Table 3.1 Summary of field description for Solfatara lava sequence.....	35
Table 3.2 Summary of field description for Solfatara pyroclastic sequence.....	36
Table 3.3 Summary of field description for Ischia and Vulcini pyroclastic sequence .....	37
Table 3.4 Representative chemical weathering indices.....	39
Table 3.5 Major geochemical properties of weathered/altered volcanic rocks from Solfatara, Ischia and Bolsena.....	39
Table 3.6 chemical weathering indices for volcanic rocks from Solfatara Ischia and Bolsena. ....	41
Table 4.1 Summary of physical properties of weathered/altered volcanic rocks.....	54
Table 4.2 Summary of mechanical properties of weathered/altered volcanic rocks .....	55
Table 4.3 Summary of mechanical properties of weathered/altered volcanic rocks described in the literature .....	55
Table 4.4 Summary of peak strength values and the corresponding confining pressures. Back calculated $\phi$ and $c$ from Mohr-Coulomb criterion and $m_i$ from Hoek-Brown criterion is included .....	74
Table 5.1 Experimental intact rock properties and calculated rock mass strength values from literature. ....	92
Table 5.2 Rheological properties used in the numerical model .....	94
Table 5.3 Parameters used in the scaling procedure in analogue modeling. illustration of the main geometrical parameters of the models: opening angle ( $\alpha$ ) and the ductile layer offset ( $d_{\text{Model}}$ ) varied during experiments (Andrade and van Wyk de vries, 2010). ....	96

---

## ACKNOWLEDGEMENTS

Agradezco sobremanera el apoyo económico brindado por El Consejo Nacional de Ciencia y Tecnología.

Agradezco al Gobierno Italiano y al Instituto Italiano de Cultura de la ciudad de México, en especial al Dr. Luigi Pironti por su siempre gentil y humano trato.

Este trabajo fue desarrollado gracias a la invitación de mi tutor, el Dr. Giovanni Crosta, a participar en uno de sus tantos proyectos de investigación. Aprecio y agradezco su empeño y disposición para atender mis propuestas. Me da mucho gusto reconocer que gran parte de mis conocimientos, en este último periodo, han sido obra de su apoyo constante.

Mi estancia en Italia no hubiera sido posible sin la ayuda de mi co-tutor el Dr. Víctor Hugo Garduño Monroy. Agradezco sus atenciones que desde hace ya algunos años me ha brindado. Agradezco sobremanera la dulce compañía de Tania y Shantal.

Envío un fuerte abrazo a Sergio Chiesa. Agradezco además su siempre cariñoso trato y sus mágicas conversaciones.

Los trabajos de laboratorio no hubieran sido posibles sin la ayuda de Valentina Barberini y Nicoletta Fusi. Permanezco en deuda por su siempre gentil trato y su inagotable disposición. Agradezco en especial a Nicoletta por haberme dado la oportunidad de conocer a sus hijas, por ser siempre muy atenta y siempre preocuparse por mi bienestar, además por haberme incluido en su vida familiar.

Gran parte de las pruebas de laboratorio se realizaron con la ayuda de Gianluca Gaspari, Agradezco su generosidad y simpatía.

Los trabajos petrográficos en gran medida fueron desarrollados con la asesoría y colaboración del Dr. Pedro Corona. Agradezco sus agradables conversaciones.

Gran parte de mis dudas fueron resueltas por Federico Agliardi, agradezco su entera disposición y su inagotable simpatía.

Los trabajos de campo fueron posibles gracias a la ayuda de Gianluca Norini. Agradezco los comentarios y las discusiones que sin duda han enriquecido este trabajo.

Agradezco a Gianluca Gropelli por los trabajos en campo y las agradables reuniones.

Agradezco sobremanera la dulce amistad brindada por Paolo Frattini, Rafa, Mía y Miguel. Gracias por haber hecho mi estancia en Italia inolvidable. Gracias además por haberse interesado en mi vida personal.

Mi vida de cierta manera se ha transformado gracias a la compañía de mis amigos. Agradezco la felicidad contagiosa de Matteo, el valor de Antonio, la siempre agradable compañía de Serena (La Biondina), la sinceridad de Estefano (Rambo), el espíritu de Marco (El Biondo), la expresividad de Ricardo (El Panda) y la simpatía y sencillez de Seferino. Un fuerte abrazo a Francesco, Rossana, Elena, Samuel, Alberto y Bouchra.

A mi madre y hermanos que han sabido mantener una atmósfera de amor entre nosotros. Gracias por haberme enseñado a vivir, a imaginar y a soñar.

A Ivonne por cuidar, dirigir y darle brillo a nuestra relación, por compartir su vida y por estimular e impulsar la mía. Te quiero.

---

## ABSTRACT

Geomechanical characterisation of altered volcanic rocks and their role in flank volcanoes stability are evaluated in this study. Physical and mechanical properties and their variation with the degree of alteration are described in detailed. A series of multidisciplinary tests were performed to identify and quantify the progressive degradation of the properties. They are as follow: 1) petrographical and chemical studies (thin-sections, x-ray diffractions and x-ray fluorescence); 2) effective and total porosity (standard test procedure, mercury intrusion porosimetry, pycnometer tests, two-dimensional and x-ray CT image analysis); 3) Ultrasonic pulse velocity measurements; 4) uniaxial compressive tests (with p-wave measurements, cyclic loading); tensile tests (with strain gauge measurements); and 5) triaxial tests (single-stage and multi-stage). Preliminary numerical modelling was mainly focus on the effect of altered rocks content and gravity effects, even if different perturbations such as pore water pressure (e.g. rainfall, vapour and gas), and regional or local tectonics (e.g. faults, earthquakes and dynamic loading) are presented in volcanoes nature.

Collected samples are representative of four different classes of volcanic deposits: i) trachytic lava with abundant crystals; ii) pyroclastic deposits, with lava clasts and pumice elements with different sizes; iii) Green tuff, constructed prevalently by pumice clasts; and iv) ignimbrite deposits characterized by low density. Petrographical and chemical characteristics, in particular weathering indexes reveal large differences not only between lithotypes, but also between samples. These differences are well quantified by physical properties, in particular porosity and shear wave velocity values. Decay of the properties, well represented by regression analysis with significant correlation parameter ( $R^2 > 85$ ), is observed when average values of the compressive strength, tensile strength and Young's modulus are compared with the average porosity value, fractal dimension and grade of alteration. Failure of rocks were well documented by the evolution of elastic properties, differences between each lithotype are discussed. Post-failure reconstruction of samples reveals that the nature of deformation is controlled by textural properties (e.g. grains, pores, and cement) and the behaviour strongly influences the response of the specimen. Anisotropy of rocks is clear represented by triaxial tests post-failure reconstruction, abrupt differences between fresh and altered samples are observed. Finally, a simplified 2-D numerical stress-strain modelling was carried out in order to visualize the effects of rock properties degradation in volcanic flank failure. Modelling was aimed at clarifying the role of the altered volcanic rocks in the evolution of volcano stability. The results, in terms of maximum computed values of shear strain and displacements, show that degradation of rock properties is capable of defining and controlling large zones of instability.

## 1. INTRODUCTION

The volcano history is represented by continued growth with episodes of instability that lead to structural failure (e.g. landslides and debris avalanches) (Lagmay et al., 2000). Debris avalanche is one of the most catastrophic events produced by the slope failure of a volcanic edifice. The term “debris avalanche” is used to refer to the sudden and very rapid gravitational movement (e.g. velocities of 80-90 m/s have been calculated at Saint Helens by Voight et al., 1983) of a poorly sorted and incoherent mass of rock and soil, which is moved by gravity and often exceed a cubic kilometer in volume (Siebert 1984). These kinds of event may occur without warning, move great distances on low-angle slope, cover large areas (area of 98 km<sup>2</sup> have been estimated at Shiveluch by Ponomareva et al., 1998) and generate catastrophic blasts (Brantley & Glicken., 1986). Stability of a volcano depends on several factors, some of them contribute to reduction in shear strength of the volcanic materials and some others increase the shear stress (Voight and Elsworth 1997). These factors include hydrothermal alteration as observed in Mount Rainier and Mount Hood, Cascade Range Volcanoes (Reid et al., 2001; Watters et al., 2000), regional tectonics events as the reactivation of a regional fault, which may drastically change the boundary conditions around a volcano, as observed in Kamchatka, eastern Russia (Kozhurin et al., 2006), and increase in pore pressures in potential failure zones generated as a result of magmatic intrusion, as described in Bezimianny and Mt. Saint Helen volcanoes (Donnadiou et al., 2001; Glicken, H., 1998).

The role of alteration as cause of volcano instability and destructive debris flows is addressed in a still limited way in the literature, and lacks of analytical tools for the hazard assessment, despite hydrothermal alteration is a common phenomenon in the volcanic environment. In the literature, it is absent a systematic study on the spatial distribution and changes in the behaviour of materials involved in the alteration, in response to the exceptional environmental conditions and their effect on the stability of large volcanic edifices. Some studies propose material properties degradation as an important factor in inducing volcanic flanks collapse. A relationship between superficial and depth zone of alteration, and fast cohesive debris-flow generation have been proposed to explain instability in some volcanic edifices (Finn et al., 2001, 2007, Reid et al., 2001; Capra et al., 2002). Failure surface in volcanoes is controlled by the distribution of altered zones and it is deeper than failures surfaces in not volcanic events (Reid et al. 2000; Siebert 2002). Within the lateral spreading cases, failure is the extreme consequence of interbedded volcanoclastic layers deformation provoked by the load generated by volcanic edifice (van Wyk de Vries et al. 2000; Reid et al. 2001; Cecchi et al. 2004). This deformation process is not also for hydrothermal alteration of the basement rock (Lopez and Williams, 1993; Kempter and Rowe, 2000; vanWyk de Vries et al., 2000; Reid et al., 2001), but also for the presence of materials with ductile behaviour (Borgia et al., 1992; van Wyk de Vries and Francis, 1997; van Wyk de Vries et al., 2001). Evaluating the hazards and instability mechanisms associated with volcano composed with altered rocks is a difficult task because of difficulties in defining the alteration grade, materials distribution within volcano and their properties are unknown for almost all active volcanoes worldwide (Finn et al., 2001, 2007; del Potro and Hurlimann, 2009). There is a lack of knowledge with regard to typical mechanical processes that could generate a volcanic collapse by a progressive alteration of the materials. Analysis of stability made using limit equilibrium method generally indicates stable conditions, also in saturated conditions, due to the fact that the properties (e.g. strength) of altered volcanic rocks are usually not considered. The circulation of pressurized and hot fluids rich in acid and/or corrosive elements is the first cause of alteration. Hydrothermal systems

are presented in many volcanic edifices, where groundwater interacts with intrusive bodies generating hot and often acidic fluids (Day 1996; Giggenbach et al., 1990; Almendros et al., 2001; Nishi et al., 1996; Edmonds et al., 2003; Gerlach and Casadevall, 1986; Sturchio et al., 1988; Ingebritsen and Scholl, 1993; Finizola et al., 2002; Hase et al., 2005; Hurwitz et al., 2002; Aizawa et al., 2005; Frank, 1995). The presence of weathered materials and pore pressure of fluids augment and make the edifice more unstable (Lopez and Williams 1993; Day 1996; Vallance and Scott 1997; Iverson et al. 1997), by favouring rocks dissolution and clay minerals formation along geologic structures (discontinuities, lithological contacts, faults and dikes; Frank 1983; Carrasco-Nunez et al. 1993; López and Williams 1993; Watters et al. 2000). The effect of hydrothermal alteration is not easy to quantify (López and Williams 1993; Watters and Delahaut, 1995; Watters et al. 2000) and not always related to a reduction in the mechanical properties of the materials (Watters et al. 2000). In literature many papers deal with processes of mineral alteration, but few are focused on the effects of this alteration in terms of strength reduction of weathered materials (Watters and Delahaut, 1995; Zimbelman et al., 2003; del Potro and Hürlimann, 2008). Failure surface in volcanic edifices subjected to alteration is localized in the weakest zone of alteration, leading to slope failures, lateral spreading or debris avalanches.

The understanding of volcanic collapses requires a detailed geotechnical characterization, the definition of geometrical distribution of the materials, the analysis of slope evolution and failure mechanisms. In this way, the purpose of this work is to provide new information (e.g. geotechnical studies and numerical modeling), to develop a series of stability scenarios, necessary to accomplish a hazard assessment. Moreover, a risk evaluation will result by the combination of collapse-induced hazard with respect to the element at risk around volcanoes (e.g. population and structures). To raise this purpose, the project is developed by the following steps: 1) revision of existing studies; 2) physical-mechanical characterization of materials at intact rock scale (laboratory tests); 3) generation of a geological and geomechanical conceptual model; 4) numerical modelling of the failure process and sensitivity analysis of the relevant parameters to be used for hazard assessment in similar conditions. Numerical modelling, performed by using different codes, it is mainly focused on the effect of altered rocks content and gravity effects, even if different perturbations such as pore water pressure (e.g. rainfall, vapour and gas), magmatic-hydrothermal processes (e.g. alteration), and regional or local tectonics (e.g. faults, earthquakes and dynamic loading) are included in the model.

## 1.1 Goals

The main goal of this project is a detailed comprehension of the studied phenomena and a development of new capacity of analysing and modelling instability processes related to rock alteration in volcanic environments. Fundamental steps are: the comprehension of predisposing processes of triggering in a volcanic area; the study of physical-mechanical behaviour of materials; the development of instruments of physical and numerical modelling.

The project plans a multidisciplinary approach integrated as follow:

- Engineering geology: geo-mechanical behaviour in general and in particular of weathered materials and on instability processes and their spreading in different environments.

Experimental campaign and laboratory tests for the mineralogical-petrographical and geomechanical characterization of the materials are also based on:

- Data collection: sampling of a wide gamma of alteration in different volcanic rocks (e.g. lava, pyroclastic deposits and ignimbrite flows),
  - Laboratory analysis: a) Quality of the adopted and proposed standards, b) used of advanced testing equipments; c) Design and construction of new experimental apparatuses capable of a complete simultaneous control of different physical mechanical variables (e.g. measurement of p-wave velocity and micro-strain in uniaxial tests);
  - Use of up-to-date non destructive investigation techniques (e.g. X-ray micro CT, Multi Light Scanning, elastic or sonic wave velocity).
  - Use of up-to-date destructive investigation techniques (e.g. uniaxial and triaxial tests, both under stress and strain control, will be completed for materials characterized by different grades of alteration and the changes in sonic velocities will be monitored to study the evolution of damage during loading).
- Volcanology: analysis of structure and its evolution, geometry of feeding conducts and spatial distribution of weathered materials. Bibliographic research for the chosen study areas (see chapter 2).
  - Numerical modelling: analysis of triggering phenomena through numerical modelling of the case studies and development of specific numerical instruments, integrating laboratory rheological test results.
    - Application of numerical codes for the analysis of the stability of volcanic edifices induced by progressive alteration; and phenomena that not are associated to the properties of rocks outcropping at the volcano surface.
    - Analysis of capability and suitability of the model to simulate processes of different type by using variables that have a physical mechanical meaning (obtained from in situ and laboratory measurements).

## 2. STATE OF THE ART

### 2.1 Instability in volcanic edifice

Edifice instability typically occurs in response to one or more triggering agents, including magma emplacement, the overloading or over-steepening of slopes, hydrothermal alteration, climatic effects, and peripheral erosion (Figure 2.1). Similarly, structural failure of a destabilized volcano may occur in response to a number of triggers of which seismogenic (e.g. tectonic or volcanic earthquakes) or magmatic (e.g. pore-pressure changes due to magma intrusion) are common (McGuire, 1996). Several factors have been proposed to trigger the collapse of volcanoes; these may act independently, if the collapse is the product of a predominant factor, or, more commonly, simultaneously, when the collapse results from some hybrid mechanism. According to Voight and Elsworth (1997), these factors are classified as follows: a) inherent factors (e.g. slope forming process history, movement history, seismic damage and its history, initial composition, physicochemical settings and discontinuity system), b) causes that contribute to the reduction in shear strength (e.g. hydrothermal alteration, weathering, changes in groundwater flow regime, pore-pressure changes due to hydrothermal processes, and changes in structure (Voight and Elsworth, 1997)); and c) causes that increase shear stress (e.g. magma pressures, regional or local tectonics, and vibrations from volcanic earthquakes, explosions and eruptive processes) (see Voight and Elsworth 1997, for a complete review).

The detailed studies derived from Mount St. Helens mass movement provide the best documented case to help interpret old, poorly-exposed deposits at volcanoes around the world, moreover, to test diverse gravitational stability methods (e.g. Reid et al., 2000 and Donnadieu et al., 2001). Nowadays, many volcano-collapses have been identified and studied around the world, as example we could mention the large sector-collapses occur in several volcanoes in Kamchatka region, including Shiveluch, Bezymianny, Kamen' and Kliuchevskoy (Ponomareva et al., 1998; Kozhurin et al., 2006; Ponomareva et al., 2006; Dirksen et al., 2006; Melekestsev 2006).

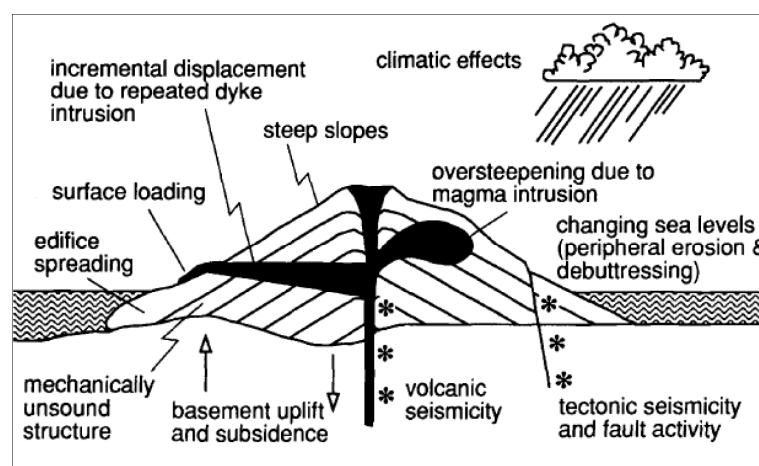


Figure 2.1 Factors contributing the development of structural instability at active volcanoes (McGuire, 1996).



### 2.1.1 Volcano instability induced by magma-intrusion

Preferential fracture patterns at volcanic edifice, can be related to the rates of magmatic input and/or tectonic stresses (dikes lie in the plane of  $\sigma_1$  and  $\sigma_2$  and they open in the direction of  $\sigma_3$ ) (Acocella and Funiciello, 1999; Concha-Dimas et al., 2005; Acocella and Neri, 2009). Moreover, the mechanisms by which magmas ascend and the rates of magma ascent play a critical role in the dynamics of volcanic environment. Several possible mechanisms may contribute to the eventual geometry of a dike propagation pathway and to dike arrest. These mechanisms include stress effects due to topography and dike–dike interaction, as well as the effects of cooling of the magma in a propagating dike (Gudmundsson and Philipp, 2006). Magmatic intrusions in volcanic systems are varied in form and often lead to eruptive activity away from the summit of a host volcano. For example: at Hawaiian shields, dikes are typically injected into rift zones that extend from summit calderas. In contrast, shield volcanoes of the Galapagos archipelago are characterized by dikes that have circumferential and radial orientations with respect to the summit region (Poland et al., 2008). Intrusive arc stratovolcanoes are characterized by radial dikes that are subject to regional stress conditions. On the other hand, magmatic intrusions constitute a major contributory factor in the progressive development of instability, with local seismicity, edifice overpressures, and large changes in hydrothermal circulation.

The behavior of magmatic extrusion is also important, with overload at the surface having the potential to increase instability. When magma is intruded within a saturated porous medium, it strains the surrounding medium. This strain, in turn, produces changes in pore fluid pressures that may dissipate with time Voight and Elsworth (1992). According to Voight and Elsworth (1995) the destabilizing influence of mechanically induced pore pressure is maximized as the intruded width, or corresponding overpressure, of the dike is increased. Magma overpressure [e.g. elevated gas pressures produced by dehydration (boiling) of active hydrothermal systems during volcanic eruption] augments the forces driving failure, and indirectly reduces the resistance along the basal failure plane through several mechanisms of pore fluid pressurization. According to Voight and Elsworth (1997), the fluid pressurization mechanisms directly associated with magmatism include:

- a) pore pressures developed mechanically in porous elastic media around rapidly-intruded dykes. Velocity of dike intrusion and volumetric rate of magma transport depend on several factors; the most important is the thickness or aperture of the sheet intrusion. In some dyke swarms the sheet aperture depends on its dip which, in turn, affects the length of the pathway along which the magma is transported (Gudmundsson and Brenner, 2005).
- b) Thermal expansion of aquifer pore fluids heated by intrusions or by eruption feeder dykes, accompanied by long-distance lateral pressure transmission within aquifer.
- c) Pressurized volatile separation in high-level intrusions, in association with cooling, crystallization, and retrograde boiling processes, leading to hydro-fracturing and/or steam-drive pressure transmission in adjacent aquifers. Voight and Elsworth (2000) have presented an analysis of the mechanics of gas-pressurized dome failure. The authors have developed a model to calculate gas overpressure in a lava dome, and embed these pressures data into instability analyses to demonstrate how gas pressurization can promote deep-seated failure. In addition, physical experiment and numerical analysis of the effects of gas pressurization have been carried out by Thomas et al., (2004). According to the authors, the surface expression and geometry of the failure surfaces resulted from physical experiments appear similar to those observed at Mount St. Helens, Mount Etna, and La Palma; moreover, numerical model

results show that the potential critical failure surface migrates to increasingly deeper levels with increasing internal pressure.

### 2.1.2 Volcano instability induced by regional and local tectonics

Volcano instability may be heavily influenced by cumulative long-term movement on underlying tectonic faults. Where volcanoes are situated above or close to a fault-plane, fractures can propagate through the edifice. As we mentioned above, such superficial faulting also interacts with magmatic and hydrothermal systems and may control its emplacement. In addition, the size and direction of collapse may be heavily influenced by tectonic faulting. Where faults occur in proximity to a volcano, modification to the position and form of faulting within the basement and its propagation through the edifice takes place (Wooller, L. et al., 2003).

At the surface, faulting deforms volcanic edifices, influencing the evolution of structures associated with calderas and resurgence during episodes of unrest, as well as controlling the alignment of vents (Kozhurin et al., 2006). Structural characterization of volcanic edifices and their basement is important to determine potential collapse sectors and sliding mechanism. In addition, strain characterization and, specifically, precise measurements of fractures in volcanic edifice are important because the structural discontinuities represent potential failure zones and because they enhance the influence of fluids (Concha-Dimas et al., 2005).

One of the first papers dealing with the influence of the regional basement stress field on the distribution of volcanic emplacement is from Nakamura (1977). This work provided basic information that will help in understanding the close relationship between regional tectonic stress field and volcanic morphology. For example, the author proposed that cone elongation and alignment of dikes and their surface manifestation occur parallel to the maximum horizontal compressive stress direction (MHC). Moreover, statistical works (Siebert, 1984) bring out the preferred orientation of the axis of avalanche calderas normal to the dominant dike trend, it means that debris-avalanche phenomena occurs perpendicular to MHC (Figure 2.2). The same author emphasize the fact that not all volcanoes show a response to regional stress field, in contrast direction failure in these volcanoes is influenced by other factors, including geometry of internal structures such as pre-existing lava domes and internal fault patterns.

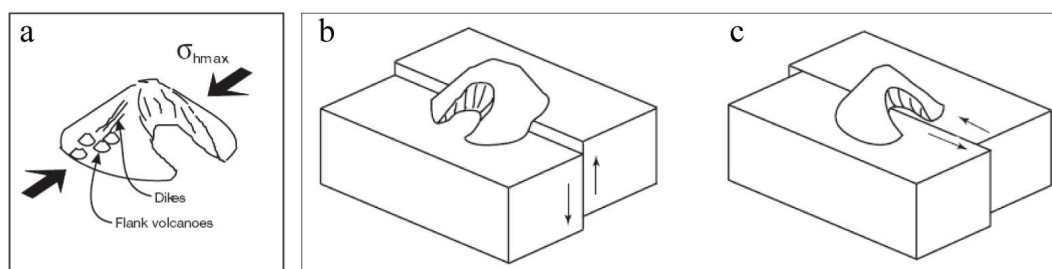


Figure 2.2 a) model relates flank failure perpendicular to the regional maximum horizontal stress direction ( $\sigma_{hmax}$ ), the cone elongation and alignment of dikes (Lagmay et al., 2000). b) model that relates vertical faults underneath a volcanic cone to the flank failure. c) model that relates strike slip faulting underneath volcano cones to the flank failure (Concha-Dimas et al., 2005).

Recently analogue models related to the recognition of the effects of basal displacements have been developed. For instance, Lagmay et al., (2000) explore the effects of strike slip faulting underneath volcanoes, and its role in inducing instability in volcanic structures. The authors used an analogue modelling to determine how brittle deformation occurs in volcanic cones above strike-slip faults by identifying the type of structures developed, their magnitude, location, and rates and extent of propagation. The analogue models describe the geometry and type of structures at volcanoes; for example: sigmoid patterns are so clearly developed on the upper flanks; scarps at the surface formed due to faulting may become accentuated by erosion (Figure 2.2). On the other hand, in terms of rapid destabilization, as in the case of magmatic intrusion, the authors evaluate how brittle deformation influences the path of magma. The regional stress field and structures found on volcanic flanks may be used to predict the collapse direction of volcanoes built on top of strike-slip faults. In addition, Woller et al. (2003) investigate the importance of the cone position above the fault by constructing models with varying degrees of offset. This produces a distinct deformation pattern, often leading to large-volume collapses normal to the fault (Figure 2.3). After all, fault position may be a crucial factor in determining the volume of lateral collapses.

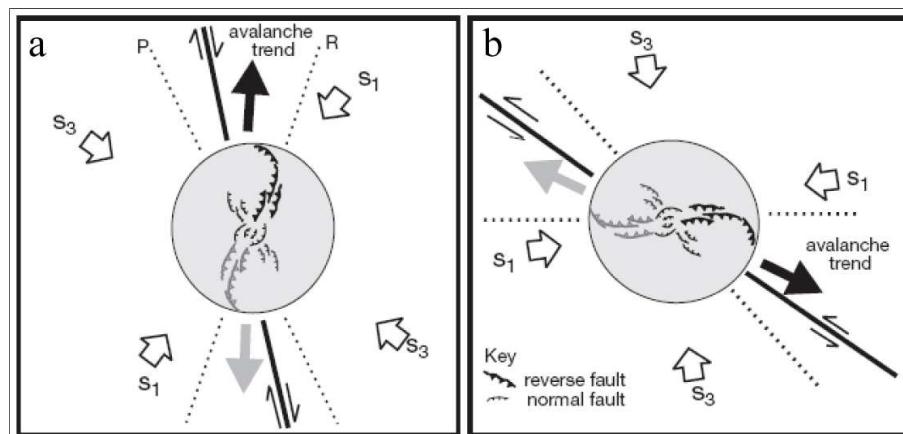


Figure 2.3 Summary of model results for cones overlying strike-slip faulting zones. a) Right-lateral strike-slip fault. b) Left-lateral strike-slip fault.  $\sigma_1$  and  $\sigma_3$  are respectively, the maximum and minimum horizontal stress.  $P$  and  $R$  are synthetic faults generated at acute angles to the main strike-slip shear. From Lagmay et al., (2000).

Vidal and Merle. (2000) have explored the effects of vertical faults underneath a volcanic cone. The authors suggest that reactivation of a vertical fault beneath a cone results in the appearance of a major normal arc-shaped fault that forms gradually and cuts across the upper part of the cone below the summit. The warping, associated with an upturning of the layers deforms the adjacent part of the cone. This upturning may become a reverse fault structure; consequently, the warping of the layers increases its dip, which allows the flank collapse. The deformation is the most intense at the summit of the cone on the deformed flank. The destabilization creates a clear scar with a typical horseshoe-shaped form Figure 2.3.

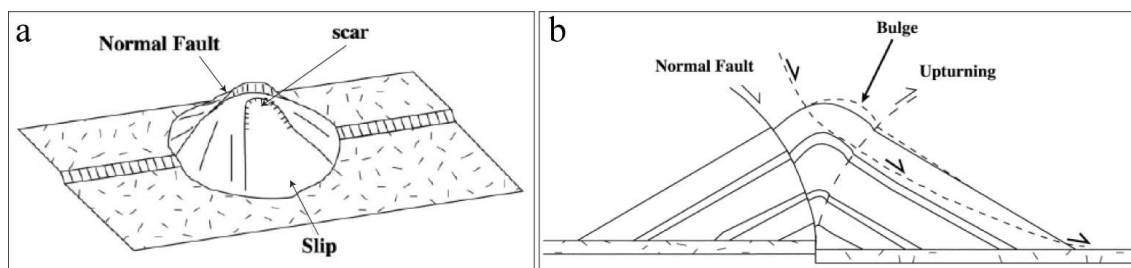


Figure 2.4 a) Formation of a normal fault sector collapse creating a typical horseshoe-shaped caldera. b) Schematic drawing of the deformation of the flank by the vertical faulting beneath a stratified heterogeneous cone. From Vidal and Merle, (2000).

However, the influence of regional tectonics does not imply that large-magnitude fault movement is concurrent with failure, but that instabilities resulting in failure are inherited from movement along the fault over the lifetime of the volcano, concurrent with at least part of the main period of edifice construction (Watt et al., 2008).

### 2.1.3 Volcano instability induced by hydrothermal alteration

Rock alteration implies means changing of the rock mineralogy. The old minerals are replaced by new ones because of a change in conditions. These changes include temperature, pressure, chemical and mineralogical characteristics of the parent rock, and time available for equilibrium. Certain components are selectively leached from the rock and are added to the fluids, and other components are selectively taken up by rock and are removed from the hydrothermal fluid (Barnes, 1979). Hydrothermal fluids ( $H_2S$ ,  $CO_2$ ,  $HCL$ ,  $HF$  and  $H_2O$  as the most abundant) react with volcanic rocks over a broad range of temperatures to produce diverse alteration mineral assemblages (Griffith and Shock, 1995) by passing through the rocks and changing their composition by adding or removing or redistributing components.

The original texture of the rock may be only slightly modified or completely obliterated in this processes. Several periods of alteration, apparently developed at different times, are also common. The fact that the alteration process can change in space and time means that physical properties of rocks also change spatially and temporally. In addition, the substitution of a mineral by one of lower density can also occur, such as clay replacing olivine or pyroxene, and can locally reduce density, porosity and permeability. To the well-documented triggers, hydrothermal activity is recognized to play an important role in weakening the rock mass, reducing its strength and rendering it more susceptible to mechanically induced structural failure. Alteration can extend progressively over long periods (>100 yr), allowing deformation, controlled by the size of altered region, volume and position relative to the edifice. (e.g. van Wyk de Vries et al., 2000; Reid et al., 2001; Cecchi et al., 2005) (Figure 2.5 and ). For example, interbedded volcanoclastic layers within the edifice define weak surface along which landslides can detach, leading to catastrophic slope failure (e.g. Lopéz and Williams 1993; Kerle and van Wyk de Vries, 2001). High fluid pressure in the hydrothermal system favors fracturing and results in a loss of strength. Furthermore, altered rocks are more likely to permit very high pore pressure compared with fresh rocks as cumulative fluid pressure increases can occur in zones surrounded by areas of low permeability (Cecchi et al., 2005). On the other hand, evaluating the hazards associated with hydrothermal alteration is

difficult because alteration has been mapped on few active volcanoes and the volume, distribution, and grade of subsurface alteration is largely unknown on any active volcano. According to (van Wyk de Vries et al., 2000), Casita volcano serves as a general model in which hydrothermal activity is weakening an edifice. Its morphology (deformed convex-concave profile) and its structure are consistent with the deformation of the hydrothermally active volcano core. Deformation of the original constructional shape has generated steepened flanks, and these flanks have begun to fail along the deep basal layer. While the connection between deformation and hydrothermal alteration appears clear at Casita, the relationship between the position and extent of alteration and the style of deformation is unclear (Cecchi et al., 2005). In addition, at Mount Rainer (south-central Washington): the distribution, intensity, and style of edifice-materials alteration were identified as a priority to evaluate hazard of edifice collapse (Reid et al., 2001).

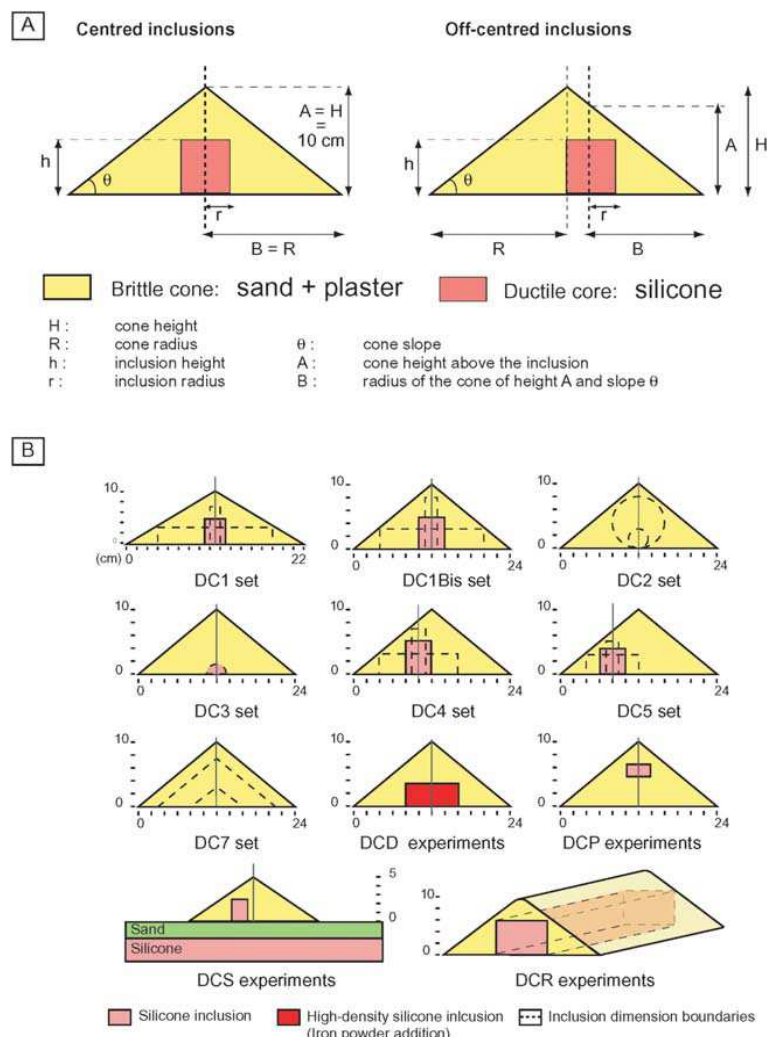


Figure 2.5 Analogue models. a) Sketches of an inclusion centred model and an off-centred inclusion model, with the different important geometrical parameters. b) The different sets of experiments (Cecchi et al., 2005).

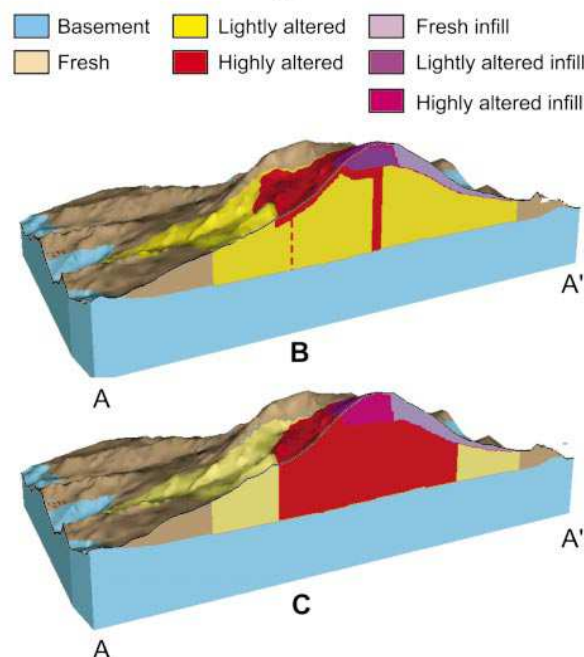


Figure 2.6 A: Three-dimensional perspective with cutaway showing best estimate interpretation of internal edifice geology from detailed geologic mapping and geophysics. Dashed line shows western limit of intense alteration that extends to basement in Sunset Amphitheater north of line of section. B: Three-dimensional perspective showing simplified internal geology if widespread intense subsurface alteration is assumed.

#### 2.1.4 Volcano instability induced by deformation of dipping substrata

Physical and mechanical characteristics of the bedrock situated below a volcano play an important role in volcano deformation and instability as reacting to load in different ways (e.g. compaction, flexure, sagging and spreading). Outward movement of rocks from under the cone by plastic deformation may also occur. According to van Wyk de Vries and Borgia (1996) loading has the initial effect of producing a depression of the basement beneath the volcano, by crustal subsidence and substratum compaction. The main way the volcanic edifice adjusts to deformation of weak basement underneath is volcano spreading, involving subsidence of the central summit part and centrifugal lateral expansion at its peripheries (Szakács et al., 2006); spreading promotes gradual deformation in the volcano, because slopes are reduced and stresses relaxed; deformation in the edifice also favors fracturing and promotes hydrothermal circulation. Evaluating the role of this interplay between basement and volcanoes can also be important in the assessment of natural geological hazards such as landslides and volcanic eruptions. The data of the basement will contribute to a better understanding of how basement structures react to the formation of volcanic cones and calderas (Tibaldi et al., 1995). In addition, analogue models could recreated natural systems at laboratory scale and have been successfully applied to study volcano spreading. As an example we can mention the work presented by van Wyk de Vries and Merle (1996). In this work, the authors recreated the interaction between a volcanic cone, rifting, ductile substratum and regional stresses. They demonstrate, that volcano edifice and ductile substratum are necessary conditions for controlling fault reorientation patterns in rift zone. In fact, the presence of volcanic masses can be so important to create perturbation of the regional tectonic stress field and induce variation in the geometry and kinematics of faulting in the basement.

On the other hand, basal bedrock dipping is important for volcano instability, as it can limit spreading to down slope sectors and increase sector-collapse volumes. Moreover, dip substrata layers strongly control the spreading style and direction (Wooller et al., 2004). Finally, van Wyk de Vries and Borgia (1996) investigated field evidences of volcano deformation controlled by geometry, rheology and boundary conditions of substrata localized below. The authors use finite elements for analyzing volcano deformation and they conclude that the stress imposed on a volcano and its substratum will deform them with a typology that is a function of rheology of the materials involved, of the geometry, and of the boundary conditions of the system; the authors also describe a strong feedback between stress and deformation in the volcano and in the substratum: the deformation of the substratum under the stress imposed by the load of the volcano feeds back stress into the volcano, in turn influencing its deformation.

## 2.2 Debris-avalanche

The volcano history is represented by continued growth with episodes of instability that lead to structural failure (e.g. landslides and debris avalanches) (Lagmay et al., 2000). Debris avalanche is one of the most catastrophic events produced by the slope failure of a volcanic edifice. The term “debris avalanche” is used to refer to the sudden and very rapid gravitational movement (velocities of 80-90 m/s have been calculated at Saint Helens volcano by Voight et al., 1983) of a poorly sorted and incoherent mass of rock and soil, which is moved by gravity and often exceed a cubic kilometer in volume (Siebert 1984). These kinds of event have been regarded as relatively dry, inasmuch as steam, gas or air, rather than liquid water, were considered the dominant pore fluids. In addition, they may occur without warning, move great distances on low-angle slope, cover large areas (area of 98 km<sup>2</sup> have been estimated at Shiveluch by Ponomareva et al., 1998) and generate catastrophic blasts (Brantley & Glicken, 1986).

### 2.2.1 Geomorphic characteristics

Massive landslides create specific morphology and deposits i.e., horseshoe-shaped indents into the edifice and a high, steep-sided break-away scarp having an amphitheatre shape (Ballard et al., 2000). Natural levees, a marginal cliff, and a distal cliff are characteristic topographic features in a well-preserved debris avalanche deposit. In addition, debris avalanches typically form a hummocky terrain with water-filled depressions and steep flow margins, thick hummocky deposits with block and matrix facies of largely unsorted and unstratified angular-to-subangular debris (Figure 2.7a Thouret 1999). Hummocks are variable and irregular in shape; moreover they are divided into three different types based on the relation of block facies to matrix facies Figure 2.7b. Block facies consists of fragments derived from the source volcano. These blocks are fractured (Jigsaw cracks are commonly observed) and deformed but preserve many of the primary textures and geologic structures of the source volcano. Matrix facies is an unconsolidated mixture of all rock types; it contains clasts that range in size from microns to meters (Glicken, 1996). The size of the hummocks and the maximum size of breccia blocks within them tend to decrease away from the source.

Debris avalanches exhibit a horizontal run-out distance ( $L$ ) that can be 5–20 times the vertical fall height ( $H$ ) and that is dependent on the magnitude of the event. The ratio ( $L/H$ ) is termed the “relative run-out” and is a measure of the efficiency of debris-avalanche movement. According to Siebert (1984), the ratio of vertical drop ( $H$ ) to travel length ( $L$ ) range from 0.09 to 0.18 for Quaternary volcanic avalanches between 0.1 and 1 km<sup>3</sup> in volume and from 0.04 to 0.13 for avalanche > 1 km<sup>3</sup>. The ratio of ( $H$ ) and ( $L$ ) for volcanic avalanche is much lower than the ratio for non-volcanic deposits of similar volume; this suggest that low-rigidity perhaps partially fluidized avalanches are capable of travelling great distances. The greater mobility of volcanic debris avalanche can be attributed to the presence of pyroclastic and altered materials, the pre-failure development of fractures due to magma intrusion, and the presence of hydrothermal fluids within the edifice (Voight et al., 1983) (see also Figure 2.8). In contrast, some debris avalanches transform during transport to clay-rich lahars and spread more widely than ordinary debris avalanches. As an example we can mention the existence of long run-out debris avalanche deposits which have been shown at Colima and Citlaltépetl volcanoes, México. The source region for the latter is thought to be centered in hydrothermally altered materials in a water-saturated condition (e.g. Luhr and Prestegard 1988; Stoores and Sheridan 1992; Capra and Macías 2002; and Zimbelman et al., 2004).

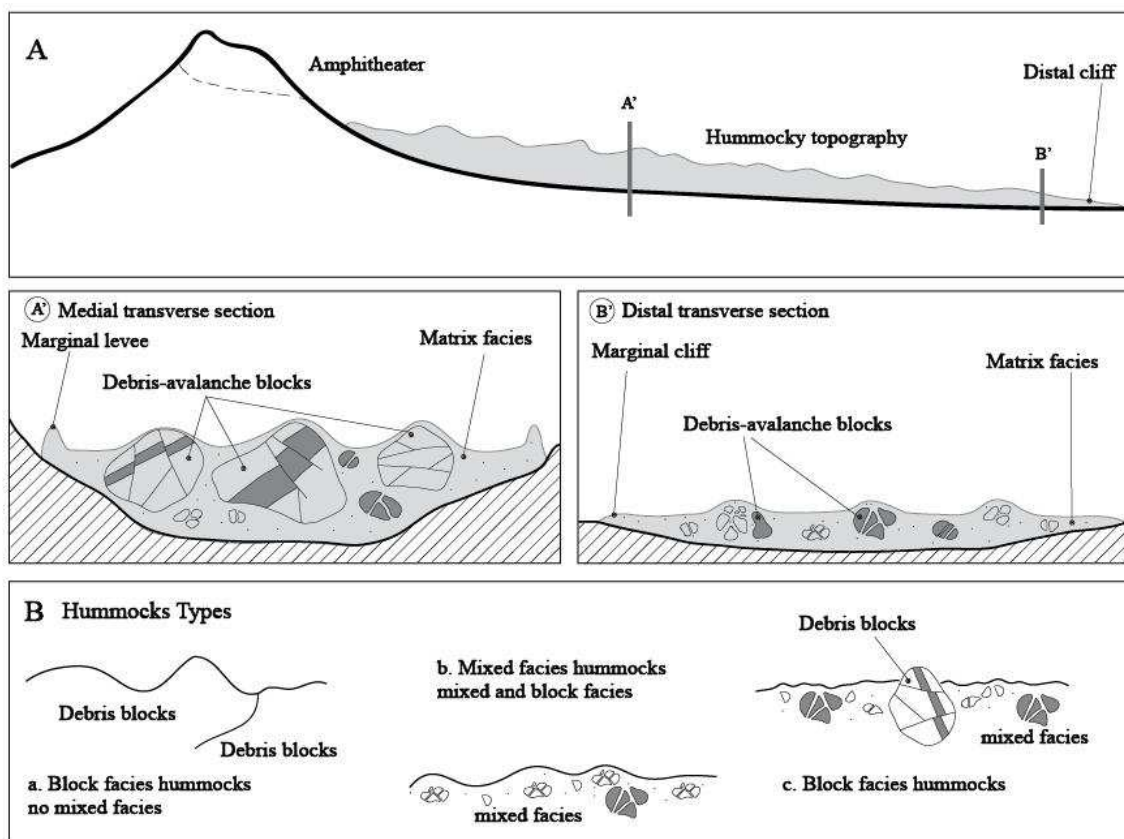


Figure 2.7 Debris Avalanche Schematic Section. a) Longitudinal section stretching from the source amphitheater to the distal end; A' transverse section of the medial region; B' transverse section for the distal region (Ballard et al., 2000). b) Hummocks types. Type a, block facies with no matrix facies. Type b, predominantly matrix facies, debris-avalanche blocks scattered throughout. Type c, debris-avalanche block suspended in matrix facies; matrix facies probably carried debris-avalanche block. (Glicken 1996).

In addition, in literature there are several works related to physical analogue modeling of gravitational spreading (Merle and Borgia 1996; van Wyk de Vries and Francis, 1997; van Wyk



de Vries et al., 2000; Woller et al., 2004; Cechi et al., 2005; Delcamp et al., 2008; Andrade and van Wyk de vries 2010) (Figure 2.9, Figure 2.10), the main goal of some of these studies is establish the size and shape of the substratum segments, weak-cores and magma intrusion that will be detached and expelled from underneath the volcano during collapse (see Andrade and van Wyk de vries 2010); another goal of these physical models is reconstruct the major structures observed in other natural examples like Etna, Colima, Kilauea, Mombacho, and Mt. Saint Helens (e.g. Capra et al., 2002; Morgan et al., 2003; Borgia et al., 1992; Ward and Day, 2006; Shea et al., 2008).

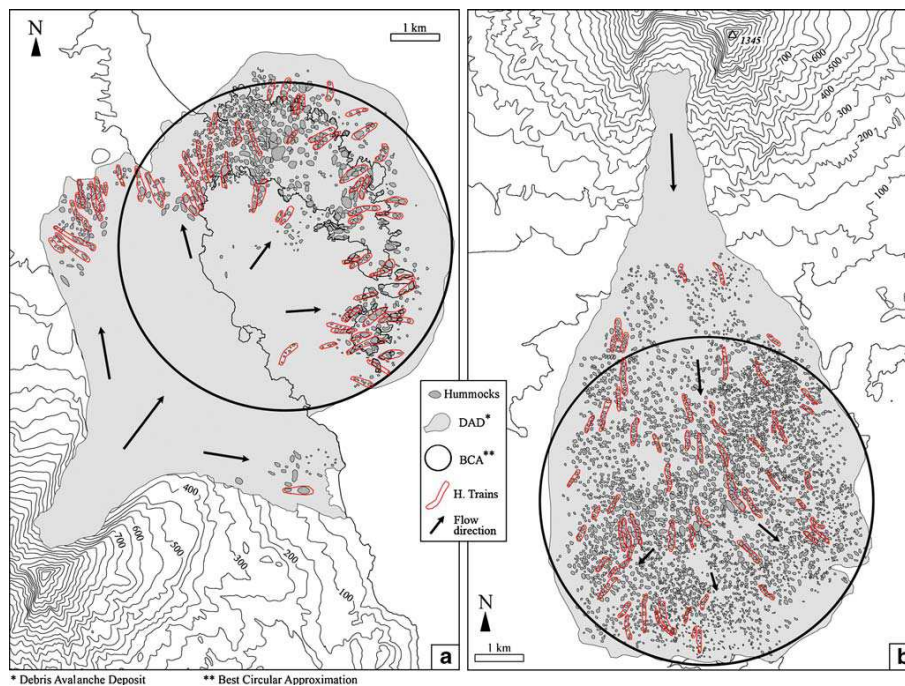


Figure 2.8 a) map of hummock distribution and hummock trains, hummocks are generally large and concentrated in distal zones and, b) at crater, hummocks are smaller and cover a larger area (Shea et al., 2008).

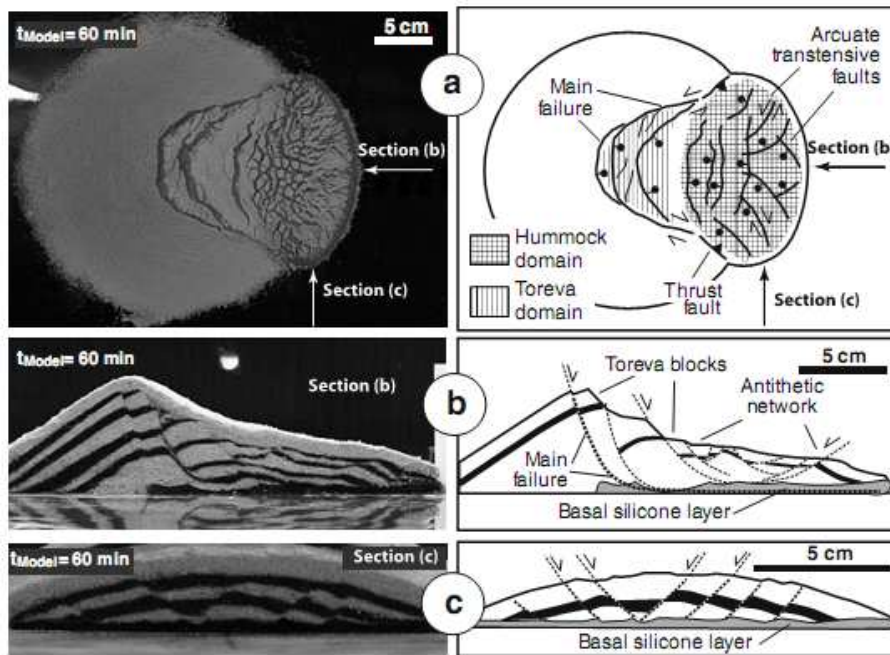


Figure 2.9 a) surface structures, b) longitudinal section, and c) transversal section of analogue model of lateral spreading with  $\alpha=\pi/3$  and  $d/R_{Model}=0$ , at  $t_{Model}=60$  min (Andrade and van Wyk de vries 2010)

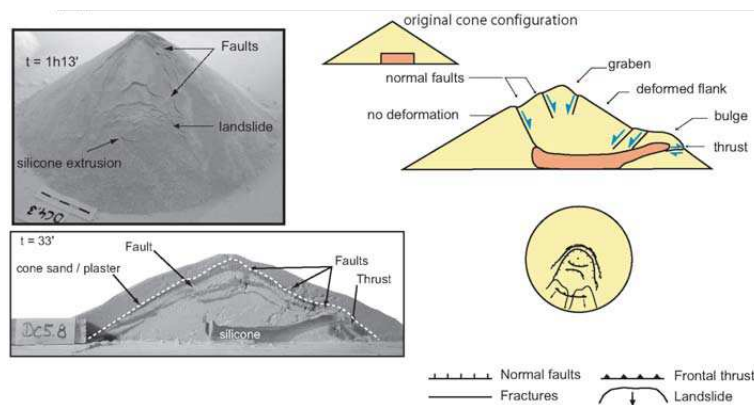


Figure 2.10 Experimental results of analogue modelling: The asymmetric deformation type. Preferential spreading occurs with normal faults developing at the cone summit, sometimes grabens, and thrusts at the front slump. A bulge appears and leads to frequent landslides (Cecchi et al., 2005)

### 2.3 Geotechnical properties of weathered/altered volcanic rocks

In recent years, rock mechanics investigations associated with mechanical degradation have gained more attention worldwide. Parameters, such as rock strength, cohesion, friction angle, dynamic properties, among others, are essential to understand the stability of volcanic terrains (Rodríguez-Losada et al., 2009). These measurements become more difficult if the rocks

encountered are influenced by weathering (drastic modification of mineralogy and texture of the geological materials), as it is considered to be one of the greatest sources of potential difficulties in geotechnical engineering. The analysis of the stability of volcanic edifices or rock masses in volcanic rocks is often problematic because of the variability of the materials (e.g. individual lava flows, pyroclastic deposits, and interbedded units), their heterogeneity, the presence of abundant voids and variable degree of cementation. These characteristics make sometimes extremely difficult to reach a correct and representative characterization of the physical mechanical behavior. As a result, analyses of slope stability and slope evolution are necessarily based on limited geological evidence, laboratory tests only of near-surface materials and simplified numerical models and constitutive laws (Rotonda et al., 2010).

On the other hand, most studies of volcanic-mass wasting around the world have focused on detailed characterizations of debris avalanche deposits, including stratigraphic positions, areas of deposition, travel distances, mechanisms and way of emplacement (Siebert et al 1984; Luhr and Prestegard, 1988; Siebe et al 1992; Stoopes and Sheridan 1992; Glicken 1996; McGuire, 1996; Glicken, 1998; Belousov et al., 1999; Lagmay et al., 2000; Capra et al., 2002; Melekestsev 2006). In recent years, some investigations have enhanced the importance of physical and mechanical behavior of weathered/altered volcanic rocks (Lumb 1983; Moon 1993; Moon et al., 2005; Tommasi et al., 2007; del Potro and Hürlimann 2008; del Potro and Hürlimann 2009; Rodríguez-Losada et al., 2009; Marques et al., 2010), that control initial failure, rock mass and shear strength for fresh and hydrothermally altered rocks (e.g. lava flows and pyroclastic deposits) as well as rock structure (Watters et al., 1997). Many of the more difficult geotechnical problems arise when conditions preclude simplification and appreciation of the behavior of natural material provided a better understanding of the limitations to the idealizations often used in the analysis (Morgenstern and Cruden, 1977). Strength assessment of volcano requires a geotechnical characterization of individual units, using field and laboratory measurements. Characterization of individual units is not easy because of their great variability and heterogeneity, as a result of their geological and altered history (Irfan, 1999). In this way, an appreciation of the material behavior requires an intimate understanding of the geological history of the site and therefore an evaluation of geotechnical complexity (e.g. weathering processes) (see Morgenstern and Cruden, 1977) with the geological mapping and interpretation of the site. This is way; some scientists have enhanced the importance of grouping volcanic materials into geotechnical units, based on the degree of alteration.

Rock weathering can be described following a relatively simple scheme compiled from recommendations given in BS 5930 (1981), or from more elaborated schemes of which BS 5930 (1999) is an example (see table 1, 2 in appendix 1). Descriptive terms for weathering of rock material were established on the basis that weathering involves a combination of mechanical disintegration and chemical decomposition. The factors entering into the description of weathering are the condition of the discontinuities and of the intact material between the discontinuities. Weathering is a gradational feature; this is why, it is necessary to impose boundary conditions within them so they are divided into various grades defined by a range of characteristics (see Dearman 1981 and Price 2009). Otherwise, as Dearman (1981) mentions; the BS 5930 (1981) descriptive scheme for weathering is too restricted in scope and not easily applicable to a wide range of rock types and structural situations. Any scheme of description and classification of weathered rocks has to take into account the fact that minerals in rocks respond differently to the weathering process; consequently properties that govern geotechnical behavior (e.g. Strength and deformability) vary across a wide range. Lee

and de Freitas (1989) have reviewed the commonly occurring difficulties associated with the description and classification of weathered granite. The proposed rock classification is based on both qualitative geological information obtained by visual inspection of chemical decomposition (e.g. the decomposition of biotite and feldspar) and physical disintegration (e.g. microfracturing) in hand specimen, and qualitative mechanical information derived from manual tests. Irfan (1999) examines the applicability of various quantitative weathering indices from the results of chemical and petrographical analyses, in characterizing the degree of weathering of fine-grained volcanic rocks (e.g. weathering potential index and weathering product index among others. see Irfan 1996). Ohta and Arai (2007) used chemical weathering indices to characterize weathering profiles and determine the extent of weathering in igneous rocks. The authors present an alternative statistical index of chemical weathering, extracted by the principal component analysis of a dataset derived from un-weathered igneous rock and their weathering profiles. However, to define mineralogical and chemical changes, many geochemical weathering indices have been discussed in literature (Duzgoren-Aydin et al. 2002; Duzgoren-Aydin and Aydin 2003; Price and Velbel 2003; Ohta and Arai 2007). Nevertheless, despite their influence on volcanic stability, the relationships among physical and mechanical characteristics of weathered/alterated volcanic rocks are complex and still poorly understood. Physical and mechanical properties of the rocks are greatly influenced by alteration grade and the presence of voids in the rock, especially microcracks.

The influence of alteration degree on strength in rocks have been previously discussed by many authors (e.g. Lump, 1983, Kate 1993, Al-Harathi et al., 1999; Tillerson and Nimick, 1984; Hudyma et al., 2004; Gupta and Rao, 2000, Avar and Hudyma, 2007, Marques et al., 2010) In these articles, it is well established that strength is controlled by porosity, the abundance of macro-pores and the pore structure and size distribution. Among other things, the authors also discussed the correlation between strength and some physical properties like rock density, modulus of elasticity, compressive waves velocity, and saturation water content. Recently, the structure and sizes of different particles (e.g. clasts and minerals) have been characterized by X-ray tomography and two-dimensional images. Some works describe automated methods to extract grain characteristics (Sahagian and Proussevith 1998; Butler et al., 2000; Gualda and Rivers 2006) and others applied image analysis procedures to quantify heterogeneity in clastic rocks (Geiger et al., 2009). Variation of rock structure could also be detected and quantified by the use of compressional ( $V_p$ ) and shear ( $V_s$ ) wave velocity (Vinciguerra et al., 2009; Marques et al., 2010), but this velocity-medium rock relationship becomes complicated when micro-cracks exist in the rocks, because the elastic properties of a rock are more affected by the micro-cracks than by open porosity (Sousa et al., 2005; Martínez- Martínez et al. 2006).

On the other hand, scientists recently realized the importance of grouping volcanic materials based on alteration degree. Mass wasting studies at Cascade Range volcanoes (Mount Rainier, Mount St. Helens, and Mount Shasta) proposed a linkage between volcano collapse, landsliding, and hydrothermal derived clay minerals (Watters et al., 2000). The authors describe a methodology for obtaining rock strength values that control initial failure by applying rock mechanics classifications (e.g. Rock Mass Rating System RMR Bieniawski, 1989) and structural information obtained from field studies. Moon et al, (2005) analyze the geotechnical properties of jointed lava flow units from an active island stratovolcano in Bay Plenty, New Zealand. In this paper, RMR and Geological Strength Index (GSI) values (Marinos and Hoek, 2000) were calculated and converted to Mohr–Coulomb strength parameters using the Hoek–Brown criterion. Moreover, back-analysis of known landslide scarps was used to derive strength parameters for brecciated rock and hydrothermally altered

rock masses. Concha-Dimas and Watters et al. (2003) made a geotechnical study concentrated on obtaining intact rock properties (UCS,  $m_i$ ,  $s$ ) samples with different degrees of hydrothermal alteration. The alteration classification was based on visual observation of alteration, as described in Watters and Delahaut (1995). However, more papers focused on physical and geomechanical behaviour of volcanic rocks (e.g. Karpuz and Pasamehmetoglu, 1997; Morales et al., 2004; Cecchi et al., 2005; Tommasi et al., 2007), and all consider that one of the major uncertainty in slope stability analysis takes place in the strength values used to represent volcanic rock masses. Recently, Del Porto and Hürlimann (2008) propose a general classification for volcanic material; the authors combine and adapt standard geotechnical classifications and those suggested by different authors (e.g. Moon et al, 2005). The authors provide a combination of new data from the slopes of Teide stratovolcano in Tenerife, Spain, and data from literature review which was normalized to provide average strength values for each geotechnical unit. The global unifying geotechnical classification of volcanic material uses four main geotechnical units, (lavas, autoclastic breccias, pyroclastic rocks and volcanic soils) and this classification is subdivided on the basis of hydrothermal alteration, welding and interlocking. In addition, these authors enhance the importance of proposing a new geotechnical classification scheme for volcanic materials. They conclude that this scheme may be a more systematic approach to quantifying the material strength, which is an important step towards assessing the stability of volcanic slopes (improvement of values used to model processes on volcanic edifices). In contrast, the paper is unclear about intended applicability of this classification to other areas outside of Teide stratovolcano. Moreover, very important physical and mechanical rock characteristics as mineralogy and its changes are forgotten, this could completely change the behavior of materials. Otherwise, considering the peculiarities of volcanic environment and volcanic products, specific geotechnical characterization should be performed for every single case.

### 3. SAMPLING SITES

The analysis of the stability of volcanic edifices or rock masses in volcanic rocks is often problematic because of the variability of the materials (e.g. individual lava flows, pyroclastic deposits, and interbedded units), their heterogeneity, the presence of abundant voids and variable degree of cementation. These characteristics make sometimes extremely difficult to reach a correct and representative characterization of the physical mechanical behavior. Volcanic rocks are frequently composed of both matrix material and pores, and they are often found in altered/weathered conditions because of the highly active volcanic environment and the presence of hydrothermal conditions. Generally, the strength, the deformability and stiffness of these rocks shows a dependence on the porosity. Porosity can be formed by voids, between grains or minerals, of different size and shape, with a particular frequency distribution of size and it can be interconnected or disconnected. Various researchers investigated the physical mechanical behavior of rocks as a function of their porosity.

Volcanic rocks (e.g. basalts, scoriae, lithophysae-rich tuffs, tuffs and pyroclastic deposits) often present a brecciated, porous or vesicular texture characterized by abundant vesicles and pores, with different sizes, that sometimes are filled with secondary minerals (Al-Harthi et al., 1999, Tillerson and Nimick, 1984, Hudyma et al., 2004). Previous studies on similar rock lithology suggest that the compressive strength is controlled by total porosity, the abundance of macro-pores and the pore structure and size distribution as well as the type of forming particles (Luping, 1986; Nimick, 1988; Al-Harthi et al., 1999; Price et al., 1994; Aversa and Evangelista, 1998; Avar et al., 2003; Avar and Hudyma, 2007; Hudyma et al., 2004).

The Phlegraean Fields (Solfatara and Ischia volcano) and Bolsena volcano have been selected as test sites of the geotechnical analysis. These places represent excellent settings to study the evolution of physical and mechanical properties in weathered/altered volcanic rocks (e.g bulk density, p-s wave velocities, geometry and topology of pore network and grain size and shape, uniaxial and tensile strength, cohesion and friction angle).

This chapter is divided into three main parts. The first part includes a brief description of the geological setting of the Solfatara, Ischia and Bolsena volcanoes (Figure 3.1), including structural, morphological and hydrothermal characters. In the second part of this chapter, description of study areas and sampling are presented. The third part, include the petrographical study of all series. Description of each single phase of alteration and the mineralogical and petrographical changes are also included. Finally, a summary of the most important field characteristics for all samples are included as tables (Table 3.1, Table 3.2 and Table 3.3).

#### 3.1 Brief geological description of Solfatara

Solfatara is part of the Phlegraean Fields volcanic area which in turn belongs to the Campanian province. It is located near the city of Naples and represents the southernmost sector of the plio-quadernary volcanic belt along the Italian peninsula (Washington, 1987). The Phlegraean Fields caldera is an active volcano, dominated by phreatomagmatic eruptions in which magma interacts with surface water, primarily sea water or deep aquifers beneath the

caldera. The Strombolian and Plinian eruptions produced the largest volumes of material (Brand, 2008). The calderas have been affected over the last 60 ka by an intense volcanic activity and at least two caldera collapses. The oldest caldera collapse is related to the eruption of the Campanian Ignimbrite (39 ka), whereas the youngest one, is related to the eruption of the Neapolitan Yellow Tuff (15 ka). The volcanism younger than 15 Ka has been characterized by several explosive events which generated a large number of cones and craters, which represent the main feature of the area (Orsi et al., 1996). The last period of intense volcanic activity of the Phlegraean Fields occurred between 4.8 and 3.8 kyr BP. The volcano of Solfatara (Figure 3.1) was formed during one of the last eruption of this period between 4.1 and 3.8 kyr BP (Di Vito et al., 1999). The volcano of Solfatara is a hydrothermal altered tuff cone which suffered a typical post eruption caldera collapse. It is the only currently active centre in the Phlegraean Fields. In the caldera there are fumarolic fluids (Figure 3.3), which according to the geochemical model of the hydrothermal system proposed by Caliro et al. (2007) are mixture between fluids degassing from magma body and the vapour generated at about 360°C by the vaporization of hydrothermal liquids. These authors also reveal that recurrent seismic activity, ground uplift, ground deformation and slow seismic periods of subsidence are triggered by periodic injections of CO<sub>2</sub>-rich magmatic fluids at the bottom of the hydrothermal system. Solfatara crater is made up of a sequence of pyroclastic deposits: at the base is a phreatomagmatic breccias overlain by pyroclastic-flow deposits. These products also cover the Accademia dome, which have been previously emplaced (Giacomelli and Scandone 1992). In addition, Cipriani et al. (2008) studied the pyroclastic sequence from Solfatara. From the combined interpretation of in situ data, SEM, XRF and grain-size analysis, the authors suggest that eruptive activity in Solfatara changed from phreatomagmatic to magmatic repeatedly throughout the eruption. From compositional point of view, the authors classified the juvenile fraction of pyroclastic sequence as trachytic; similar to the eruptions of Phlegraean Fields occurred in the last 5000 years, particularly those from Astroni volcano and Accademia dome.

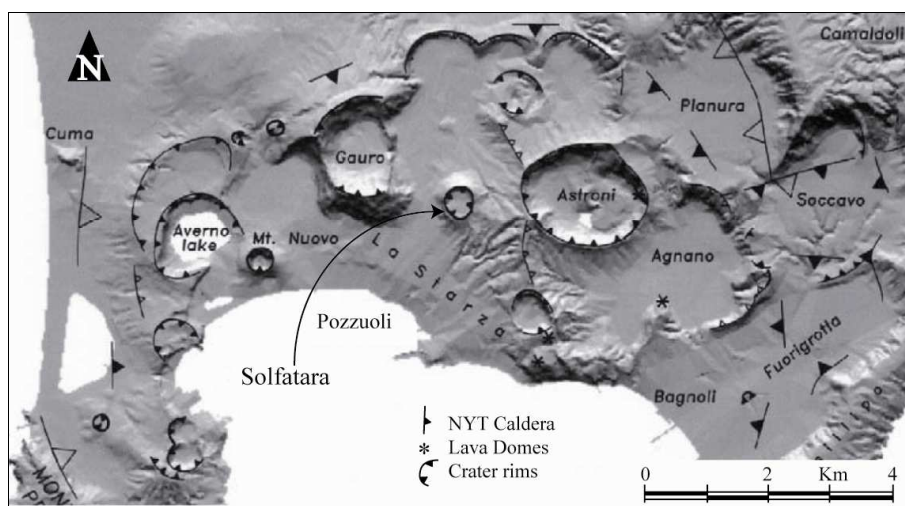


Figure 3.1 Localization map of Solfatara. Some structural features are included in the map. Modified from Isaia et al., 2004.

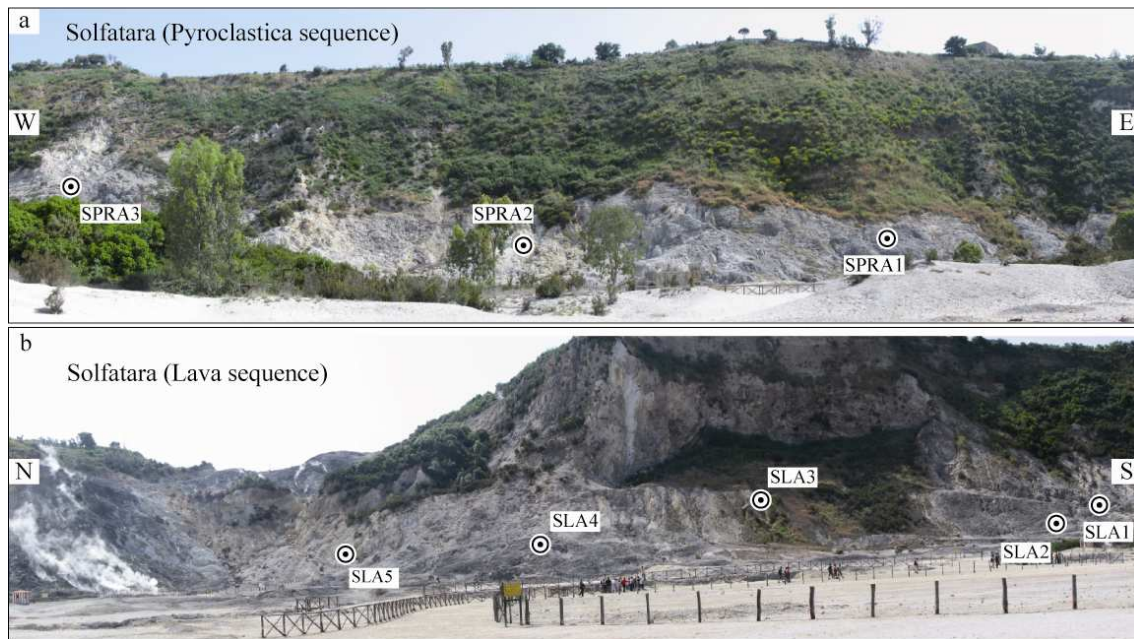


Figure 3.2 Location map of field study area (Solfatara). a) Outcrop of Pyroclastic sequence. b) Outcrop of lava sequence. The solid circles indicate the sampling points.



Figure 3.3 Active fumaroles inside Solfatara caldera. Contact between pyroclastic and lava sequence is also visible.

### 3.2 Brief geological description of Ischia

Ischia is located 35 Km west of the Gulf of Naples and it represents the remnants of a larger volcano. Ischia is one of the active volcanic areas belonging to the so-called Neapolitan volcanic region, including the Campi Flegrei caldera and Mount Vesuvio (Cipriani et al., 2008). The structural setting of the island has been determined by deformations induced by both regional tectonics and volcano-tectonics. The regional tectonics is the cause of two main fault systems with NW-SE and NE-SW directions (Vezzoli 1988). Stratigraphic studies and radiometric dating indicate four phases of activity. The oldest rocks (<150 ka) consist of intercalated pyroclastic and lava. This sequence underlies lava domes of the 150 – 75 ka phase (e.g. Gillot et al., 1982, Chiesa et al., 1987, Civetta et al., 1991 and Orsi et al., 1992).



New geological data (Sbrana et al., 2009) show that after the second phase (73 – 56 ka) intense explosive volcanic activity occurred with numerous trachytic Plinian and ignimbrite-forming eruptions that led to the formation of a caldera. The last caldera-forming eruption originated the Green Tuff, a welded pyroclastic flow deposit emplaced 56-55 ka in the Monte Epomeo area (Figure 3.1). The Green Tuff was followed by a third phase of explosive and effusive eruptions at different centers from 55 to 20 ka (Gillot et al., 1982; Chiesa et al., 1987; Civetta et al., 1991; Orsi et al., 1992). In this phase, large volumes of welded and unwelded ash-flow tuffs were deposited inside the caldera and around the island, across the Campi Flegrei area. The last phase of volcanism of Ischia, from 10 ka to 1302 AD, originated lava and pyroclastic deposits from N-S-aligned vents on the eastern side of the island, where normal faults bound the eastern edge of the Mt. Epomeo resurgent block (Orsi et al., 1991). The resurgence of this block occurred from 55 to 5 ka, exposing the Green Tuff deposit on the north-western flank of the Monte Epomeo (Sbrana et al., 2010). The faults bounding the resurgence block are associated with still active intense fumaroles. Actually, the Green Tuff deposit is subjected to strong hydrothermal alteration, which is visible along the Monte Epomeo fault scarps (Figure 3.13).

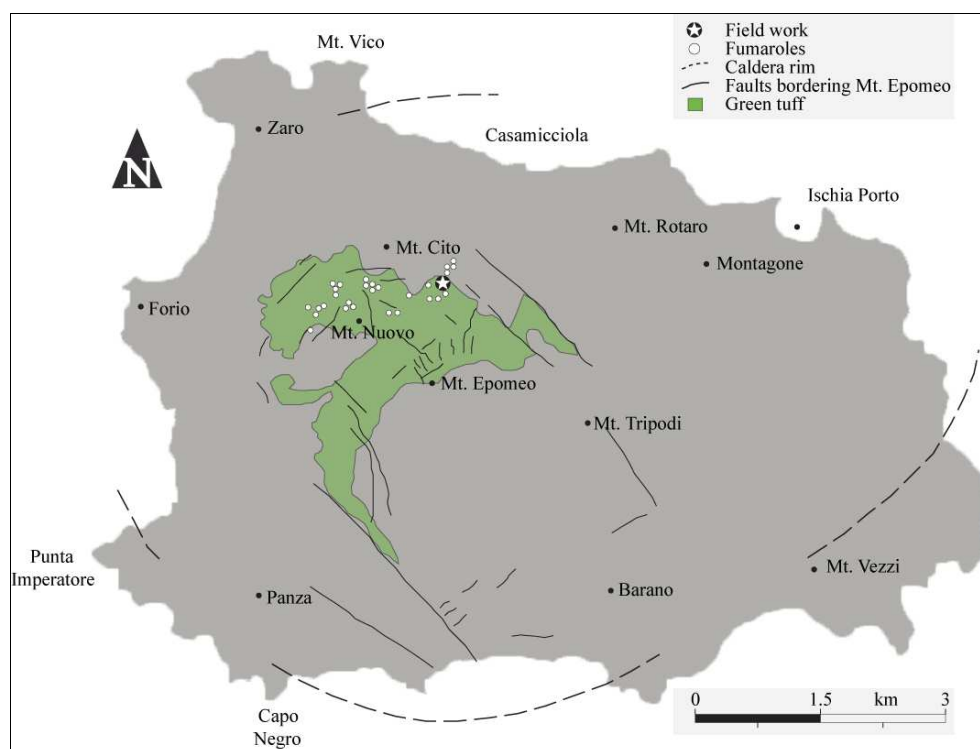


Figure 3.4 Localization map of field study area (Ischia). The solid circles indicates the position of field study where samples were collected.

### 3.3 Brief geological description of Bolsena volcanic zone

Bolsena volcanic zone, where samples were collected, is part of The Vulsini volcanic District which in turn belongs to the northern part of Quaternary Roman Volcanic Province (QRVP); this province extends from southern Tuscany to Campania (Beccavula et al., 1991). According to Nappi et al. (1991), the Vulsini Volcanic District (VVD) is made up of four

volcanic complexes (Paleo-Bolsena, Bolsena, Montefiascone and Latera), characterized by one or more eruptive cycles, which are summarized as follow: the initial phase, mainly effusive with lava flows and associated Strombolian activity; explosive activity, predominantly of Plinian type, at the intersection of major regional faults; final phase, marked by volcanic collapse and associated hydromagmatic and magmatic activity. Bolsena volcanic zone (BVZ) is localized in the eastern part of VVD. According to Nappi et al. (1998) ten eruptive phases, characterized by a wide range of magma compositions, have been recognized in this area. The oldest products, attributed to Plinian-type activity, have been dated at  $576 \pm 6.5$  ka; but most of the BVZ volcanic products are younger than about 400 ka (Nappi et al., 1995). Otherwise, the outcropping rock of this study area is comprised in the last two eruptive phases. According to Nappi et al. (1998), the penultimate phase is characterized by several lava flows and scoria cones with large amounts of calcic plagioclase, augite, and nepheline or leucite (Leucitic Tephrite in composition). The last phase is mostly represented by effusive activity. Trachytic Plinian pumice fall and trachytic ignimbrite were emplaced from a source located in NE sector of the Bolsena caldera (Nappi et al., 1994).

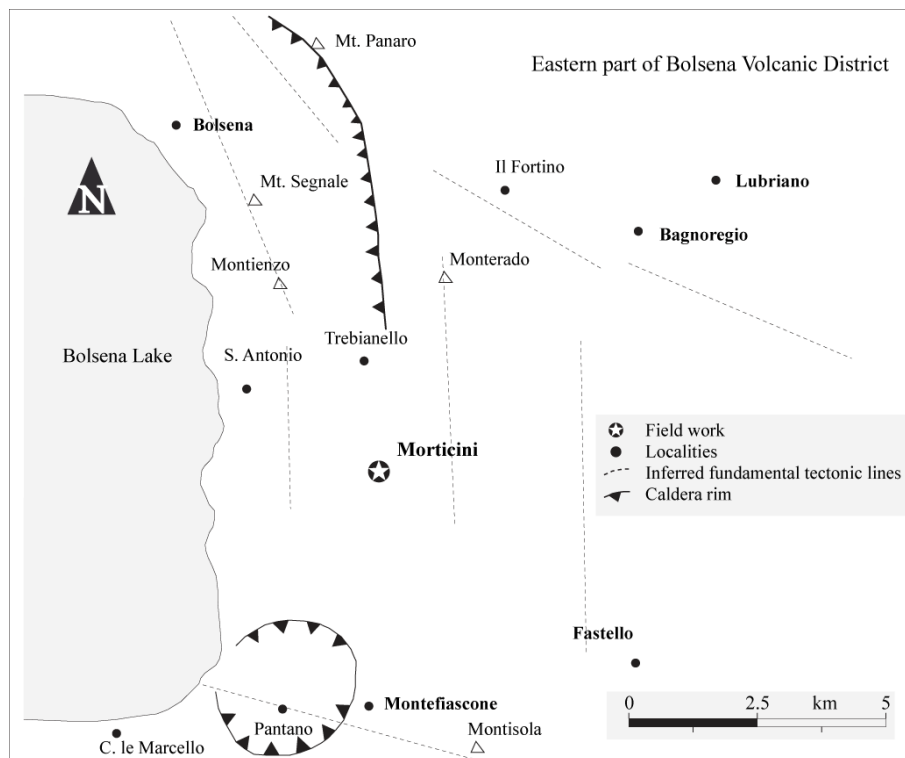


Figure 3.5 Localization map of field study area of Bolsena. The star indicates the position where samples were collected (After, Nappi et al., 1998).

### 3.4 Sampling

Different weathered/altered volcanic rocks characterized by different degrees of alteration were collected from Solfatara, Ischia and Bolsena sites. We have chosen these sites, because they provide an excellent setting to study the mechanical evolution with respect to physical properties (e.g. geometry and topology of pore network) in weathered volcanic rocks.

The research work, pertaining to the rock mechanics characteristics of volcanic rocks in relation to the degree of weathering, was carried out in two phases. The first phase includes

field investigations and the second phase involved laboratory tests. Field investigation includes a field work where a total of thirteen block samples of volcanic rocks (lava and pyroclastic rocks) were collected. Sampling was focused on covering the entire range of alteration range of each unit and each sample consists of a block weighting between 30 to 50 kg and with a minimum thickness of 15 cm to allow coring of samples at least 5.4 cm in diameter and 13 cm high. In general all the samples have a size much larger than both the larger and average particles/crystal and pore at their interior (1-2 cm). The operational procedures and initial description of alteration followed the BS standard methods (BS 5930, 1999) (Appendix 1). From such a description rocks samples were classified as fresh (F), slightly weathered (SW), moderately weathered (MW), highly weathered (HW), completely weathered (CW) and residual soil (RS). A first classification was based on visual description of the following factors: degree of discoloration, presence of original texture, degree of physical disintegration, among others (Table 3.1, Table 3.2, Table 3.3) (see Lee and Freitas, 1989; Irfan T.Y., 1999; and Haskins and Bell 1995 for a good review). Samples were marked according to the origin and alteration grade. Mineralogical and petrographical changes in samples, which represent different and progressive weathering grades were examined by optical microscopy, moreover, all descriptions were completed by X-ray diffraction and X-ray fluorescence data.

### 3.5 Petrographical study

Mineralogical and petrographical changes in samples, which represent different and progressively increasing weathering grades, were examined by means of optical microscopy, X-ray diffraction and X-ray fluorescence analyses. The weathered/altered volcanic samples have been studied by means of thirteen thin-sections which can be considered as representative among rock blocks collected in fieldtrip. Thin-sections were prepared and studied following standard methods. The analyses include a basic petrographical description, visual estimation of grain size, sorting, porosity varieties, mineral abundances and fabric. Petrographical changes in samples were pointed out and were illustrated, some in plane-polarized light (PPL), and some others in cross-polarized light (XPL). All descriptions and petrographical characterization were performed on the basis of the descriptive system in MacKenzie et al. (1990) (Figure 3.14). Petrographical description derived from thin-section analyses was reinforced by X-ray powder diffraction (XRD) technique and X-ray fluorescence. XRD is one of the most powerful techniques for qualitative and quantitative analysis of crystalline materials. The technique provides information as nature of crystalline phases present, degree of crystallinity and amount of amorphous content. These results were represented graphically in diffractograms (Figure 3.14). The identification of minerals was performed by comparing X-ray diffraction pattern with a database (power diffraction file) implemented in the X-ray diffraction system. In addition, by plotting the results of chemical analysis on TAS diagram, the rocks in SLA and IGT series were classified as trachy-dasitic in composition. In contrast, SPRA, BoPRA and the most altered samples of SLA series were not classified because of the high percentage of SiO<sub>2</sub> content promoted by high grade of alteration (Figure 3.6).

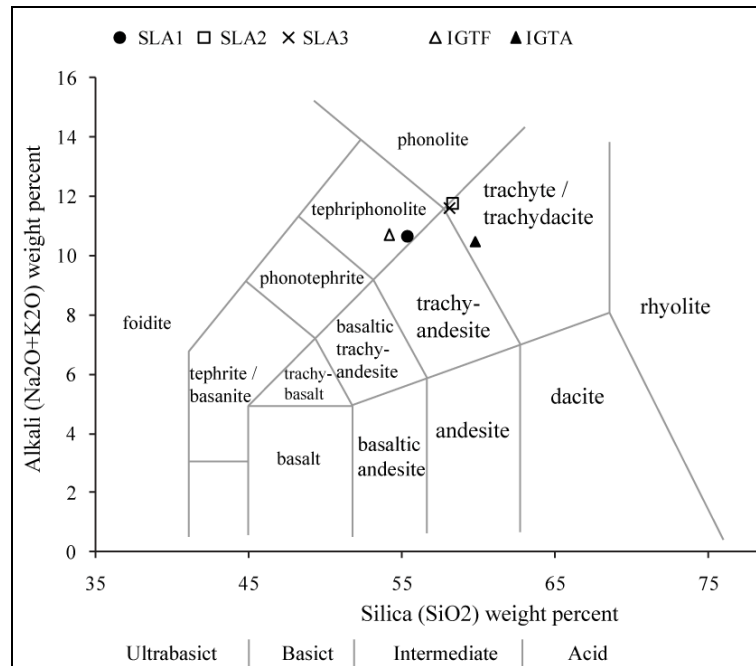


Figure 3.6 TAS diagrams (Total Alkali vs. Silica) for volcanic rocks from Solfatara, Ischia and Bolsena.

### 3.5.1 Lava from Solfatara (SL)

The lava rock mass from Solfatara is heavily fractured, joints are often infilled of loose material and are strongly altered suggesting that widespread fumarolic and thermal springs activity followed preferential pathways (Figure 3.7). Discontinuities are often of very small size and sometimes not visible with a naked eye. Outcrop observations show that altered lava varies significantly on a short distance especially when approaching to fumarolic activity. We easily identified the effects produced by hydrothermal alteration: the rock fabric and texture in some places are completely lost making the in situ identification of the original rock very difficult. In the following we describe the petrographical characterization of the altered samples.

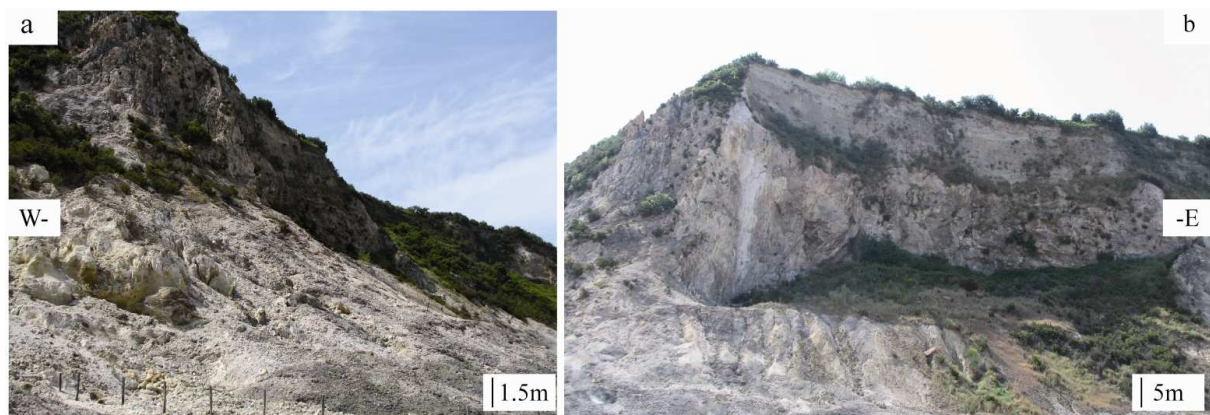


Figure 3.7 Heavy fractured lava sequence from Solfatara; lava varies significantly on a short distance especially approaching to fumarolic activity

*Fresh lava SLA1*

This represents the less altered sample of the studied sequence. The sample has a porphyritic texture (P.I. = 30%) in which predominantly euhedral phenocrysts are plagioclase with an average size of 3 mm. Sample major constituents are sodic plagioclase (oligoclase and andesine) and potassic feldspar with minor amounts of pyroxene and a small amount of biotite. The matrix presents a sub-parallel arrangement of micro-pyroxenes and micro-plagioclases (pilotaxitic texture) with 200 and 100  $\mu\text{m}$  of maximum size respectively. Micro-plagioclases represent the 60 % of the matrix, while micro-pyroxenes represent just the 30 %. Remaining part of the matrix is composed by 5 % of pores and 5 % of argilization stains. Two main types of alteration are observed: oxidation within the boundary of most minerals, affecting all biotite crystals, and as stains into the macles of plagioclases; argilization is presented in the matrix and around minerals as blurred stains. Significant variation in the mineralogy throughout the weathering sequence was identified by x-ray diffraction data. In this way, mineralogical changes along all weathered/altered sequence were identified by interpreting the values of characteristic peaks of diffractograms. According to Figure 3.9, SLA1 sample contains mainly sanidine, nepheline, and pyroxene (Augite). Small peaks of biotite and albite are also identified.

*Slightly weathered lava SLA2*

Second grade of alteration presents a trachytic texture in which predominantly euhedral phenocrysts are sanidine with an average size of 4 mm, minor amount of plagioclase with an average size of 1.5 mm, and a small amount of pyroxene and biotite with an average size of 0.8 and 1.2 mm, respectively. The matrix is composed principally by micro-plagioclases (sanidine) and microcrystals of biotite with 200 and 70  $\mu\text{m}$  of maximum size respectively. Micro-plagioclases represent the 60 % of the matrix, while biotite represents just the 20 %. Remaining part of the matrix is composed by 5 % of pores with 35  $\mu\text{m}$  of maximum size and 15 % of argilization stains. In this sample we can observe argilization and oxidation along micro-fractures and within the boundary of minerals. Biotite is almost totally replaced. According to diffractograms presented in Figure 3.9, this sample contains mainly sanidine. Peak of biotite and pyroxene (augite) shows a slight reduction in its intensity. Small peaks of gypsum and hematite are present.

*Moderately weathered lava SLA3*

This sample represents the third grade of alteration. Its major constituents are potassic feldspar (sanidine) with minor amount of sodic plagioclase and a small amount of pyroxene, 1.2 mm as maximum size; biotite is almost missing. Relatively large crystals of sanidine (2 mm of average size) are surrounded by micro-plagioclases and micro-pyroxenes. The matrix is composed principally by micro-plagioclases and micro-pyroxenes with 90 and 30  $\mu\text{m}$  of maximum size, respectively. Micro-plagioclases represent the 60 % of the matrix, while pyroxenes represent just the 10 %. Remaining part of the matrix is composed by 5 % of pores with 70  $\mu\text{m}$  of maximum size and 20 % of argilization stains. In this sample, oxidation

increases affecting all crystals boundaries, whereas biotite and pyroxene are almost completely replaced (Figure 3.8) Argilization is present into the matrix and all around minerals as blurred stains. According to diffractograms, presented in Figure 3.9, this sample contains mainly sanidine. Peaks of biotite and pyroxene (augite) show a slight reduction in its intensity. Small peaks of gypsum and hematite are present.

#### *Highly weathered lava SLA4*

This sample represents the fourth grade of alteration. Although all minerals are altered, sanidines prevail over pyroxenes and plagioclases. X-ray power diffraction shows that alunite (derived from acidic alteration of potassic feldspar) is very abundant. Matrix is totally replaced by argilization and a new process of silicification can be observed into the potassic feldspar and within the matrix. Silica-amorphous minerals with 40  $\mu\text{m}$  of maximum size appear all around the sample. According to diffractograms presented in Figure 3.9, this sample contains mainly sanidine, even if their peaks show big reduction. Peaks of biotite and pyroxene disappear; on the contrary peaks of alunite and amphibole can be identified.

#### *Totally weathered lava SLA5*

Complete alteration of all minerals occurs at this alteration grade, but some pyroxenes can still be recognized from its partially-distorted geometry. Matrix is totally replaced by argilization and silica-amorphous minerals, with 40  $\mu\text{m}$  as maximum size, can be observed (Figure 3.14, Figure 3.9). According to diffractograms (Figure 3.9) this sample is totally replaced by amorphous silica. All peaks disappear; in contrast amorphous silica large content can be identified by a well defined concave curve.

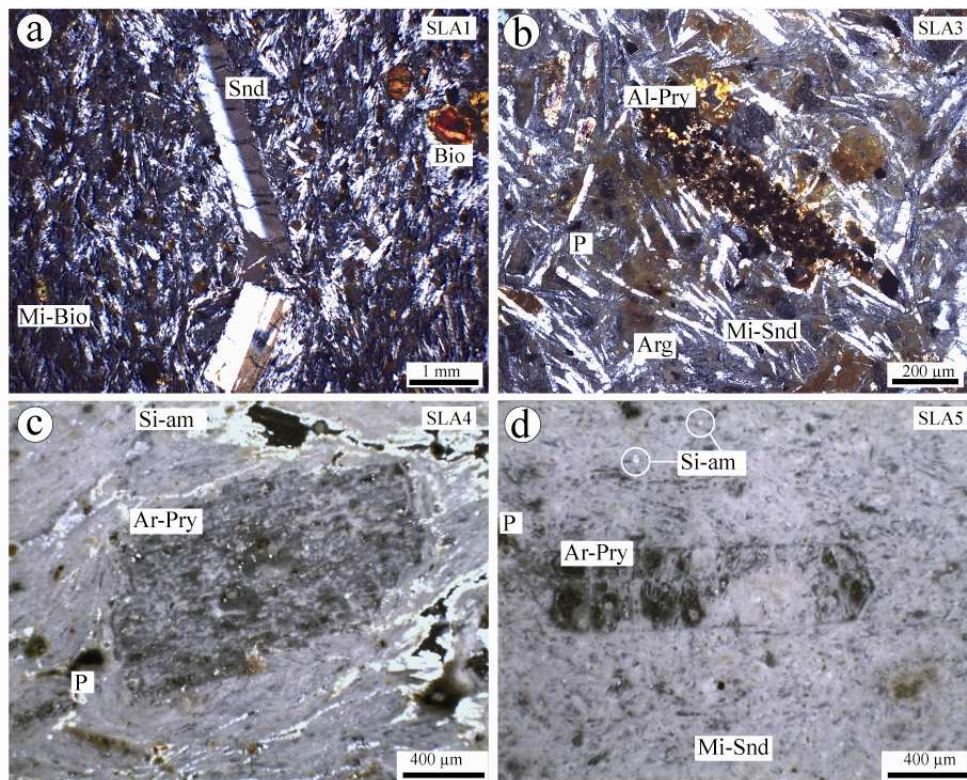


Figure 3.8 Polarized light microscope images of the lava rocks from Solfatara, Plg Plagioclase, Snd Sanidine, Prx Pyroxene, Bio Biotite, P pores, Ar-Pry Argilized pyroxene, Si-am Silica-amorphous, Li-la lithic fragments of lava, Arg Argilization, Gl-fr Glass fragment, Mi-QZ micro-Quartz

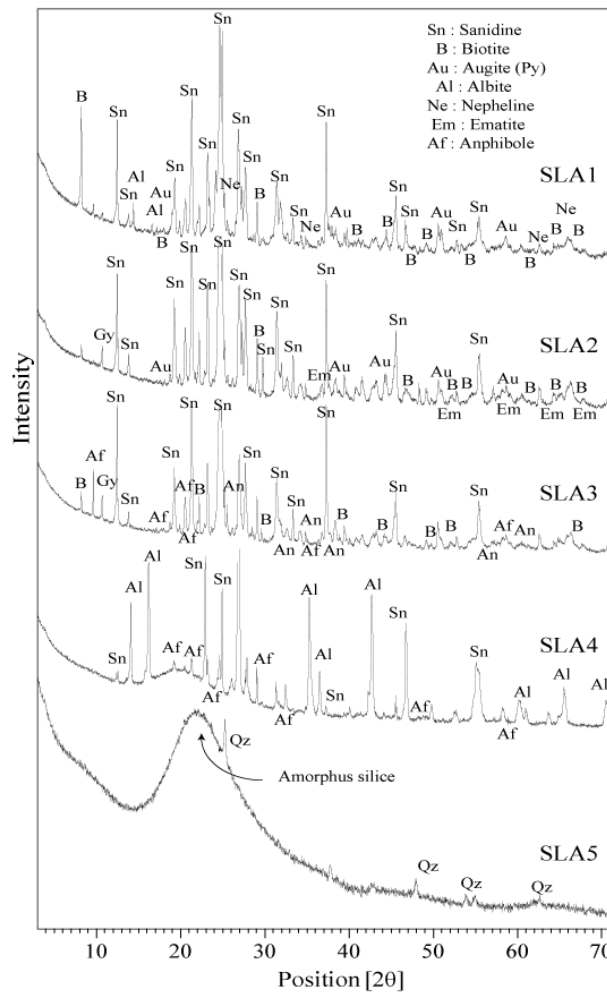


Figure 3.9 X-ray diffractograms of fresh and weathered varieties of lavas from Solfatara.

### 3.5.2 Pyroclastic rocks from Solfatara (SP)

One stratigraphic section that shows a representative pyroclastic sequence from Solfatara crater was selected. Fresh part of the section is located outside the crater, about 500 m from its north side. The sequence is composed of slightly stratified deposits with highly variable textures and grain sizes characteristics (Figure 3.13a). The lithofacies consist of decimetre- to metre-thick layers made up of breccia, lapilli, fine-coarse ash and sub-angular pumice lapilli with scattered lithic fragments (weathered/altered lavas). A breccia layer is composed by pumice lapilli, scoria fragments and angular lava blocks immersed in a coarse ash matrix. Layers are thinner in the upper part of the sequence, where fine ash and well-stratified surges are found, composed by coarse ash and pumice lapilli fragments. On the contrary, the stratigraphic sequence inside the northwestern flank of the Solfatara crater, where we collected the samples, is chaotic and affected by fumarolic fluids (Figure 3.10b) which according to Caliro et al. (2007) derive from the degassing of magma body and from the vaporization of hydrothermal liquids. Fumarolic fluids could replace part of pyroclastic rocks structure with microcrystals (feldspars and quartz), which work as a cement and keep all



grains together. In addition, lithofacies of the pyroclastic sequence are not easy recognizable, they varies significantly on a very short distance (> 5 m)

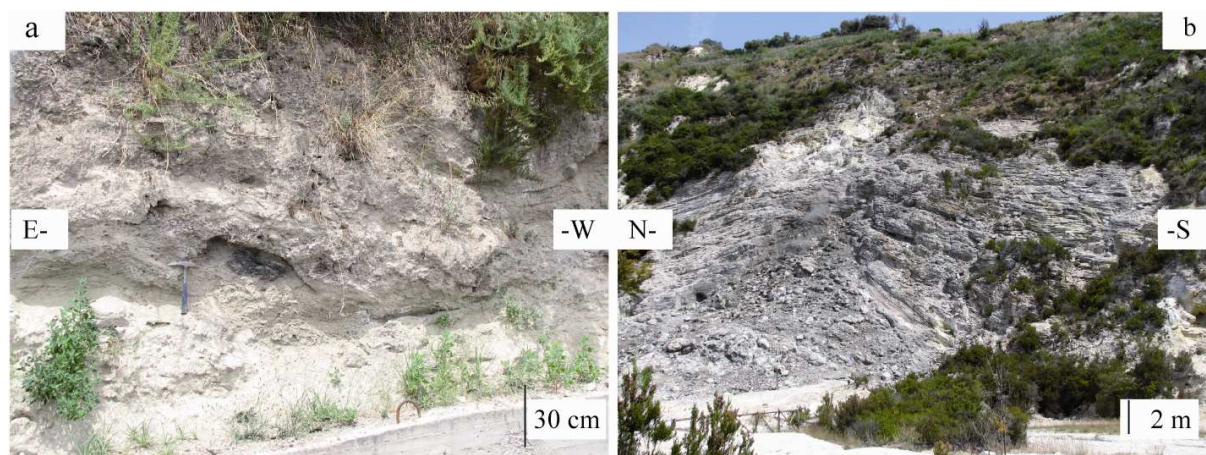


Figure 3.10 a) Fresh pyroclastic sequence from Solfatara. b) Chaotic Weathered/alternated pyroclastic sequence from Solfatara. Fumarolic activity is observed.

#### *Highly weathered pyroclastic SPRA1*

This sample has a pyroclastic texture composed prevalently by sub-angular glass fragments with an average size of 0.5 mm. The matrix is very dense and presents glass fragments. Oxidation appears as small stains all around the largest fragments of glass (fragments of pumice) with 0.4 mm of maximum size and replacing the phenocrystals of feldspars, which can be identified by their preserved geometry. Cracks, sub-rounded lithic fragments of lava and pyroclastic rocks are common. The biggest fragments of glass contain elongated-shape micro-crystals. According to diffractograms presented in Figure 3.12, this sample contains mainly alunite, jarosite and quartz. Amorphous silica large content is identified by a well defined concave curve.

#### *Highly weathered pyroclastic SPRA2*

This sample has a pyroclastic texture composed prevalently by sub-angular glass fragments with an average size of 4 mm. The matrix is integrated by micro-fragments of glass surrounded by micro-crystals of feldspars and quartz (Figure 3.14e). Oxidation appears as stains all around the matrix and in the largest fragments of glass (fragments of pumice) with 5 mm of maximum size. Very big sub-rounded lithic fragments of lava and pyroclastic rocks are common (7 mm as maximum size). In hand specimen, the size of lithic fragments rises up to 10 mm. According to diffractograms (Figure 3.12) this sample contains mainly sanidine, alunite, pyrite and quartz. Amorphous silica large content is also identified by a well defined concave curve.

#### *Highly weathered pyroclastic SPRA3*

This sample has a pyroclastic texture composed prevalently by sub-angular glass fragments with an average size of 6 mm. The matrix is integrated by merged medium sand fragments of glass. Oxidation appears as stains all around the matrix. Very large sub-rounded lithic fragments of lava and pyroclastic rocks are common. Lithic fragments are very altered, but original trachytic structure and crystals of sanidine are easily identified. In hand specimen, the size of lithic fragments rises up to 5 cm.

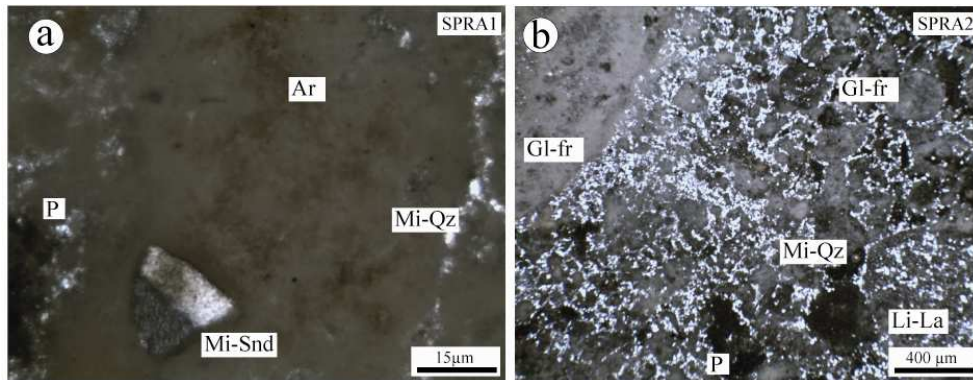


Figure 3.11 Polarized light microscope images of the pyroclastic rocks from Solfatara, Plg Plagioclase, Snd Sanidine, Prx Pyroxene, Bio Biotite, P pores, Ar-Pry Argilized pyroxene, Si-am Silica-amorphous, Li-la Lithic fragments of lava, Arg Argilization, Gl-fr Glass fragment, Mi-QZ micro-Quartz

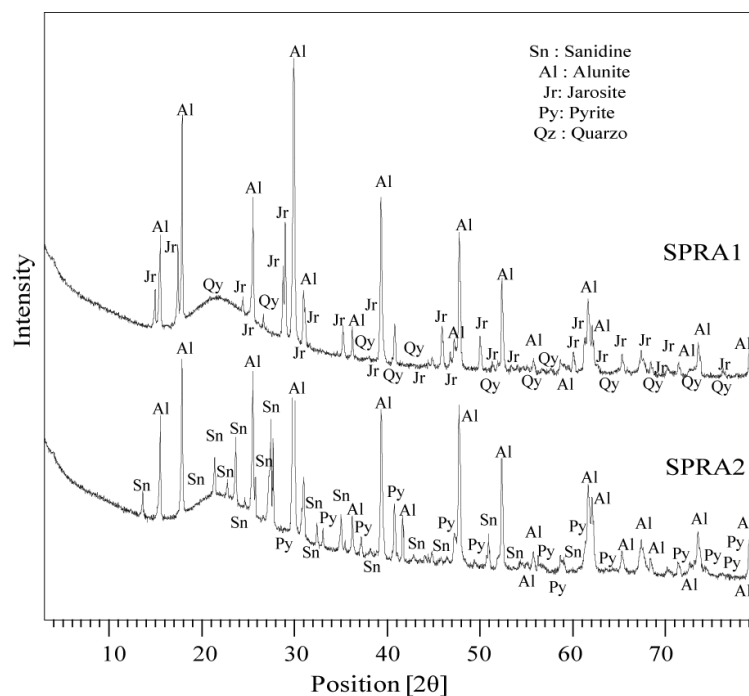


Figure 3.12 X-ray diffractograms of weathered varieties of pyroclastic rocks from Solfatara

### 3.5.3 Green-Tuff deposit from Ischia (IGT)

One stratigraphic section along the northern flank of the Monte Epomeo resurgent block has been selected (Figure 3.1). This stratigraphic section is affected by a dense net of faults and fractures (Vezzoli et al., 1988) (Figure 3.13b). The samples were collected on a vertical

outcrop of the Green Tuff unit, partly affected by hydrothermal processes. The hydrothermal alteration of this unit is induced by hot fluids migrating along the main faults delimiting the flanks of the Monte Epomeo resurgent block (Inguaggio et al., 2000). According to Sbrana et al. (2010), this hydrothermal circuit is linked to a deep reservoir and is recharged by sea and meteoric water. In this way, collected samples are representative of both fresh and hydrothermally altered portions of the Green Tuff.

The fresh Green Tuff unit consists of a pumice- and crystal-rich pyroclastic density current deposit. This deposit is welded, massive, matrix supported, with sub-rounded pumice of less than 10 cm in diameter and angular lithics fragments of less than 5 cm in diameter. The matrix consists of medium ash made of crystals, lithics and pumice fragments. The matrix colour is green due to primary alteration of the pyroclastic flow entering the cold sea water during emplacement. In the studied outcrop, the deposit shows 0.1-1 cm secondary vesicles formed by the collapse of the pumice structure in some juvenile fragments.

The fresh Green Tuff unit passes to the altered portion of the pyroclastic deposit near the active and inactive fumaroles exposed on the Monte Epomeo flank (Figure 3.13b). The altered Green Tuff is composed by hydrothermalized, red to white, compacted soft rock. The pumice juvenile fragments of this altered portions of the deposit are not vesiculated, due to compaction and filling eventually promoted by the hydrothermal processes.

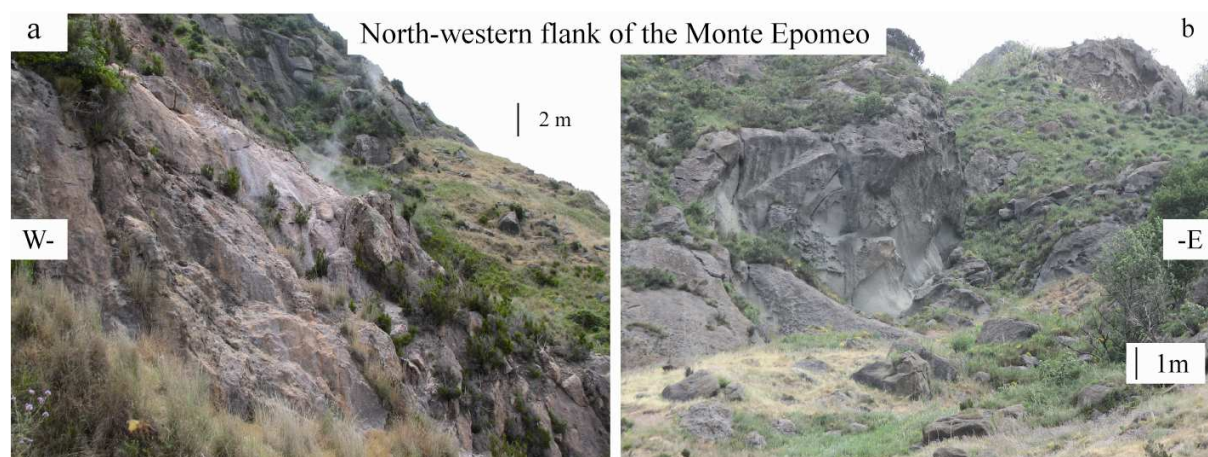


Figure 3.13 a) hydrothermal alteration of Green Tuff (active intense fumaroles are visible). b) Outcrop of the Green tuff (faults and cracks are easy identified).

### *Fresh Ischia Green-Tuff IGTF*

This sample has a pyroclastic texture composed prevalently by glass. Curved and elongated pumice fragments are very common. Sample major constituents are plagioclase and sanidine with minor amounts of pyroxene and biotite with a maximum size of 0.8 mm. The matrix is hypocrySTALLINE integrated by micro-crystals of plagioclases, alkali-feldspars (Sanidine), biotite and pyroxenes. Micro-plagioclases and micro-sanidine represent the 10 % of the matrix, while pyroxenes and biotites represent just the 5 %. Remaining part of the matrix is composed by 20 % of pores with 300  $\mu\text{m}$  of maximum size, 10 % of oxidation and 55 % of glass. Oxidation appears as small stains into the biggest fragments of pumice. Sub-rounded lithic fragments of lava with 548  $\mu\text{m}$  of maximum size are very common. Crystals of

sanidine, plagioclase and biotite from lithic fragments of lava are easily recognizable, although a high percentage of argilization is present.

### *Highly weathered Ischia Green-Tuff IGTA*

It represents the weathered/altered sample of IGT sequence. It has a pyroclastic texture composed prevalently by glass. Among the phenocrysts, plagioclase and sanidine are the most abundant followed by small amount of biotite. The matrix is hypocrySTALLINE and contains the same minerals as the phenocrysts. Micro-plagioclases and micro-sanidine with a maximum size of 70 and 50  $\mu\text{m}$  respectively, represent the 5 % of the matrix, while biotites represent just the 3 %. Remaining part of the matrix is composed by 15 % of pores with 50  $\mu\text{m}$  of maximum size, 10 % of oxidation and 67 % of glass. Sub-rounded lithic fragments of lava with trachytic texture are very common; moreover crystals of sanidines and biotites are easily recognizable, although a high percentage of argilization is present.

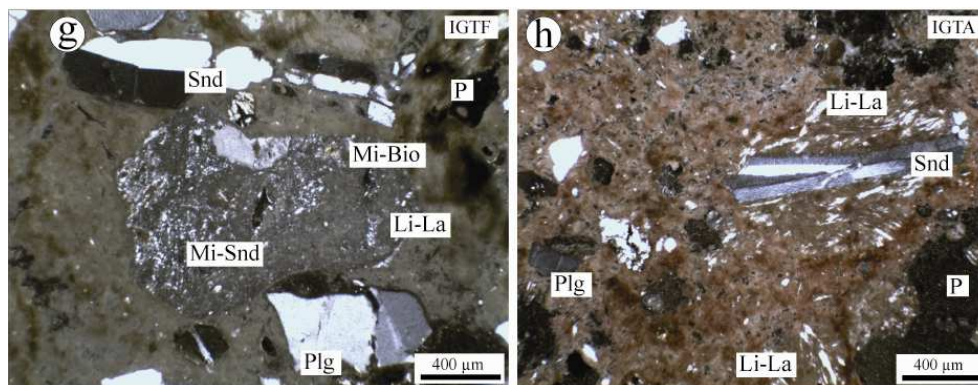


Figure 3.14 Polarized light microscope image of the volcanic rocks from Ischia. Plg Plagioclase, Snd Sanidine, Prx Pyroxene, Bio Biotite, P pores, Ar-Pry Argilized pyroxene, Si-am Silica-amorphous, Li-la Lithic fragments of lava, Arg Argilization, Gl-fr Glass fragment, Mi-QZ micro-Quartz

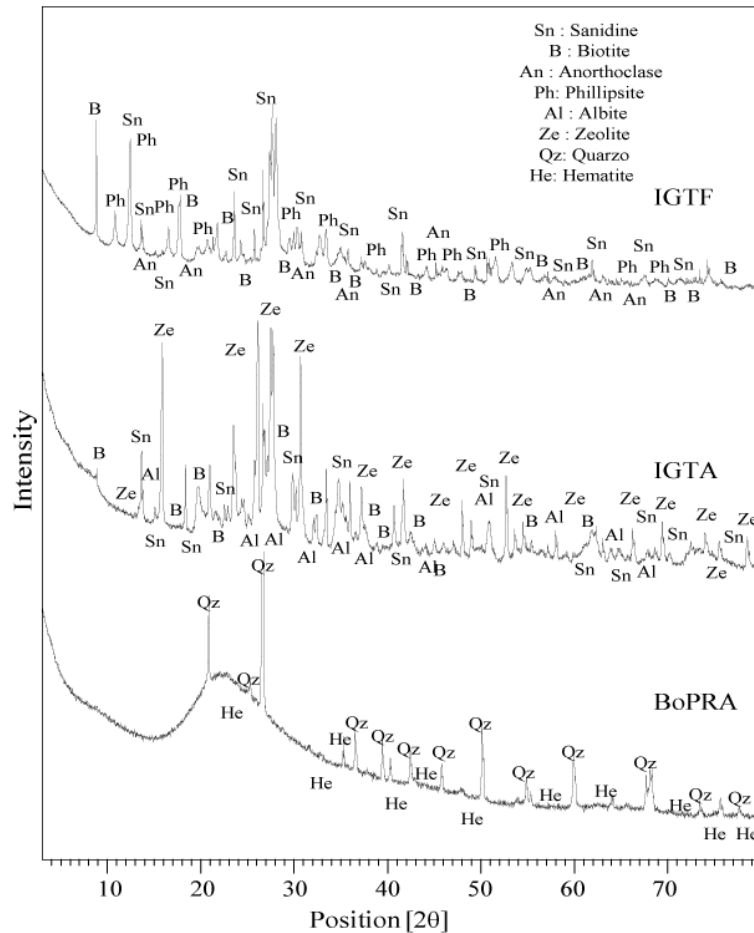


Figure 3.15 X-ray diffractograms of fresh and weathered varieties of Green Tuff from Ischia and weathered pyroclastic rocks from Bolsena area.

#### 3.5.4 Pyroclastic rock from Bolsena (BoPRA)

One stratigraphic section that shows a representative pyroclastic sequence from Bolsena was selected. More precisely, the outcrop is located 3.5 Km east of the Bolsena lake and 4 km north of Montefiascone. It represents the remnants of the ninth and tenth eruptive phases of Bolsena volcanic Zone (Nappi et al., 1998). The stratigraphic section is composed by a sequence of pyroclastic flows, pyroclastic falls and lava layers. The stratigraphic framework is visualized in Table 3.3, layers are described from the top to the base as follow. The top of the outcrop is completely covered by 30 cm of soil, under this layer there is a 2 m thick altered lava flow. Underlying the lavas, there is a sequence of un-welded pyroclastic flow deposits with very low density. This sequence consists of metre-thick layers made up of sub-angular pumice lapilli with scattered lithic fragments; some crystals and large amount of pores are also visible. These deposits are characterized also by decimetre-thick yellow stains, probably generated by some weathering/altering process. Well-stratified surges, composed prevalently by coarse ash and pumice fragments, are also identified. Under the pyroclastic and surge deposits, there is a sequence of fall deposits, separated by thin ash layers. These deposits are clast-supported, with angular pumices ranging from 1 to 20 mm. Some of the fall levels are compacted and slightly cemented, with intraclasts fine ash.

*Slightly weathered Bolsena Pyroclastic rock (BoPRA)*

This sample has a pyroclastic texture composed prevalently by small sub-angular silica-amorphous minerals with an average size of 0.6 mm. Sub-rounded lithic fragments of lava and pyroclastic rocks are also common. The matrix is composed by well defined micro-fragments of glass and micro-crystals of feldspars and quartz (Figure 3.14). Micro-crystals appear to be unaltered. Nonetheless, two main types of alteration are observed: oxidation along micro-cracks and within the largest clasts; argillization within the matrix as blurred stains. Microcracks filled by oxidation and silica-amorphous minerals are also present in the sample (Figure 3.14).

Table 3.1 Summary of field description for Solfatara lava sequence






Hand specimen ID and weathering grade	Visual Effects Identification description	Mineral Composition					
	<p>SLA1. <i>Fresh lava</i>: Grey coloured, fresh, and very dense lava with porphyritic texture (euhedral phenocrysts are plagioclase with an average size of 3 mm). Microcracks are not visible, some pores and grains are bonded by oxidation. argilization is present in the matrix and around minerals as blurred stains</p>	Plg	Snd	Prx	Bio	Ox	Arg
		+	+	+	+	+	-
		+	+	+		-	
		+	+				
	<p>SLA2. <i>Slightly weathered lava</i>: Grey coloured, slightly stained, dense lava with trachytic texture (euhedral phenocrysts are sanidine with an average size of 4 mm). Microcracks are visible, we can observe argilization and oxidation along them and within the boundary of minerals. Biotite is almost totally replaced</p>	Plg	Snd	Prx	Bio	Ox	Arg
		+	+	+	+	+	+
		+	+				-
			+				
	<p>SLA3. <i>Moderately weathered lava</i>: Greenish, yellowish, dense lava with preserved porphyritic texture (major constituents are potassic feldspar with <math>\phi=2</math> mm). Oxidation affects all crystals boundaries whereas biotite and pyroxene are almost completely replaced. Argilization is present into the matrix and all around minerals as blurred stains.</p>	Plg	Snd	Prx	Bio	Ox	Arg
		+	+	+	+	+	+
			+		-	+	+
	<p>SLA4. <i>Highly weathered lava</i>: reddish, yellowish lava. Texture is not preserved. Although all minerals are altered, sanidines prevail over pyroxenes and plagioclases. Pores are presented along visible cracks. Matrix is totally replaced by argilization.</p>	Plg	Snd	Prx	Bio	Ox	Arg
		-	+	-	-	+	+
						-	+
							+
	<p>SLA5. <i>Totally weathered lava</i> : White lava. texture is not preserved. Complete alteration of all minerals occurs, some pyroxenes could be recognized from its partially-distorted geometry. Matrix is totally replaced by argilization</p>	Plg	Snd	Prx	Bio	Ox	Arg
		?	-	?	-	-	+
							+
							+

Note. Plg = Plagioclase, Snd = Sanidine, Prx = Pyroxene, Bio = Biotite, Ox = Oxidation, Arg = Argilization.  
 +++ = abundant, ++ = modest, + = few, +- = rare, - = absent, ? = difficult or uncertain identification.

Table 3.2 Summary of field description for Solfatara pyroclastic sequence



Hand specimen ID and weathering grade	Visual Effects Identification description	Grain sizes proportions visual estimation	
	SPRA1. <i>Highly weathered</i> : White to yellowish pyroclastic rock, composed prevalently by sub-angular glass fragments. Matrix is very dense, with micro-fragments of glass and micro-crystals. Oxidation appears all around the largest fragments (pumice). cracks and Sub-rounded lithic fragments of lava and pyroclastic rocks are common.	Pe (>4 mm)	0
	SPRA2. <i>Highly weathered</i> : Gray or white discoloured. It is friable, but contains relict texture from the original unit. It is composed by subrounded fragments of glass and very altered-lithics (trachytic lavas >4 mm). Matrix is composed by medium sand fragments of glass.	Pe (>4 mm)	20
	SPRA3. <i>Highly weathered</i> : Gray or white discoloured with yellow stains, wholly decomposed rock. It is friable, but well sorted strata are easy to be identified. Subrounded fragments of pumice and very altered-lithics are common. In general, matrix is composed by medium sand fragments of glass.	Gr (2-4 mm)	5
		CoS (0.5-2 mm)	15
		MeS (0.25-0.5 mm)	10
		FiS (0.06-0.25 mm)	10
		Si (0.06> mm)	20 %
		CoS (0.5-2 mm)	10
		MeS (0.25-0.5 mm)	5
		FiS (0.06-0.25 mm)	10
		Si (0.06> mm)	30 %

Note. Pe = Pebbles, Gr = Granules, CoS = Coarse sand, MeS = Medium sand, FiS = Fine sand, Si = silt  
 Visual estimation was performed following charts to aid the visual estimation of modal proportions of grains and minerals (in Best, 2003)



Table 3.3 Summary of field description for Ischia and Vulsini pyroclastic sequence



Hand specimen ID and weathering grade	Visual Effects Identification description	Fragment size proportions visual estimation	
<p>IGTF</p>	<p>IGTF. <i>Fresh green tuff</i>: Greenish, composed prevalently by glass. Curved and elongated pumice fragments are very common. High percentage of argilization and oxidation appears as small stains into the largest fragments of pumice (friable). Sub-rounded lithic fragments of lava with 5 mm of maximum size are very common.</p>	Pe (>4 mm) 15 Gr (2-4 mm) 10 CoS (0.5-2 mm) 20 MeS (0.25-0.5 mm) 15 FiS (0.06-0.25 mm) 5 Si (0.06> mm) 30 % Ox + Arg -	
<p>IGTA</p>	<p>IGTA. <i>Highly weathered</i>: Reddish, composed prevalently by glass. Matrix is very dense, large pores seem filled. Sub-rounded lithic fragments of lava are very altered, but crystals (sanidines and biotites) are recognizable. High percentage of argilization is present.</p>	Pe (>4 mm) 15 Gr (2-4 mm) 15 CoS (0.5-2 mm) 20 MeS (0.25-0.5 mm) 5 FiS (0.06-0.25 mm) 5 Si (0.06> mm) 40 % Ox ++ Arg +++	



<p>BoPRA</p>	<p>BoPRA. <i>Slightly weathered</i>: Pinkish rock, composed prevalently by small sub-angular silica-amorphous minerals. Sub-rounded lithic fragments of lava and juvenils are also common. The matrix is composed by micro-fragments of glass and micro-crystals. Oxidation is present along micro-cracks and within the largest clasts. Argillization is presented within the matrix.</p>	Pe (>4 mm) 0 Gr (2-4 mm) 5 CoS (0.5-2 mm) 30 MeS (0.25-0.5 mm) 5 FiS (0.06-0.25 mm) 20 Si (0.06> mm) 30 % Ox ++ Arg +++	
--------------	--	--	--

Note. Pe = Pebbles, Gr = Granules, CoS = Coarse sand, MeS = Medium sand, FiS = Fine sand, Si = silt  
 Ox = Oxidation, Arg = Argilization, +++ = abundant, ++ = modest, + = few, +- = rare, - = absent.  
 Visual estimation was performed by following charts to aid the visual estimation of modal proportions of grains and minerals (in Best, 2003)

### 3.6 Geochemistry

In nature, geochemical characteristics of weathered rocks are controlled principally by their mineral composition. This variation gives information about different degree of weathering and could be related to the differences in physical-mechanical properties. Weathering processes change not only mineralogical, petrographical and geochemical characteristics of rock, but also physico-mechanical properties. The relationship between chemical changes and weathering can be specified by using Chemical Weathering Indices (CWI). They are principally based on the basic assumption that distributions of chemical elements, as well as loss on ignition content (LOI) are mainly regulated by the degree of weathering (Duzgoren-Aydin et al., 2002).

Indices take in account the variation of elements during alteration ( $K_2O$ ,  $Na_2O$ ,  $CaO$ ,  $MgO$ ,  $Al_2O_3$ ,  $SiO_2$ ,  $Fe_2O_3$ ,  $FeO$ ,  $TiO_2$  and  $H_2O$ ). on the contrary they do not explain the relationships between physical and mechanical properties which are also dependent on the rock fabric (arrangement of minerals and voids) and bonding (Irfan 1996). However, many investigators have proposed CWI to quantify and classify the mineralogical and chemical characteristics of weathered rocks (Ruxton 1968; Parker 1970; Nesbitt and Young 1982; Harnois and Moore 1988; Fedo et al., 1995; Irfan 1996). Some of them have been used to describe weathering in granites and pyroclastic rocks (see Irfan 1999; Kim and Park 2003; Ohta and Arai 2007;). In particular, a review of CIW used in igneous rocks (granite) is given in Irfan (1996). In this study the Mobiles index ( $I_{mob}$ ) have been also proposed. This index compares the different behaviour of “mobile” and “immobile” elements during weathering using the fresh rock as a comparative component for the index derivative. Afterwards, Irfan (1999) concluded that the most suitable indices for characterizing the weathering in volcanic rocks with variable mineralogy and chemical composition are: the weathering potential index (WPI), the weathering product index (WPI), alumina to potassium sodium ratio (AKN), silica to alumina ratio (SA), and the mobiles index ( $I_{mob}$ ) (Table 3.4). In addition, some other examples of CIW that monitor the decomposition of unstable mineral include the chemical index of alteration (CIA); plagioclase index of alteration (PIA), and chemical index of weathering (CIW).

The CIA was pioneered by Nesbitt and Young (1982) to quantitatively evaluate weathering history recorded in sediments and sedimentary rocks. It reflects changes in the proportion of feldspar and various clay minerals in the weathering product. The WPI, SA, WP and AKN were formulated by Ruxton (1968). WPI reflects a loss in the mobile cations from the weathering system. SA provides a measure of the total element loss as a ratio of the alumina content. Harnois (1988) developed the CIW, which is identical to the CIA, except that it eliminates  $K_2O$  from the equation, because the CIW does not account for the aluminum associated with K-feldspar.

The chemical indices shown in Table 3.4 have been applied to the weathered volcanic rocks at Solfatara, Ischia and Bolsena sites to assess its degree of weathering and to attempt to relate these indices to some physical-mechanical properties (e.g. bulk density, porosity, and strength among others). These indices have been calculated using the molecular proportions of major element oxides, listed in Table 3.1 and graphically represented in Figure 3.16. They were selected according to their capability of best describing chemical alteration by a mineral degradation pattern.

Table 3.4 Representative chemical weathering indices

Index	Formula	Reference
Chemical index of alteration (CIA)	$(Al_2O_3)/(100)/(Al_2O_3+CaO+Na_2O+K_2O)$	Nesbitt and Young (1982)
Alumina to calcium-sodium oxide ratio (ACN)	$Al_2O_3/Al_2O_3+CaO+Na_2O$	Harnois and Moore (1988)
Silica to alumina ratio (SA)	$SiO_2/Al_2O_3$	Ruxton (1968)
Alumina to potassium-sodium oxide ratio (AKN)	$Al_2O_3/K_2O+Na_2O$	Ruxton (1968)
Plagioclase index of alteration (PIA)	$(Al_2O_3-K_2O)(100)/(Al_2O_3+CaO+Na_2O+K_2O)$	Fedo et al. (1995)
Chemical index of weathering (CIW)	$(Al_2O_3(100)/(Al_2O_3+CaO+Na_2O))$	Harnois (1988)

The concentrations of the main geochemical components in lava, pyroclastic and ignimbrite rocks in Solfatara, Ischia and Bolsena obtained from X-ray fluorescence are listed in Table 3.5. Changes in the various elements during alteration were compared to each other. Major oxides in each series range as follow: SiO<sub>2</sub>: 44-90.4%; Al<sub>2</sub>O<sub>3</sub>: 0.40-19.02%; Fe<sub>2</sub>O<sub>3</sub>: 0.23-5.89%; CaO: 0.03-5.02%; MgO: 0.02-2.55%; Na<sub>2</sub>O: 0.03-4.29%; K<sub>2</sub>O: 0.05-8.33%; MnO: <0.01-0.37%; TiO<sub>2</sub>: 0.43-1.19%; P<sub>2</sub>O<sub>5</sub>: 0.04-0.33%. Generally, in all series (SLA, SPRA and IGT), the concentrations of Fe<sub>2</sub>O<sub>3</sub>, CaO, MgO, MnO and TiO<sub>2</sub> decrease with alteration grade, while the concentrations of SiO<sub>2</sub> and Na<sub>2</sub>O increase with alteration grade. Fe<sub>2</sub>O<sub>3</sub>, MgO, and MnO have an opposite trend in IGT series, suggesting an increment in chemical elements deposition. Finally, Loss on ignition (LOI) increases drastically in SLA4 sample and SPRA series.

Table 3.5 Major geochemical properties of weathered/altered volcanic rocks from Solfatara, Ischia and Bolsena

Site	Sample	SiO <sub>2</sub>	Al <sub>2</sub> O <sub>3</sub>	Fe <sub>2</sub> O <sub>3</sub>	CaO	MgO	Na <sub>2</sub> O	K <sub>2</sub> O	MnO	TiO <sub>2</sub>	P <sub>2</sub> O <sub>5</sub>	Ba	LOI	Total
Solfatara	SLA1	55.4	16.70	5.89	5.02	2.55	2.80	7.86	0.14	0.68	0.33	0.13	2.67	100.2
	SLA2	58.3	17.37	4.53	3.08	1.04	3.42	8.33	0.13	0.52	0.14	0.07	2.50	99.46
	SLA3	58.1	17.93	4.45	3.40	1.26	3.30	8.31	0.11	0.56	0.22	0.07	2.43	100.1
	SLA4	44.0	19.02	1.49	0.15	0.02	0.62	5.98	<0.01	0.43	0.21	0.07	27.85	99.81
	SLA5	91.2	0.65	0.24	0.03	0.02	0.16	0.12	<0.01	0.99	0.03	0.11	5.60	99.13
Solfatara	SPRA1	52.6	12.87	4.33	0.09	0.03	0.17	4.58	<0.01	0.59	0.16	0.13	23.78	99.36
	SPRA2	55.2	14.89	1.16	0.19	0.02	0.70	5.35	<0.01	0.53	0.09	0.09	21.34	99.52
Ischia	IGTF	54.2	16.31	2.73	2.50	0.85	3.60	7.10	0.10	0.40	0.11	0.03	11.74	99.66
	IGTA	59.8	17.96	2.77	0.37	1.15	4.29	6.17	0.37	0.57	0.04	0.02	6.58	100.1
Bolsena	BoPRA	90.4	0.40	0.23	0.04	0.02	0.03	0.05	<0.01	1.19	0.04	0.17	6.55	99.17

Changes in elements concentrations along alteration sequences are better illustrated in Figure 3.16. The major oxides results for the altered volcanic rocks samples were normalized to those of unaltered samples ( $X_{Altered}/X_{fresh}$ ). In SLA series, the amount of SiO<sub>2</sub>, Al<sub>2</sub>O<sub>3</sub>, Na<sub>2</sub>O, and K<sub>2</sub>O changes little in samples SLA2 and SLA3, while they change a lot in samples SLA5 (most altered sample). This sample has a large amount of SiO<sub>2</sub> and TiO<sub>2</sub> and very little amount of Al<sub>2</sub>O<sub>3</sub>, Fe<sub>2</sub>O<sub>3</sub>, MgO, Na<sub>2</sub>O, K<sub>2</sub>O, MnO, and P<sub>2</sub>O<sub>5</sub>. In all series, the content of Fe<sub>2</sub>O<sub>3</sub>, CaO, MgO, Na<sub>2</sub>O and MnO, present a notable decrease, when the altered samples are compared with fresh sample, in particular, these contents decrease from 1 to 0.08 in samples SLA4 and SPRA2 and SPRA3 (Figure 3.16). All components presented in SPRA series present little variation. Otherwise, the components of the most altered sample in IGT series

changes drastically, in particular values of CaO, MgO, MnO, and P<sub>2</sub>O<sub>5</sub>. In addition it is clear in Figure 3.16, that MnO reaches a value of 3.7.

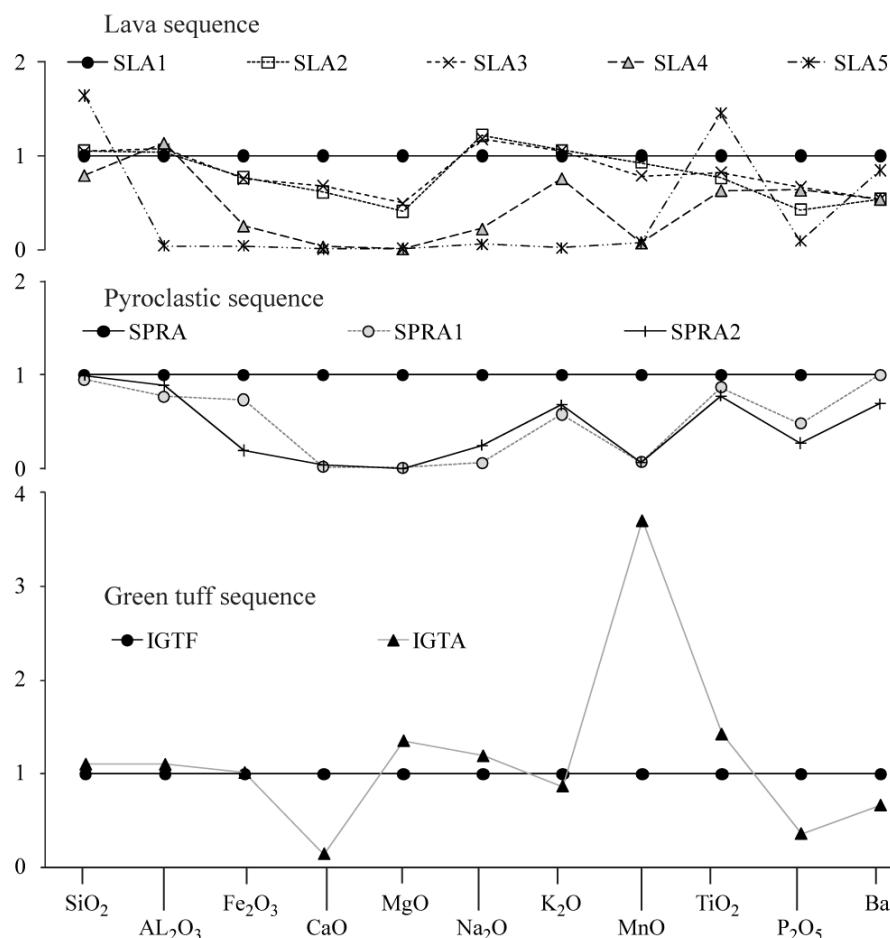


Figure 3.16 The unaltered rock-normalized diagram for volcanic altered rocks from Solfatara, Ischia and Bolsena.

The results of chemical weathering indices used in this study are summarized in Table 3.6. CIA index ranges from 42.73 to 70.93 Moles, ACN index ranges from 0.55 to 0.97 Moles, SA ratio ranges from 3.93 to 6.94 Moles (SLA5 and BoPRA samples exhibit very high values due to the large content of amorphous silica), AKN ratio ranges from 1.17 to 3.81 Moles, PIA index ranges from 37.13 to 94.60 Moles, while CIW index ranges from 54.63 to 96.61 Moles. In general all values are within the range of values described by Irfan (1999) and Ohta and Arai (2007). Note that the index values for CIA, ACN, AKN, PIA, and CIW increase with progressive weathering, whereas SA decreases. Base on previous description, the increment in CIA and CIW index could be associated to the dissolution of the plagioclases (Albite) (see, Table 3.1, Table 3.2, Table 3.3 and Figure 3.9). The rest of the indexes seem not to reflect the decomposition and/or chemical reaction of a single mineral, even if SA index change drastically in SLA5 and BoPRA due to the abundance of secondary amorphous silica.

However, the above description demonstrates that the chemical indexes of weathering exhibit appropriate and useful trend of mineral degradation processes.

Table 3.6 chemical weathering indices for volcanic rocks from Solfatara Ischia and Bolsena.

Site	Sample	CIA	ACN	SA (Mole)	AKN	PIA	CIW
Solfatara	<b>SLA1</b>	42.73	0.55	5.63	1.26	37.13	54.63
	<b>SLA2</b>	45.98	0.60	5.70	1.17	42.30	60.39
	<b>SLA3</b>	46.33	0.60	5.50	1.23	43.15	60.37
	<b>SLA4</b>	70.93	0.93	3.93	2.53	90.46	93.50
	<b>SLA5</b>	58.80	0.67	238.10	1.62	61.50	66.63
Solfatara	<b>SPRA1</b>	70.41	0.97	6.94	2.45	94.60	96.61
	<b>SPRA2</b>	67.04	0.91	6.29	2.13	85.60	90.68
Ischia	<b>IGTF</b>	47.09	0.61	5.64	1.18	44.76	60.51
	<b>IGTA</b>	55.13	0.69	5.65	1.29	58.69	69.35
Bolsena	<b>BoPRA</b>	69.24	0.76	383.52	3.81	73.68	76.40

## 4. LABORATORY ANALYSIS

### 4.1 Experimental methodology

Degradation and transformation can occur both at the surface and at large depth causing a progressive change in the physical mechanical properties. Fracturing, loosening of grain boundaries, increasing in porosity and leaching of constituents minerals can control the rock behaviour. Several studies have highlighted the weathering effects on physical and mechanical behaviour (e.g Ghayoumian et al., 1993, Moon 1993, Gupta and Seshagiri Rao 2000, Martínez- Martínez et al., 2007, Binal 2009, Vinciguerra et al., 2009). Ghayoumain et al (1993) suggested specific gravity and absorption as simple indicators of weathering. Moon (1993) presented geomechanical data for an ignimbrite, the author reported the great influence of groundmass fabric (texture, fabric of the crystals, clasts and pores shape) on geomechanical behaviour. Gupta and Seshagiri Rao (2000) compared values of uniaxial compressive tests performed on three lithological units with different categories of weathering. The deformational behaviour was studied in terms of variation in tangent modulus ( $E_{t50}$ ) and initial modulus ( $E_i$ ) due to weathering. Comparisons of  $E_{t50}$  and  $E_i$  values have shown that  $E_{t50}$  decreases more gradually than  $E_i$ , and reduction with an increased degree of weathering is more drastic for  $E_i$  values in all three types of rock. Martínez- Martínez et al. (2007) suggested the measurement of P, S-waves propagation velocities as a tool in quantifying the petrographical characteristics of highly complex rock-fabric materials. Binal (2009) presented physical-mechanical properties of moderately welded and non-welded ignimbrite (e.g. apparent porosity, ultrasonic velocities, point load index, compressive strength and modulus of elasticity). These properties were used in statistical evaluations, as input parameters in multiple regression analysis. As a result, the author determined equations to estimate mechanical properties of non-welded and moderately welded ignimbrite using index tests (e.g. statistical evaluation of point load index tests and  $I_{s(50)}$ ). Otherwise, Vinciguerra et al. (2009) investigated change in P and S waves propagation velocity. According to the authors, these changes reveal significant differences between units and indicate how, within the same lithology, the presence of clasts can affect significantly physical property values.

This section includes a comprehensive and systematic summary of the methodology used to determine physical and mechanical properties on weathered/altered volcanic rocks from Solfatara, Ischia and Bolsena. The adopted methodology focuses on the correlation between the individual properties of each sample and the expanding field of applications in geotechnics, in particular volcano collapse promoted by weathered/altered rocks. In other words, investigations were performed for evaluating and discussing the relationships between physical properties (e.g. porosity characteristics, micro-structure and texture) and the mechanical behaviour of weathered/altered volcanic rocks. Physical properties including unit weight ( $\gamma$ ), apparent porosity ( $\eta$ ), and ultrasonic pulse velocities were determined for each sample (54 mm in diameter). All tests were undertaken following the procedures recommended by ASTM international standards (D2938; D3148-02; D 3967-95a; ). To this aim, measurements like weights and ultrasonic pulse velocities along specimens, were made both under saturated and dry conditions. Before destructive tests were performed, an automatic 2D and 3D X-Ray tomographi apparatus was used to determine porosity size and shape for both thin-section and cylindrical samples (54 mm of diameter). As we have described previously X-ray diffraction and thin section analyses were used to determine mineralogical and petrographical changes in samples. In order to estimate strength and deformability of intact rock, we have performed tensile, uniaxial, triaxial compressive

strength and oedometric tests. Young's Modulus, which is the key parameter for defining relationships between stress and strain, was obtained by uniaxial stress-cycling experiments. Moreover P-wave velocities measured during testing suggest pore structure damage and cracking. Tensile strength of samples was evaluated by Splitting tensile test; significant loss of micro-structural integrity was evaluated with stress-strain ratio of the initial elastic response which according to Aydin and Basu (2006), is considered to be a useful means for quantifying changes induced by weathering. Resistance parameters of intact rock such as cohesion and friction angle were deduced from Mohr-Coulomb and Hoek-Brown criteria, the stress-strain relation was stroked by multi-stage triaxial tests at different confining pressures. Finally, a complete description of the mechanical behaviour is obtained and a detailed description is performed through a series of pre and post failure non destructive analyses. X-Ray tomographies have been completed and compared showing deformation and compaction within the samples and allowing the analysis of the influence of porosity distribution. Porosity values have been related to stress and strain curves. Results are interpreted in the key of degree of weathering and its related characteristics. An empirical link between the change in strength and the degree of alteration is presented and discussed.

#### 4.1.1 Ultrasonic pulse velocity measurements

P-wave velocity measures the travel speed of a longitudinal wave in the material, while S-wave velocity measures the travel speed of a shear wave. The propagation of elastic waves through rocks can give some indication of other properties, such as strength, density and elastic modulus (Price, 2009) as it depends on elastic properties of the material. Wave velocities are also commonly used to assess the degree of rock mass fracturing at large scale. Values of P wave velocities for some volcanic rocks vary from 1.47 to 6.75 km/s (see Kiliç and Teymen 2008). However, compressional and shear waves (also called longitudinal or P-waves and transverse or S-waves, respectively) were measured using a Pulse Velocity Test Instrument. This instrument transmits a wave into the sample and the receiving transducer, at a distance L (13 cm in our case), receives the pulse propagated through the sample. The pulse velocity instruments displays the transit time, it takes to travel through rock sample. Test are carried out following the steps as described in Naik et al. (2004).

The velocities of waves through  $\varnothing$  5.4 cm and 13 cm long cylindrical samples have been measured accurately. Young's Modulus ( $E_d$ ) and Poisson's ratio ( $\nu$ ) were determined using both longitudinal and transverse shear wave velocities from the following equations:

$$E_d = 2(1 + \nu) \rho V_s^2 \quad (1)$$

$$\nu = \frac{(V_p^2 / V_s^2) - 2}{2[(V_p^2 / V_s^2) - 1]} \quad (2)$$

where  $V_p$  and  $V_s$  are compressional and shear wave velocities,  $\rho$  is the density,  $E_d$  is dynamic Young's modulus,  $\nu$  is Poisson's ratio.

In addition, deformation properties of a rock can be determined either from geotechnical compression testing. The main differences between the two tests (static tests and dynamic tests) lie in the frequency of the measurements and the strain amplitude used in the tests. When an acoustic wave propagates through a porous medium the deformation of the grains is

elastic. In the geotechnical test the strain is larger and a non-elastic deformation of the sample can occur (Casper et al., 2004). Ultrasounds offer some advantages over static measurements. They are non-destructive tool and can be performed in the field. However, the problem lies in the fact that static and dynamic elastic modulus differ in values (Wang, 2000; Cicotti and Mulargia, 2004; Song et al., 2004). Divergence between static and elastic modulus is justified by differences in stress-strain conditions associated to the presence of fractures, cracks, cavities and planes of weakness. Al-Shayea (2004) reports the ratio of the dynamic modulus to static modulus in the literature for limestones, varies from 0.85 to 1.86. On the contrary, values from 1 to 1.23 in same lithotype are reported by Cicotti and Mulargia, (2004). Investigating the effect of stress cycles on static and dynamic moduli for volcanic rocks, Heap and Faulkner (2008) and Heap et al., (2009) show that static Young's modulus, during small amplitude cycles, is similar to the dynamic Young's modulus measured along the stress direction. In all cases (e.g. dry and wet samples) where the maximum stress increases in successive cycles, the Young's modulus is seen to decrease by about 30%. The authors attribute these changes to an increase in the level of damage by cracking with increasing stress of each cycle. They also demonstrated that stress-strain cycles are useful tools to explore the relationships between static and dynamic properties of rocks.

#### 4.1.2 Effective porosity by different techniques

Effective porosity ( $\eta_e$ ) was initially obtained following the standard test procedure by ISRM (1972). Procedure consists in calculating dry density ( $\gamma_{dry}$ ) and saturated density ( $\gamma_w$ ) of cylindrical core samples through measure of their volume and weight (Appendix 2). Effective porosity can be obtained by the following equation:

$$\eta_e = e / 1 + e \quad (3)$$

$$e = (G\gamma_w / \gamma_{dry}) - 1 \quad (4)$$

where  $e$  is the void ratio,  $\eta_e$  is the effective porosity and  $G$  the apparent specific gravity of the material. In order to measure the degree of saturation and water absorption, 70 cylindrical specimens ( $\approx \varnothing 5.4 \text{ cm} \times 13 \text{ cm}$ ) (Appendix 2) from 10 different volcanic rocks were submerged in distilled water under a constant air vacuum pressure.

Effective porosity was also obtained by Mercury intrusion porosimetry. This technique is more advanced and frequently adopted. It consists in applying a set of increasing pressure steps to a dry specimen and measuring the corresponding mercury intrusion volume. The pore size intruded at each step is determined by the pressure applied to force mercury into a pore against the opposing force of the liquid's surface tension. Pore size frequency and connected porosity, and mean pore size were obtained by a Pascal 140/240 Thermo-Fisher mercury porosimeter. Pore size distribution or equivalent radii are presented as a cumulative pore size distribution or a distributive curve (Appendix 3). Finally, pore volume, total pore area and bulk density as well as a value for effective porosity were obtained.



#### 4.1.3 Total porosity by different techniques

Porosity ( $\eta_t$ ) was obtained indirectly by pycnometer tests (Appendix 4), following the standard test procedures described in Germaine & Germaine (2009). The method defines the specific gravity of the material as the ratio of the mass of a given volume of soil particles to the mass of an equal volume of distilled water:

$$(G_s = \gamma_s / \gamma_w) \quad (5)$$

where  $\gamma_s$  is mass density of solids. Then porosity value is determined through the phase relationships, which include water content, density, void ratio, and saturation (see Bardet 1997).

Total Porosity ( $\eta_t$ ) was obtained also by two-dimensional digital image analysis. In this study, digital images were obtained by scanning 13 thin-sections using a photogrammetric scanner at 600 dpi resolution. In order to distinguish pore spaces and improve the contrast with transparent minerals, the images were acquired with a colour background. Image segmentation, which consists in pores identification, definition and differentiation from minerals or other clasts, was carried out by using Adobe Photoshop software. Pores have been isolated by using a color-scheme selection tool. This step was supported and confirmed by thin section analysis and petrographical description (mineral constituents, rock texture, crystal size range, and porosity types). Final processing included a more accurate image segmentation and image calibration performed by the ImageJ code (Image Processing and Analysis in Java) (<http://rsb.info.nih.gov/ij/index.html>). Once each pore has been identified (Figure 4.2), porosity shape parameters (location, perimeter, surface area, circularity and aspect ratio) have been automatically extracted.

Different techniques to characterize spatial structure and sizes of randomly distributed particles/voids from two-dimensional sections are available and can result in different values. Stereological methods could allow determining the number of particles for each particular size and shape enclosed by a given volume from the observed number of particle cuts, of a particular size and shape, on a randomly oriented cross-section through the volume (Sahagian and Proussevitch, 1998). Stereological conversion techniques have been used for geosciences fields (Higgins 2000; Morgan and Jerram, 2006). Higgins (2000) applied stereology to quantify textural aspects of igneous rocks (e.g. crystals sizes and distribution) by processing a sequence of thin-section images. On the contrary, we followed a simpler approach proposed by Farmer et al. (1991) to compute the 3D porosity by 2D shapes by applying the following relationships:

$$V = Ab \quad (6)$$

$$V = [A(a+b)/2] \quad (7)$$

where A is pore area, a and b are the major and minor axes, respectively. Because of the subspherical geometry a and b are similar and the results of the two methods are comparable.

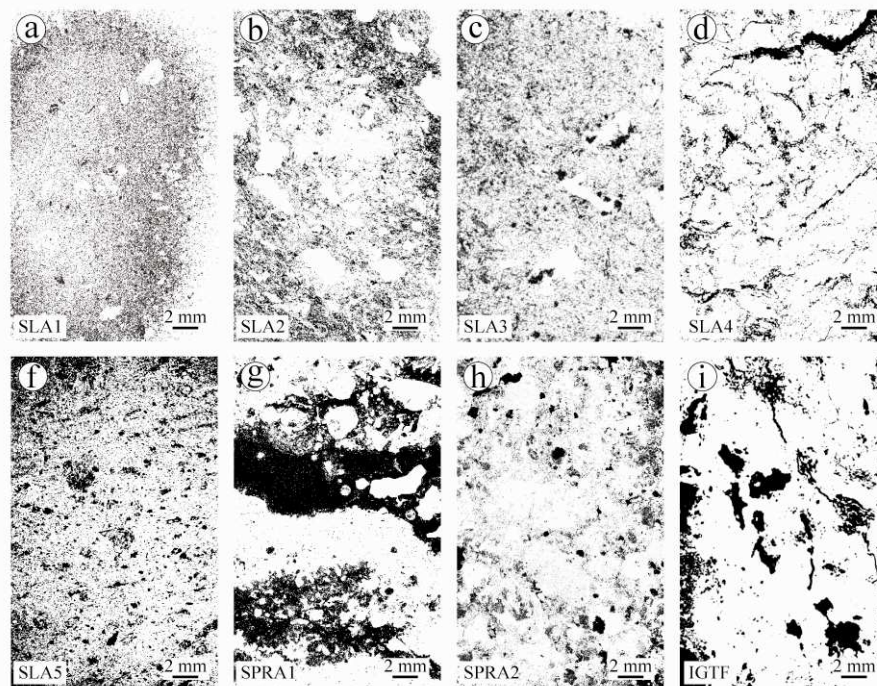


Figure 4.1 Illustration of total Porosity ( $n$ ) in black colour extracted from two-dimensional digital image analysis. The matrix and minerals are shown in white. a-f) total porosity for Solfatara lava sequence (12.8, 16.9, 18.4, 15, 9.5 %, respectively); g-h) total porosity for Solfatara pyroclastic rock (24.8, 17.8 %, respectively); i) total porosity for Ischia pyroclastic rock (15.3 %).

A more complete three dimensional reconstruction of rock sample structure and porosity characteristics were obtained from a set of contiguous two dimensional X-ray computerized tomography images (CT) (5 to 650  $\mu\text{m}$  of resolution) (Figure 4.2c). X-ray CT reconstructs internal images based on the distribution of the X-ray linear absorption coefficient deduced from the projection of X-rays through a sample (Ohtani et al., 2000).

X-ray CT images have been obtained by means of a GE D-600 medical CT hybrid scanner and a BIR Actis 130/150 Micro CT/DR system. The advantages of medical scanner include high image acquisition velocity and configuration versatility. On the contrary, a Micro CT/DR system allows the acquisition of images at higher resolution (40-60  $\mu\text{m}$ ). Image processing, data extraction and data analysis were carried out by means of a 3D visualization software (Avizo 6) the following steps (Figure 4.2a): 1) image rectification, which consists in defining not only image brightness, but also in applying a series of filters to reduce noise; consequently, this makes easier the identification of elements of interest (Figure 4.2b); 2) identification and isolation of elements of interest (e.g. porosity and voids distribution for our case) (Figure 4.2c) 3) Once each pore has been identified, porosity shape parameters (location, perimeter, surface area, circularity and aspect ratio) are automatically extracted by the Avizo 6 software (Figure 4.2d). The results of image processing are: a geometrical, morphological and topological description of the features inside the investigated pore volume. Moreover, in any case, the quality of final results depends on a series of noise reduction, filtering, thresholding, and particle separation steps (Gualda and Rivers, 2006; Ketcham, 2005).

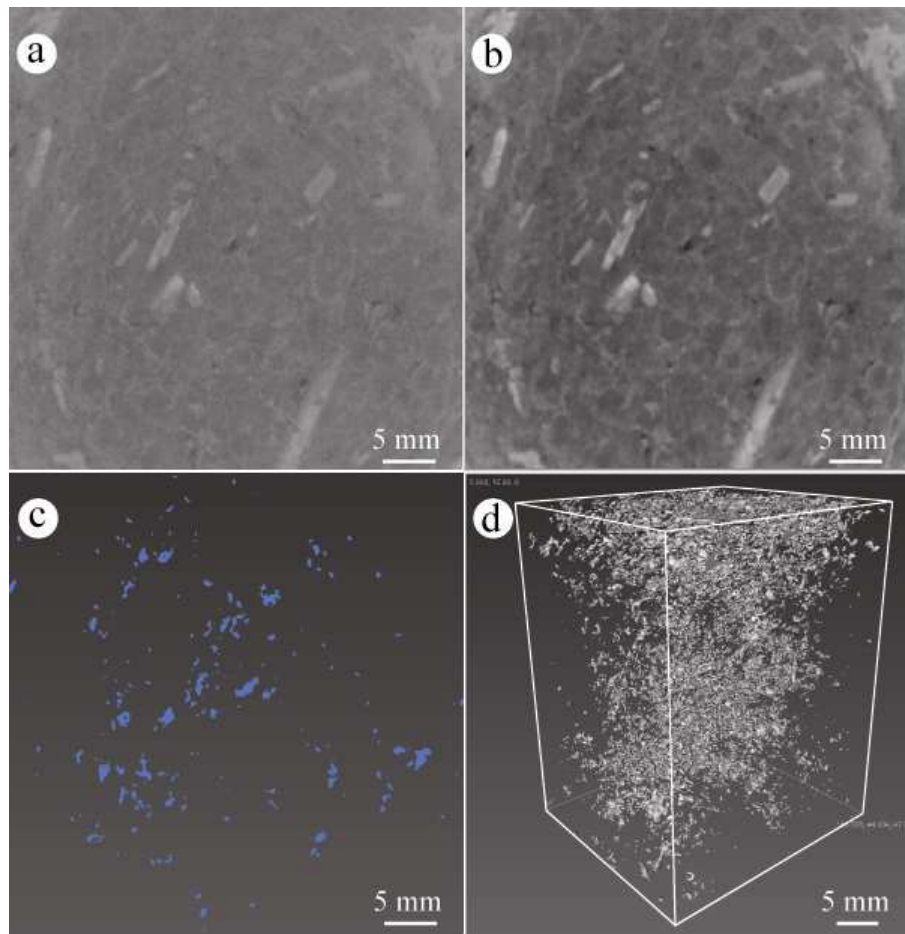


Figure 4.2 (a) X-ray micro CT original images (b) Example of a filtered image reconstructed from a tomographic slice through sample SL4. (c) pore distribution obtained from thresholding of image b (d) 3D pore-system reconstruction.

Quantitative study of pore distribution is very important in mechanical studies. Distribution of pores has a big influence on rock behaviour and it controls the mode of failure, moreover it may reflect the rock alteration grade. In this way, to assess the influence of alteration grade on pore size distribution, we applied the fractal dimension to pore distribution values obtained by mercury porosimeter, X-ray tomography, and thin section analysis.

A fractal is an element that can be subdivided in parts, each of which is a smaller copy of the whole. Fractals are generally self-similar and independent of scale (Higgins, 2006). Fractal distributions were identified using a bi-logarithmic diagram: On y-axis was plotted the number of pores larger than  $r$  and on x-axis the range of size of the pores  $r$ . The pore-size frequency distribution obeys a power law where power law exponent corresponds to the fractal dimension ( $D$ ) (Figure 4.3). In addition, fractal dimension values are simply related to the overall properties of pores: the increase of  $D$  values corresponds to more graded particle size distributions and a larger number of fine pores (see Turcotte, 1992 and Higgins 2006 for a more complete review of the methods).

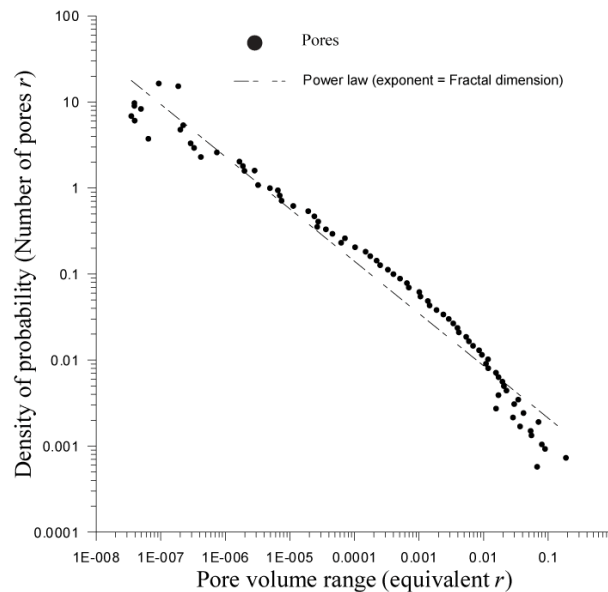


Figure 4.3 An example of a bi-logarithmic diagram used to examine fractal dimension ( $D$ ). The Power law fitting relationship is shown, its exponent corresponds to the fractal dimension.

#### 4.1.4 Uniaxial compressive strength and P-waves measurements

Uniaxial compressive strength (UCS) is one of the most important input parameters used in rock engineering (Sonmez et al., 2006) therefore it is crucial to understand rock nature and rock behaviour. Elastic modulus ( $E$ ) and Poisson's ratio ( $\nu$ ) derived from this test are the key to define stress and strain relationship. Uniaxial compression test is conducted by loading a cylindrical specimen along its axis and recording the displacements produced as the force is increased. Then, axial force is divided by the original cross-sectional area of the specimen to give the axial stress ( $\sigma_a$ ), and displacement is divided by original length to give the axial strain ( $E_a$ ). In terms of progressive fracture development and accumulation of deformation, the stress-strain responses of rock material in uniaxial compression generally exhibit various stages of mechanical behaviour (see Brady and Brown 2004) until UCS ( $\sigma_c$ ) is reached. The typical stress-strain curves under uniaxial stress conditions can be seen in Figure 4.4c.

UCS testing of all weathered/altered volcanic samples was performed following the steps described in ASTM international standards D 2938. Testing was carried out in a servo-controlled hydraulic testing frame (25 kN, GDS-Virtually infinite stiffness). Constant displacement rate was imposed when conducting the test (4 mm/hr) and load was measured using a load cell.

40 cylindrical samples were prepared from the 10 different weathered/altered rocks ( $\varnothing = 18$  and 54 mm in diameter) to perform compression test. Small samples have been tested to compute some of the values of uniaxial compressive strength and for statistical purposes (Appendix 5). On the contrary, axial and radial deformations were measured by means of strain gauges on 54 mm samples. Axial and radial strain gauges were wired into a full Wheatstone bridge circuit, constructed with a dummy sample of the same lithology. Elastic modulus ( $E_{av}$ ) was calculated by fitting the linear portion of axial stress-strain curve and Poisson's ratio ( $\nu$ ) was calculated by dividing the slope of radial strain curve by slope of axial strain curve in terms of (ASTM D3148-02) (Figure 4.4c).

In order to investigate the evolution of static elastic properties as rock approaches failure, samples of 54 mm in diameter were subjected to increasing-amplitude cyclic loading experiments. Moreover, two P-waves ultrasonic transducers were installed in contact with the upper and lower load bearings to perform continuous measurements during the test under loading and unloading conditions. Furthermore, ultrasonic velocities have been measured for all the samples under no load both in dry and wet conditions. For the unloaded condition, both the compression and shear waves have been measured, whereas only P waves have been measured during the loading tests. Loading cycles were programmed according to the results obtained from previous tests (specimens 19 mm in diameter): of each stress cycle the load was increased by 20 % until sample failed.

#### 4.1.5 Tensile strength

We carried out the Brazilian test to measure tensile strength by developing tension across the diameter of a rock disk subjected to compression through vertical load (ASTM D 3967-95a). Test was carried out in a servo-controlled hydraulic testing frame (GDS-Virtually infinite stiffness). A constant displacement rate was applied when conducting the test (6 mm/hr) and load was measured using a load cell. 60 circular disk samples, 54 mm in diameter, were prepared for these tests. In general all the samples have a size much larger than both the larger and average particles/crystal and pore at their interior. At least four tests were undertaken for each lithotype. the splitting tensile strength was calculated using the next expression:

$$\sigma_t = 2P / \pi LD \quad (8)$$

where  $\sigma_t$  is splitting tensile strength (MPa), P is maximum applied load (N), L is thickness of the specimen (mm), and D is diameter of the specimen (mm). Tensile strength investigation also involved testing of 11 specimens fitted with a 2 cm long strain gauge along its horizontal plane (perpendicular to the loading axis) (Figure 4.4b). Compressional load and corresponding tensile strains were recorded. Tensile stress-strain curves are presented with both the corresponding weathering grade and lithotype. Behaviour of each curve is described and discussed in next paragraphs. Moreover the most representative characteristics were highlighted.

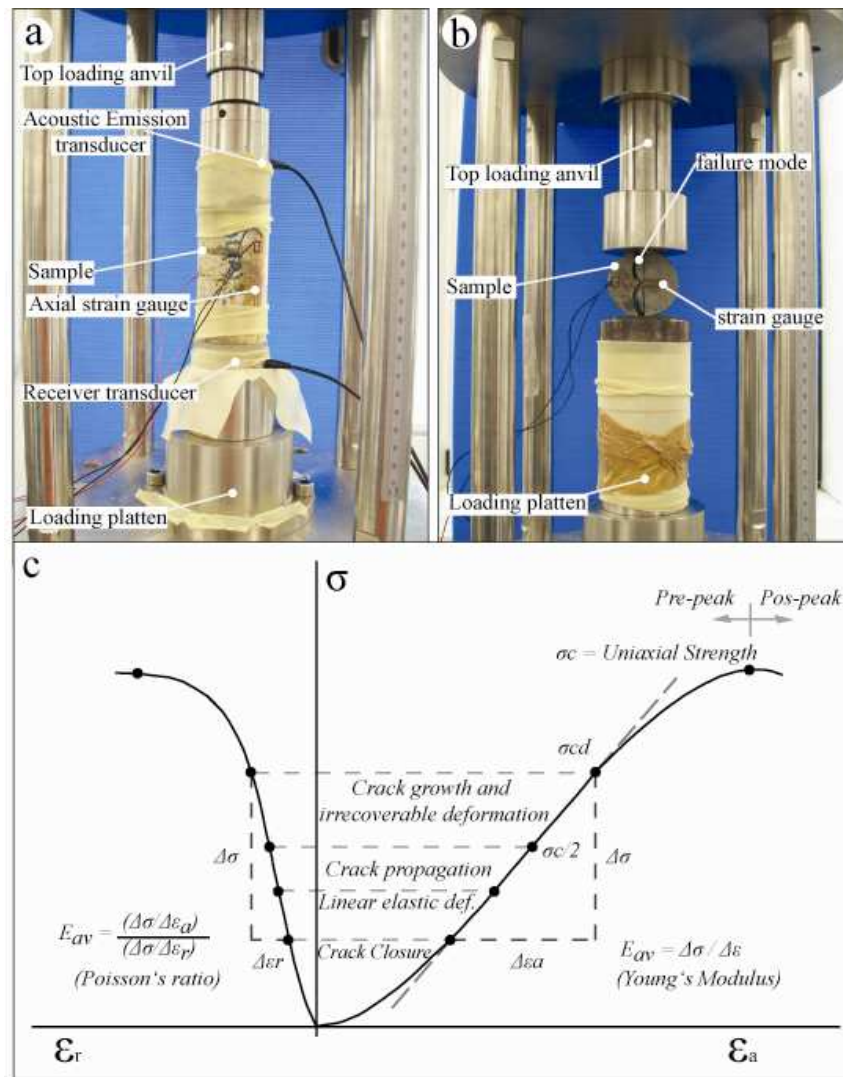


Figure 4.4 Sketch of uniaxial test arrangement. P-wave transducers and strain gauges are shown. b) Sketch of tensile test arrangement. c) Sketch of the general shape of the stress-strain curve illustrating mechanical parameters. Methods for calculating Young's Modulus and Poisson's ratio are also illustrated (from Brady and Brown 2004)

#### 4.1.6 Triaxial compressive strength

The test is intended to measure strength of cylindrical rock specimens as a function of confining pressure. Kovari et al, (1983) suggest three methods for determining the strength of rock materials in triaxial compression (individual test, multiple failure state test and continuous failure state test). The concept of a multi-stage triaxial test is exactly the same as the conventional single-stage triaxial test, except that only one test specimen is used for different confining pressures (Youn and Tonon, 2010). Confining pressure in a multi-stage test is increased after imminent failure point has been reached. Imminent failure point is defined in the stress-axial strain curve as the point where deviator stress does not increase when axial strain increase (Figure 4.4) (see Kovari et al., 1983; Youn and Tonon 2010). We have performed multistage triaxial tests and individual triaxial test for samples where

imminent failure point or post-peak reduction in strength could be not easily recognized (BoPRA, SPRA1, SPRA2, SPRA3). The confining pressure at which the post-peak reduction in strength disappears and the behaviour becomes fully ductile is known as the brittle-ductile transition pressure and varies with rock type. The nature of the brittle-ductile transition with increasing pressure is demonstrated in experiments on different rocks. Paterson and Wong, (2005), describe the progression in the nature of the stress-strain curves in triaxial compression when confining pressure is increased. The authors also describe the brittle-ductile transition on different rocks observed in triaxial compression tests (e.g. Basalt, Porous lavas, Sandstone, Limestone and Marbles).

In this study, tests are carried out in a servo-controlled hydraulic testing frame (GDS-Virtually infinite stiffness). The axial load is automatically raised at a constant selected rate (10 mm/hr) while the confining pressure is kept constant. In the case of multi-stage tests, the confining pressure is kept constant until the sample exhibits signs of approaching failure. This process is repeated by increasing the confining pressure to the subsequent required values. 20 cylindrical samples (54 mm in diameter) were used to perform individual and multi-stage triaxial tests, each sample was tested under dry state and it was subjected to different confining pressures ( $\sigma_3 = 2, 3, 4, 5, 6, 8$  and 10 MPa). The strength of rocks are represented by Mohr-Coulomb and the Hoek-Brown failure criterion. Mohr-Coulomb criteria utilizes the concept of cohesion ( $c$ ) and friction angle ( $\phi$ ) to estimate the major principal stress at failure for a given minor principal stress:

$$\tau = c + \sigma_n \tan \phi \quad (9)$$

where  $\tau$  is the shear strength,  $\sigma_n$  is the normal stress,  $c$  is the intercept of the failure envelope with the  $\tau$  axis, and  $\phi$  is the slope of the failure envelope (see Jaeger et al., 2007, Brady and Brown, 2004 for a complete review). In this study, failure envelope plane was predicted by plotting  $\sigma_1$  and  $\sigma_3$  in terms of stress parameters and in terms of maximum shear stress and mean normal effective stress ( $t = \sigma_1 - \sigma_3 / 2$ ,  $s = (\sigma_1 + \sigma_3) / 2$ ) (Figure 4.5). In terms of normal and shear stresses, the linear equation obtained from  $t-s$  plot, represents the best fitting secant line to the Mohr circles. In order to pass the problem of finding a tangent equation for Mohr's envelope defined in normal and shear stresses, the previous equation was modified by means of the following equations (see also Figure 4.5):

$$\sin \phi = \tan \beta \quad (10)$$

$$c = b / \cos \phi \quad (11)$$

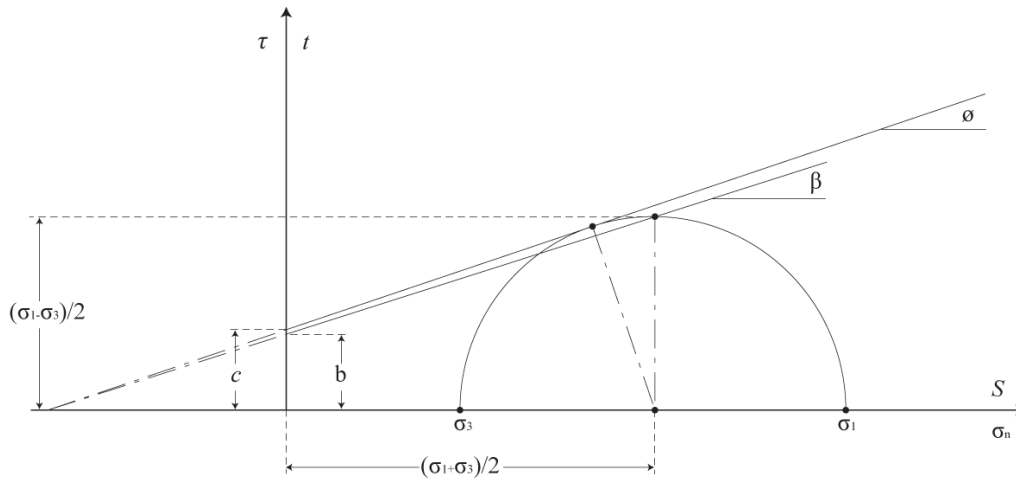


Figure 4.5 Mohr-Coulomb failure criterion in terms of stress parameters and corresponding Mohr stress circles ( $t-s$ ) and shear and normal stresses ( $\tau-\sigma$ ).

Hoek-Brown criteria is used to represent the failure envelope of intact rock plotted in  $\sigma_1 - \sigma_3$  space, whose empirical equation is expressed as:

$$\sigma_1 = \sigma_3 + \sigma_{ci} (m_i \sigma_3 / \sigma_{ci} + 1)^{1/2} \quad (12)$$

where  $\sigma_{ci}$  is the uniaxial compressive strength of the intact rock material and  $m_i$  is a material constant for intact rock. In this study constant  $m_i$  was back-calculated by plotting the major ( $\sigma_1$ ) and minor principal ( $\sigma_3$ ) stresses derived from the single and multistage triaxial tests (Figure 4.5). Once  $\sigma_1$  and  $\sigma_3$  were plotted, the constant  $m_i$  has been automatically extracted by using RocScience RocLab1, based on the generalized Hoek-Brown failure criterion (Table 4.2). In addition, the constant  $m_i$  values depends upon the mineralogy, composition and grain size of the intact rock (Rock type and rock texture) (Edelbro, 2003). From this point of view, values of the constant  $m_i$  derived from our data could be easily compared to  $m_i$  values presented by many authors (e.g. Hoek 1990, Hoek and Karzulovic 2001).

#### 4.1.7 Oedometric test

Compaction bands, which are tabular zones of pure compressional deformation, were previously observed in triaxial tests on very high porosity ignimbrite (BoPRA samples). The aim of Oedometric test is to verify the possibility to observe the formation of compaction bands. The test is designed to measure radial stresses and axial displacements for examining possible axial unloading, which is a function of the microstructure collapse (formation of compaction bands).

In this study, oedometric test is carried out according to those described in Castellanza et al. (2009). The authors designed an oedometric test device ( $\varnothing=37$  mm in diameter), called Weathering Test Device (WTD) (Figure 4.6), which in turn was mounted on the displacement controlled loading frame. The axial load (50 kN) is automatically raised at a constant selected rate ( $10^{-5}$  to 10 mm/min). Radial stress is measured by means of Oedometric ring provided by three strain gauges, which are able to detect strains of the order of  $0.3e^{-6}$  (see Castellanza et al., 2009 for a complete review). As Castellanza et al. (2009) describe, the rock coring is



placed firstly in a mold (Figure 4.6a) and then pushed into the soft oedometric ring (Figure 4.6b) through a cylinder equipped with a circular cutter (Figure 4.6a). Otherwise, each sample was tested under dry state and the final measurements are represented in four diagrams: 1) axial stress ( $\sigma_a$ ) and radial stress ( $\sigma_r$ ) versus the axial strain ( $\epsilon_a$ ); 2) stress ratio ( $K = \sigma_r/\sigma_a$ ) versus axial strain ( $\epsilon_a$ ); 3) void ratio ( $e$ ) versus the logarithm of the axial stress ( $\sigma_a$ ); and 4) stress path in the mean effective stress [ $p' = (\sigma_a + 2\sigma_r)/3$ ] – deviatoric stress [ $q = (\sigma_a - \sigma_r)$ ] plane.

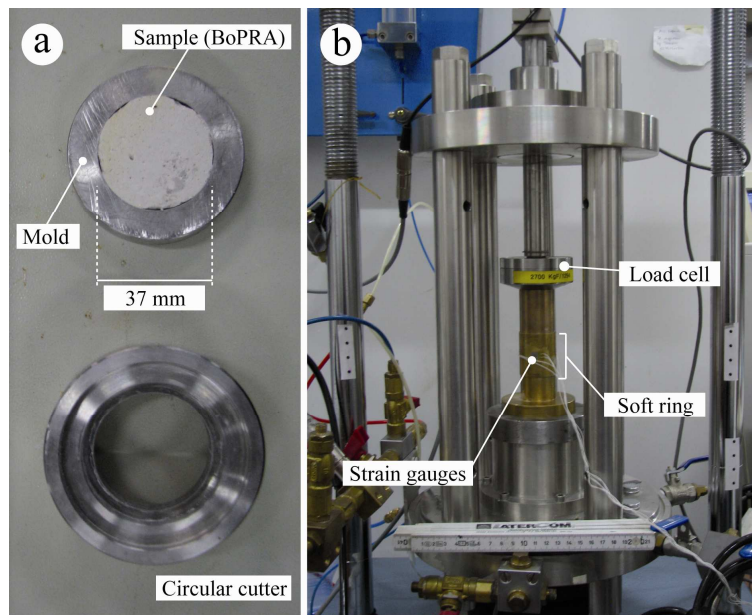


Figure 4.6 a) Circular cutter; sample 18 mm high. b) Soft oedometer ring; strain controlled Oedometer (WTD).

## 4.2 Results of laboratory investigations

Physical and mechanical data for lavas and pyroclastic rocks series are presented in Table 4.1 and Table 4.2, respectively. These tables include average measured values for bulk density ( $\gamma$ ), effective ( $\eta_e$ ) and total porosity ( $\eta_t$ ) obtained by different techniques (e.g. bulk-specific weight measurements, water immersion and Hg-porosimetry, analysis of thin sections and X-ray Computer Tomographies), fractal dimension from porosity values (D), P and S velocities waves measurements ( $V_p$  and  $V_s$ ), uniaxial compressive strength (UCS), Young's modulus ( $E_{t50}$ ) and Poisson's ratio ( $\nu$ ), dynamic Young's modulus and dynamic Poisson's ratio ( $E_D$  and  $\nu_D$ ), tensile strength (TS) and the corresponding tangent modulus as indicator of weathering degree, friction angle ( $\phi$ ), cohesion ( $c$ ) and  $m$  values from Hoek and Brown failure criterion.

The following descriptions summarise the physical-mechanical behaviour of lavas and pyroclastic rocks from Solfatara, Ischia and Bolsena. The average measurements of bulk density varies in the range  $9.60 < \gamma < 24.52 \text{ KN/m}^3$ . The average measurements of  $\eta_e$  and  $\eta_t$ , obtained by different techniques, range between  $5.4 < \eta_e < 65 \%$  and  $0.69 < \eta_t < 57.67 \%$ , the highest  $\eta_e$  and  $\eta_t$  values were calculated at 65 and 58 % through Medical scanner images and pycnometer analysis, respectively.

All these values belong to BoPRA samples, which also present the lowest value of  $\gamma$  ( $9.60 \text{ KN/m}^3$ ). The lowest value of  $\eta_e$  and  $\eta_t$  were calculated at 6 and 0.70 % through bulk specific weight measurements and Medical scanner images analysis, respectively. Both lowest values

belong to SLA1 sample, which correspond to the less altered sample. Fractal dimension is found to be between 1.60 and 2.0, and they decrease progressively from intact rocks to the most altered sample (Table 4.1) suggesting an increase in large pore frequency. Dynamic properties, as P and S waves velocity vary from 1136 to 4394 and from 867 to 2906 m/s, respectively. These properties are strongly connected with porosity and consequently with the grade of alteration. Voids in rock reduce velocity of  $V_p$ , samples with high porosity show low velocity values. It is observed in Table 4.1 that the lowest velocity in each rock series (SLA, SPRA, IGT) was determined on the most altered sample or in those which showed high porosity (SLA5 = 2700 m/s, SPRA = 1600 m/s). On the contrary, the highest value was determined in rocks with low porosity (SLA1  $\approx$ 10 %). There is one exception in IGT series where the most altered sample showed low porosity.

Table 4.1 Summary of physical properties of weathered/altered volcanic rocks

Sample	$\gamma$ (kN/m <sup>3</sup> )	$\rho$ (kg/m <sup>3</sup> )	T-S	$\eta_t$ XRT	MsI	Pm	$\eta_e$ Hg	$\rho M$	$e$	T-S	D		Waves	
											XRT	Hg	Vp	Vs
<i>Lava</i>														
SLA1	23.30	2375	12.8	6	0.69	14.6	11	6	0.06	1.59	1.92	2.13	4394.3	2123.8
SLA2	16.19	2500	16.9	6.4	2.13	15.1	15	5.4	0.06	1.44	1.84	2.06	4142.3	2906.4
SLA3	19.01	1938	18.4	25.6	7.72	28.4	18.6	23	0.30	1.47	1.80	2.07	3159.5	2000.3
SLA4	24.52	1650	15	30.7	19.90	33.1	32	21	0.27	1.35	1.63	2.03	3109.5	1000.7
SLA5	22.74	1500	9.5	31.5	22.48	30.3	26.8	19.2	0.24	1.44	1.52	2.08	2789.2	1480.5
<i>Pyroclastic</i>														
SPRA1	14.55	1483	24.8	20.3	23.90	39.3	41.5	24.7	0.33	1.31	1.59	2.15	2177.6	1021.6
SPRA2	15.14	1540	17.8	34.9	31.41	38.3	44.8	22.4	0.29	1.36	1.42	1.95	2062.8	788.0
SPRA3	13.98	1425		42.9	30.20			30.2	0.43		1.45		1654.3	518.8
<i>Tuff</i>														
IGTF	15.12	1540	15.3	25	15.67	27.8	25.5	19.2	0.24	1.57	1.31	2.05	1137.4	420.6
IGTA	17.78	1810		24	22.90	37.5	29.7	29.9	0.43		1.34	2.14	2249.0	807.4
<i>Ignimbrite</i>														
BoPRA	9.60	980		49.8	57.67	53.8	65	41.2	0.70		1.63	2.11	1136.3	867.8

All values are given as an average.  $\gamma$ : unit weight,  $\eta_t$ : total porosity,  $\eta_e$ : effective porosity, D: fractal dimension, T-S: results from thin-section, XRT: results from x-ray tomography images, MsI: results from Medical Scanner Image, Pm: results from pycnometer, Hg: results from mercury porosimetry,  $\rho M$ : results from bulk-specific weight measurements,  $e$ : Void ratio, Vp: compressional wave velocity, Vs: shear wave velocity.

Mechanical properties are summarized in Table 4.2. The average values of uniaxial compressive strength vary from a minimum of 5.7 MPa in the non welded and altered ignimbrite (BoPRA) to a maximum of 116.7 MPa in less altered samples of lava series (SLA1). All mechanical properties in SLA series suffer a drastic decrement between SLA2 to SLA3, reflecting large changes in physical properties (Table 4.1), in particular porosity content. Otherwise, the stress-strain characteristics of all samples are reflected in Young's modulus measured along the medium stress range. Young's Modulus values change from a minimum of 0.83 GPa, in the unwelded and altered ignimbrite (BoPRA), to a maximum of 18.43 GPa in the less altered sample of lava (SLA1). There is again a big change between SLA2 to SLA3 with values of 17.47 and 3.71 GPa, respectively. Young's Modulus was also measured in uniaxial stress-cycling experiments, in order to follow the progressive degradation of sample stiffness. In this way, the highest and the lowest Young's Modulus, measured in complete cycle series vary from 4.21 to 5.60 GPa and from 0.77 to 0.83 GPa, respectively. Triaxial tests were performed, in order to determine the strength parameters (angle of internal friction  $\phi$  and the cohesion  $c$ ), results are represented graphically in Figure 4.17, and they range between  $10 < \phi < 57^\circ$  and  $34.3 < c < 0.18$  MPa. Material constant for

intact rock, was also generated according to Hoek-Brown failure criterion, results vary between  $1 < m_i < 27.5$ .

Correlation analysis between results described in Table 4.1 and Table 4.2 are discussed in next sections. These correlations show, among other things, a significant relationship between porosity, unit weight and alteration grade for all the samples. In addition, correlations in almost all cases are expressed by best fitting linear equations.

Table 4.2 Summary of mechanical properties of weathered/altered volcanic rocks

Sample	UCS (MPa)	E <sub>t50</sub> (GPa)	$\nu$ (-)	E <sub>D</sub> (GPa)	$\nu_D$	K	K $\nu$	TS (MPa)	E <sub>T150</sub> (GPa)	$\theta$ (°)	c (MPa)	m <sub>i</sub>
<i>Lava</i>												
SLA1	116.7	18.4		31.6	0.32	1.7		10.4	18.8	36	34.3	27.5
SLA2	108.3	17.5		39.7	0.02	2.8		9.5	36.1	57	20.9	26.2
SLA3	25.8	3.7	0.33	18.1	0.17	4.9	0.5	3.9	6.6	23	10.2	2.2
SLA4	22.6	3.5	0.26	3.3	0.46	0.9	1.8	2.4	4.7	24	3.4	11.6
SLA5	16.8	1.8	0.10	8.6	0.30	4.8	3	2.3	3.1	26	10.5	4.7
<i>Pyroclastic</i>												
SPRA1	13.3	1.6	0.13	4.8	0.33	2.9	2.5	2.6	3.4	28	2.8	12.1
SPRA2	8.6	1.9	0.19	3.6	0.38	1.9	2	1.2	2.3	14	3.1	2.1
SPRA3	7.2	1.4	0.21	1.1	0.44	0.8	2.1	1	1.2	19	0.2	1.9
<i>Tuff</i>												
IGTF	5.7	0.7	0.11	0.9	0.42	1.3	3.8	0.8	1.9	17	1.4	2.5
IGTA	16.3	1.6	0.23	3.4	0.43	2.2	1.9	1.1	2	10	8.4	1.0
<i>Ignimbrite</i>												
BoPRA	5.7	0.8	0.36	1.0	0.22	1.3	0.6	0.2	0.5	16	1.9	5.5

All values are given as an average. UCS: uniaxial compressive strength, E<sub>t50</sub>: Young's modulus from UCS,  $\nu$ : Poisson's ratio from UCS, E<sub>D</sub>: Dynamic Young's modulus,  $\nu_D$ : Dynamic Poisson's ratio, TS: tensile strength, E<sub>T150</sub>: Tensile Young's modulus;  $\theta$ : friction angle; c: Cohesion; m<sub>i</sub>: material constant for intact rock, according to Hoek-Brown failure criterion K: ratio of the dynamic modulus to static modulus; K $\nu$ : ratio of the dynamic Poisson's ratio to static Poisson's ratio.

Some of the physical-mechanical values presented in this work (e.g. UCS, E<sub>t50</sub>, TS,  $\nu$ ,  $\eta_e$ ,  $\theta$  and m<sub>i</sub>), in particular those derived from SLA1 and SLA2 samples (Fresh and slightly altered lava) are very similar to the values of volcanic rocks described in literature (Lumb 1983; watters et al., 2000; Concha-Dimas et al., 2004; Zimbelman et al., 2004; Moon et al., 2005; del Potro et al., 2008) (table 4.3). Lumb (1983) described the relationship between UCS and  $\eta_e$  in volcanic rock. This relationship is represented graphically and a clear decreasing trend of strength with increasing porosity is evident. However, good relationship between the values obtained in this thesis work is shown, when values of UCS and  $\eta_e$  from sample SLA1, SLA2 and SLA3 samples are plotted in the same graph (Figure 4.7).

Table 4.3 Summary of mechanical properties of weathered/altered volcanic rocks described in the literature

Lithotype	$\gamma$ (kN/m <sup>3</sup> )	UCS (MPa)	$\theta$ (°)	c (MPa)	
<i>Intact rock properties for jointed lava</i>					
Crater wall sequences, white island Volcano	24.7 +- 0.3		50-62	1.16-3.39	Moon et al., 2005
Andesite lava flow, Mt. Rainier, Gibraltar	23.7 - 24.7	145.9	24-45	0.20-0.41	Watters et al., 2000
Andesite lava flow, Mt. Rainier, Cathedral	23.9	102.4			Watters et al., 2000
Altered Andesite lava flow, Mt. Rainier, Cathedral	23.5	57.5			Watters et al., 2000
Andesite lava flow, Mt. Rainier, Glacier basin	23.1	56			Watters et al., 2000
Altered Andesite lava flow, Mt. Rainier	20.7	27.9	15-25	0.1-0.20	Watters et al., 2000
Dacite Dome, Mt. Hood	20.6-26.1	79.6	19-45	0.12-0.31	Watters et al., 2000
Citlaltepētł, Espolon de Oro cone	2.33-2.55	120	30-34	0.21-0.45	Zimbelman et al., 2004
Citlaltepētł andesitic dome	2.3-2.7	50-10	19.5-4.7	0.58-3.57	Concha-Dimas et al., 2004
Tenerife lava	21.7+-2.3	36.2+-25.9	28-31		

Tenerife lava altered	10.5+-2.8	5.1+-3.1			del Potro et al., 2008
Stromboli lava unit, sciara del Fuoco area	18.63	50	31-43	1.5-3.9	Apuani et al., 2005
Lava	24.5+-1.5	110.2			
Lava altered	22.2+-3	29.6+-11.8			
Flows and clastic, Kilauea (unsaturated)	23.5-27.5	150-350	57	1.18-1.33	Okubo 2004
Flows and clastic, Kilauea (saturated)	23.5-27.5	150-350	57	1.30-1.47	Okubo 2004
Basalt, Corum, Turkey	22.25-23.23	130.20	41-49	1.16-6.75	Kocbay et al., 2006
<i>Brecciated rock</i>					
Crater wall sequences, white island Volcano	20	35	30.6-41.7	0.30-0.72	Moon et al., 2005
Tenerife autoclastic breccia	14.7 +- 1.3	27.1			Del Porto et al., 2008
Block and ash, crater rock, Mt. Hood	26.1 - 21.3	71.2 - 26.1	40.8	0.0966	Watters et al., 2000
Stromboli Breccia	8.83 - 17.46	30 - 80	29 - 20	0.8 - 2.0	Apuani et al., 2005

All values are given as an average.  $\gamma$ : unit weight; UCS: uniaxial compressive strength;  $\phi$ : friction angle;  $c$ : Cohesion.

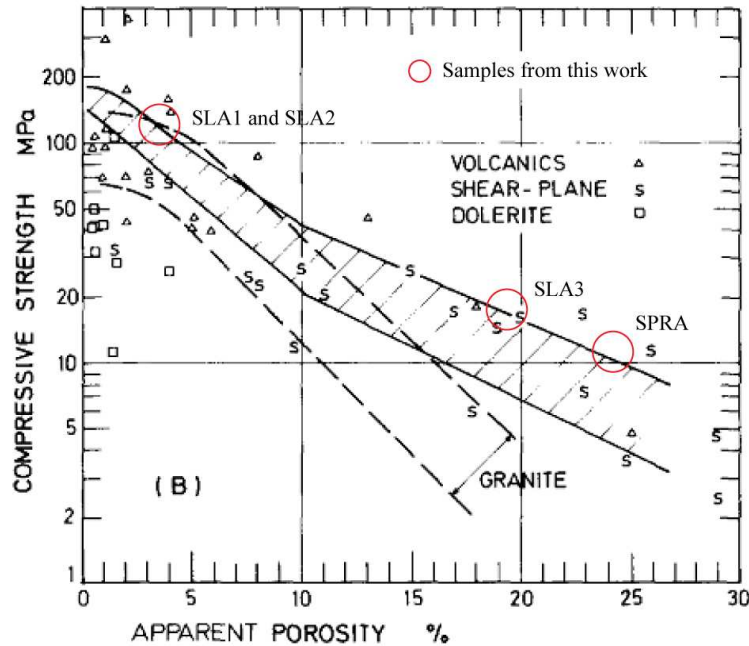


Figure 4.7 Compressive strength as a function of effective porosity. From Lumb (1983).

#### 4.2.1 Characterization of Porosity

As is explained above, total porosity ( $\eta_t$ ) was obtained from different techniques:

- pycnometer analysis;
- Thin-sections images analysis;
- Medical tomographies images analysis;
- X-ray tomographies images analysis.

Weathered/altered volcanic rocks from Solfatara, Ischia and Bolsena exhibit a wide range of  $\eta_t$  values increasing from 0.69 % for fresh lava to 57.67 % for unwelded ignimbrite, which also presents the lowest value of bulk weight  $\gamma$  (9.60 KN/m<sup>3</sup>). Figure 4.8a shows a direct relationship between total porosity and alteration grade of samples.

In general,  $\eta_t$  increases with weathering grade for all rock series (SLA, SPRA, IGT and BoPRA). Results from X-ray tomography and pycnometer tests reveal that  $\eta_t$  increases progressively with weathering grade with some minor changes in lava series, where values of SLA3 increase drastically and values from SLA5 present a small reduction. Lava series show the highest increase in porosity with alteration grade, from 0.69 % obtained with medical CT

image analysis to 31.5 % obtained with X-ray micro-tomography images. Differences in the results from X-ray micro-tomography and medical tomographies can result from the different resolution and from the consequent averaging. In particular, results reported in Figure 4.8a are obtained starting from estimated density values from which total porosity is computed by knowing the specific weight of the solid phase. In addition, for the porosity values computed from X-ray medical tomography, the density values for different slices are influenced by the coarser resolution with respect to micro CT and the adopted specific weight value of the solid phase used in the calculations. At the same time, medical CT allows to evaluate the total porosity on large rock core samples so it is able to provide a porosity value at a larger scale, where bigger pores are included. Differences could also depend on the required manual thresholding process and image sharpening, which in turn could depend on the modes of acquisition and the heterogeneous nature of the rock.

After all, image analysis represents a rapid and precise method to obtain pore structure (e.g. area, volume, shape, frequency, and spatial distribution). Results suggest an easy individual identification and quantification of pores; moreover, 3D reconstruction of its structure is available, which in turn represents a great tool in explaining pore structure evolution during mechanical tests (e.g. uniaxial and triaxial tests). Small changes as reduction in pore-sizes, closure of small fractures and mode of sample-failure could be explained easily.

Effective porosity ( $\eta_e$ ) was obtained from bulk-specific weight measurements and by mercury intrusion porosimetry. Values increase from 6 % for fresh lava obtained with bulk-specific weight measurements to 65 % to unwelded ignimbrite obtained with mercury intrusion porosimetry. Figure 4.8b shows direct relationship between  $\eta_e$  and alteration grade of samples. Results reveal that  $\eta_e$  increases progressively with weathering grade with some changes in IGT series, where values for IGTA present large decrement.  $\eta_e$  obtained from bulk-specific weight measurements seem to have no clear relationship with weathering grade (Figure 4.8b). The reason could be the percentage and size of interconnected pores and fractures contained in each samples. It means that porous system connectivity does not increase progressively with weathering degrees. The decrease in the computed porosity by imbibition could also be the result of a decrease in size of the pores with the increased alteration and then with a consequent difficulty in their saturation under low air vacuum conditions. Pore evolution is described in terms of structure of the groundmass, nature and degradation of the crystals and pumice fragments and post-depositional alteration processes:

a) In general, the evolution of pores in SLA series is related to oxidation and argilization process and connected micro-cracks, as it could be observed by optical microscop. Reduction of porosity in SLA5 is related to hydrothermal processes, as large pores have been filled by new minerals, like amorphous silica and clay minerals.

b) The evolution of pore structure in SPRA series is related to grain-size content and grade of groundmass cementation. In this way, the dominant pore types are secondary; they could be developed during and after a selective dissolution of minerals.

c) The evolution of pore structure in IGT series is related to the high proportion of pumice fragments. Pumice fragments present very open structures, moreover fragmentation of the vesicles walls is very common, degradation of pumice enhances pores connection, consequently a very open structure. The most altered sample in IGT series presents a very dense structure and a drastic reduction in pores content. In this case, pores have been filled by

clays, amorphous minerals and small fragments of other materials transported by hydrothermal processes.

d) High porosity values in BoPRA series is related to the depositional processes. Reconstruction of pore structure and microscopy observations reveal also a high percentage of interconnected pores, which is also promoted by degradation and fragmentation of pumice content.

The combination of techniques described above, give a good presentation of grain size and pore size distribution of weathered/altered volcanic rocks. They provide qualitative and quantitative evaluations of total and effective porosity and allow the quantification of spatial pore structure and size distribution. The most relevant conclusions are as follow:

- Significant relationship exists between porosity and alteration/weathering grade for all the samples. Total porosity increases with grade (Figure 4.8a, b).
- Thin section image analysis allows describing pore shape characteristics on a plane (e.g. area, perimeter, circularity, and roughness). Thin section preparation, orientation and size could influence the final estimates.
- Porosity values obtained from mercury porosimeter are generally slightly higher than the values obtained by water immersion method. This could result by the forced of mercury intrusion and damaging or opening of small fractures.
- Connectivity and effective porosity estimates can be obtained from bulk specific weight and mercury porosimeter measurements.
- 3D values of porosity can be computed starting from 2D data obtained by means of analysis of images of thin sections (e.g. see Farmer et al., 1991). The final value is controlled by the adopted transformation relationship.
- X-ray tomography is the fastest and more precise technique to obtain 3D textural information. This method allows measuring pore size and pore distribution.

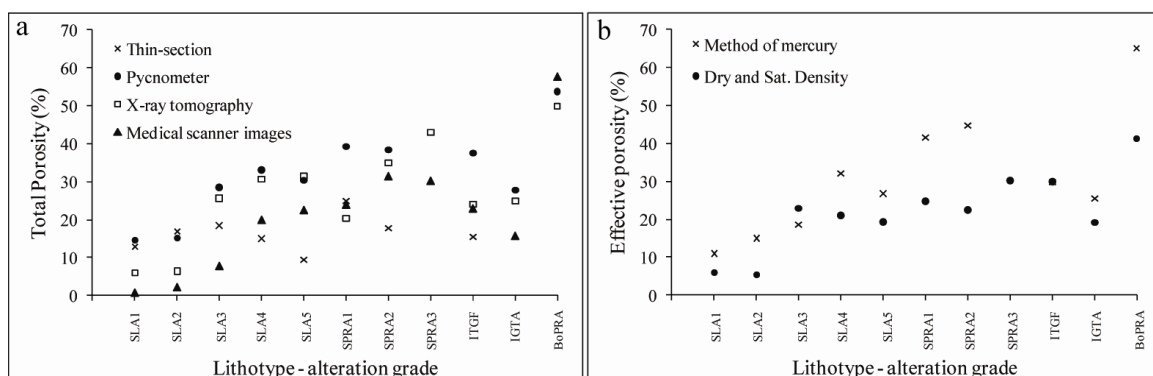


Figure 4.8 a) Total porosity as a function of lithotype obtained from pycnometer test, thin section analysis (3D) and X-ray tomography (Micro CT). b) Effective porosity as a function of lithotype obtained from bulk specific weight measurements, water immersion and mercury porosimeter.

The fractal nature of weathered/altered volcanic rocks is a function of the lithology and the grade of alteration. Fractal dimension was determined from pore volume values collected in thin sections, x-ray tomographies and mercury porosimeter. A simpler approach proposed by Farmer et al. (1991) was followed to compute the 3D porosity by 2D shapes collected from thin section images. Once, 2D conversion was made, values collected from x-ray tomographies and thin sections, which represent connectivity of pores, were wide comparable. Fractal dimension is very useful in interpreting pore frequency distribution. Pore frequency distribution in lava series (SLA), suggests a fractal behaviour of porosity with values between 1.35 and 1.92. While, pore frequency distribution in pyroclastic sequence (SPRA), suggests a fractal behaviour of porosity with values between 1.36 and 1.45. Otherwise, D in IGT series ranges between 1.31 to 1.57 (see also, Table 4.1). In all series, D decreases progressively with weathering sequence, suggesting a relative increase in frequency of large pores (Figure 4.9b-f). The fractal dimension corresponding to the most altered lava rock (SL5) and most altered ignimbrite (IGTA), deviate from this trend, suggesting an increment of the relative frequency of smaller pores, as well as large pores filled by new minerals (amorphous silica and clay minerals). This hypothesis is supported by thin section observations and XRD analyses.

Fractal dimension obtained from Mercury porosimeter, represents distribution of non interconnected pores. Variation of D values estimated from  $\eta_c$  data is lower than D values estimated from  $\eta_t$ , in particular variation is small in SLA and IGT, where D vary from 2.03 to 2.13 and from 2.05 to 2.14, respectively. Larger variation is observed in SPRA series (1.9 to 2.15) where large anisotropy in the matrix is observed and is associated to hydrothermal processes (leaching and deposition). As well as, D values estimated from  $\eta_t$ , these values decrease progressively with weathering sequence, even if some variations are observed in SLA2, SLA5 and IGT.

Figure 4.9a indicates that different values of the fractal dimension occur at different scale ranges. These results suggest that scaling relationships based on fractal geometry may be very useful in describing a more real distribution of pores. In addition, scaling relationship in pore fractal dimension is restricted principally by the mode of data acquisition. For example, acquisition of pore values in thin-section depends principally on the area of the thin-section, the resolution of the image and the quality of final results depends on a series of noise reduction, filtering, thresholding, and particle separation steps.

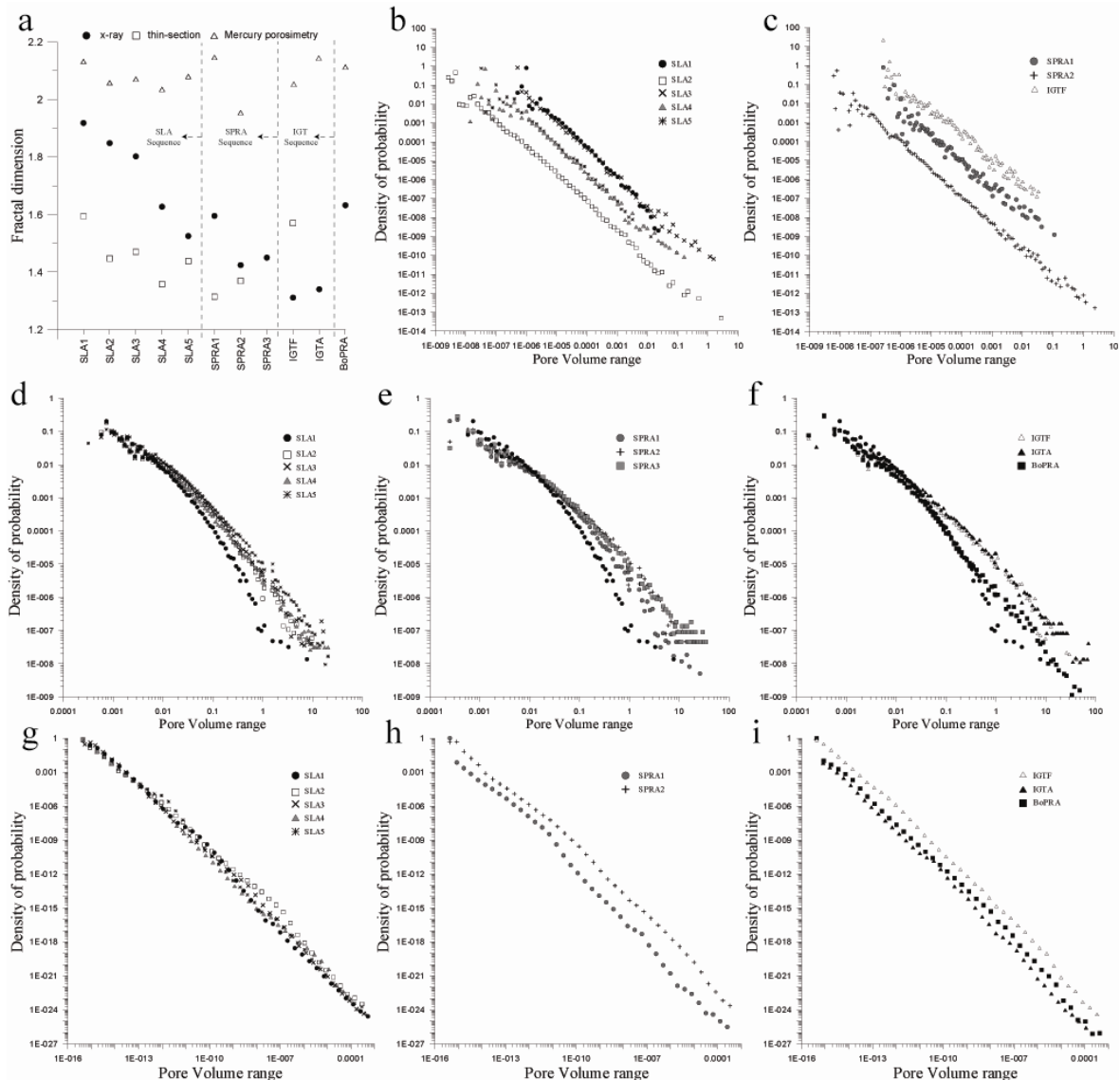


Figure 4.9 a) Fractal dimension calculated from pores size distributions obtained by different techniques (see legend); b) Pore volume distribution of SLA sequence from thin-section image reconstruction; c) Pore volume distribution of SPRA and IGT sequence from thin-section image reconstruction. The lack of information corresponds to the difficulty in preparing thin-sections in very soft samples. d) Pore volume distribution of SLA sequence from x-ray tomography image reconstruction; e) Pore volume distribution of SPRA sequence from x-ray tomography image reconstruction; f) Pore volume distribution of IGT sequence and BoBRA from x-ray tomography image reconstruction. g) Pore volume distribution of SLA sequence from mercury porosimetry; h) Pore volume distribution of SPRA sequence from mercury porosimetry; i) Pore volume distribution of IGT sequence and BoBRA from mercury porosimetry.

#### 4.2.2 Evaluation of P and S waves velocity

Nature of rock materials is anisotropic. Changes in physical properties are dependent upon the lithology of the rock sample and the evolution of its environment. At the same time, the presence of voids in the rock, especially microcracks, affects physical and mechanical properties and is responsible for the anisotropy found in many rocks. In this way, pore structure, texture of the rock (geometric arrangement and sizes of grains, crystals, pores and



glass, fluid saturation), fracturing and severe mineralogical changes in a rock are commonly quantified. These variations in rock medium could be detected and quantified by the use of compressional ( $V_p$ ) and shear ( $V_s$ ) wave velocities.  $V_p$  and  $V_s$  generally decrease with increasing porosity for certain kind of rock. Recently, Vinciguerra et al. (2009) found that the  $V_p$  of tuff, with 10 to 30 % in porosity, ranges between 3.1 to 4.1 km/s. At the same time, Marques et al. (2010) found that high values in  $V_p$  ( $\approx 5.5$  Km/s) correspond to lower values of porosity in gneiss ( $< 2$  %). However, this velocity-porosity relationship becomes complicated when micro-cracks exist, because the elastic properties of a rock are more affected by the micro-cracks than by open porosity (see Sousa et al., 2005 and Martínez- Martínez et al. 2006). Furthermore, the aspect ratio (i.e. longer dimension to shorter dimension) of cavities could also have a pronounced effect on the elastic properties, even though they have little contribution to total porosity. In addition, previous description could be reinforced by Martínez- Martínez et al. (2007) studies. The authors quantified the most influential aspects in  $V_p$  and  $V_s$  by a series of petrographical parameters. They conclude that the variation in  $V_p$  and  $V_s$  are explained by density of brecciation, fine-grained matrix content, clast size distribution and preferred orientation of clasts.

Statistical evaluation of compressional ( $V_p$ ) and shear ( $V_s$ ) wave velocities and relationship between lithotype and alteration grade are presented in Figure 4.10c and d, respectively. In general  $V_p$  values follow a decreasing trend with increasing alteration grade in all series. This decrement seems to be constant ( $\pm 7$  %), in particular for SLA sample, decreasing from 4.3 Km/s, for SLA1, to 2.7 Km/s, for SLA5 (totally altered).

On the contrary, samples from IGT series follow an increasing trend with increasing alteration grade.  $V_p$  values increase drastically from 1.1 Km/s for IGTF to 2.2 Km/s for IGTA. Based on thin section and x-ray CT images observations, IGT are composed by interconnected pores, which in some cases form flat and elongated cavities. On the other hand, fractal dimension analysis, in particular values derived from mercury porosimeter reveals that IGTA sample is composed prevalently by small pores.

In this way, significant variations in  $V_p$  observed in Figure 4.10c are closely related with physical changes, consisting of the development of new pores, clay minerals and the increased and decreased width of previous interconnected cavities by hydrothermal processes. On the other hand,  $V_s$  values seem to have no clear relationship with weathering grade in all series (Figure 4.10d). Large differences are presented not only between each alteration grade, but also between each sample. For example, large variations in  $V_s$  measurements are observed along SLA series; in particular SLA1 and SLA5 vary from 1.4 to 3.9 km/s and from 0.68 to 2.4 Km/s, respectively. The reason could be the percentage and size of interconnected pores and fractures contained in each sample. A smaller variation is observed in samples from SPRA series, which seems to present a more persistent network of pores and microfractures (Figure 4.10d).

In addition, an exponential change in rock structure is observed when average values for  $V_p$  are compared with the average of  $\eta_e$  obtained from bulk-specific weight measurements. In this way, best fitting exponential relationships between these properties are shown together with their coefficient of determination ( $R^2 = 0.82$ ) in Figure 4.10a. In general, all values are well correlated, although, few dispersed values are observed in SLA3, SLA4, and SLA5 samples.  $\eta_e$  obtained from bulk-specific weight measurements seems to have no clear relationship with  $V_s$  (Figure 4.8b). Best fitting exponential relationship between these properties has a very low correlation coefficient ( $R^2 = 0.40$ ). In particular,  $V_s$  values in SLA1, SLA2, SLA5 and BoPRA show large variation. This variation could be attributed to a greater abundance of small cracks

or micro fissures (previous described) and difference in pore network arrangement (SLA1 and BoPRA cases).

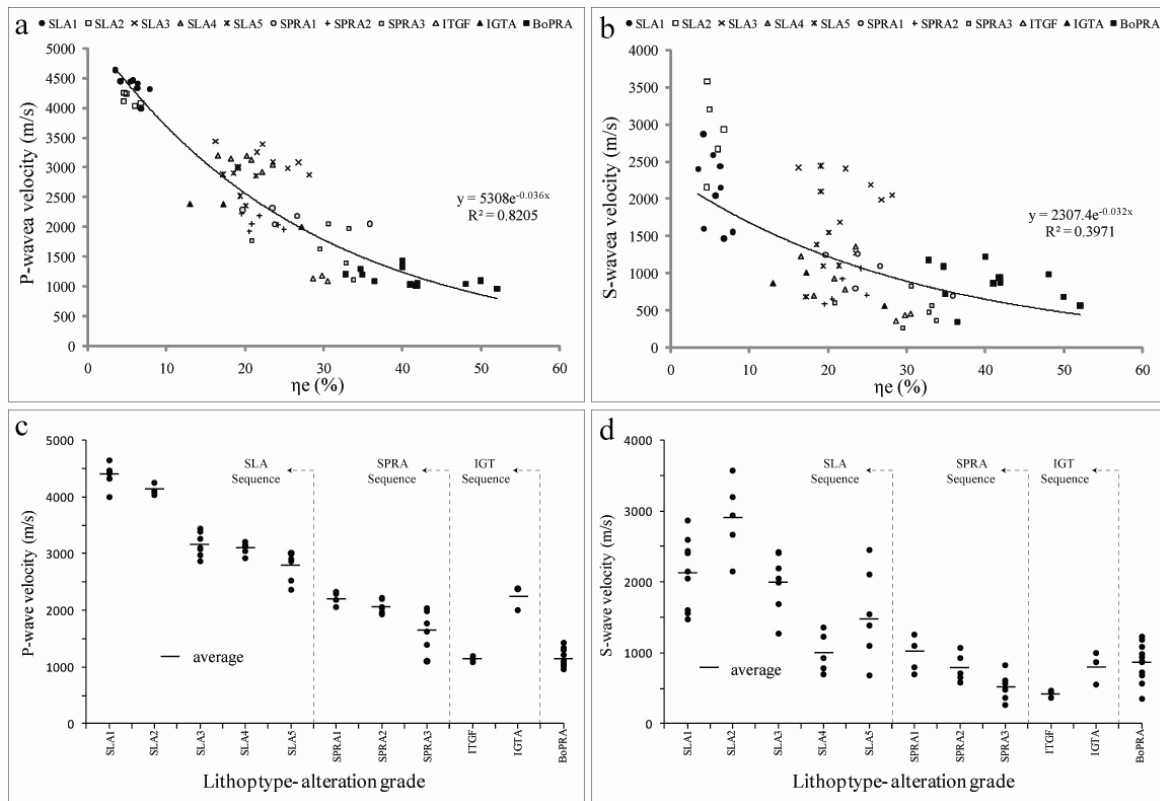


Figure 4.10 P-S wave velocity a) propagation velocity of P-wave as a function of effective porosity. b) propagation velocity of S-wave as a function of effective porosity. c) propagation velocity of P-wave as a function of lithotype and grade of alteration. d) propagation velocity of S-wave as a function of lithotype and grade of alteration.

#### 4.2.3 Evaluation of uniaxial compressive strength

The influence of alteration degree on rock strength has been previously discussed by many authors (e.g. Lump 1983, Kate 1993, Gupta and Rao 2000, Avar and Hudyma 2007, Marques et al., 2010, among others) In these, articles it is well established that Uniaxial Compressive strength (UCS) of rock decreases with the increase in porosity and grade of alteration, Moreover correlations between physical properties as rock density, modulus of elasticity, compressive waves velocities, and saturation water content are discussed. In this way, the influence of degree of alteration on the strength and rock behaviour was estimated by Lump (1983). Regarding the definition of an index for establishing the influence of weathering on the strength and deformability, the authors suggest that UCS and wave velocities are the most appropriate. Physical, petrographical and mineralogical experiments were performed by Kate (1993). The results were analysed and related each other to understand the nature of the relationship between rock strength and deformations. Gupta and Rao (2000) have also performed petrographical and mechanical tests. Even though, the data in some of these experimental studies is scattered and exhibit large variations in elastic modulus and strength,

they show a significant reduction with increasing porosity. Otherwise, Avar and Hudyma (2007) analyzed the variations in elastic modulus and strength with respect to porosity. The authors suggest strength versus elastic modulus plots as a tool in explaining the heterogeneous nature of tuff. Experimental program carried out by Marques et al., (2010) showed that basic physical (e.g. porosity, saturation water content and P-S wave velocities) and mechanical characterization could be used to establish the weathering state of rocks, as well as the degree of anisotropy of the rocks.

Statistical evaluations of UCS values ( $\sigma_c$ ) and its relationship between lithotype and alteration grade are presented in Figure 4.11a. In this figure, all sequences (e.g. SLA, SPRA, IGT and BoPRA) are separated by a dash line. In general, the strength in all series varies with alteration grade, ranging from the strongest measured values 116.7 MPa for less altered lava sample (SLA1) to the weakest measured value of 5.7 MPa for un-welded ignimbrite (BoPRA). The strength also presents variation with rock type; in general, strength values follow a decreasing trend with increasing alteration grade in all series. The average values of strength in SLA series vary from a minimum of 16.8 MPa in the most altered sample (SLA5) to a maximum of 116.7 MPa in the less altered sample (SLA1) (see also, Table 4.2). This variation is relatively small. In particular variation is small ( $\pm 5-10$  MPa) when values are considered for almost all the alteration grades and all sequences. There is one exception between SLA2 and SLA3 where strength value seems to change drastically (from 108 to 25 MPa, see Figure 4.11a, b and c). Strength values in SPRA series vary from a minimum of 7.23 MPa (SPRA3) to a maximum of 13.3 MPa (SPRA1). Variation is very small and it probably depends on the size of grains and clasts, contained in each specimen.

Strength values in IGT series follow an increasing trend with increasing alteration grade. The average values vary from 5.74 MPa in the less altered sample (IGTF) to 16.30 MPa in the most altered sample (IGTA). A Change in trend behaviour suggests a drastic transformation of sample structure due to hydrothermal processes. In this sequence, total, effective porosity and bulk density range from 25 to 24 %, from 25.5 to 29.7 % and from 15.1 to 17.8 KN/m<sup>3</sup>, respectively.

Typical variations between axial stress ( $\sigma_a$ ) and axial strain ( $\epsilon_a$ ) for all lithotypes are illustrated in Figure 4.11c and Figure 4.11d. All stress-strain curves in each sequence present a decrement of slope and consequently changes in the static elastic properties and stiffness with increasing alteration. Curves from SLA series show that fresh and slightly weathered samples (SLA1 and SLA2, respectively) behave almost linear over the full stress range (quasi-elastically), these curves show a clear strength peak with a fragile peak/post peak behaviour (Figure 4.11b). On the contrary, curves from SLA3 to SLA5 show a more developed crack closure behaviour along the initial part after which they behave elastic (Figure 4.11c). At certain stress level, these curves present a decrement-increment of stress after which they finally raise sharply to a smooth and/or irregular strength peak passing from low to high alteration grades.

Curves from SPRA, IGT and BoPRA series show a clear and a more developed crack closure behavior along the initial part of the curve, in particular curves from IGT series (Figure 4.11d). At all stress level, these curves present several decrement-increment of stress after which they finally raise sharp to smooth and not clear strength peak. Almost all the specimens failed by longitudinal splitting performed nearly parallel to the axis of the specimens. In BoPRA and IGTA samples particularly large deformation were also observed.

The average of Young’s modulus and Poisson’s ratio for all lithotype is included in (Table 4.2). Results were calculated at 50 % of the axial stress-strain curve presented in Figure 4.11b-d, using linear fitting as described in previous section. In all cases, both Young’s Modulus and Poisson’s ratio are seen to decrease with alteration grade. The decrement of these properties not always corresponds to a decrement in strength. For example, between SPRA1 and SPRA2 samples there is a decrease in strength (from 13.3 to 8.6 MPa) and an increase in Young’s modulus and Poisson’s ratio (from 1.6 to 1.9 GPa and from 0.13 to 0.19 GPa, respectively). Again, the variation probably depends on grains sizes, its gradation and height of each layers, contained in each specimen. In addition, static modulus for the most altered rocks range from 0.8 to 3.7 GPa. These values are smaller than those reported by Losada et al., (2009); Heap et al., (2009); Avar and Hudyma (2007), probably because of the differences in alteration, which causes differences in stiffness.

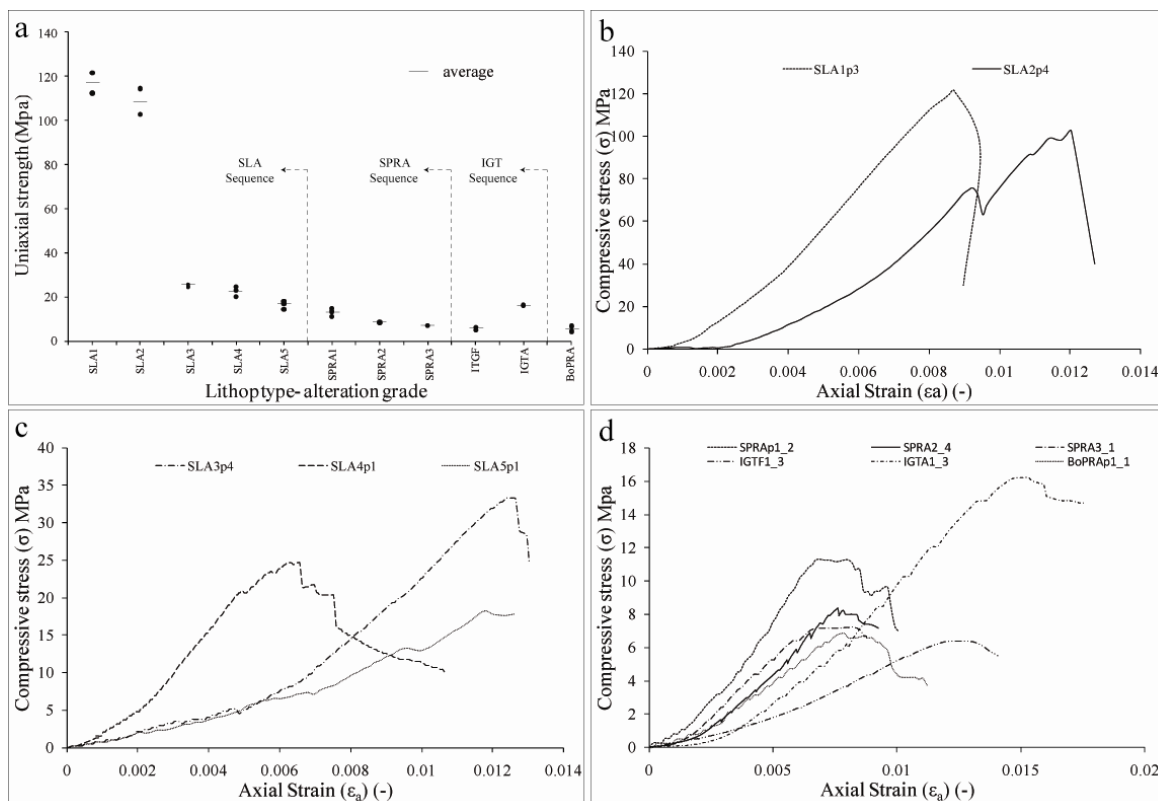


Figure 4.11 a) Lithotype vs uniaxial compressive strength. b) Young’s Modulus vs uniaxial compressive strength. c) Stress-strain behaviour for lava rock (ø 18 mm in diameter). d) Stress-strain behaviour for pyroclastic rocks (ø 18 mm in diameter).

However, an exponential decay of the properties is observed when average strength values are compared with the average of P-S wave velocities, porosity (total and effective) and dynamic Young’s modulus. In this way, best fitting linear and exponential relationships between these properties are shown together with their coefficient of determination ( $R^2$ ) in Figure 4.12a-f. The coefficient of determination,  $R^2$ , is relatively high and ranging between 0.67 and 0.97. In general, all properties are well correlated, but drastic changes in the properties are observed between SLA2 and SLA3. The best linear correlation is observed between Young’s modulus and UCS (Figure 4.12f). Reduction in both properties with increasing grade of alteration is

gradual for pyroclastic sequence (SPRA) and unwelded ignimbrites (IGT and BoPRA), whereas for SLA a sharp reduction is observed.

Structure and texture of samples which probably control strength and deformability, seem to be represented by P-S wave velocities and total and effective porosity. These relationships are described by exponential function. Figure 4.12a-d show that the most common physical characteristics controlling strength are the porosity and P-S waves velocity, as values of strength decrease with increasing porosity and decreasing P-S waves velocity. In Figure 4.12c and Figure 4.12d, for high porosity values, larger than 20 % a clear exponential decrease in strength is evident. Dynamic Young's modulus derived from P-S waves measurements are linearly correlated with UCS (Figure 4.12e). The coefficient of determination,  $R^2$  (0.89), is relatively high, even if some samples from SLA series (SLA2 and SLA3) present a sharp decrease. Finally, the pattern of the best linear relationship between UCS and Young's Modulus showed in Figure 4.12f, seems to be associated with microfractures (SLA1 to SLA2) and severe mineralogical changes (SLA3 to SLA5 and IGTF to IGTA).

The static and dynamic Young's modulus obtained for the investigated rocks are analyzed and compared as follow: the ratio of the dynamic to static modulus ( $K$ ) varies between 0.8 to 2.9 with drastic changes in SLA3 and SLA5 (4.9 and 4.8 GPa, respectively). Discrepancy between values exposed in this study suggests changes in sample structure, shape and aspect ratio of pores. Morphology of cavities has large influence in most altered samples. For example, microscopic inspection on sample SLA3, suggests an increment in pore alignment and pore elongation. In this case when length of pores increases the dynamic modulus decreases in all samples. On the contrary a decrement in static modulus is not always observed. However, the ratio of the dynamic to static modulus values is larger than those reported by Al-Shayea (2004), Cicotti and Mulargia, (2004) in limestone rocks, where values range from 0.9 to 1.9 and from 1 to 1.2, respectively.

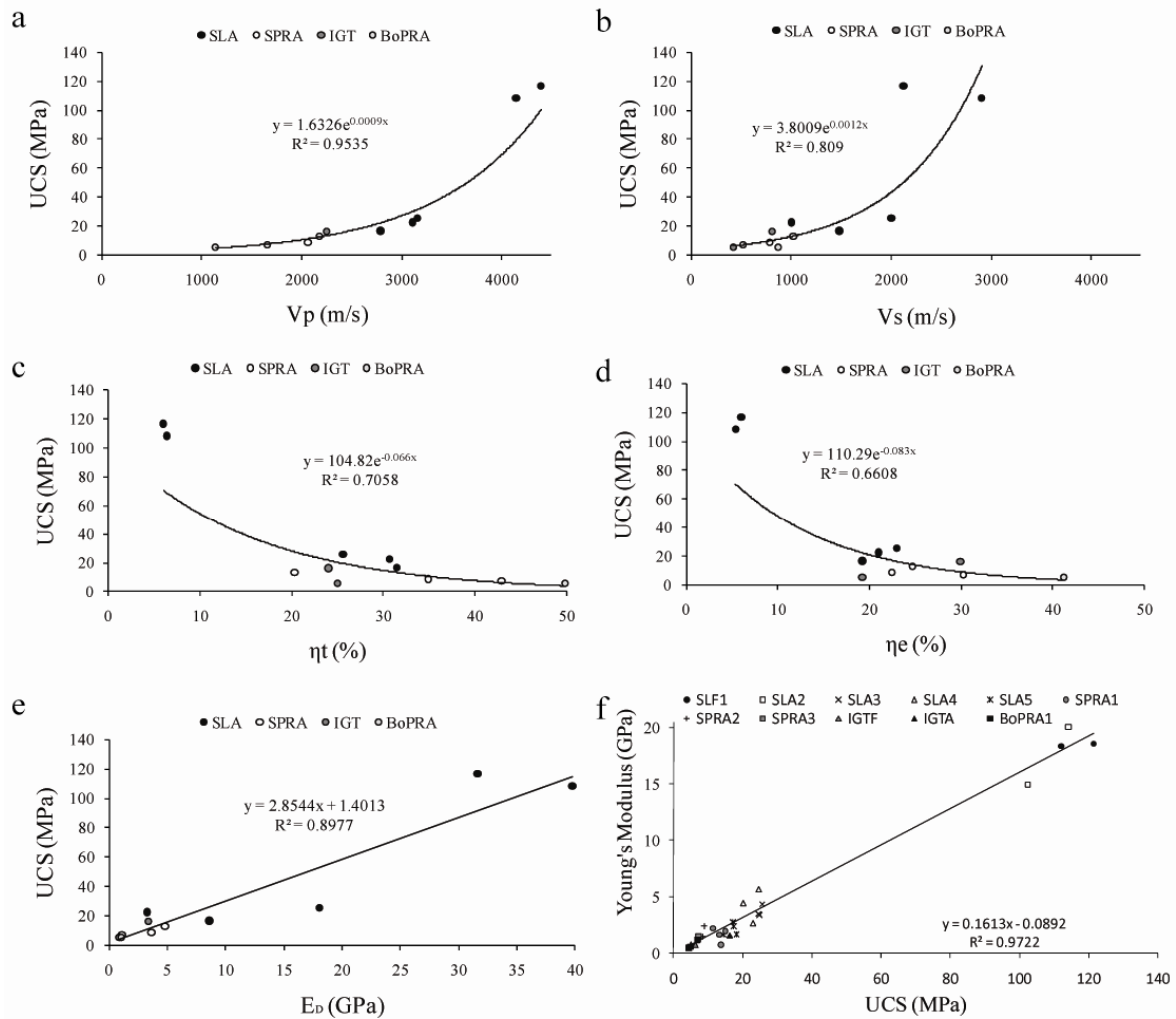


Figure 4.12 a) Uniaxial compressive strength as a function of: a) Vp, b) Vs, c)  $\eta_t$ , d)  $\eta_e$ , e) dynamic Young's Modulus, f) Young's Modulus vs Uniaxial strength.

#### 4.2.4 Evaluation of uniaxial compressive strength under stress-cycling experiments

Typical stress-strain curves under uniaxial stress-cycling experiments are presented in Figure 4.13b-d. In all samples, curves show a low to very low gradient in the initial part (crack closure region), in particular curves corresponding to IGTA sample. From these regions, gradient of the curves increases with the alteration grade in all series. All curves show a permanent strain accumulated of each cycle. Amplitude of each unloading-reloading cycle increases according to the alteration grade with minimum stress equal to 5 %. Again, the most altered samples (SLA5 and IGTA) show behaviour opposite to this pattern. In particular, larges changes are observed between IGTF and IGTA samples (Figure 4.13d), where the amplitude of cycles in IGTA sample are smaller. This is probably due to the large content of clay minerals and/or drastic changes in the mineralogy of the rocks. All curves present astrain-softening behaviour as seen in Figure 4.13b-d.

The accumulated damage in samples under cycle loading is represented by the evolution of static properties as rock approach failure Heap et al. (2008). In this way, Young's modulus

was calculated with respect to number of cycles from stress-strain curves (Figure 4.13b, c and d) by fitting the maximum and minimum condition of stress in each cycle. The relationship and evolution between the Young's modulus and uniaxial compressive stress is shown in Figure 4.13a. It can be seen that elastic modulus increases with cycle number. These increments are represented by the slope of the best linear fitting, characterized by values of the coefficient of determination,  $R^2$ , that are very high and ranging between 0.85 and 0.99. Slope of the line increases rapidly in SLA3 and SLA4, from 5.2 to 19 MPa and from 3.8 to 10.2 MPa respectively. In contrast, in the rest of the samples it seems to increase modestly. All stress-strain curves present a very clear strain-softening phase, where structure of pores seems to be crushed and micro-fractures seems to be closed. After this phase, Young's modulus increment is primary attributed to an augment of sample stiffness, consequently to a modestly increase in the level of crack damage within the samples (e.g. propagation of pre-existing and new cracks). These patterns are opposite to the patterns reported by Heap et al., 2008 and Heap et al., 2009 in crystalline rock with a low porosity and low initial crack density. In this study, the progressive degradation of sample stiffness is represented by a progressive Young's modulus reduction (11 and 30 % over the total sequence, respectively) and Poisson's ratio increment (increase by a factor of 1.7 and  $3\pm 5$ , respectively). The authors suggest that the evolution of these characteristics depends on the variation of pre-existing microcrack damage and increase in damage level with increasing stress. However, it is well known that the presence of cracks reduces Young's modulus and that its evolution depends on physical characteristics as porosity and grain sizes (Wong et al., 1996, Palchik 1999, Palchik and Hatzor 2002, Hudyma et al., 2004 and Goodwin et al., 2010).

Figure 4.13a and Table 4.1, show that Young's modulus in all series increases with decreasing both effective and total porosity. For example, the strongest sample (SLA3,  $E = 4.21-5.60$  GPa,  $\eta_t \approx 25\%$  and  $\eta_e \approx 18\%$ ) exhibits higher elastic modulus and lower porosity with respect to the weaker sample (BoPRA,  $E = 0.77-0.83$  GPa,  $\eta_t \approx 60\%$  and  $\eta_e \approx 50\%$ ). Samples SLA5 and IGTA, with a notable increment in strength and relative decrement in porosity with respect to SLA1-4 and IGTF, respectively, exhibits very high elastic modulus range ( $E = 3.16-4.39$  GPa and  $E = 2.04-2.79$  GPa, respectively). Figure 4.26 and Figure 4.27, show that Young's modulus in samples from SPRA series could be directly influenced by the grain sizes, the length of grain to grain contacts and matrix cementation (see also Figure 4.1). This assumption could be reinforced by failure patterns observations (from Figure 4.19 to Figure 4.26). Stress seems to be localized around grains and seems to follow grains arrangement.

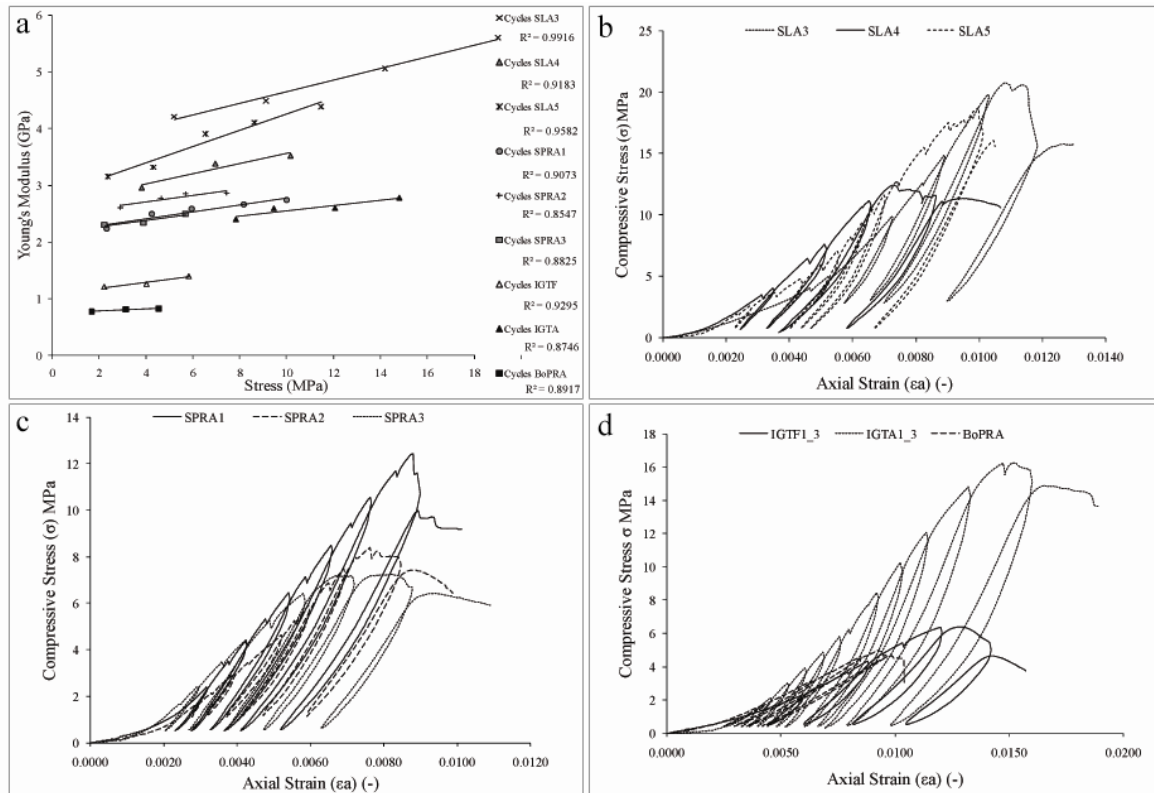


Figure 4.13 a) Evolution of Young's modulus as a function of lithotype, during increasing-amplitude cyclic stressing experiments. Stress-strain behaviour during increasing-amplitude cyclic stress experiments for: b) lavas series (SLA). c) pyroclastic rocks series (SPRA) d) pyroclastic rocks series (IGT and BoPRA).

#### 4.2.5 Evaluation of tensile strength

The behaviour of rocks in tension may be an effective indicator of their microstructure, anisotropy and hence state of weathering (Aydin and Basu, 2006). Tensile strength, as almost all mechanical properties, could be modified as a result of weathering; at the same time, the magnitude of the modification would depend on the type of the weathering processes. This section is concerned with the tensile strength patterns exhibited by different weathered/alterated volcanic rocks. Our studies analyse patterns at various stages of weathering. Minor variations in tensile behaviour (micro-structural state of rock and deformation) at initial stage of loading was quantified by tangent modulus (see Aydin and Basu, 2006 for a review).

Averages of tensile strength from each sample are shown in Table 4.1 and Table 4.2. The relationships between lithotype and alteration grade are presented in Figure 4.14a. Best fitting linear relationship between tensile strength and bulk density are shown together with their coefficient of determination ( $R^2=0.80$ ) in Figure 4.14b. Tensile strength patterns for all series of rock are illustrated in Figure 4.14c-d. The average values of tensile strength vary from a minimum of 0.2 MPa in the unwelded and altered ignimbrite (BoPRA) to a maximum of 10.4 MPa in the less altered samples of lava (SLA1) (Table 4.2). Figure 4.14a shows a constant decreasing trend in tensile strength associated to the grade of alteration ( $\approx 1.5$  MPa) in almost all weathering series. On the contrary, this decrement is drastic in the SLA series, where reassign from SLA2 to SLA3 the values change from 10 to 4 MPa. On the other hand, the tensile strength in IGT series increases with alteration grade from 0.8 to 1.1 MPa. Comparison of bulk density and tensile strength is represented in Figure 4.14b, this relationship is very



significant, moreover it suggest that tensile strength depends on the intrinsic properties of each specimen (e.g. pores content, rock texture and proportions of clasts for pyroclastic and ignimbritic rock cases [SPRA and BoPRA series]).

The more representative tensile stress-strain curves for all series reconstructed from strain gauge data are presented in Figure 4.14c and Figure 4.14d. Curves are compared with the corresponding weathered/altered grade as follow: decrement of the slope in stress-strain curves suggest gradual decay in tensile strength and gradual increase in strain. In this way, SLA series changes from linear elastic (SLA1) to elastic-plastic behaviour (SLA5). Particularly, SLA5 suffers this change in the first part of the curve (see inset in Figure 4.14c). Samples of SPRA and IGT series seem to behave linearly elastic-plastic during all stress-strain range. There is one exception in IGTA, where clear linear elastic behaviour is observed along the first part of the curve. Another exception is that it exhibits higher value of strength than its fresh side (IGTF).

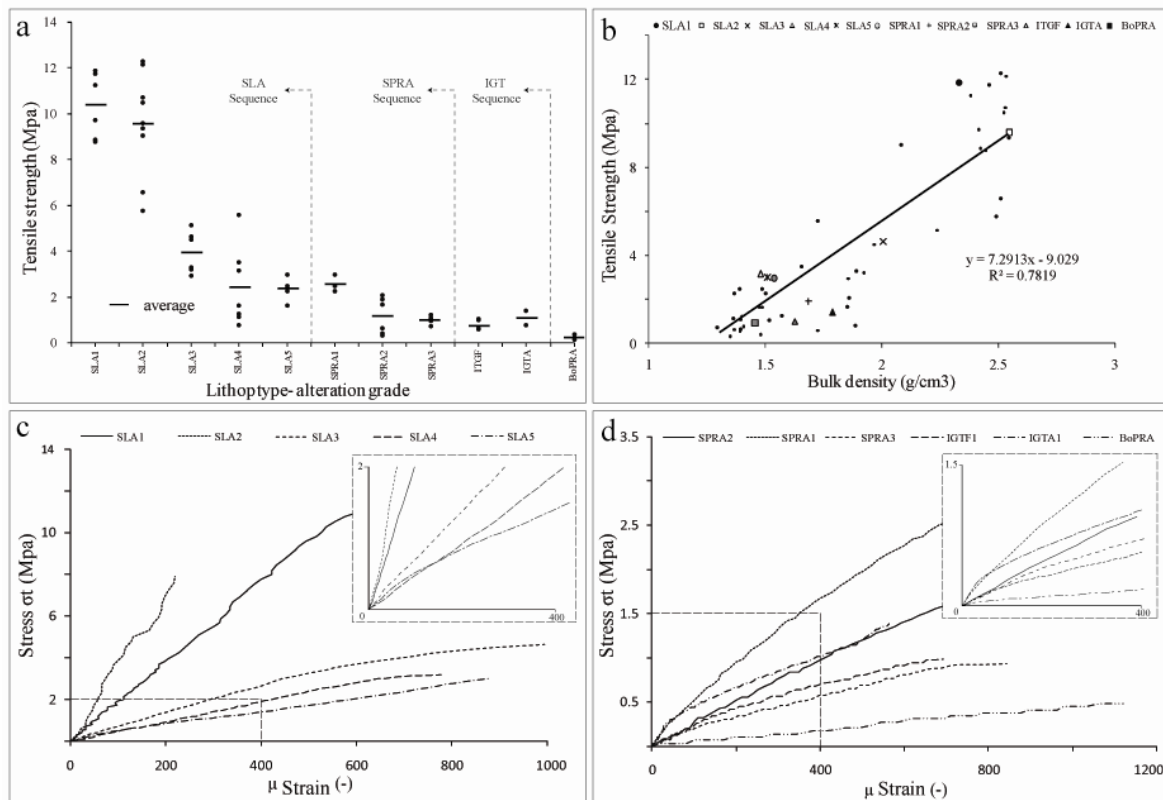


Figure 4.14 Tensile strength (Brazilian test) as a function of: a) Lithotype b) Bulk density. Tensile stress-strain behaviour for: c) lava rock (disks of  $\phi$  54 mm in diameter). d) pyroclastic rocks (disks of  $\phi$  54 mm in diameter).

An exponential decay of the properties is observed when average values for tensile strength and  $E_{T150}$  are compared with both the average  $\eta_t$  and  $\eta_e$  values (Figure 4.15a-d). The computed best fitting curves are characterized by values of the coefficient of determination in the  $(0.67 < R^2 < 0.81)$  interval. In general, each weathering sequence shows a significant degree of correlation among bulk density, tensile strength and  $E_{T150}$ . Values obtained for  $E_{T150}$  clearly reflect the influence of changes in intrinsic properties, and they seem to represent better the changes in rock structure. The most rapid rate of decrease in  $E_{T150}$  is observed between SLA2

and SLA3 (from 36 to 6 MPa), where corresponding total, effective porosity and bulk density range from 6.4 to 25 %, from 5.4 to 23 % and from 16 to 19 KN/m<sup>3</sup>, respectively. Failure mode in all samples is characterized by vertical or sub-vertical fracturing, parallel to the direction of loading. Tensile strength and fracturing in SLA1 and SLA2 samples are conditioned by crystals size and microstructure, respectively. SLA4 and SLA5 samples are conditioned by their matrix structure, interconnected pores and recrystallization of amorphous silica. Tensile strength and fracturing in the IGT sequence are conditioned by structural characteristics of lithics and pumice fragments content. Tensile strength and fracturing in SPRA sequence are conditioned by the sizes and localisation of grains.

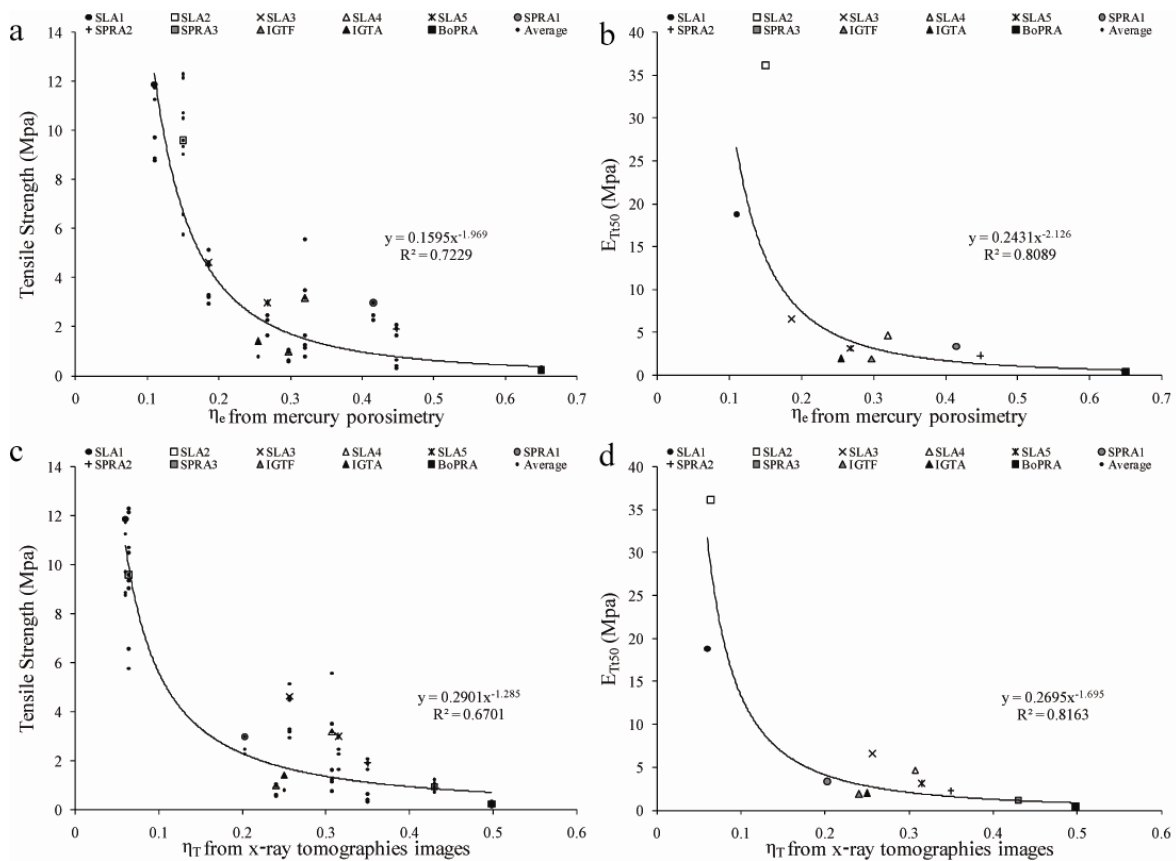


Figure 4.15 a) Tensile strength vs  $\eta_e$ , b)  $E_{T150}$  vs  $\eta_e$ , c) Tensile strength vs  $\eta_T$ , d)  $E_{T150}$  vs  $\eta_T$

#### 4.2.6 Multiple linear regression

The statistical analysis is an effective tool for analysing large quantities of data. The relation between these data could be studied through univariate statistics and bivariate statistics. Otherwise, this behaviour could be explained by multivariate analysis. In general, there are several techniques of multivariate analysis, explanatory (linear regression, discriminant analysis, conjoint analysis, among others) and descriptive (factor analysis, principal component analysis, correspondence analysis, among others). Linear regression is a statistical technique used to analyze the relationship between one dependent variable and one or more

independent variables. In this way, a regression model that contains more than one independent variable is called a multiple linear regression, and its equation is:

$$y = \beta_0 + \beta_1 X_1 + \beta_2 X_2 + \dots + \beta_n X_n \quad (13)$$

Where  $\beta_0$  denotes a vector coefficient,  $\beta_{1,n}$  are regression coefficients and  $X_{1,n}$  are the independent variables. Therefore, the success in obtaining a multiple linear regression could depend on the presence of simple linear correlation of each independent variable. Results could be improved by removing less important independent variables (those with  $\beta \approx 0$ ).

The analysis of available data could be very complicated when a large amount of information is grouped in many variables. There are two multivariate analysis methods to avoid this problem: factor and principal component analysis. They are based on combining many variables in order to identify which input variables are important for contributing to the prediction of the output variable and also to quantify how changes in the values of the input parameter alter the values of the outcome variable.

Multivariate analysis (e.g. factor and principal component analysis) was carried out using the code SPSS v.15 (from SPSS Inc.) and following the methodology described in Martínez-Martínez et al (2008) and Martínez-Martínez (2009). Physical and mechanical properties were not considered together. To compare relationships between  $V_p$ ,  $\eta_e$ ,  $\eta_T$ ,  $\gamma$ , UCS, and E a number of different relationships were tested in turn. The best multiple linear relationships founded are represented in equation 14 and 15. UCS and E are considered as dependent variables, contrary,  $V_p$ ,  $\eta_e$ ,  $\eta_T$ , and  $\gamma$  are considered as independent variables.

$$\log UCS = 0.603 + 0.401(V_p / 1000) + 0.004(\eta_e) - 0.008(\eta_T) - 0.014(\gamma) \quad (14)$$

$$\log E = -0.175 + 0.478(V_p / 1000) - 0.009(\eta_e) + 0.004(\eta_T) - 0.032(\gamma) \quad (15)$$

In these equations it is observed that  $V_p$  is very important in predicting UCS and E, whereas the rest of the physical parameters ( $\eta_e$ ,  $\eta_T$ ,  $\gamma$ ) are important for improving the equation. Relationship between the estimated and real values measured in laboratory are represented in Figure 4.16a and Figure 4.16b. It is observable that a very good relationship is represented by the computed best linear fitting, which is characterized by high values of the coefficients of determination ( $R^2 > 0.97$ ). Predicted UCS and E are controlled basically by  $V_p$ . This is due to the fact that values of E, UCS, and  $V_p$  depend on the geometry and number of discontinuities and cavities contained in each sample. In other words, ultrasonic parameters are a useful tool to investigate or predict UCS and E behaviour of rocks. Finally, relationships between physical and mechanical properties, described previously, are corroborated by equation 14 and 15

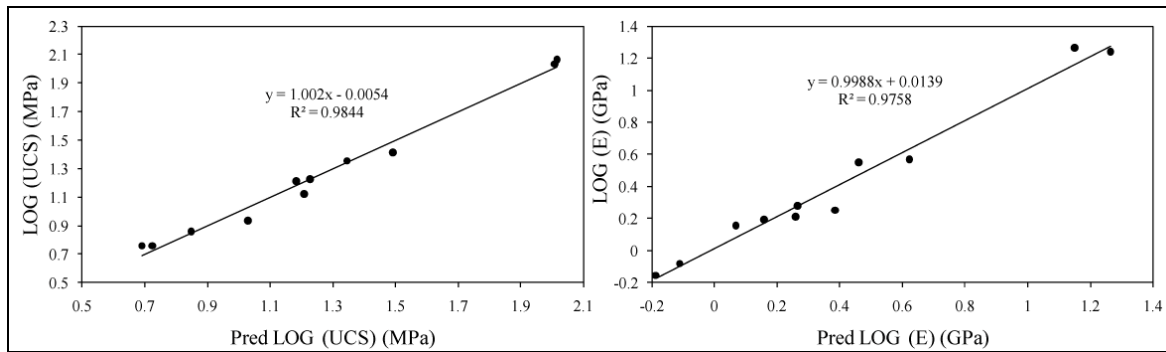


Figure 4.16 relationships between observed and quantified (predicted from Multiple Linear Regression). a) UCS eq. 13 b) Young's modulus eq.14

#### 4.2.7 Triaxial strength

A series of multistage triaxial compression tests were conducted to determine the rock mechanical properties of weathered/altered volcanic rocks. Behaviour of samples during tests and changes in deformation (from brittle to ductile) were also identified and discussed. Each sample in multistage triaxial tests was subjected to at list four confining pressures (SLA2, SLA3, SPRA1-3, IGTF and IGTA) (Figure 4.18b-d). Several triaxial tests were conducted on samples, where imminent failure point, were not easily recognizable. The stress-strain curves at different confining pressures are presented in Figure 4.17b-d. Curves show that stress peak of each step and strength increase with confining pressure. Slope decrease of the curves in all series is related to the increment in alteration grade. There are just two exceptions between SLA4 – SLA5 and IGTF – IGTA, where most altered samples are characterized by a strength increment. As it was described in precedent paragraphs, an increase in strength and changes in stiffness, appear to be associated with severe mineralogical changes promoted by hydrothermal processes. For example, matrix in SLA5 is totally replaced by argilization and silica-amorphous minerals. On the contrary, IGTA sample is composed by a very dense structure with a drastic reduction in porosity. In this case, pores have been filled by clays, amorphous minerals and small fragments of other materials.

Comparison of the stress-strain curves clearly shows a well developed strain-softening phase in sample SLA2, SLA3 and SLA5 (Figure 4.17b and Figure 4.17). This could correspond to the compaction of pores and cracks oriented perpendicular to the axis. Contrary, curves from SLA1 behave almost linearly over the full stress range (quasi-elastically) and it shows a clear peak strength. This behaviour could be related to growth of new and propagation of existing cracks. Curves from SLA4, IGT and SPRA series show an elasto-plastic behaviour over the full stress range. This behaviour could be related to large percentage of fractures, pore structure, size of grains and matrix components for SPRA series case.

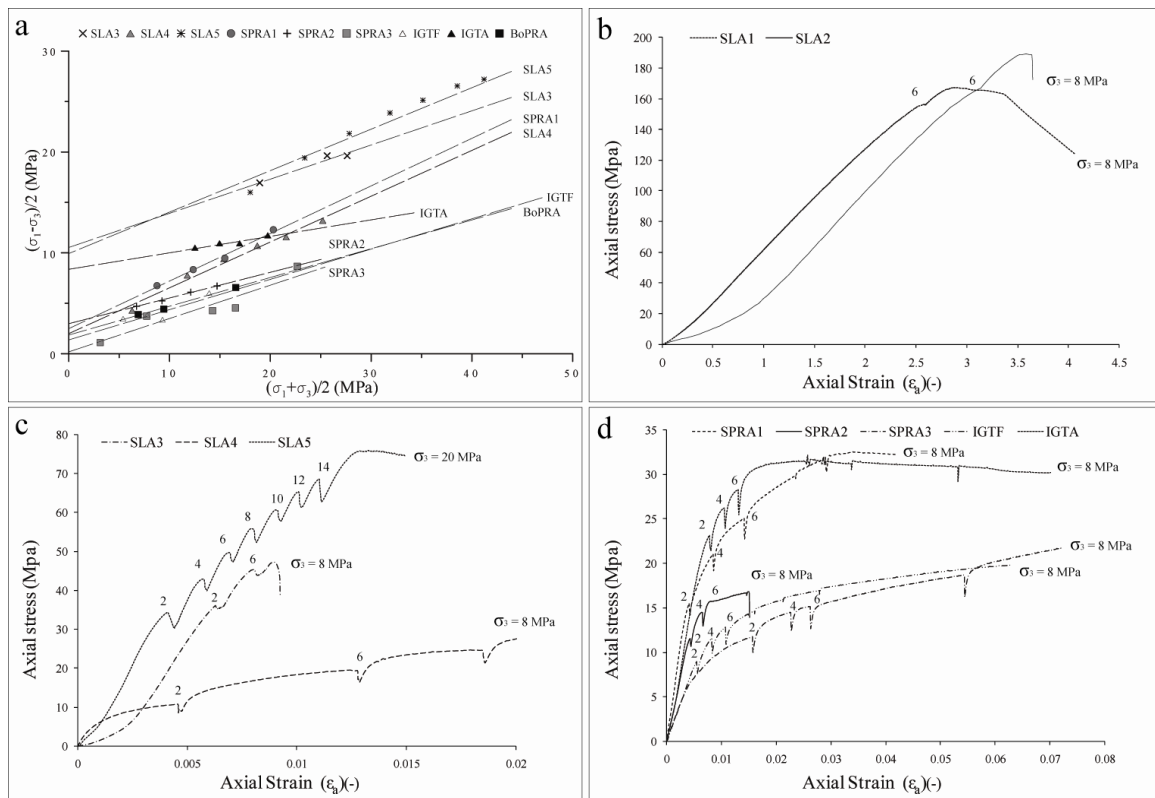


Figure 4.17 a) Mohr-Coulomb criterion in terms of maximum shear and mean normal effective stress ( $t-s$ ) points are interpolated by means of a linear relation. As shown in Figure 4.5, the  $b$  value is located where interpolation line crosses the  $x$  axis; the slope of this line corresponds to the angle  $\beta$  (see also Table 4.3). b,c) Stress-strain behaviour for lava rock from multi-stage triaxial test. d) Stress-strain behaviour for pyroclastic rocks from multi-stage triaxial test. Confining pressure values are shown for all curves.

Strength and the corresponding confining pressure values are presented in Table 4.4. In general, the strength in all series varies with alteration grade, ranging from the strongest measured values 167.1 MPa for less altered lava sample (SLA1) to the weakest measured value of 19.9 MPa for less altered ignimbrite (IGTF). Not all confining pressures and its corresponding strength are included in Table 4.4, but they are described graphically in Figure 4.17b-d. As previously described, the strength envelopes have been traced for all the data obtained from triaxial tests, in order to determine the strength parameters of weathered/altered volcanic rocks (angle of internal friction  $\phi$  and the cohesion  $c$ ), and the results are represented in Figure 4.17a. Each envelope line was plotted in terms of maximum shear stress and mean normal effective stress ( $t-s$ ); in this way, the envelope line represents the best fitting secant line to the Mohr circles. In order to find a tangent equation for Mohr's envelope, defined in normal and shear stresses, equations 10 and 11 were used. Finally, the results of altered samples give values of friction angles from 10 to 23°, and abrupt difference in results is observed in fresh samples, where values range from 57 to 36°. These values are smaller than those described in Concha-Dimas (2003) and Zimelman (2004), where friction angle range between to 25 to 40° and 32 to 40°, respectively. The low values obtained in this study could be inputed to the high grade of alteration and consequently to the increasing of heterogeneity. Intercept cohesion ( $c$ ), ranges from 34.3 to 0.2 MPa. Again, the same patterns as for the other mechanical properties between weathered rock series are visible. Textural characteristics in SPRA2 sample seem to have large influence not only on physical and mechanical properties

but also on the mode of failure. In this way, specimens with large proportion of lithic fragments (< 2 cm) could be not representative of the behaviour of SPRA2 sample under any tests.

Table 4.4 Summary of peak strength values and the corresponding confining pressures. Back calculated  $\phi$  and  $c$  from Mohr-Coulomb criterion and  $m_i$  from Hoek-Brown criterion is included

Sample	$\sigma_1$ (MPa)	$\sigma_3$ (MPa)	$(\sigma_1+\sigma_3)/2$ (MPa)	$(\sigma_1-\sigma_3)/2$ (MPa)	B (MPa)	$\beta$ (°)	$\phi$ (°)	c (MPa)	$m_i$
<i>Lava</i>									
SLA1	167.11	8	87.55	79.55	27.60	30.68	36	34.29	27.48
SLA2	320	8	164	156	11.36	40.03	57	20.93	26.23
SLA3	47.25	8	27.62	19.62	9.32	21.90	23	10.18	2.23
SLA4	38.39	12	25.19	13.19	3.12	21.89	24	3.41	11.61
SLA5	75.63	20	47.81	27.81	9.44	23.80	26	10.52	4.68
<i>pyroclastic</i>									
SPRA1	32.59	8	20.29	12.29	2.46	25.40	28	2.79	12.14
SPRA2	21.42	8	14.71	6.71	2.96	14.31	14	3.06	2.061
SPRA3	31.33	14	22.66	8.66	0.17	18.42	19	0.18	1.89
<i>Tuff</i>									
IGTF	19.86	8	13.93	5.93	1.34	16.83	17	1.40	2.55
IGTA	31.48	8	19.74	11.74	8.50	8.97	10	8.36	1.00
<i>Ignimbrite</i>									
BoPRA	23.13	10	16.56	6.56	1.87	15.73	16	1.94	5.53

$\sigma_1$ : triaxial compressive peak strength;  $\sigma_3$ : the corresponding confining pressure;  $(\sigma_1+\sigma_3)/2$  and  $(\sigma_1-\sigma_3)/2$ : Mohr stress circles plotted in terms of t-s; b: point where interpolated line cross the x axis in terms of t-s;  $\beta$ : Slope angle of linear relation in terms of t-s;  $\phi$ : friction angle; c: Cohesion;  $m_i$ : material constant for intact rock, according to Hoek-Brown failure criterion.

Figure 4.18 shows stress-strain behaviour of unwelded-ignimbrite (BoPRA) under triaxial compression. Curve consists of typical stress-strain response behaviour, with not easy recognizable imminent failure point. Over the full stress range, it behaves almost quasi elasto-plastic. Clear strength peak with fragile peak/post peak behaviour is evident after a notable increment of the stress-strain relation. The study of the state of sample after failure was performed by a series of x-ray tomographies image, revealing a localized failure which involves compaction bands and several high angle shear fractures. According to Aydin et al., (2006) and Castellanza et al., (2009) compaction bands are described as tabular zones of pure compressional deformation that form orthogonally (oriented at high angles) to the maximum compressive stress. Field observations and laboratory results suggest that compaction bands are a common feature in high porosity rocks (e.g. Baxemanis et al., 2006, Kodaka et al., 2006 and Fossen, 2009). In this way, the nature of deformation within individual bands is controlled by textural properties of the parent rock (e.g. grains, pores, and cement) and the behaviour strongly influences the response of the specimen. In addition, grain crushing and pore collapse are the integral parts of the compaction band formation (Das et al., 2010). Compaction bands in diatomaceous mudstone (a highly structured and very porous rock) were identified by a series of drained shear tests performed with different confining pressure (Kodaka et al., 2006). The authors describe the trend of compaction bands using a series of x-ray CT images sections. In this way, compaction bands seems to be related to the confining pressure, as shear bands were clearly observed in the cases of tests under low confining pressure. On the contrary, compaction bands were observed in the cases of tests under high

confining pressure. This behaviour seems to be commonly observed and it is corroborated by Wong et al. (2001) and Baud et al. (2004).

Post-failure reconstruction of BoPRA ( $\eta > 50\%$ ) sample under triaxial compression was made by a series of X-ray tomographic image. Figure 4.18c shows a network of compaction bands made up of four distinct sets. Microstructural observations revealed intragranular cracks and interconnected pore collapses. Moreover, Figure 4.18b and Figure 4.18c show a strong relationship between the location of compaction bands and interconnected pores, as vertical stress concentration seems to occur principally around lithic fragments and along large and interconnected pores. X-ray post-failure reconstruction of samples reveals that compaction bands seem to be the transition mechanism between elasto-plastic and hardening behavior (Figure 4.18a), as the failure of the specimen took place along several conjugate shear planes of high angle ( $\approx 60^\circ$ ).

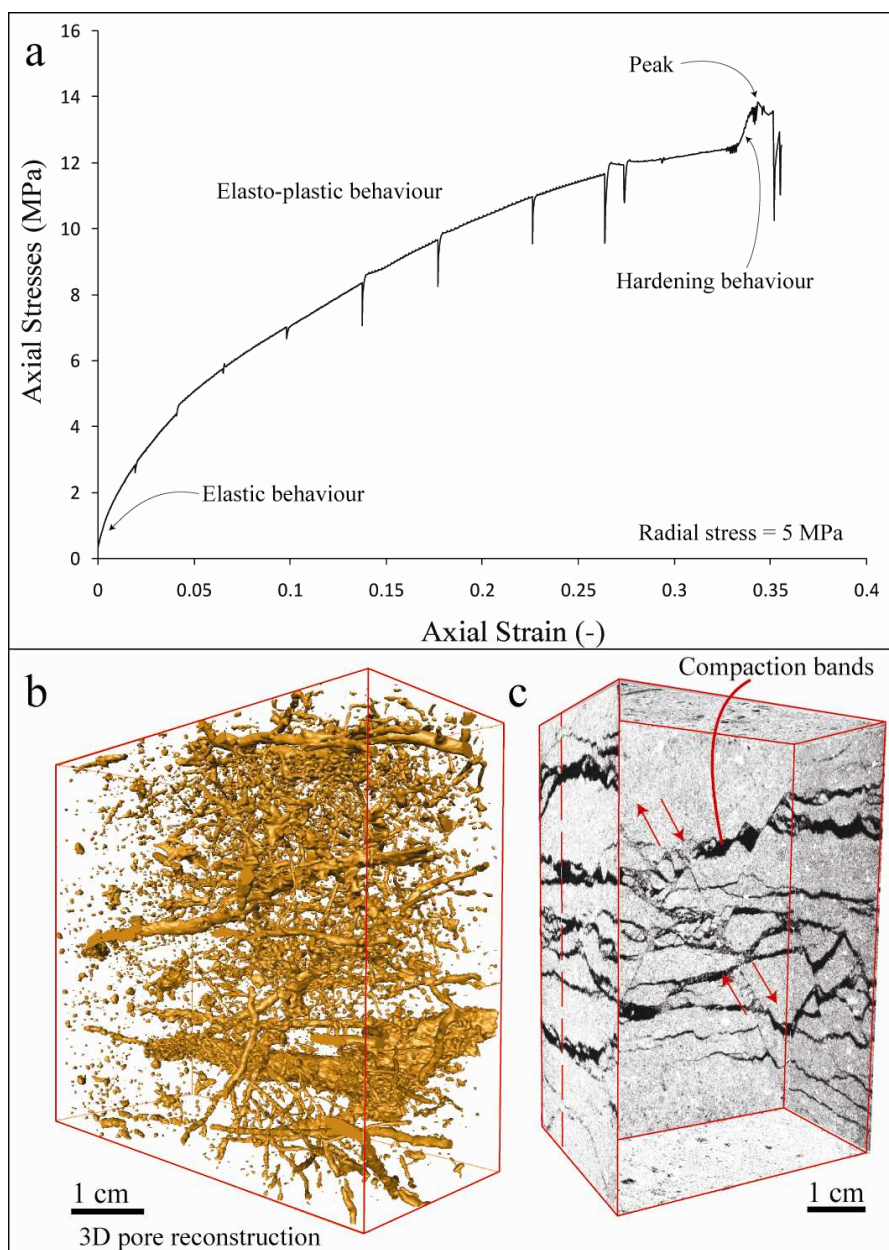


Figure 4.18 a) Stress-strain behaviour for pyroclastic rock in triaxial test (BoPRA sample of 54 mm in diameter) (confining stress = 5 MPa). b) 3D pore reconstruction from intact sample. c) 3D reconstruction after triaxial test. It shows four set of compaction bands and several conjugate shear planes

#### 4.2.8 Failure patterns in triaxial test

The mode of failure in weathered/altered volcanic rocks is influenced prevalently by its intrinsic properties and the degree of weathering. The strength of samples depends also on the strength of constituting grains and the nature of cement supporting the grains. In turn, grain mineral composition plays an important role in failure processes due to differences in shape, sizes, and chemical stability. Simple visual inspection strongly suggests a correlation between strain rate and particle size of the fragments resulting from triaxial tests. Figure 4.26 and Figure 4.27 illustrate this perception. Based on this, pore structure and clast-size in pyroclastic rocks (SPRA), seem to be crucial in the mode of failure, as cracks concentration is localized around clasts in failed specimens (Figure 4.23; Figure 4.24; Figure 4.25). Sizes and alignments of crystals seem to have influence just in fresh and slightly weathered lavas (SLA). The primary controls on ignimbrite (TGT) are the groundmass, composed prevalently by altered pumice, which in some cases; has been replaced by porosity. In unwelded ignimbrite, the mode of failure is controlled by the large content of pores ( $\approx 50\%$ ).

In order to follow failure patterns of each sample, series of x-ray tomographic images were prepared. Images were acquired in post-failure phases of triaxial tests. The acquisition of the images of fresh and slightly weathered lava was not possible because of their violent failure mode. In this way, schematic illustrations of failure are presented in Figure 4.26 and Figure 4.27. They could be described as follow:

SLA1: Failure mode of fresh sample is characterized by conical shearing. In this sample, intrinsic properties of material as crystals arrangement and pore structure seem to have little influence on mode of failure (Figure 4.19).

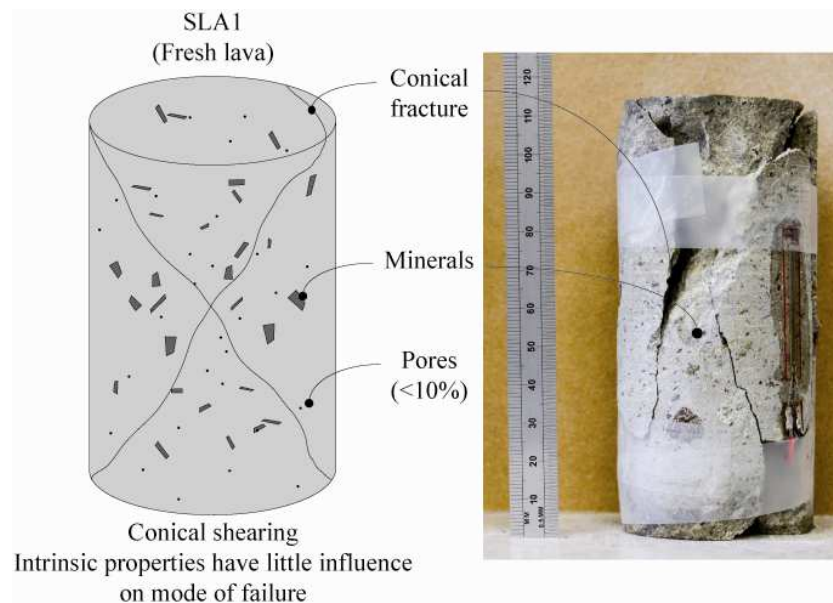


Figure 4.19 a) 3D Schematic illustration of structures resulting from failure modes in SLA1 sample. b) Post-failure photo of the specimen



SLA2: Failure mode of slightly weathered sample is characterized by vertical fracturing, parallel to the direction of loading. In this case, the size of the crystals and its arrangement seem to strongly influence the mode of failure. Moreover microfractures aligned sub-perpendicular with respect to axial load seems to influence some samples (Figure 4.20).

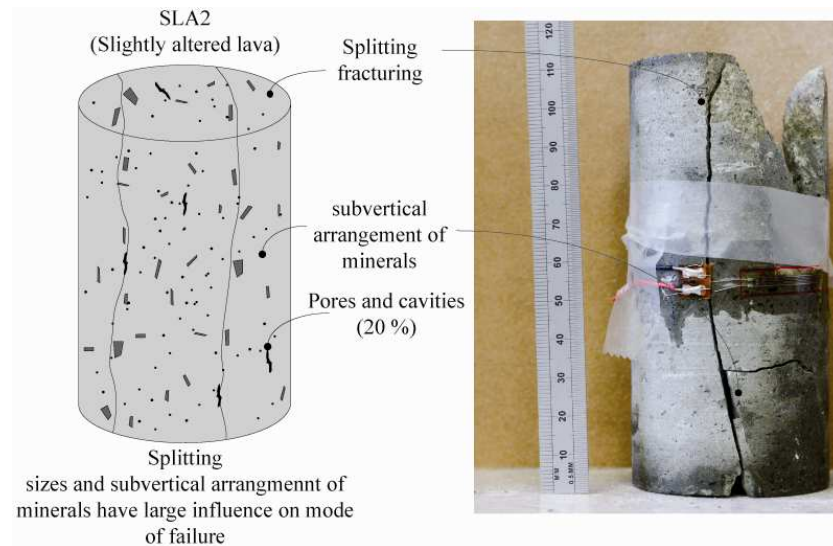


Figure 4.20 a) 3D Schematic illustration of structures resulting from failure modes in SLA2 sample. b) Post-failure photo of the specimen

SLA3: Failure mode of this specimen is characterized by localized deformation along a fracture plane inclined  $\approx 60^\circ$  with respect to the horizontal direction. The pattern of this fracture suggests that weathered/altered stains and crystals arrangement are the primary characteristics in controlling failure (Figure 4.21 and Figure 4.27a).

SLA4: Again, failure mode of this specimen is characterized by localized deformation along a fracture plane inclined  $\approx 60^\circ$  with respect to the horizontal direction. Plane is localized at the bottom of the sample, where rock material is highly fractured and a large proportion of cavities is localized. Perpendicular to the deformation plane there are some fractures; they follow the crystals alignment (Figure 4.21b and Figure 4.27b).

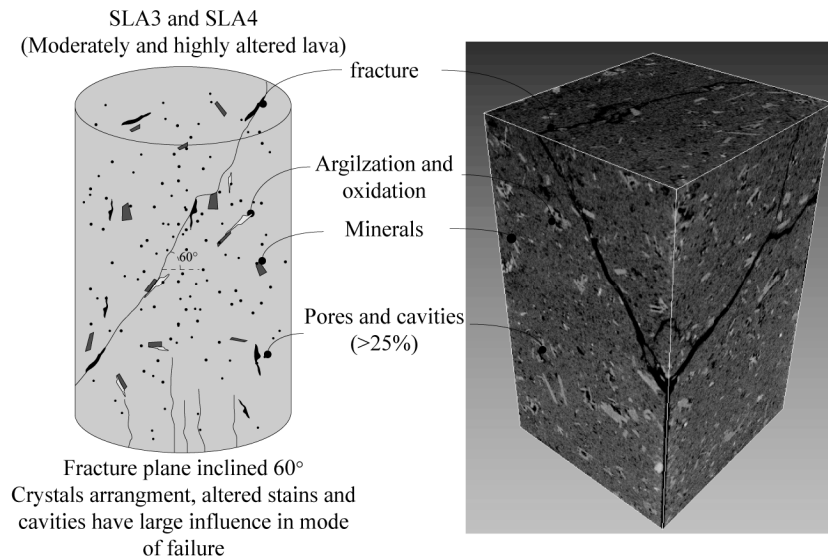


Figure 4.21 a) 3D Schematic illustration of structures resulting from failure modes in SLA3 and SLA4 samples. b) Illustration is reconstructed with series of x-ray tomography images

SLA5: Failure mode of this sample is characterized by large cracks, parallel to its longitudinal axis. Complete fracture occurs along a possible pre-existing plane of weakness oriented  $\geq 60^\circ$  with respect to the horizontal direction (Figure 4.22c and Figure 4.27c). Porosity in this sample is reduced and seems to have little influence in mode of failure.

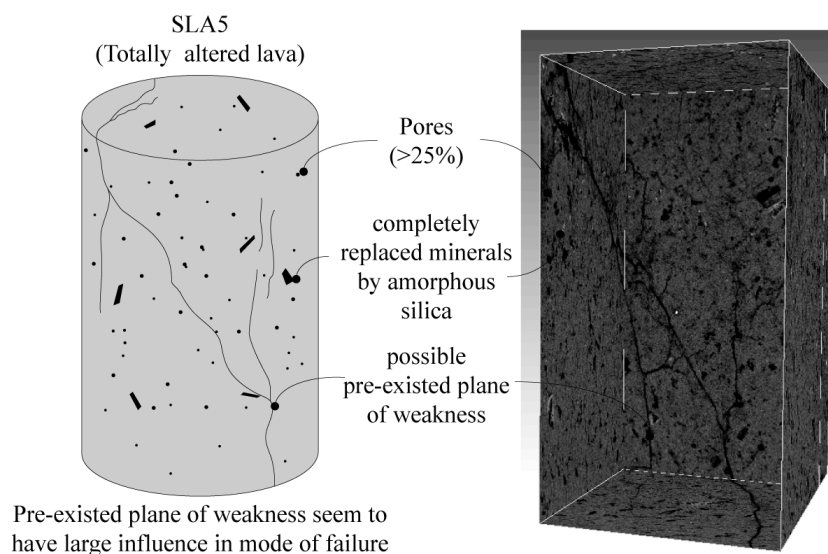


Figure 4.22 a) 3D Schematic illustration of structures resulting from failure modes in SLA5 samples. b) Illustration is reconstructed with series of x-ray tomography images

SPRA1: Failure mode is controlled by a variable texture and grain sizes characteristics. This specimen is composed by a density grading sequence of four different poorly stratified layers, from bottom to top they are described as follow: first layer is made up of fine coarse and sub-angular pumice lapilli with scattered lithic fragments. Second layer is made up of very fine sand; texture is closed or very dense with interlocked clasts. Third layer is made up of well-sorted coarse sand fragments of pumice and lithics. Top layer is made up of fine to coarse

sand fragments of sub-angular pumice lapilli prevalently. Failure mode is characterized by stress differentiation along layers. Sub-verticals and conical fractures are localized at the bottom of the specimen. On the contrary, in the middle of the sample, there are two sub-horizontal compaction bands, mainly controlled by stratification and grains arrangement. Finally, the top of the specimen is characterized by localized deformation along a curved fracture (Figure 4.23e and Figure 4.27d).

SPRA3: Failure mode of this specimen is controlled by variable texture and grain sizes characteristics. Failure pattern is sub-horizontal (compaction bands) and it is mainly controlled by stratification and grains arrangement (Figure 4.23 and Figure 4.27f).

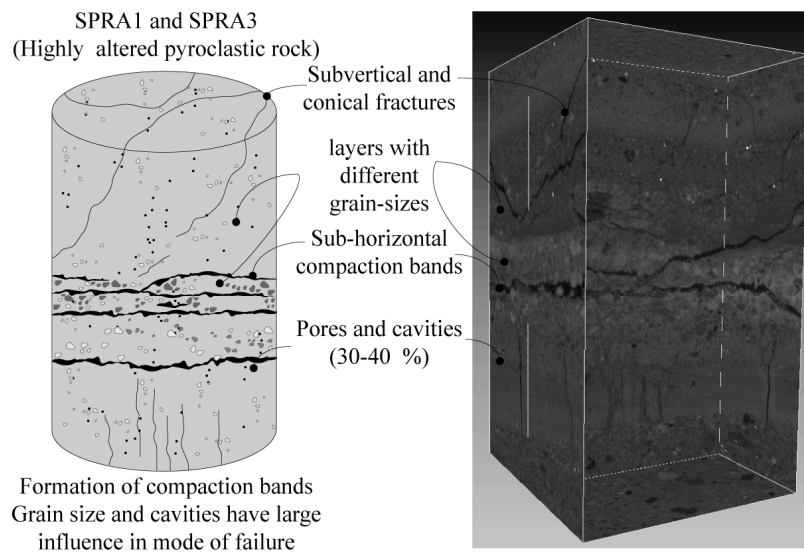


Figure 4.23 a) 3D Schematic illustration of structures resulting from failure modes in SPRA1 and SPRA3 samples. b) Illustration is reconstructed with series of x-ray tomography images

SPRA2: Failure mode of this specimen is characterized by a fracture performed through the rock matrix, controlled by lithic fragments ( $\approx 1.5$  cm), which influence the concentration of stresses (Figure 4.24f and Figure 4.27e).

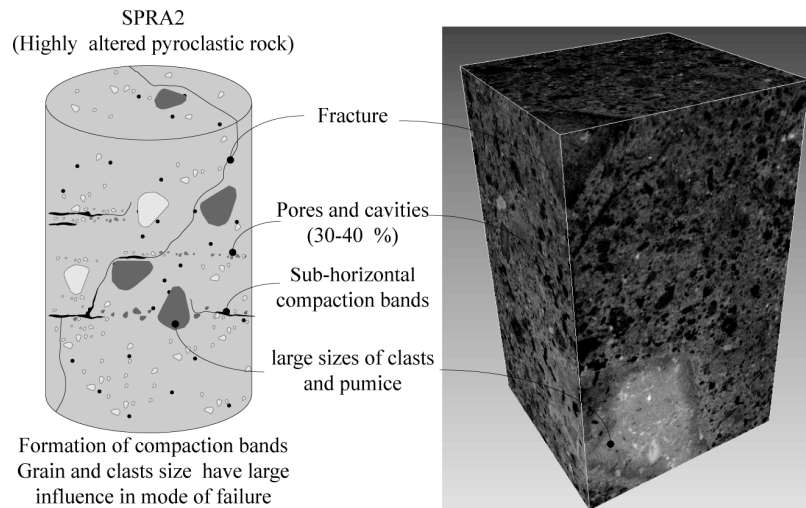


Figure 4.24 a) 3D Schematic illustration of structures resulting from failure modes in SPRA2 sample. b) Illustration is reconstructed with series of x-ray tomography images

IGTF: Large proportion of pumice clasts with open structures plays an important role in the failure process of this specimen. Failure mode involves changes in shape and size of pumice clasts, moreover fragmentation of their structures could control the strength of the rock (Figure 4.25 and Figure 4.27h).

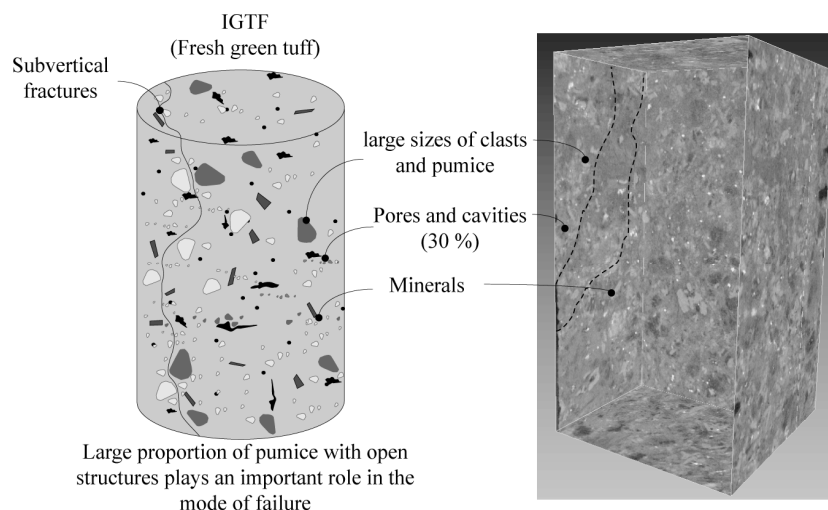
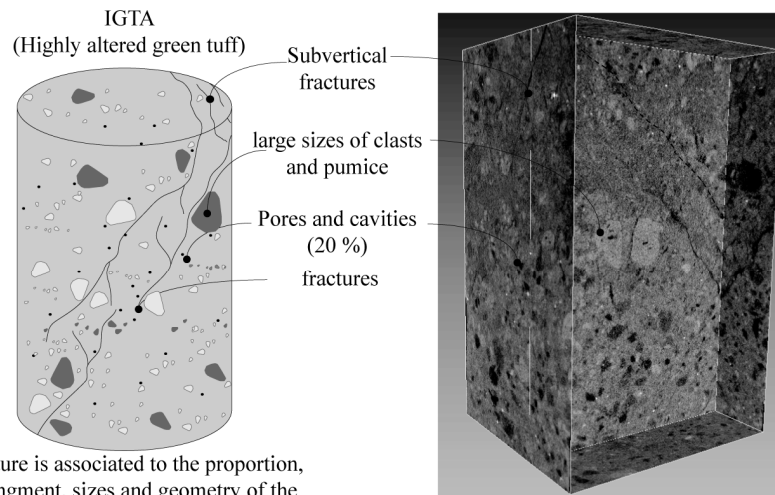


Figure 4.25 a) 3D Schematic illustration of structures resulting from failure modes in IGTF sample. b) Illustration is reconstructed with series of x-ray tomography images

IGTA: Failure mode of this completely weathered specimen is characterized by a fracture developed through the rock matrix. Fracture is associated to the proportion, arrangement, sizes and geometry of the grains (crystals and pumice clasts) contained within the groundmass. Post-failure observations, suggest pore structure as a minor characteristic in controlling failure (Figure 4.26d and Figure 4.27g).



Fracture is associated to the proportion, arrangement, sizes and geometry of the grains (lithics and pumice)

Figure 4.26 a) 3D Schematic illustration of structures resulting from failure modes in IGTA sample. b) Illustration is reconstructed with series of x-ray tomography images

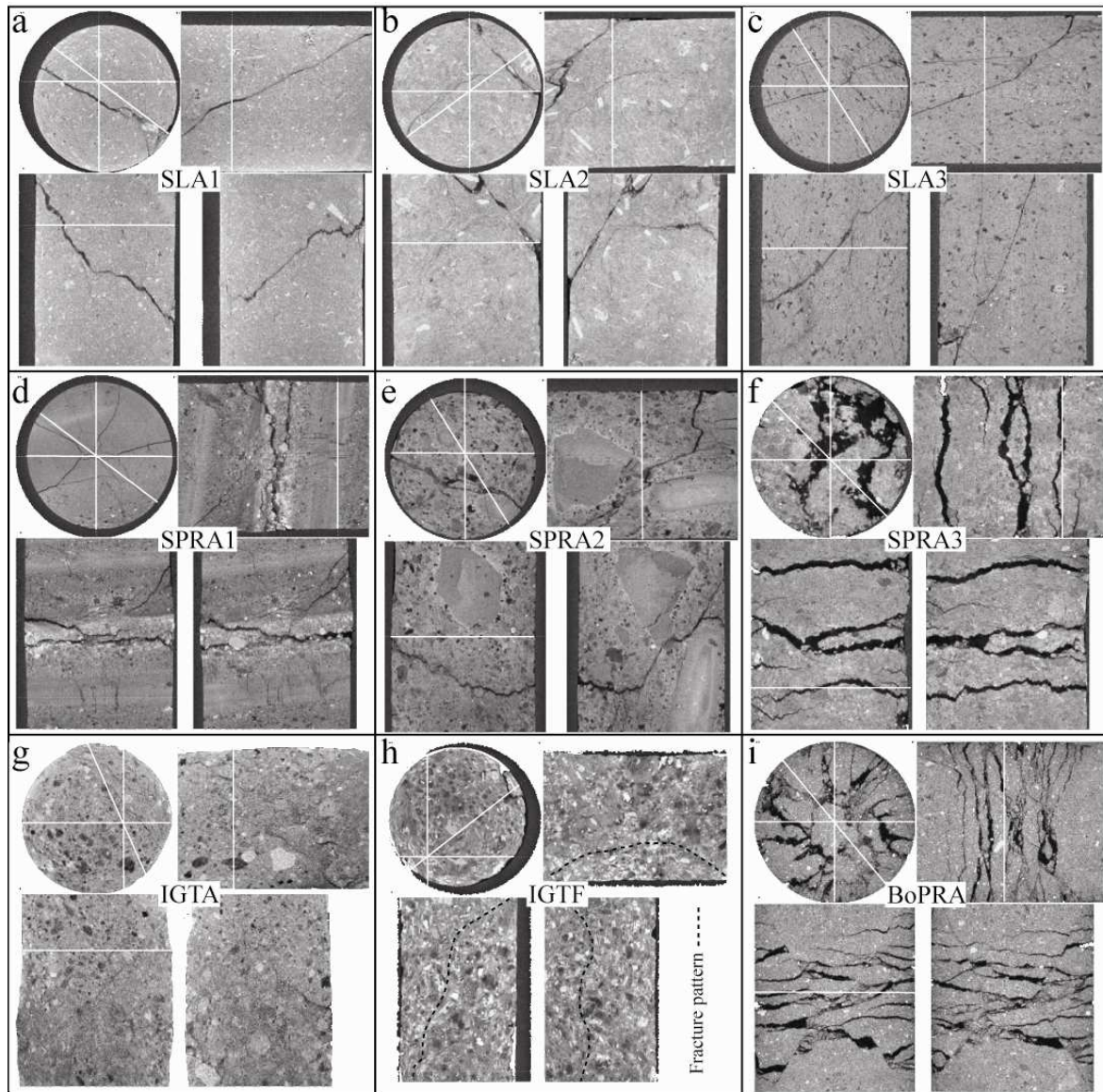


Figure 4.27 2D Schematic illustration of structures resulting from various failure modes in weathered/altered volcanic rocks. Fracture mode is represented by four different profiles. Base of each sample has 54 mm of diameter. Fracture pattern in IGTF is highlighted by a dash line.

#### 4.2.9 Results of oedometric test

As it is described in previous paragraphs, BoPRA sample is characterized by a very high porosity content (60 %) related to its depositional processes. Reconstruction of pore structure (X-ray tomography images) and microscopy observations reveal high percentage of interconnected pores, which is also promoted by degradation and fragmentation of pumice content. Otherwise, state of sample after failure in triaxial tests was performed by a series of x-ray tomographies image, revealing a localized failure which involves compaction bands and several high angle shear fractures. Based on these, BoPRA sample is also examined by oedometric test. Behaviour of stress-strain curves (axial and radial), plotted in Figure 4.28a, show that sample presents a yielding point at 4 MPa, after which it exhibits a marked

increment in strain, over the rest of stress range (slope decrement). After the yielding point, the micro-structure collapse probably occurs in the form of compaction bands.

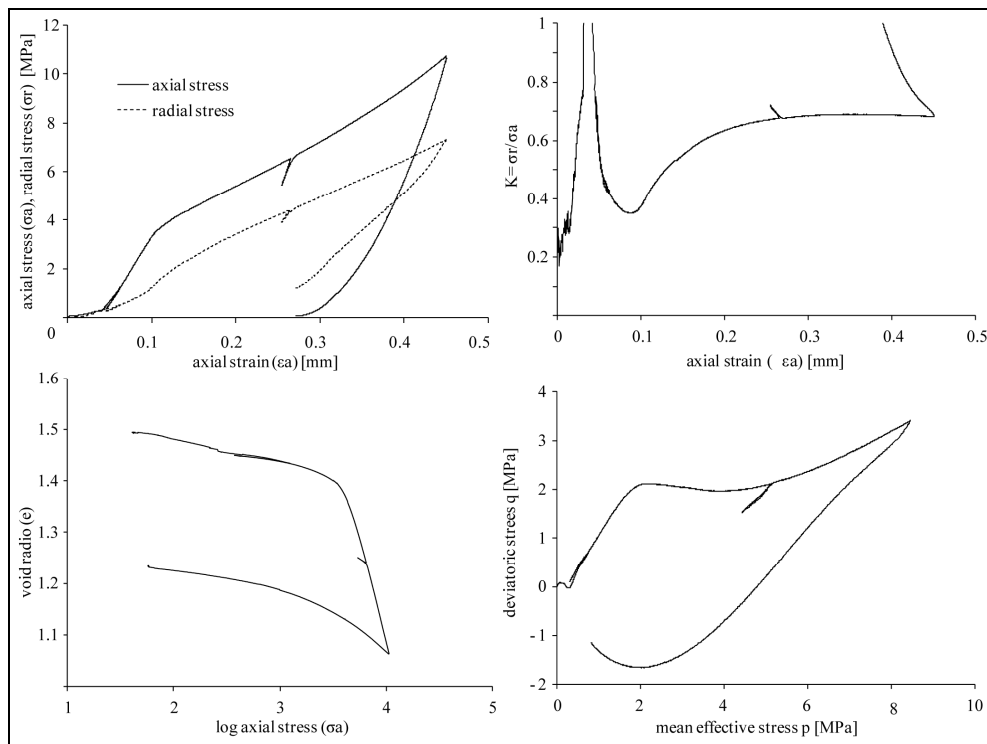


Figure 4.28 Results of oedometric test. a) axial and radial stress vs axial strain; b) stress ratio vs axial strain; c) void ratio vs log axial stress; d) deviatoric stress vs mean effective stress.

The stress path, shown in Figure 4.20d, exhibits three principal phases: one phase corresponds to a linear increment of both deviatoric and mean normal stress; in the second phase, the deviatoric stress increase less than the mean effective stress. This phase is associated to the progressive destruction of the specimen; the third phase (after deviatoric peak has been reached) corresponds to a simultaneous reduction of both deviatoric and mean normal stress. According to the experiments performed by Castellanza et al. (2009), this behavior corresponds to rock transformation into a granular non-cohesive soil.

### 4.3 Conclusions of laboratory analyses

Different procedures to quantify physical and mechanical properties of altered/weathered volcanic materials from Solfatara, Ischia and Bolsena volcano, have been implemented and compared. Results demonstrate that physical and mechanical properties of rock change with the degree of weathering. As the degree of weathering increases, mechanical properties decrease whereas total and effective porosity increase. i.e.

- A direct relationship between  $\eta_t$ ,  $\eta_e$  and alteration grade of samples is observed. In general  $\eta_t$  and  $\eta_e$  increase progressively with weathering grade for all rock series (from 0.7 to 57.7 % and from 6 to 41.2 %, respectively).  $\eta_t$  results obtained from X-ray tomography and pycnometer tests reveal some minor changes in lava series, where values from SLA2 to SLA3 increase drastically (from 6.4 to 25.6 %) and values from SLA4 to SLA5 present small reduction (from 33 to 30 %).  $\eta_e$  results obtained from mercury intrusion porosimetry

tests reveal some changes in IGT series, where values from IGTA present 5 % Of decrement (from 25.5 to 30 %) (Figure 4.29a, b).

$\eta_e$  values obtained from bulk-specific weight measurements seem to have no clear relationship with weathering grade. The reason could be the percentage and size of interconnected pores and fractures contained in each samples.

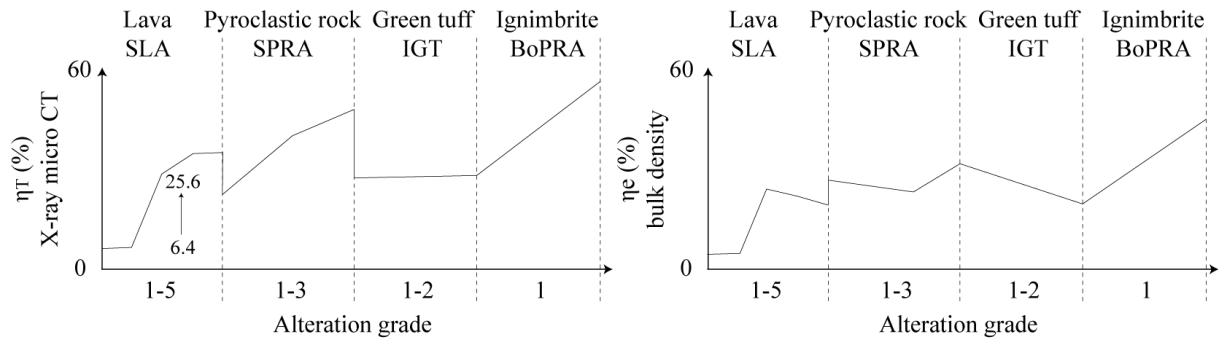


Figure 4.29 schematic view of: a)  $\eta_T$  obtained from X-ray tomography images analysis as a function of lithotype and grade of alteration. b)  $\eta_e$  obtained from bulk specific weight measurements as a function of lithotype and grade of alteration

- Fractal dimension (D) obtained from  $\eta_t$  and  $\eta_e$ , decreases progressively with weathering grade in all sequences (from 1.31 to 2.14), even if some variations are observed in SLA2, SLA5 and IGT. This trend suggests a relative increase in frequency of large pores. While the deviations (SLA2, SLA5 and IGTA) suggest an increment of the relative frequency of smaller pores, as well as large pores infilling. D obtained from Mercury porosimeter, represents distribution of non interconnected pores. Variation of D values estimated from  $\eta_e$  data is lower than D values estimated from  $\eta_t$ , in particular variation is small in SLA and IGT. Larger variation in D values is observed in SPRA series where large heterogeneity in the matrix is observed. In addition, an increase in the values of compressive and tensile strength is observed for increasing fractal dimensions (Figure 4.30).



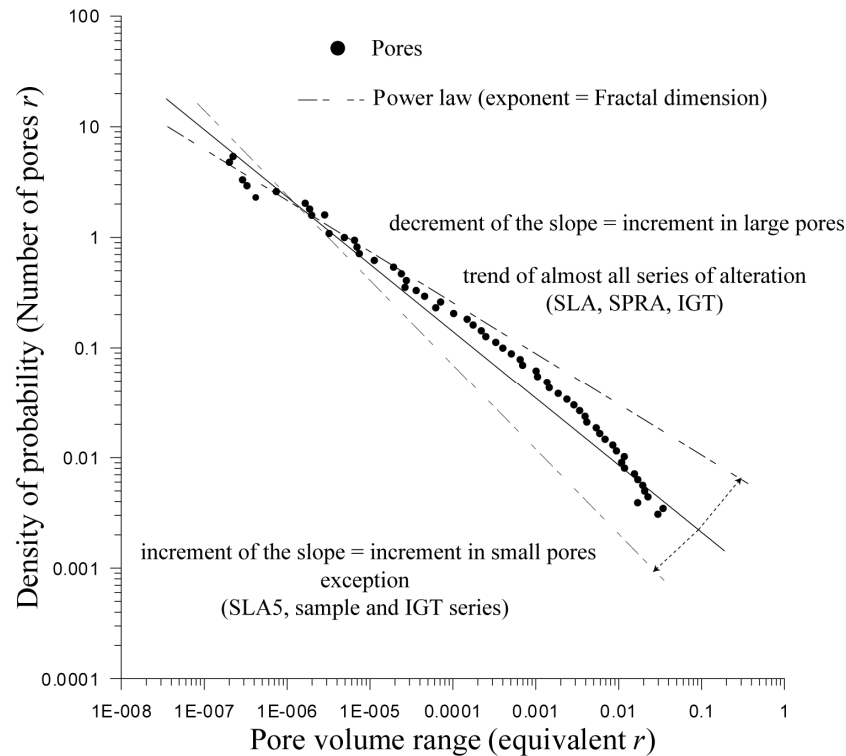


Figure 4.30 schematic view of the principal characteristics of the fractal dimension.

- Statistical analysis of  $V_p$  and  $V_s$  wave velocities and their relationship with lithotype and alteration grade vary as follow:  $V_p$  values follow a decreasing trend with increasing alteration grade in all series (Figure 4.31a, b). This decrement seems to be constant, in particular for samples from SLA. On the contrary, samples from IGT series follow an increasing trend with increasing alteration grade. These could be the result of the development of new pores, clay minerals and the increased and decreased width of previous interconnected cavities.
- $V_s$  values show no clear relationship with weathering grade. Large differences are presented not only between each alteration grade, but also between each sample. The reason could be the percentage and size of interconnected pores, severe mineralogical changes and fractures contained in each sample. Less variation is observed in samples from SPRA series, which seems to have a more persistent network of pores and microfractures. In addition, same variations within the samples are shown when dynamic Young's modulus derived from  $V_p$  and  $V_s$  (eq. 1 and 2) are correlated with uniaxial strength.

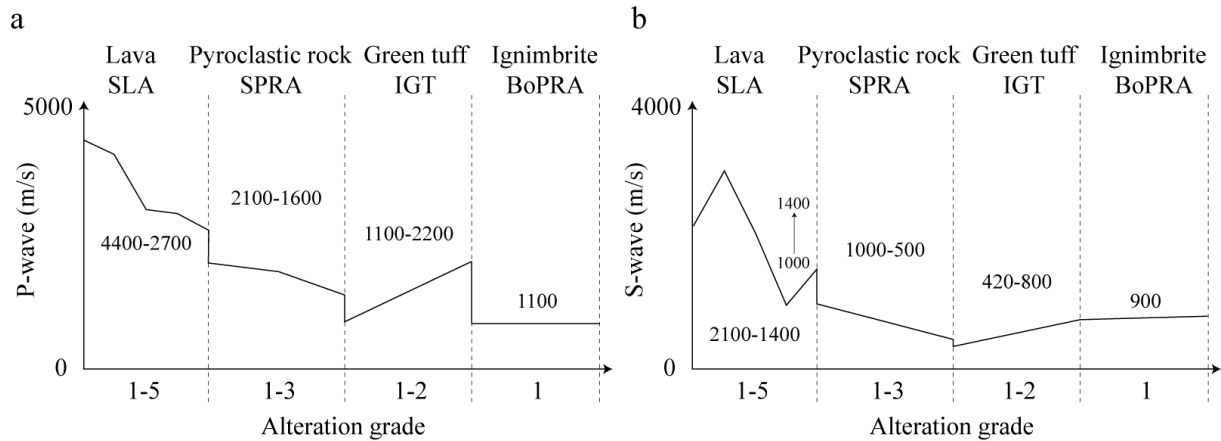


Figure 4.31 schematic view of: a) P wave; and b) S wave as a function of Lithotype and grade of alteration.

- An exponential change is observed when average values for  $V_p$  and  $V_s$  are compared with the average of  $\eta_e$  obtained from bulk-specific weight measurements. Best fitting exponential relationships between these properties are presented together with their coefficient of determination ( $R^2 = 0.80$ ).  $V_p$  values are well correlated, although, few dispersed values are observed in SLA3, SLA4, and SLA5 samples. On the contrary,  $V_s$  values seem to have no clear relationship with  $\eta_e$ . In particular,  $V_s$  values in SLA1, SLA2, SLA5 and BoPRA show large variations. This variation is attributed to a greater abundance of small cracks or micro fissures and the difference in the arrangement of pore network (Figure 4.32).

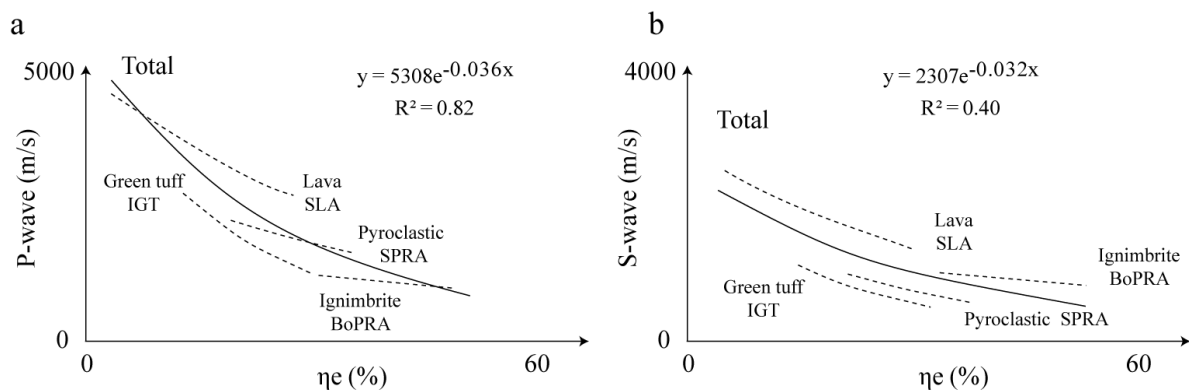


Figure 4.32 schematic view of: a) P wave; and b) S wave as a function of  $\eta_e$  obtained from bulk specific weight measurements.

- The strength in all series varies with alteration grade (from 5.7 to 116.7 MPa). Reduction in strength and Young's modulus with increasing grade of alteration is gradual for pyroclastic sequence (SPRA) and unwelded ignimbrites (BoPRA). Reduction for lava sequence (SLA) is strong. The most rapid rate of decrease is observed between SLA2 and SLA3, where porosity ranges from 10 to 30 % and drastic changes in rock structure are identified (Figure 4.33a,b).
- Strength values in IGT series follow an increasing trend with increasing alteration grade. The average values vary from 5.74 MPa in less altered sample (IGTF) to 16.26 MPa in

most altered sample (IGTA). Change in trend behavior suggests a drastic transformation of sample structure due to hydrothermal processes. In this sequence,  $\eta_t$ ,  $\eta_e$  and  $\gamma$  ranging from 25 to 24, from 25.5 to 29.7 % and from 15.12 to 17.78 KN/m<sup>3</sup>, respectively.

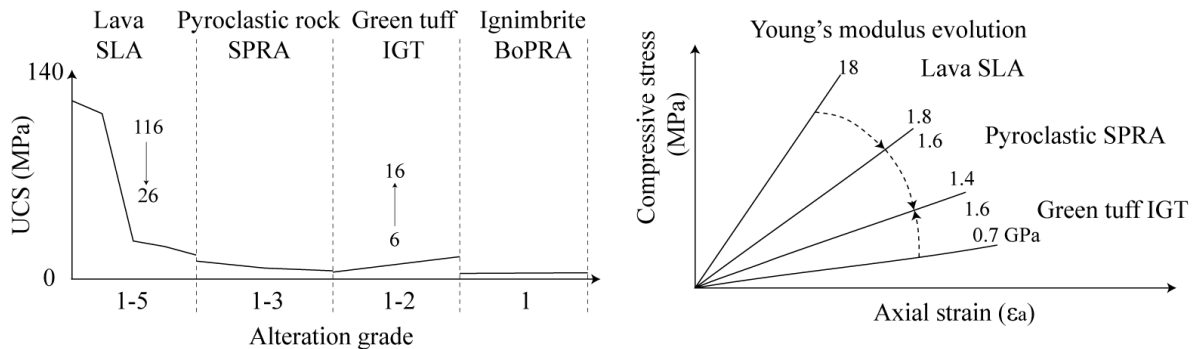


Figure 4.33 schematic view of: a) uniaxial compressive strength as a function of alteration grade. b) Young's modulus evolution; compressive stress as a function of axial strain.

- The uniaxial compressive strength decreased non-linearly with increasing  $\eta_t$  with a minimal to moderate data dispersion that is quite reduced for high alteration grade samples (SLA5 sample, and SPRA and IGT series) (Figure 4.34)

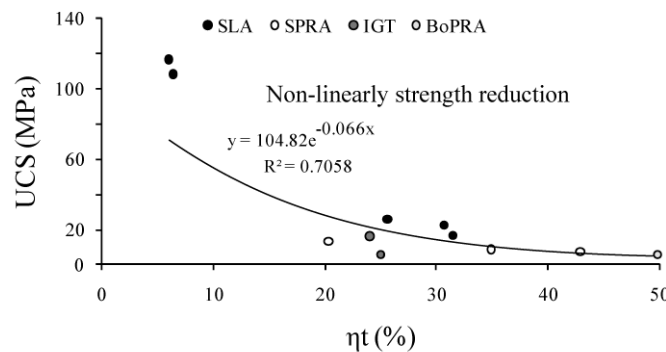


Figure 4.34 schematic view of UCS as a function of  $\eta_t$ .

- The ratio of the dynamic to static bulk modulus ( $K$ ) varies between 0.77 to 2.96 with drastic changes in SLA3 and SLA5 (4.9 and 4.8 GPa, respectively). Discrepancy between values exposed in this study suggests changes in sample structure; shape and aspect ratio of pores. Morphology of cavities has a large influence in most altered samples. Microscopic inspection, reveals that when length of pore increases the dynamic modulus decreases in all samples. On the contrary a decrement in static modulus is not always observed.
- Evolution of Young's modulus is explained by uniaxial compressive stress cycle tests: Young's modulus in all series increases with increasing stress. In general, the first two values, measured in the first two stress-cyclic (crack closure region) increase rapidly, while in the rest of the cycles the increase is constant. Increment in each sample is represented by the slope of the best linear fitting ( $0.85 < R^2 < 0.98$ ). Slope of the line increases rapidly in SLA3 and SLA4 samples. In the rest of the samples it seems to increase modestly. Young's modulus in all series increases with decreasing both  $\eta_t$  and  $\eta_e$ . The strongest sample (SLA3,  $E = 4.2-5.6$  GPa,  $\eta_t \approx 25\%$  and  $\eta_e \approx 18\%$ ) exhibits higher elastic modulus

and lower porosity with respect to the weaker sample (BoPRA,  $E = 0.77-0.83$  GPa,  $\eta_t \approx 60\%$  and  $\eta_e \approx 50\%$ ). Sample SLA5, with a notable increment in strength and a relative decrement in porosity with respect to the series pattern, exhibits very high elastic modulus range ( $E = 3.16-4.39$  GPa). Young's modulus in samples from SPRA series is directly influenced by the grain sizes, the length of grain to grain contacts and matrix cementation (Figure 4.35).

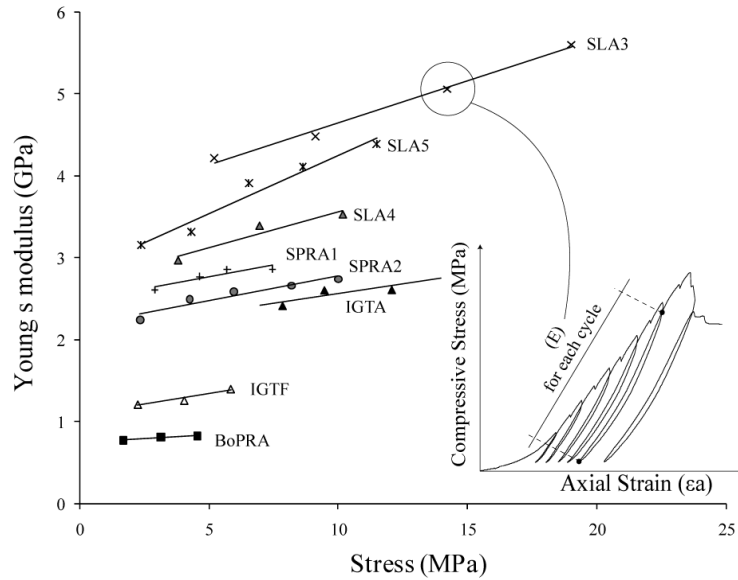


Figure 4.35 schematic view of Young's modulus evolution during Uniaxial compressive stress cycle test.

- Tensile strength, as uniaxial strength value decreases with increasing alteration grade and  $\eta_t$  and  $\eta_e$  ( $0.22 \text{ MPa} < \text{tensile strength} < 10.37 \text{ MPa}$ ). The variation of this decrement is constant for almost all samples ( $\approx 1.5 \text{ MPa}$ ). Although, decrement is drastic between SLA2 and SLA3 (from 10 to 4 MPa). On the contrary to this trend, tensile strength in IGT series slightly increases with alteration grade (from 0.8 to 1.1 MPa) (Figure 4.36a, b).

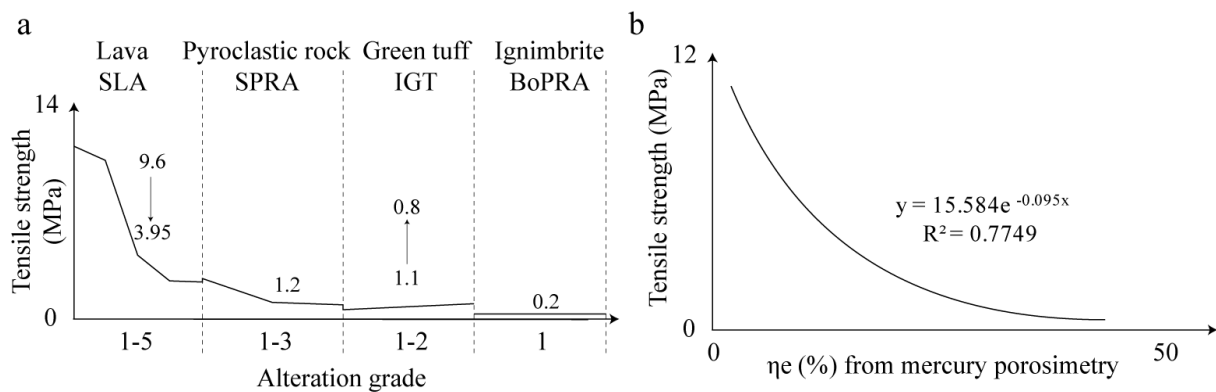


Figure 4.36 schematic view of tensile strength as a function of grade of alteration.

- Relationship between tensile strength and bulk density suggests that tensile strength depends on the intrinsic properties of each specimen. For example, in lava rock series, tensile strength depends on the pore structure, alignment and proportion of crystals. For

pyroclastic and ignimbrite rock series cases, tensile strength depends on pore structure, rock texture, matrix cementation and proportions of pumice clasts. IGTF sample with large content of pumice clasts have relative low strength value (0.8 MPa) compared with IGTA sample, where pumice clasts are filled by materials coming from hydrothermal processes (Figure 4.37).

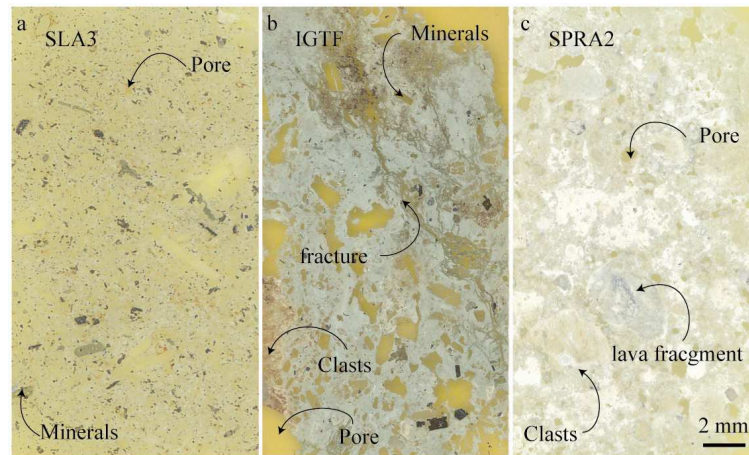


Figure 4.37 Intrinsic properties of: a) lava series (SLA), b) green tuff series (IGT), c) pyroclastic rock series (SPRA).

- Tensile stress-strain curves for all series suggest gradual decay in tensile strength and gradual increase in strain. Behaviour in SLA series change with respect to level of degradation from linear elastic to elastic-plastic behaviour. Particularly, SLA5 sample suffers this change along the first part of the curve. Samples of SPRA and IGT series seem to have an elastic-plastic behaviour during all stress-strain curve. There is one exception in IGTA, where clear linear elastic behaviour is observed along the first part of the curve (Figure 4.38).

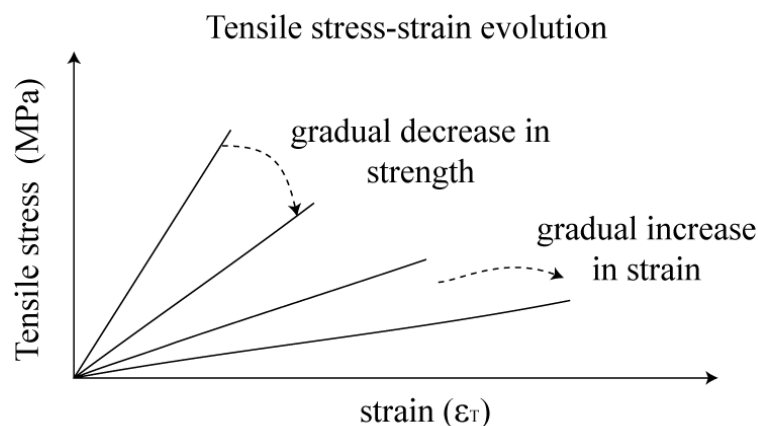


Figure 4.38 Schematic behaviour of tensile stress-strain curves.

- Tensile and compressive strength results suggest a notable decrease in stiffness with the level of degradation. Dispersion of the values is minimal for the case of SLA series, in particular for the case of the maximum alteration grade. This is reasonable if we consider that the porosity increases but generally for minor pore sizes and so excluding large

imperfections and weaknesses that instead are more frequent at lower alteration grades. On the contrary, dispersion in some samples is larger. For example, dispersion of strength values in SLA2 depends on microfractures alignment, while dispersion in SLA4 depends on sizes of cavities and interconnected pores.

- An exponential decay of the properties is observed when average values of the compressive strength, tensile strength and young's modulus are compared with the average porosity value, fractal dimension and grade of alteration. As it is discussed previously, all mechanical properties decrease with increasing alteration grade, fractal dimension and  $\eta_t$  and  $\eta_c$ . Again, this trend is not visible in the most altered samples (SL5 and IGTA).
- Slope decrement of the stress-strain curves obtained in triaxial tests in all series is related to the increment in alteration grade. Exceptions between SLA4 – SLA5 and IGTF – IGTA are observed, where most altered samples are characterized by strength increment.

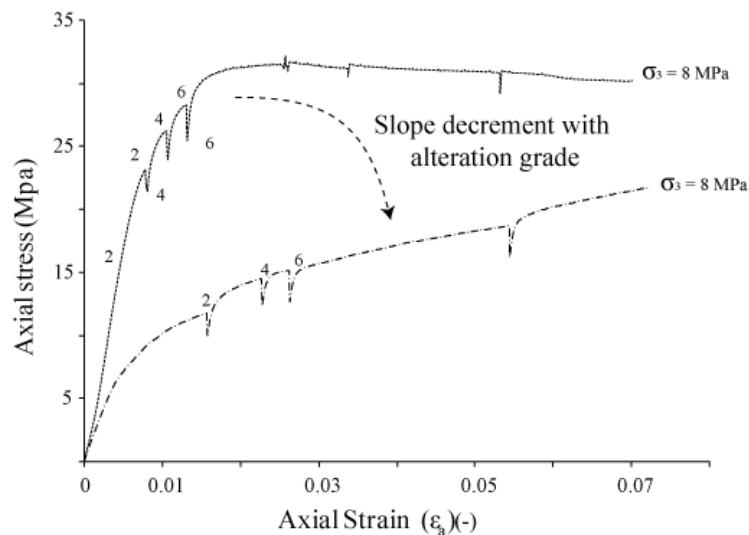


Figure 4.39 Schematic behaviour of stress-strain curves in triaxial tests.

- Friction angles obtained from triaxial tests range from  $10^\circ$  to  $23^\circ$  for the most altered samples. Abrupt difference in results is observed in fresh samples, where values range from  $57^\circ$  to  $36^\circ$ . The low values obtained in this study could be assumed related to the high grade of alteration and consequently to the increasing effect of heterogeneity.
- Cohesion ( $c$ ) ranges from 34.3 to 0.2 MPa. Again, values decrease with increasing alteration grade. Some exceptions, both for the tensile and the compressive strength pattern, are identified. Textural characteristics in SPRA2 sample seem to have large influence not only on physical and mechanical properties but also on the mode of failure. In this way, specimens with large proportion of lithic fragments ( $<2$  cm) could be considered as not representative of the standard behaviour of SPRA2 sample under any tests.
- X-ray post-failure reconstruction of samples under triaxial compression shows a network of compaction bands. Micro-structural observations revealed intragranular cracks and interconnected pore collapses. Reconstruction also shows a strong relationship between the

location of compaction bands and interconnected pores, as vertical stress concentration seems to occur principally around lithic fragments and along large and interconnected pores. Post-failure reconstruction of sample, in particular BoPRA sample, reveals that compaction bands seem to be the transition mechanism between elasto-plastic and hardening behaviour. In this way, it is assumed that the nature of deformation within individual bands is controlled by textural properties of the parent rock (e.g. grains, pores, and cement) and the behaviour strongly influences the response of the specimen (from Figure 4.19 to Figure 4.26).

## 5. STABILITY ANALYSIS

A simplified numerical stress-strain analysis was carried out in order to support the role played by the rock properties degradation, obtained by laboratory tests, on volcano edifice stability.

In literature, altered volcanic rocks are considered as materials where potential failure surfaces can develop. Modeling studies to analyze volcano deformation and collapse have been performed in the literature using physical and numerical models (e.g. Reid et al., 2001; van Wyk de Vries, 2000; Concha-Dimas and Watters., 2003; Merle et al., 2003; Zimbelman et al., 2004; Apuani et al., 2005; Tommasi et al., 2007; Andrade and van Wik de Vries, 2010).

Reid et al. (2001) conclude that the distribution of rock shear strength controls the location of the flank failure. The authors consider that hydrothermal alteration can lower rock shear strength over wide areas. Consequently, alteration could be very important for promoting and localizing large edifice collapses.

Concha-Dimas and Watters (2003) model the stability of a volcano by progressively changing rock strength and extending hydrothermal altered zone. Examining the final strain conditions, the authors conclude that hydrothermal alteration by itself is the dominant process which defines the unstable zones.

Zimbelman et al. (2004) prove a potential collapse event of Citlaltépetl volcano, through geologic mapping alteration mineralogy, geotechnical studies and stability modeling. Apuani et al. (2005) present a stability analysis of the Stromboli volcano edifice. In this work, the model is defined on the basis of stratigraphical, lithological and structural data collected from in-situ surveys and laboratory tests. The authors identify external forces (e.g. magma pressure and seismicity) as potential triggering mechanism of lateral collapse. Tommasi et al. (2007) use stress-strain modeling to identify the presence of weak basement as potential triggering mechanism of shallow slope failures. On the contrary, on these works, samples usually are collected in superficial materials without considering effects of alteration and temperature (hydrothermal processes, pore pressure); moreover, in some cases, the plane of stability is previously imposed by the distribution and the geometry of the materials.

Because of the aim of the present thesis and of the relevance of the material properties and behaviors in the numerical modeling it is important to resume the set of values adopted in the literature to carry out similar studies (see van Wyk de Vries and Mantela 1998; Reid et al., 2000 (a); Reid et al., 2000 (b); Concha-Dimas and Watters, 2003; Zimbelman et al., 2004; Apuani et al., 2005; Crosta et al., 2005; Tommasi et al., 2007; del Potro and Hürliemann 2009; Reid et al., 2010; for a complete review). A summarizing table, just for some of these works, is integrated as follow:

Table 5.1 Experimental intact rock properties and calculated rock mass strength values from literature.

Sample	$\rho$ (g/cm <sup>3</sup> )	UCS (MPa)	Alteration Degree	GSI	c (MPa)	$\phi$ (°)	
Andesite	2.7-2.3	50-1	1-4	35	3.57-0.58	19.5-4.7	Concha Dimas and Watters, 2003
Andesite	2.4-1.9		1-3	50	1-0.1	40-15	Reid et al., 2000
Dacite	2.5-0.8	146-35	1-4		0.96-0.07	34-24	Zimbelman et al., 2008
Basaltic-Andesitic	2.6-1.9	50-162		55-40	3.9-1.5	32-22	Apuani et al., 2005
pyroclastic	1.4	50-10		20-8	1.4-0.6	23-15	Apuani et al., 2005



## 5.1 Numerical model

On the basis of these available models, the modeling effort of this work is performed by four general steps:

- (1) developing the conceptual model,
- (2) defining the numerical model condition (Model set-up),
- (3) calibrating and verifying the model,
- (4) simulation and evaluation.

1. The conceptual model is a basic graphical representation of a complex natural volcano system. The basic components of a conceptual model include defining the extents and characteristics of the system. This requires a precise definition of the physical boundaries of the region, internal and external factor of the system, and the rock properties distributed throughout the region. In addition, developing a good model requires compiling detailed information on the geology (e.g. properties and spatial distribution and its degradation history), groundwater flow within volcano, heat transport (e.g. locations of hydrothermal leakage at the surface and amount of excess heat discharge, and magmatic heat source). A well-defined site conceptual model is a useful tool for compiling and interpreting site data. Moreover, conceptual model development is the most important step in modelling the stability of volcanic edifices.

2. Model set-up, including selection of the computer program, designing numerical grid and discretization (e.g. dimensions of the layers and cells that make up a model), representation of the geology in the numerical model, and implementation of boundary conditions. The numerical grid also has to be designed such that the geological heterogeneities are resolved by the numerical model; moreover, time step has to be chosen and initial conditions should be specified.

3. Calibrating and verifying the model, imply that the model can obtain the best reproduction of the physical-system as observed in nature; usually, the structure of the model is fixed during the calibration process.

4. Simulation and Evaluation, including analysis and interpretation of the results required to fulfil the objectives of the study. Basically, stability models for a volcanic edifice are adopted to obtain information about the possibility of a progressive failure as a consequence of the stress-strain behavior of the affected materials.

## 5.2 Material properties

The model domain includes five units representing different components of the volcanic system: (a) the underlying basement made of limestones and intrusive rocks (unit “B” in Figure 5.1 and Table 5.2); (b) the volcanic rocks forming the volcano edifice (unit “VR” in Figure 5.1 and Table 5.2); (c) the altered volcanic rocks made of pyroclastic deposits (unit “AVR1” in Figure 5.1 and Table 5.2); (d) and the altered volcanic rocks made of altered pyroclastic rocks and ignimbrite deposits (unit “AVR1 and AVR2, respectively” in Figure 5.1

and Table 5.2). Typical values for materials forming the basement, units “B”, were obtained from the literature (Terzaghi et al., 1996; Hoek and Brown, 1997). For volcanic materials (units “VR” Figure 5.1 and Table 5.2), rock mass properties were estimated according to the methodology proposed by Del Potro and Hürlimann (2008). Intact rock properties of not altered rocks were assumed within the range of the properties obtained in this study and literature values (Watters et al., 2000; Hürlimann et al., 2001; Reid et al., 2001; Zimbelman et al., 2004, Moon et al., 2005), whereas rock mass quality and structure were assessed in terms of RMR (Bieniawski, 1989) and GSI (Hoek et al., 1995; Hoek and Brown, 1997; Hoek et al., 2002). These properties were combined to derive the Hoek-Brown parameters and the equivalent Mohr- Coulomb parameters representative for the stress ranges expected in the ideal volcano. Adopted values of equivalent rock mass cohesion were obtained according to the approach of Bieniawski (1989) to avoid overestimation and are consistent with those published by other authors for volcanic rock masses (Watters et al., 2000; Moon et al., 2005), While the properties of the altered rocks were assumed directly from physical and mechanical tests, performed in this study (Table 5.2).

Table 5.2 Rheological properties used in the numerical model

Rock properties	B1	VR	AVR1	AVR2
Mass-Density (Kg/m <sup>3</sup> )	2600	2200	1480	980
Elastic Modulus (Pa)	3.6e <sup>10</sup>	1.0e <sup>10</sup>	1.6e <sup>9</sup>	8.3e <sup>8</sup>
Poisson's Ratio	0.30	0.32	0.13	0.36
Tensile strength (Pa)	1e <sup>6</sup>	1e <sup>5</sup>	2.57e <sup>6</sup>	2.4e <sup>5</sup>
Friction angle (°)	36	32	14	16
Cohesion (Pa)	5e <sup>6</sup>	5e <sup>5</sup>	3.06e <sup>6</sup>	1.94e <sup>6</sup>
Dilation angle (°)	0	21		

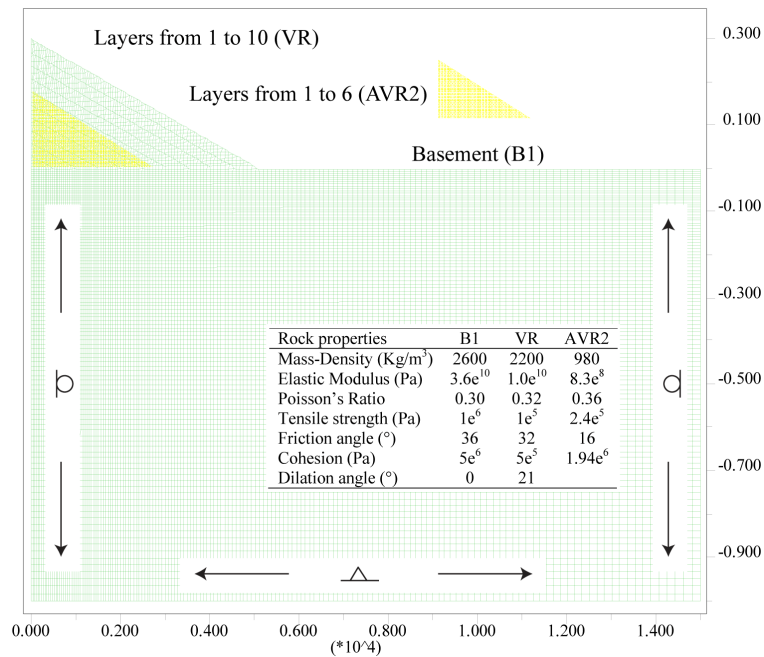


Figure 5.1 The model domain includes five units representing different components of the volcanic system

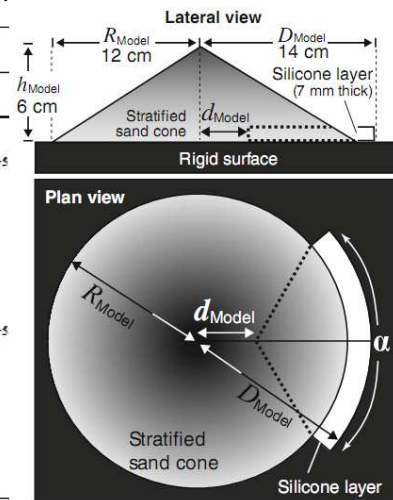
### 5.3 Model elements and boundary conditions

The model was set up using FLAC 6.0 (two-dimensional explicit finite difference commercial code “Fast Lagrangian Analysis of Continua”; Itasca, 2010) to analyze the progressive failure and simulate the stress-strain behavior of different rock layers under different boundary and initial conditions.

The base of the volcano, the geometry of volcanic rock sequence, and the simplified geometry of the volcanic units were located according to the available geometrical and geological data (Allan 1985; Finn et al., 2001; Reid et al., 2001; Cortes et al., 2005; Reid et al., 2010), on the topographical cross sections extracted from SRTM data for different volcanoes (Shiveluch, Bezymianny, Iriga, and Lullailaco, Citlaltépetl, Mount St. Helens, Colima) affected by historical and prehistorical flank collapses, and according to analogue and numerical models presented in literature (see Merle and Borgia 1996; van Wyk de Vries and Matela, 1998; Cecchi et al., 2005; Andrade and van Wyk de Vries 2010; for a complete review).

Table 5.3 Parameters used in the scaling procedure in analogue modeling. illustration of the main geometrical parameters of the models: opening angle ( $\alpha$ ) and the ductile layer offset ( $d_{\text{Model}}$ ) varied during experiments (Andrade and van Wyk de vries, 2010).

Variable	Definition	Unit	Value		
			Model (M)	Nature (N)	Ratio M/N
$h$	Edifice height	m	0.06	2900–1300	$2 \times 10^{-5}$ – $5 \times 10^{-5}$
$R$	Edifice radius	m	0.12	10000–7000	$1.2 \times 10^{-5}$ – $1.7 \times 10^{-5}$
$C$	Edifice cohesion	Pa	0–100	$10^{-4}$ – $10^{-7}$ #	$0$ – $10^{-5}$
$\rho$	Edifice density	kg m <sup>3</sup>	1500	2200 §	0,7
$\alpha$	Basal layer angle	rad	$\pi$ – $\pi/6$	$\pi/6$ – $\pi/3$	1–0.33
$D$	Basal layer length	m	0.14	13000–8000	$10^{-5}$ – $1.8 \times 10^{-5}$
$d$	Basal layer vertex distance	m	0–0.08	??	–
$T$	Basal layer thickness	m	0.007	300–200	$2.3 \times 10^{-5}$ – $3.5 \times 10^{-5}$
$\mu$	Basal layer viscosity	Pa s	20000	$10^7$	0.002
$\gamma$	Basal layer density	kg m <sup>3</sup>	1000	1500–2100	0.5
$t$	Observation time	s	7200	60	120
$V$	Velocity	m s <sup>-1</sup>	$10^{-5}$ – $10^{-6}$	100–10	$10^{-6}$ – $10^{-7}$
$g$	Gravity acceleration	m s <sup>-2</sup>	9.8	9.8	1



However, the model is constructed by a basement block and a cone. The basement is 10 km long and 5 km deep and the cone is 4 km in width and 3 km high. The edifice is composed by ten different slope dipping layers (Figure 5.1).

The domain was discretized using zones to form a grid composed by vertical columns of 4-noded square elements with typical size ranging from 40 to 50 m (Figure 5.1).

Boundary conditions were imposed to the model in terms of displacements, by fixing the model bottom and preventing model side displacements in the horizontal direction (Figure 5.1). Modeling was performed according to a sequential approach by simulating the stress-strain evolution of the volcano edifice in different stages, including:

- emplacement of layers 1 to 10,
- progressive degradation of the rock properties in layer 1 and 2,

- progressive degradation of the rock properties in layer 3 and 4,
- progressive degradation of the rock properties in layer 5.

Perfectly elastic behavior was assumed for the basement to account for the values of confining stresses expected during construction. After, the basement was generated, all displacements were imposed equal to zero to avoid large differences between the new displacements generated by the construction of the volcano edifice.

All the layers were constructed by assuming an elasto-perfectly plastic behavior according to a Mohr-Coulomb failure criterion. Each layer was added by 22 steps of density increment to minimize inertial effects. Degradation of the volcano edifice was simulated by changing the properties of layer 1, 2, 3, 4 and 5.

#### 5.4 Model analysis

Model results were evaluated in terms of maximum computed values of shear stress, shear strain and displacement (Figure 5.2, Figure 5.3, respectively).

In general, the concentration of shear stresses occurs after layer four was added and the first, more internal layer was degraded. During volcano construction and volcano degradation, the concentration of the stresses migrates upward to the lowest zone of layer six (last degraded layer, last model step) (Figure 5.2).

The computed pattern of total displacement suggests a subsidence, probably generated by the deformation of weathered the volcanic rocks (Figure 5.4). In this zone, the displacement vectors show a maximum value of 9.5 m. The pattern of the horizontal displacements during modeling is visible in Figure 5.5. The horizontal displacements change with degradation of the volcano; maximum horizontal displacements (negative and positive) are concentrated in the central part of the edifice. Negative horizontal displacements are visible in the altered zone (layer 1 to 6), whereas positive and maximum horizontal displacements are visible in layer 7 and 8. This occurs because of the deformation of the altered zone. Major changes in displacements occur with the emplacement of layer 10 and degradation of layer 6.

Moreover, contemporaneously to these events, a continuous shear strain increment localization band occurs along layer 6 and in the upper part of layer 7. This band could suggest that the subsequent emplacement of a layer and/or subsequent degradation of a zone could influence the stability of the volcano.

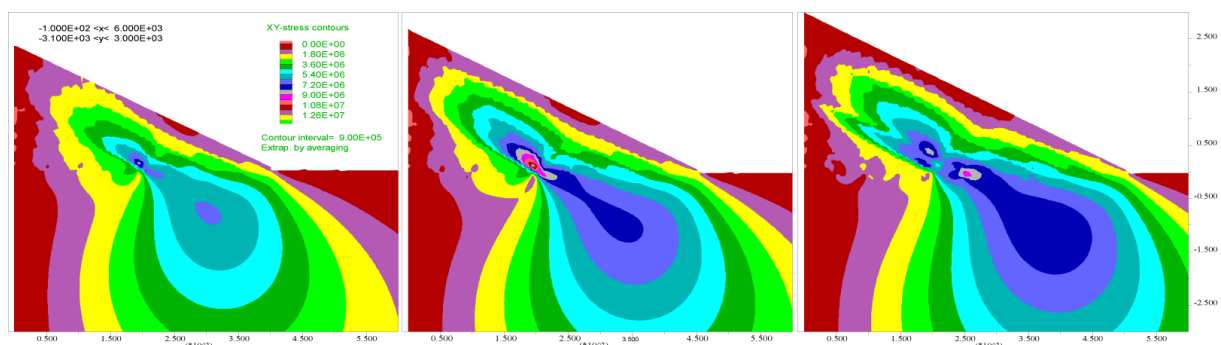


Figure 5.2 Distribution of stresses during volcano construction and layers degradation. From left to right: construction of layer 8; construction of layer 9; construction of layer 10 and degradation of layer 6.

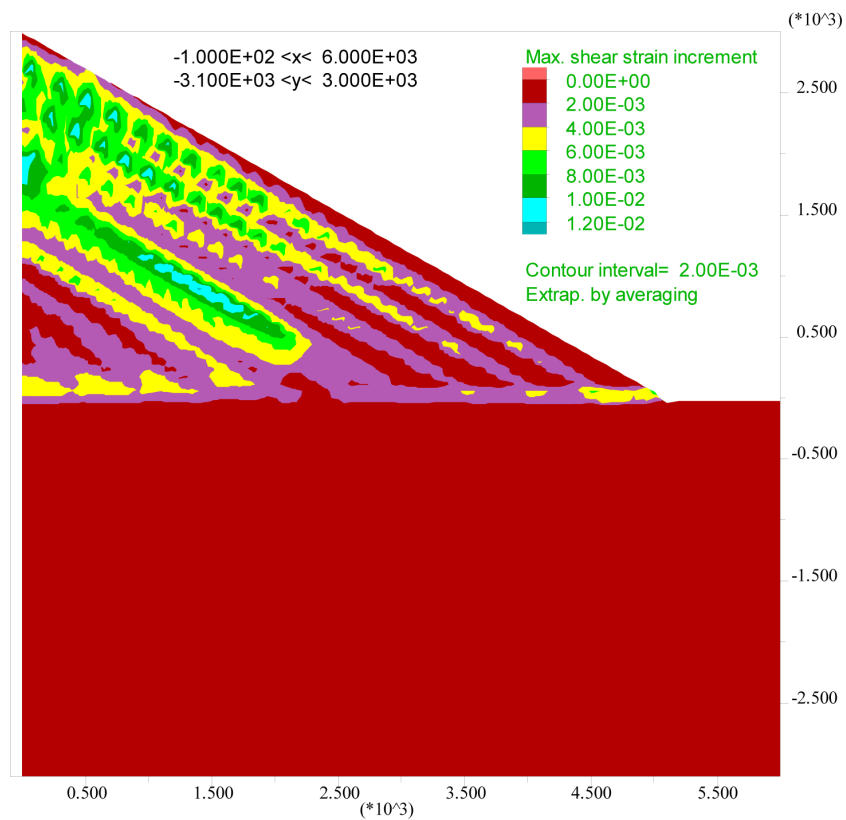


Figure 5.3 Maximum shear strain increment distribution at final step of the model (construction of layer 10 and degradation of layer 6)

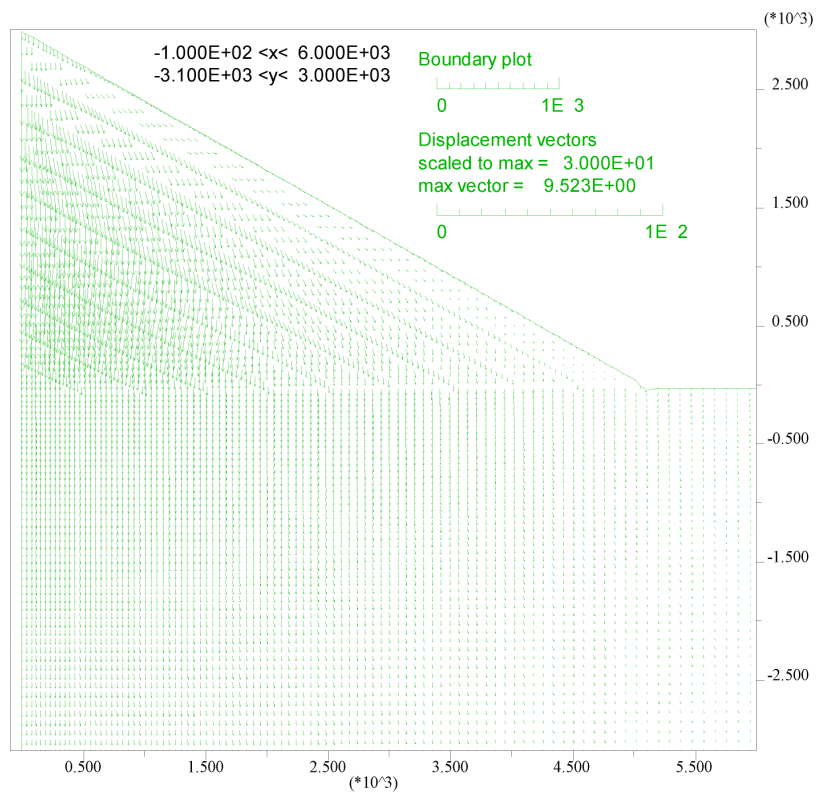


Figure 5.4 Distribution of total displacements at the final phase of the model.

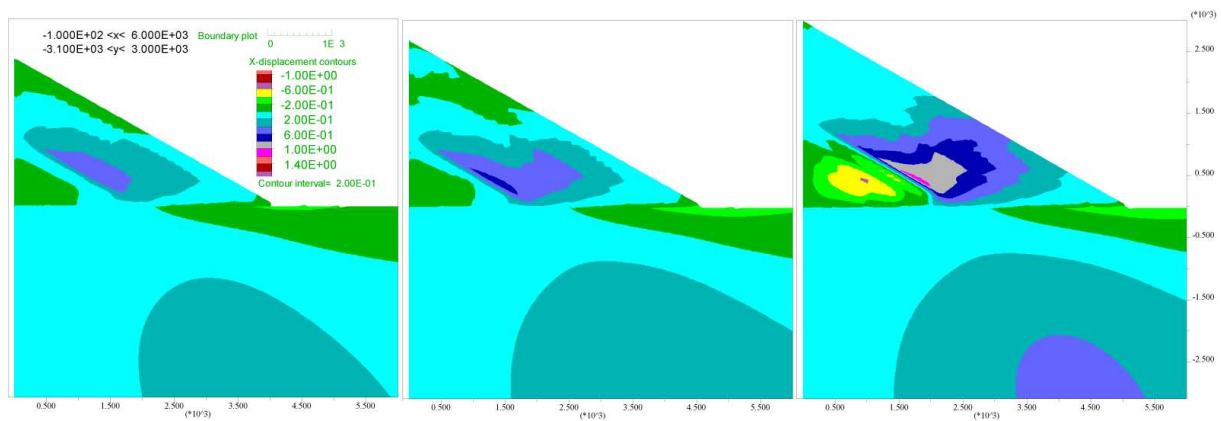


Figure 5.5 Distribution of horizontal displacements. From left to right: construction of layer 8; construction of layer 9; construction of layer 10 and degradation of layer 6.

This model is a very simplified representation of how the stability of a volcano is affected by the alteration of the materials. It should be taken into account that different perturbations such as pore water pressure (e.g. rainfall, vapour and gas), and regional or local tectonics (e.g. faults, earthquakes and dynamic loading) also affect the stability of a volcano and they are not included in the model.

Even if, a volcanic collapse is not hypothesized by degrading materials and by gravitational forces, this model indicates:

- deformation of weak materials localized into the bottom of the volcano (layer 1 to 6);
- continuous shear strain increment, along layer 6 and in the upper part of layer 7;
- concentration of the stresses along the contact of degraded and not degraded materials.

Finally, this model represents the first step of a series of numerical model that are in course of completion. A better understanding of how different factors (distribution and grade of altered materials, water pressure, earthquakes and dynamic loading) act on slope stability is necessary for evaluating the hazards and mechanisms associated with volcanoes composed with altered rocks.

## 6. CONCLUSIONS

In this study, a detailed and comprehensive geomechanical characterization of different altered volcanic rocks was assessed in order to determine the effects on volcanic stability. As a first step, weathering classification based on chemical, mineralogical, petrographical and visual characteristics was performed. As a very important second step, different laboratory tests were performed in order to find out the physical-mechanical behaviour of volcanic materials. As a final step, preliminary definition of possible failure deformation mechanisms and instability scenarios were performed by numerical modelling investigations. Finally, the most important conclusions are briefly summarised as follow:

- **Sampling Sites**, described in present work, represent excellent places to analyze data concerning the behavior (Petrographical, Chemical, and Geotechnical) of altered volcanic rock. The most common controlling alteration is the hydrothermal processes. Joints and faults also appear as a control factor, as they control fumaroles activity.
- According to the variability of **Petrographical, Chemical, and Geotechnical characteristics**. The collected altered volcanic rocks are classified or subdivided into five quality categories (fresh, slightly altered, moderately altered, highly altered, and completely altered) and into four lithotype series (lava, pyroclastic, tuff and ignimbrite series).
- The relationship between chemical changes and **weathering** can be specified by using Chemical Weathering Indices (CWI). They are principally based on the basic assumptions that distributions of chemical elements are mainly regulated by the degree of weathering. In this study, CWI, in particular the Chemical Index of Alteration is well correlated with the degradation trend exhibit by physical-mechanical properties.
- Most of the physical and mechanical properties of altered volcanic rocks are mainly influenced by **porosity** (voids, cavities, and fractures). In general  $\eta_t$  and  $\eta_e$  increase with weathering grade for all lithologies. X-ray tomography and pycnometer tests reveal some minor changes in lava series, where values from SLA3 sample increase drastically and values from SLA5 sample present small reduction. The reason could be the percentage and size of interconnected pores and fractures contained in each samples.
- **Fractal dimension (D)** obtained from  $\eta_t$  and  $\eta_e$ , decreases progressively with weathering grade. This trend suggests relative increase in frequency of large pores
- **Ultrasonic wave propagation**, in particular, **Vs** values reveal large differences not only between each alteration grade, but also between each sample. Less variation is observed in samples from SPRA series, which seems to have a more persistent network of pores. Variations within the samples are corroborated when dynamic Young's modulus derived from  $V_p$  and  $V_s$  wave measurements are correlated with uniaxial strength.
- An exponential decay of the properties is observed when average values of the **compressive strength, tensile strength and Young's modulus** are compared with the average porosity value, fractal dimension and grade of alteration.

- 
- **Compressive strength** varies with **alteration grade** (5.7 - 116.7 MPa). In general, reduction in strength and Young's modulus with grade of alteration is gradual. Strength decreases considerably between SLA2 and SLA3 samples, where drastic changes in rock structure, density (1900-2500 kg/m<sup>3</sup>) and porosity (10-30 %) are identified.
  - Evolution of **Young's modulus** is explained by uniaxial compressive stress cycles tests: Young's modulus in all series increases with increasing stress. In general, the first two values, measured in the first two stress-cyclic (crack closure region) increase rapidly. Increment in each sample is represented by the slope of the best linear fitting ( $0.85 < R^2 < 0.98$ ). Young's modulus in all series increases with decreasing both  $\eta_t$  and  $\eta_e$ . Young's modulus in SPRA series is directly influenced by the grain sizes, the length of grain to grain contacts and matrix cementation
  - Relationship between **tensile strength** and bulk density suggests that tensile strength depends on the intrinsic properties of each specimen. For example, in lava rock series, tensile strength depends on the pore structure, alignment and proportion of crystals. While for pyroclastic and ignimbrite rock series cases, tensile strength depends on pore structure, rock texture, matrix cementation and proportions of pumice clasts.
  - **Friction angles** obtained from triaxial tests range from 10 to 23° along the most altered samples. Abrupt difference in results is observed in fresh samples, where values range from 57 to 36°. Heterogeneity of each sample is clear represented by low values of friction angles.
  - Characteristics in **rock texture** seem to have large influence not only in physical and mechanical properties but also in the mode of failure. In this way, specimens with large proportion of lithic fragments (<2 cm) could be not representative
  - Post-failure reconstruction of samples, in particular those with high percentage of porosity (BoPRA), reveals that **compaction bands** seem to be the transition mechanism between elasto-plastic and hardening behavior. In this way, it is assumed that the nature of deformation within individual bands is controlled by textural properties of the parent rock (e.g. grains, pores, and cement) and the behavior strongly influences the response of the specimen.
  - Measured physical and mechanical values show ignimbrite sample (BoPRA) to be the most altered and the most representative. It exhibits very low density (980 kg/m<sup>3</sup>) and very high porosity (60 %). Mode of failure and compaction bands formation during mechanical tests were easily observed and described in this sample, because of its groundmass fabric.
  - **The evolution of altered** volcanic rocks is identified as a potential cause of **large volcanic landslides**. Maximum computed values of shear strain and displacements; showing that degradation of rock properties is capable of defining large zones of instability



- The **Numerical model** presented in this study, is a very simplified representation of how the stability of a volcano is affected by the alteration of the materials. It should be taken into account that different perturbations such as pore water pressure (e.g. rainfall, vapour and gas), and regional or local tectonics (e.g. faults, earthquakes and dynamic loading) also affect the stability of a volcano and they are neglected in the model.
- Even if, a volcanic collapse is not hypothesized by degrading materials and by gravitational forces, this **numerical model** shows three important characteristics: 1) deformation of weak materials localized into the bottom of the volcano (layer 1 to 6); 2) continuous shear strain increment, along a plane; 3) concentration of the stresses along the contact of degraded and not degraded materials.

## 7. REFERENCES

- Acocella V., Funiciello R., 1999. The interaction between regional and local tectonics during resurgent doming: the case of the island of Ischia, Italy. *Journal of Volcanology and Geothermal Research*. 88.109-123
- Acocella V., Neri M., 2009. Dike propagation in volcanic edifices: Overview and possible developments. *Tectonophysics*. V. 471, n. 1-2, p 67-77
- Aizawa et al., 2005 K. Aizawa, R. Yoshimura, N. Oshiman, K. Yamazaki, T. Uto, Y. Ogawa, S.B. Tank, W. Kanda, S. Sakanaka, Y. Furukawa, T. Hashimoto, M. Uyeshima, T. Ogawa, I. Shiozaki and T. Hurst, 2005. Hydrothermal system beneath Mt. Fuji volcano inferred from magnetotellurics and electric self-potential, *Earth Planet. Sci. Lett.* 235, p 343–355.
- Al-Harthi, A.A., Al-Amri, R.M., Shehata, W.M., 1999. The porosity and engineering properties of vesicular basalt in Saudi Arabia. *Engineering Geology*. 54, p 313–320.
- Allan, J.F., 1986. Geology of the Northern Colima and Zacoalco grabens, southwest Mexico: Late Cenozoic rifting in the Mexican Volcanic Belt, *Geol. Soc. Am. Bull.*, 97, 473–485.
- Al-Shayea N., 2004. Effects of testing methods and conditions on the elastic properties of limestone rock. *Engineering Geology*, 74, p 139-156
- Almendros J., Chouet B., and Dawson, P., 2001. Spatial extent of a hydrothermal system at Kilauea volcano, Hawaii, determined from array analyses of shallow long-period seismicity. *Journal of Geophysical Research*. 106, pp. 12318–12330.
- ASTM. Standard D 2938 Standard test method for unconfined compressive strength of intact rock core specimens.
- ASTM. Standard D 3148 - 02. Standard test method for elastic moduli of intact rock core specimens in uniaxial compression. In: *Annual book of ASTM standards*. West Conshohocken, PA: American Society of Testing Materials; 1993.
- ASTM. Standard D 3967 – 95a. Standard test method for splitting tensile strength of intact rock core specimens. In: *Annual book of ASTM standards*. West Conshohocken, PA: American Society of Testing Materials; 2001.
- Avar, B.B., Hudyma, N., Karakouzian, M., 2003. Porosity dependence of the elastic modulus of lithophysae-rich tuff: numerical and experimental investigations. *International Journal of Rock Mechanics and Mining Sciences*. 40, p 919– 928.
- Avar B.B. and Hudyma N.W., 2007. Observations on the influence of lithophysae on elastic (Young's) modulus and uniaxial compressive strength of Topopah Spring Tuff at Yucca Mountain, Nevada, USA. *International Journal of Rock Mechanics and Mining Sciences*. 44, p. 266-270
- Aversa, S., Evangelista, A. 1998. The Mechanical Behaviour of a Pyroclastic Rock: Yield Strength and “Destructuratio” Effects. *Rock Mechanics and Rock Engineering*. 31 (1), p 25-42
- Aydin, A. and Basu A., 2006. The use of Brazilian Test as a Quantitative Measure of Rock Weathering. *Rock Mechanics and Rock Engineering*. no. 39, v. 1, p. 77-85
- Aydin A., Borja R.I., and Eichhbl P., 2005. Geological and mathematical framework for failure modes in granular rock. *Journal of Structural Geology*. 28, p 83-98.
- BS5930 1999. Code of practice for site investigations. British Standards Institution, London.
- Ballard, R.D., 2000. *Encyclopedia of volcanoes*. Academic Press. Printed in United States of America. 1417 p.
- Bardet J.P., 1997. *Experimental Soil Mechanics*. 1st ed. Prentice Hall. 583 pp.
- Barnes H.L., 1979. *Geochemistry of hydrothermal ore deposits*. Wiley-Interscience publications 2nd edition. 798 p.
- Baud P., Klein E., Wong T.f., 2004. Compaction bands in porous sandstone: spatial evolution of damage and acoustic emission activity. *Journal of Structural Geology*. 26, p 603-624
- Baxevanis T., Papamichos E., Flornes O., Larsen I., 2006. Compaction bands and induced permeability reduction in Tuffeau de Maastricht calcarenite. *Acta Geotechnica*. 1, p 123-135
- Beccaluva, L., Di Girolamo, P., Serri, G., 1991. Petrogenesis and tectonic setting of the Roman Volcanic Province, Italy. *Lithos* 26, 191–221.

- Belousov, A., Belousova, M., Voight, B., 1999. Multiple edifice failures, debris avalanches and associated eruptions in the Holocene history of Shiveluch volcano, Kamchatka, Russia. *Bull. Volcanol.* 61, 324–342.
- Best M.G., 2003. *Igneous and Metamorphic petrology*. Second edition. Blackwell publishing, 729 p.
- Bieniawski, Z.T., 1989. *Engineering Rock Mass Classifications: A Complete Manual for Engineers and Geologists in Mining, Civil and Petroleum Engineering*. John Wiley and Sons, New York. 251 p.
- Binal A., 2009. Prediction of mechanical properties of non-welded and moderately welded ignimbrite using physical properties, ultrasonic pulse velocity, and point load index tests. *Quarterly Journal of Engineering Geology and Hydrogeology*. 42, p. 107-122
- Brady B.H.G. and Brown E.T., 2004. *Rock Mechanics for underground mining*. Kluwer Academic Publishers New York, Boston, Dordrecht, London, Moscow. 3th edition. 645 p.
- Brand H., 2008. *Volcanism and the Mantle. Campi Flegrei*. Planetary Science. C004. <http://cires.colorado.edu/~bilham/tiltmeter.file/CampiFlegreiHelenBrand.pdf>
- Brantley, S. and Glicken, H. 1986. Volcanic debris avalanches. In: *Earthquakes and Volcanoes*. US Geological Survey Report, EV, 5, 195-206.
- Caliro S., Chiodini G., Moretti R., Avino R., Granieri D., Russo M., and Fiebig J., 2007. The origin of the fumaroles of La Solfatara (Campi Flegrei, South Italy). *Geochimica et Cosmochimica. Acta* 71, p 3040-3055
- Capra L., and Macías J.L., 2002. The cohesive Naranjo debris-flow deposit (10 km<sup>3</sup>): A dam breakout flow derived from the Pleistocene debris-avalanche deposit of Nevado de Colima Volcano (México). *Journal of Volcanology and Geothermal Research*, v. 117, p. 213-235.
- Casper O., Fabricius I.L., Krogsgaard A., Prasad M., 2004. Static and dynamic Young's Modulus for lower Cretaceous chalk. A low frequency scenario. AAPG International Conference: October 24-27, 2004; Cancun, Mexico
- Castellanza R., Gerolymatou E., and Nova R., 2009. Experimental observations and modelling of compaction bands in oedometric tests on high porosity rocks. *Strain*, An international journal for experimental mechanics. 45, p. 410-423
- Cecchi E., van Wyk de Vries., Lavest J.M., 2005. Flank spreading and collapse of weak-cored volcanoes. *Bulletin of Volcanology*, v. 67, p. 72-91.
- Chiesa S., Poli S., Vezzoli L., 1986. *Studio dell'ultima eruzione storica dell'isola d'Ischia: la colata dell'Arso - 1302*. Dipartimento di Scienze della Terra, Università di Milano, Centro Alpi Centrali, CNR, Milano.
- Chiesa S., and Poli S., Vezzoli L., 1988. Island of Ischia. Petrology. In Vezzoli L (ed) *Island of Ischia*. *Quad Ric Sci CNR Rome* 114, 10: p. 72-93
- Ciccotii M. and Mulargia F., 2004. Differences between static and dynamic elastic moduli of atypical seismogenic rock. *Geophysical Journal International*. 157, p 474-477
- Cipriani F., Marianelli P., and Sbrana A., 2008. Studio di una sequenza piroclastica del vulcano della Solfatara (Campi flegrei). *Considerazioni vulcanologiche e sul sistema di alimentazione*. *Atti. Soc. tosc. Sci. nat., Mem., Serie A*, 113. p 39-48
- Civetta L., Gallo G., Orsi G., 1991. Sr- and Nd-isotope and trace element constrains on the chimica evolution of the magmatic system of Ischia (Italy) in the last 55 Ka. *Journal of Volcanology and Geothermal Research*, v. 46. p 213-230
- Concha-Dimas A. and Watters R.J., 2003. Preliminary evaluation of volcanic flank stability using finite difference modeling: Citlaltépetl volcano, México. In: Cilligan, E., Whittle (Eds.), 12th. *PanAmerican Conference on Soil Mechanics and Geotechnical Engineering*. MIT, Verglag Gluckauf (Germany), 2483-2488 p.
- Concha-Dimas A., Cerca M., Rodríguez S.R., Watters R.J., 2005. Geomorphological evidence of influence of pre-volcanic edifices at the Cofre de Perote-Pico de Orizaba chain and implications for avalanche generation. *Geomorphology*, v. 72, p. 19-39.
- Concha-Dimas A. and Watters R.J., 2003. Preliminary evaluation of volcanic flank stability using finite difference modeling: Citlaltépetl volcano, México. In: Cilligan, E., Whittle (Eds.), 12th.

- PanAmerican Conference on Soil Mechanics and Geotechnical Engineering. MIT, Verlag Gluckauf (Germany), p. 2483-2488
- Cortes, A., Garduno V.H., Navarro C., Komorowski J.C., Saucedo R., Macias J.L., and Gavilanes J.C., 2005. Carta Geológica del Complejo Volcánico de Colima, Con Geología del Complejo Volcánico de Colima. Cartas Geológicas Y Mineras, Universidad Nacional Autonoma de Mexico, 10.
- Crisci G.M., De Francesco A.M., Mazzuoli R., Poli G., Stanzione D., 1989. Geochemistry of recent volcanics of Ischia Island, Italy: evidences for fractional crystallization and magma mixing. *Chemical Geology*. 78. p. 15-33
- Crosta G.B., Imposimato T.S., Roddeman D., Chiesa S., Moia F., 2005. Small fast-moving flow-like landslides in volcanic deposits: The 2001 Las Colinas Landslide (El Salvador). *Engineering Geology*. 79, p 185–214
- Das A., Nguyen G., and Einav I., 2010. Compaction bands in porous rocks: localization using breakage mechanics. *Geophysical Research Abstracts*. Vol. 12
- Day 1996 Hydrothermal pore fluid pressure and the stability of porous, permeable volcanoes. In *Volcano Instability*, Geol Soc Spec Publ 110 77-93
- Dearman W. R., 1995. Description and classification of weathered rocks for engineering purposes: the background to the BS5930: 1981 proposals. *Quarterly Journal of Engineering Geology*, 28, p 267-276.
- del Potro R. and Hürlimann M., 2008. Geotechnical classification and characterisation of materials for stability analyses of large volcanic slopes. *Engineering Geology*, v. 98, p. 1–17
- del Potro R. and Hürlimann M., 2009. The decrease in the shear strength of volcanic materials with argillic hydrothermal alteration, insights from the summit region of Teide stratovolcano, Tenerife. *Engineering Geology*, v. 104, p. 135–143
- Delcamp A, van Wyk de Vries B, James M (2008) The influence of edifice slope and substrata on volcano spreading. *J Volcanol Geotherm Res* 177:925–943
- Dirksen, O., Humphreys, M. C. S., Pletchov, P., Melnik, O., Demyanchuk, Y., Sparks, R. S. J. & Mahony, S. 2006. The 2001–2004 dome-forming eruption of Shiveluch Volcano, Kamchatka: Observation, petrological investigation and numerical modelling. *Journal of Volcanology and Geothermal Research* . 155, p 201-226.
- Di Vito, M.A., Isaia ,R., Orsi, G., Southon, J., deVita, S., D'Antonio, M., Pappalardo, L., and Piochi, M., 1999. Volcanic and deformational history of the Campi Flegrei caldera in the past 12ka. *Journal of Volcanology and Geothermal Research* 91: 221–246.
- Donnadieu P., Matsuda K., Epicier T., Douin J., 2001. Measurements of strain fields due to nanoscale precipitates using the phase image method. *Image Analysis and Stereology*, v. 20, n. 3, p 213 –218
- Duzgoren-Aydin N.S. and Aydin A., 2003. Chemical heterogeneities of weathered igneous profiles: implications for chemical indices. *Environmental Engineering Geosciences*. 9(4). P. 363–376
- Duzgoren-Aydin N.S., Aydin A., Malpas J., 2002. Re-assessment of chemical weathering indices: case study on pyroclastic of Hong Kong. *Engineering Geology*. 63, p 99–119
- Edelfro, C., 2003. Rock Mass Strength, A review. Technical Report. LULEA UNIVERSITY OF TECHNOLOGY Department of Civil Engineering, Division of Rock Mechanis. ISSN: 1402-1536- ISRN: LTU-TR-03/16-SE.
- Edmonds, H.N., Michael, P.J., Baker, E.T., Connelly, D.P., Snow, J.E., Langmuir, C.H., Dick, H.J.B., German, C.R., and Graham, D.W., 2003. Discovery of abundant hydrothermal venting along the ultra-slow spreading Gakkel ridge in the Arctic Ocean, *Nature*, 421, 252–256.
- Farmer I.W., Kemeny J.M., and McDoniel, 1991, Analysis of rock fragmentation in bench blasting using digital image processing. In: *Proc. Int Cong. Rock Mech.* 2, 1037–1042.
- Fedo C.M., Nesbitt H.W., Young G.M., 1995. Unravelling the effects of potassium metasomatism in sedimentary rocks and paleosols, with implications for paleoweathering conditions and provenance. *Geology*. 23, p 921-924

- Finizola A., Sortino F., Lénat J-F., Valenza M., 2002. Fluid circulation at Stromboli volcano, (Aeolian Islands, Italy) from self-potential and soil gas surveys. *Journal of Volcanology and Geothermal Research*. 116, 1-2, 1-18.
- Finn C.A., Sisson T.W., Deszcz-Pan M., 2001. Aerophysical measurements of collapse-plate hydrothermally altered zones at Mount Rainier volcano. *Nature*. 409, p. 600-603.
- Fossen H., 2009. Deformation bands formed during soft-sediments deformation: observation from SE Utah. *Marine and Petroleum Geology*. p 1-8
- Frank, D., 1995, Surficial extent and conceptual model of hydrothermal system at Mount Rainier: *Journal of Volcanology and Geothermal Research*, v. 65, p. 51–80.
- Germaine, J.T. and Germaine, A.V., 2009. *Geotechnical Laboratory Measurements for Engineers*. John Wiley & Sons, Inc., Hoboken, New Jersey. 351 pp.
- Gerlach T.M., and Casadevall T.J., 1986. Fumarole emissions at Mount St. Helens Volcano, June 1980 to October 1981: degassing of a magma-hydrothermal system, *J. Volcanol. Geotherm. Res.* 28, pp. 141–160.
- Ghayoumian J., Nakajima S., Fatemi S.M., and Ozaki M., 1993. Weathering characteristics of slate and green rocks. *Geotechnical Engineering of Hard Soils-soft Rocks*. Balkema Rotterdam. p 105-112
- Giacomelli L. and Scandone R. 1992. *Campi Flegrei, Campania Felix*. Guida alla escursioni dei vulcani napoletani. Liguori Editore. 69 p.
- Giggenbach, W.F., Garcia, P., N., Londono, C., A., Rodriguez, V., L., Rojas, G., N. and Calvache, V., M.L., 1990. The chemistry of fumarolic vapor and thermal-spring discharges from the Nevaldo del Ruiz volcanic-magmatic-hydrothermal system, *Columbia: Journal of Volcanology and Geothermal Research*, v. 42, p. 13-39.
- Gillot P.Y., Chiesa S., Pasquare G., Vezzoli L., 1982.  $^{40}\text{K}/^{39}\text{Ar}$  dating of the volcano-tectonic horst of the Isle of Ischia, Gulf of Naples. *Nature*. 299 p. 242-245
- Glicken H., 1996. Rockslide-debris avalanche of May 18, 1980, Mount St. Helens volcano, Washington. Open-file Report 96-677, 90 p.
- Glicken, H., 1998. Rockslide-debris avalanche of May 18, 1980, Mount St. Helens Volcano, Washington. *Bull. Geol. Surv. Japan* 49, p 55-106.
- Goodwin L.B., Cook J.E., Boutt D.F., and Plourde K., 2010. Quantifying the micromechanical effects of variable cement in granular porous media. DOE Award Number FG02-05ER15738
- Griffith L.L., and Shock E.L., 1995. A geochemical model for the formation of hydrothermal carbonates on Mars. *Nature*, v. 377, p. 406 – 408.
- Gualda G.A.R. and Rivers M., 2006. Quantitative 3D petrography using x-ray tomography: Application to Bishop Tuff pumice clasts. *Journal of Volcanology and Geothermal Research* 154: 48-62
- Gudmundsson A., and Brenner S.L., 2005. On the conditions of sheet injections and eruptions in stratovolcanoes. *Bulletin of Volcanology*, v. 67, p. 768-782.
- Gudmundsson A., and Philipp S.L., 2006. How local stress fields prevent volcanic eruption. *Journal of Volcanology and Geothermal Research*, v. 158, p. 257-268.
- Harnois L. and Moore J. M. 1988. Geochemistry and origin of the Ore Chimney Formation, a transported paleoregolith in the Grenville Province of Southern Ontario, Canada. *Chemical Geology*. 69, p 267-289.
- Hase, H., Hashimoto, T., Sakanaka, S., Kanda, W. and Tanaka, Y., 2005. Hydrothermal system beneath Aso volcano as inferred from self-potential mapping and resistivity structure. *J. Volcanol. Geotherm. Res.*, 143, pp.259-277.
- Haskings D.R. and Bell F.G., 1995. Drakensberg basalts: their alteration, breakdown and durability. *Quarterly Journal of Engineering Geology*. 28, p. 287-302
- Higgins M. D., 2000. Measurement of crystal size distributions. *American Mineralogist*. vol. 85, 1105–1116

- Heap M.J., Faulkner D.R., 2008. Quantifying the evolution of static elastic properties as crystalline rock approaches failure. *Int. J. Rock Mech. Min. Sci.* 45. p 564–573.
- Heap M.J., Vicinuerria S., and Meredith P.G., 2009. The evolution of elastic moduli with increasing crack damage during cyclic stressing of basalt from Mt. Etna volcano. *Tectonophysics*. 471, p 153-160
- Hoek, E., 1990. Estimating Mohr-Coulomb Friction and Cohesion values from the Hoek-Brown Failure criterion. *International Journal of Rock Mechanics and Mining Science & Geomechanics*, vol. 27, No. 3 p 227-229.
- Hoek E., Kaiser P.K., and Bawden W.F., 1995. *Support of Underground Excavations in Hard Rock*, Balkema, Canberra, 215 pp.
- Hoek E., and Brown E.T., 1997. Practical estimates of rock mass strength, *International Journal of Rock Mechanics and Mining Sciences*, 34, 1165–1186.
- Hoek, E. and Karzulovic A., 2001. Rock mass properties for surface mines, Published in *Slope Stability in Surface Mining*, (Edited by W.A. Hustralid, M.K. McCarter and D.J.A. van Zyl), Littleton, Colorado: Society for Mining Metallurgical and Exploration (SME) 2000, p. 59-70.
- Hoek, E., Carranza-Torres C., and Corkum B., 2002. The Hoek–Brown failure criterion — 2002 edition, 5<sup>th</sup> North American Rock Mechanics Symposium and 17th Tunneling Association of Canada Conference: NARMS-TAC, Toronto, p 267–271
- <http://www.rocsience.com/hoek/references/H2000c.pdf>
- Hudyma N., Avar B.B., and Karakouzian M., 2004. Compressive strength and failure mode of lithophysae-rich Topopah Spring tuff specimens and analog models containing cavities. *Engineering Geology*. 73, p 179-190
- Hürlimann M., Ledesma A., and Martí J., 2001. Characterisation of a volcanic residual soil and its implications for large landslide phenomena: application to Tenerife, Canary Islands, *Engineering Geology* 59, 115–132.
- Hurwitz, S., S. E. Ingebritsen, and M. L. Sorey (2002), Episodic thermal perturbations associated with groundwater flow: An example from Kilauea Volcano, Hawaii, *J. Geophys. Res.*, 107
- Ingebritsen, S.E., and Scholl, M.A., 1993, The hydrogeology of Kilauea volcano. *Geothermics*, v. 22, p. 255–270.
- Inguaggio S., Pecoraino G., D'Amore F., 2000. Chemical and isotopic characterization of Fluid manifestations of Ischia Island (Italy). *Journal of Volcanology and Geothermal Research*. 99, p 151-178.
- Irfan T.Y., 1996. Mineralogy, fabric properties and classification of weathered granitic rocks in Hong Kong. *Quarterly Journal of Engineering Geology*. 29, p 5-35.
- Irfan T.Y., 1999. Characterization of weathered volcanic rocks in Hong Kong. *Quarterly Journal of Engineering Geology and Hydrogeology*, v. 32; p. 317-348
- Isaia R., D'Antonio M., Dell'Erba F., Di Vito M., Orsi G., 2004. The Astroni volcano: the only example of closely spaced eruptions in the same vent area during the recent history of the Campi Flegrei caldera (Italy). *Journal of Volcanology and Geothermal Research*. 133, p 171-192
- ISRM Committee on Laboratory Tests 1972. Suggested methods for determining water content, porosity, density, absorption and related properties and swelling and slake-durability index properties. Document no. 2: 1–36
- Iverson, R. M. (1997). The physics of debris flows, *Rev. Geophys.*, 35, pp. 245- 296.
- Jaeger J.C., Cook N.G.W., and Zimmerman R.W., 2007. *Fundamentals of rock Mechanics*. Fourth edition. Blackwell publishing, 475 p.
- Kate J.M. 1993. Geotechnical behavior of intact rock specimens. *Geotechnical Engineering of Hard Soils-Soft Rocks*, Anagnostopoulos et al. (eds). 1993 Balkema, Rotterdam, p. 569-576
- Karpuz C., and Pasamehmetoglu A.G., 1997. Field characterisation of weathered Ankara andesites. *Engineering Geology*, v. 46, p. 1-17
- Kempton K A, Rowe G L, 2000. Leakage of active crater lake brine through the north flank at Rincon de la Vieja Volcano, Northwest Costa Rica, and implications for crater collapse. *J Volc Geotherm Res*, 97: 143-159

- Kerle N., and van Wyk de Vries B., 2001. The 1998 debris avalanche at Casita volcano, Nicaragua – Investigation of structural deformation as the cause of slope instability using remote sensing. *Journal of Volcanology and Geothermal Research*, v. 105, p. 49-63.
- Ketcham, R.A. 2005. Computational methods for quantitative analysis of three-dimensional features in geological specimens. *Geosphere* 1: 32-41
- Kiliç A. and Teymen A., 2008. Determination of mechanical properties of rocks using simple methods. *Bulletin of Engineering and Geology Environ*, v. 67, p. 237-244
- Kim S.S. and Park H.D., 2003. The relationship between physical and chemical weathering indices of granites around Seoul, Korea. *Bull Eng Geol Env*. 62, p 207–212
- Kodaka T., Oka F., Otani J., Kitahara H., Ohta H., 2006. Experimental study of compaction bands in diatomaceous porous rock. *GeoX*, 2nd International workshop on X-ray CT for Geomaterials.
- Kovari K., Tisa A., Einstein H. H., Franklin J. A. 1983. Suggested methods for determining the strength of rock materials in triaxial compression: revised version. *International Journal of Rock Mechanics and Mining Science & Geomechanics*, vol. 20, no. 6, p 283–290.
- Kozhurin A., Acocella V., Kyle P.R., Lagmay F.M., Melekestsev I.V., Ponomareva V., Rust D., Tibaldi A., Tunesi A., Corazzato C., Rovida A., Sakharov A., Tengonciang A., Uy H., 2006. Trenching Studies of active faults in Kamchatka, eastern Russia: Palaeoseismic, tectonic and hazard implications. *Tectonophysics*, v. 417, p. 285-304.
- Lagmay A.M.F., van Wyk de Vries B., Kerle N., and Pyle D.M., 2000. Volcano instability induced by strike-slip faulting. *Bulletin of Volcanology*, v. 62, p. 331-346.
- Lee S.G. and de Freitas M.H., 1989. A revision of the description and classification of weathered granite and its application to granites in Korea. *Quarterly Journal of Engineering geology*, London. Vol.22 p 31-48
- Lopez, D.L., and Williams, S.N., 1993, Catastrophic volcanic collapse; relation to hydrothermal processes: *Science*, v. 260p. 1794-1796.
- Luhr J.F., and Prestegard K.L., 1988. Caldera formation at Volcán Colima, Mexico, by a large holocene volcanic debris avalanche. *Journal of Volcanology and Geothermal Research*, v. 35, p. 335-348.
- Lungarini L., Troise C., Meo M., and De Natale G., 2005. Finite element modelling
- Lumb P., 1983. Engineering properties of fresh and decomposed igneous rocks from Hong Kong. *Engineering Geology*, 19. p. 81-94.
- Luping, T.N., 1986. A study of the quantitative relationship between strength and pore size distribution of porous materials. *Cement and Concrete Research* 16, 87–96.
- Naik T.R., Malhotra V.M., and Popovics J. S., 1991. The ultrasonic pulse velocity method. *Handbook on Non-destructive testing of concrete*, CRC Press, 170 p.
- Nappi G., Renzulli E., and Santi P., 1991. Evidence of incremental growth in the Vulsinian calderas. *Journal of Volcanology and Geothermal Research*. 47, p 13-31
- Nappi G., Capaccioni B., Mattioli M., Mancini E., Valentini L., 1994. Plinian fall deposits from Vulsini Volcanic District. Central Italy . *Bull. Volcanol*. 56, p 502–515.
- Nappi, G., Renzulli, A., Santi, P., Gillot, P.Y., 1995. Geological evolution and geochronology of the Vulsini Volcanic District. Central Italy . *Bull. Soc. Geol. Ital*. 114, 599–613.
- Nappi G., Antonelli F., Coltorti M., Milani L., Renzulli A., Siena F., 1998. Volcanological and petrological evolution of the Eastern Vulsini District, Central Italy. *Journal of Volcanology and Geothermal Research*. 87, p. 211-132
- Nimick, F.B., 1988. Empirical relationships between porosity and the mechanical properties of tuff. In: Cudall, Sterling, Starfield (Eds.), *Questions in Rock Mechanics*. Balkema, Rotterdam, pp. 741–742.
- Nishi, Y., S. Sherburn, B. J. Scott and M. Sugihara. 1996. High-frequency earthquakes at White Island volcano, New Zealand: insights into the shallow structure of a volcano-hydrothermal system. *J. Volcanol. Geotherm. Res*. 72: 183-197.
- Nesbitt H.W. and Young G.M., 1982. Early Proterozoic climates and plate motions inferred from major element chemistry of lutites. *Nature*. 299, p 715–717

- MacKenzie W.S., Donaldson C.H., and Guilford C., 1984. Atlas of igneous rocks and their textures. Halsted press. Printed in United States of America. 148 p.
- Marques E.A.G., Barroso E.V., Menezes Filho A.P., Vargas Jr. E. do A., 2010. Weathering zones on metamorphic rocks from Rio de Janeiro-Physical, mineralogical and geomechanical characterization. *Engineering Geology*. 111, p. 1-18
- Marinos P., and Hoek E., 2000. GSI: a geologically friendly tool for rock mass strength estimation. In: Proceedings of the GeoEng2000 at the international conference on geotechnical and geological engineering, Melbourne, Technomic publishers, Lancaster, p. 1422–1446
- Martínez- Martínez J., Benavente D., and García del Cura M.A., and Cañaveras J.C., 2006. Applications of ultrasonic to brecciated dolostones for assessing their mechanical properties. IAEG2006 Paper number 243
- Martínez- Martínez J., Benavente D., and García del Cura M.A., 2007. Petrographic quantification of brecciated rocks by image analysis. Application to the interpretation of elastic wave velocities. *Engineering Geology*. 90, p 41-54
- Martínez- Martínez J., Benavente D., Ordoñez S., García del Cura M.A., 2008. Multivariate statistical techniques for evaluating the effects of brecciated rock fabric on ultrasonic wave propagation. *International Journal of rock Mechanics and Mining Sciences*. 45, p 609-620
- Martínez- Martínez J. 2009. Influencia de la alteración sobre las propiedades mecánicas de calizas, dolomías y mármoles. Evaluación mediante estimadores no destructivos (ultrasonidos). PHD Thesis. Universitat d'Alicant.
- Melekestsev, I.V., 2006. Large modern collapses on the active volcanoes of Kamchatka: causes and mechanisms of formation. In: Evans, S.G., Scarascia Mugnozza, G., Strom, A., Hermanns, R.L. (Eds.), *Landslides Massive Rock Slope Failure: (NATO Science Series: IV: Earth and Environmental Sciences)*. Springer, pp. 439–453.
- Merle O, Borgia A., 1996. Scaled experiments of volcanic spreading. *J Geophys Res* 101:13, 805–13,817
- Merle O. and Lénat J.F., 2003. Hybrid collapse mechanism at Piton de la Fournaise volcano, Reunion Island, Indian Ocean. *Journal of Geophysical research*. 108, n. B3.
- McGuire, W. J. 1996. Volcano instability: a review of contemporary themes. In: McGuire, W. J., Jones, A. P. & Neuberg, J. (eds) *Volcano Instability on the Earth and Other Planets*, Geological Society, London, Special Publications, 110, 1–23
- Moon V., Bradshaw J., Smith R., de Lange W., 2005. Geotechnical characterisation of stratocone crater wall sequences, White Island Volcano, New Zealand. *Engineering Geology*, v.81, p. 146–178
- Moon V.G., 1993. Microstructural controls on the geomechanical behavior of ignimbrite. *Engineering Geology*, vol. 35, p 19-31
- Morales T., Uribe-Etxebarria G., Uriarte J.A., Fernández de Valderrama I., 2004. Geomechanical characterisation of rock masses in Alpine regions: the Basque Arc (Basque-Cantabrian basin, Northern Spain). *Engineering Geology*, v. 71, p. 343–362
- Morgan D.J., and Jerram D. A., 2006. On estimating crystal shape for crystal size distribution analysis. *Journal of Hydraulic. Journal of Volcanology and Geothermal Research*. 154, p. 1–7
- Morgenstern N.R. and Cruden D., 1977. Description and classification of geotechnical complexities. *Proc. Int. Symp. Geotechnically Complex Materials, Capri*. Vol. 2, p 195-203
- Nakamura K. 1977. Volcanoes as possible indicators of tectonic stress orientation – Principle and proposal. *Journal of Volcanology and Geothermal Research*. V. 2, p. 1–16
- Ohtani, T., Nakashima, Y., & Muraoka, H. 2000. Three-dimensional miarolitic cavity distribution in the Kakkonda granite from borehole WD-1a using X-ray computerized tomography. *Engineering Geology* 56, p 1–9.
- Ohta T. and Arai H., 2007. Statistical empirical index of chemical weathering in igneous rocks: A new tool for evaluating the degree of weathering. *Chemical Geology*, 240: 280–297
- Orsi, G., Gallo, G. and Zanchi, A., 1991. Simple shearing block-resurgence in caldera depressions. A model from Pantelleria and Ischia. *Journal of Volcanology and Geothermal Research*. 47:1-11.



- Orsi G., Gallo G., Heiken G., Wohletz K., Yu E., and Bonani G., 1992. A comprehensive study of pumice formation and dispersal: The Cretaceous Tephra of Ischia (Italy). *Journal of Volcanology and Geothermal Research*. 53, p 329-354.
- Orsi G., De Vita S., Di Vito M., 1996. The restless, resurgent Campi Flegrei nested caldera (Italy): constraints on its evolution and configuration. *Journal of Volcanology and Geothermal Research*. 74, p 179-214
- Ohta T., and Arai H., 2007. Statistical empirical index of chemical weathering in igneous rocks: a new tool for evaluating the degree of weathering. *Chem. Geol.* 240, p 280–297
- Okubo, C.H., 2004. Rock mass strength and slope stability of the Hilina slump, Kīlauea volcano, Hawai'i. *Journal of Volcanology and Geothermal Research*. 138, p 43-76
- Palchik V. 1999. Influence of Porosity and Elastic Modulus on Uniaxial Compressive Strength in Soft Brittle Porous Sandstones. *Rock Mechanics and Rock Engineering*. 32 (4), p 303-309
- Palchik V. and Hatzor Y.H., 2002. Crack damage stress as a composite function of porosity and elastic matrix stiffness in dolomites and limestones. *Engineering Geology*. 63, p. 233-245
- Poland M.P., Moats W.P., Fink J.H., 2008. A model for radial dike emplacement in composite cones based on observations from Summer Coon volcano, Colorado, USA. *Bulletin of Volcanology*, v. 70, p. 861-875.
- Ponomareva, V. V., Pevzner, M. M., and Melekestsev, I. V. 1998: Large debris avalanches and associated eruptions in the Holocene eruptive history of Shiveluch volcano, Kamchatka, Russia. *B. Volcanol*, 59, p. 490–505
- Ponomareva, I.V. Melekestsev and O.V. Dirksen. 2006. Sector collapses and large landslides on late Pleistocene–Holocene volcanoes in Kamchatka, Russia, *J. Volcanol. Geotherm. Res.* 158 pp. 117–138.
- Price, R.H., Boyd, P.J., Noel, J.S., Martin, R.J., 1994. Relationship between static and dynamic properties in welded and non welded tuff. In: Nelson, P.P., Laubach, S.E. (Eds.), *Rock Mechanics: Models and Measurements Challenges from Industry, Proceedings of the First North American Rock Mechanics Symposium*. A.A. Balkema, pp. 505– 512.
- Price D.G., 2009. *Engineering Geology principles and practice*. Edited and compiled by M. H. de Freitas, Springer-Verlag Berlin Heidelberg. 450 p.
- Price R.J., and Velbel M.A., 2003. Chemical weathering indices applied to weathering profiles developed on heterogeneous felsic metamorphic parent, rock. *Chem. Geol.* 202, p 397–346
- Reid M.E., Zimbelman D.R., Bowman S.D., Crowley J.K., 2000. Rock Mass Strength Assessment and Significance to Edifice Stability, Mount Rainier and Mount Hood, Cascade Range Volcanoes, *Pure appl. geophys.* 157, p 957–976. (a)
- Reid M.E., Christian S.B., and Brien D.L., 2000. Gravitational stability of three-dimensional stratovolcano edifices. *Journal of Geophysical Research*, v. 105, n. B3, p. 6043-6056. (b)
- Reid M.E., Sisson T.W., Brien D.L., 2001. Volcano Collapse promoted by hydrothermal alteration and edifice shape, Mount Rainier, Washington. *Geological Society of America*, v. 32, n. 9, p. 373-376
- Reid M.E., Keith T.E.C., Kayen R.E., Iverson N.R., Iverson R.M., Brien L.D., 2010. Volcano collapse promoted by progressive strength reduction: new data from Mount St. Helens. *Bull Volcanol. Short Scientific Communication*.
- RocScience, RocLab1 software. <http://www.roscience.com>
- Rodríguez-Losada J.A., Hernández-Gutiérrez L.E., Olalla C., Perucho A., Eff-Darwich A., 2009. Geomechanical parameters of intact rocks and rock masses from Canary Islands: Implications on their flank stability. *Journal of Volcanology and Geothermal Research*. 182, p 67-75.
- Rotonda T., Tommasi P., and Boldini D., 2010. Geomechanical characterization of the volcanoclastic material involved in the 2002 Landslides at Stromboli. *Journal of geotechnical and geoenvironmental engineering*, p 389-401
- Ruxton B.P., 1968. Measures of the degree of chemical weathering of rocks. *Journal of Geology*, 76, p 518-527

- Sahagian D.L., and Proussevitch A.A., 1998. 3D particle size distributions from 2D observations: stereology for natural applications. *Journal of Volcanology and Geothermal Research*. 84, p 173-196.
- Sbrana A., Fulignati P., Marianelli P., Boyce A.J., and Cecchetti A., 2010. Exhumation of an active magmatic hydrothermal system in a sesurgent caldera environment: the example of Ischia (Italy). *Journal of the Geological Society*. v.166, p. 1061-1073.
- Shea T., van Wyk de Vries B., and Pilato M., 2008. Emplacement mechanisms of contrasting debris avalanches at Volcán Mombacho (Nicaragua), provided by structural and facies analysis. *Bull Volcanol*. 70, p 899–921
- Siebe, C., Komorowski, J.C., Sheridan, M.F., 1992. Morphology and emplacement collapse of an unusual debris avalanche deposit at Jocotitlán Volcano, Central Mexico. *Bull. Volcanol*. 54, p. 573-589.
- Siebert L., 1984. Large volcanic debris avalanches: characteristics of source areas, deposits, and associated eruptions. *Journal of Volcanology and Geothermal Research*, v. 22, p. 163-197.
- Sepe V., Atzori S., Ventura G., 2007. Subsidence due to crack closure and depressurization of hydrothermal systems: a case study from Mt. Epomeo (Ischia Island, Italy). *Terra Nova*, doi: 10.1111/j.1365-3121.2006.00727.x
- Song I., Suh M., Woo Y.K., Hao T., 2004. Determination of the elastic modulus set of foliated rocks from ultrasonic velocity measurements. *Engineering Geology*. 72, p 293–308
- Sonmez H., Gokceoglua C., Medley E.W., Tuncaya E., Nefeslioglu H.A., 2006. Estimating the uniaxial compressive strength of a volcanic bimrock. *International Journal of Rock Mechanics & Mining Sciences*, v. 43, p 554–561
- Sousa et al., 2005 L.M.O. Sousa, L.M.S. del Rio, L. Calleja, V.G.R. Argandoña and A.R. Rey, Influence of microfractures and porosity on the physico-mechanical properties and weathering of ornamental granites, *Eng. Geol.* 77 (2005), pp. 153–168
- Stoopes G.R., and Sheridan M.F., 1992. Giant debris avalanches from the Colima Volcanic Complex, Mexico: Implications for long-runout landslides (>100 km) and hazard assessment. *Geology*, v. 20, p. 299-302
- Sturchio, N.C., Williams, S.N., Garcia P.N., Londoño C.A. 1988. The hydrothermal system of Nevado del Ruiz volcano, Colombia. *Bulletin of Volcanology*, 50, 399–412.
- Szakács A., and Krézsek C., 2006. Volcano–basement interaction in the Eastern Carpathians: Explaining unusual tectonic features in the Eastern Transylvanian Basin, Romania. *Journal of Volcanology and Geothermal Research*, n. 158 p. 6-20
- Thomas M.E., Perford N., and Bromhead E.N., 2004. The effect of internal gas pressurization on volcanic edifice stability: evolution towards a critical state. *Terra Nova*, v. 16, n. 5, p. 312-317.
- Thouret, J.C. 1999. Volcanic geomorphology - an overview. *Earth Science Reviews*, 47, 95-131.
- Tedesco D., 1996. Chemical and Isotopic investigations of fumarolic gases from Ischia island (southern Italy): Evidences of magmatic and crustal contribution. *Journal of Volcanology and Geothermal Research*, n. 74 p. 233-242
- Terzaghi, K., Peck R.B., and Mesri G., 1996. *Soil Mechanics in Engineering Practice*, 3rd ed., John Wiley & Sons, New York, 412 pp.
- Tibaldi A., Mahar A., Lagmay F. A., Ponomareva V.V., 2005. Effects of basement structural and stratigraphic heritages on volcano behaviour and implications for human activities. (The UNESCO/IUGS/IGCP project 455), v. 28, n. 3, p. 158-170
- Tillerson, J.R., Nimick, F.B., 1984. Geoen지니어ing properties of potential repository units at Yucca Mountain, southern Nevada. Sandia National Labs Report, SAND84-0221.
- Tommasi P., Boldini D., Cigniti F., Graziani A., Lomabardi A., and Rotonda T., 2007. Geomechanical analysis of the strability phenomena at Stromboli volcano. *Rock Mechanics: Meating society's Challenges and Demands*-Eberhardt, Stead and Morrison (eds)
- Turcotte, D, L., 1992. *Fractal and Chaos in Geology and Geophysics*. Cambridge University Press, New York. 412 pp.

- Vallance, J.W., and Scott, K.M., 1997. The Osceola Mudflow from Mount Rainier; sedimentology and hazard implications of a huge clay-rich debris flow: *Geological Society of America Bulletin*, v. 109, p. 143–163.
- van Wyk de Vries, B., and Borgia, A., 1996. The effect of volcanic construction on rift fault patterns, *Geology*, v. 24, n. 7, p. 643-646
- van Wyk de Vries, B., and Merle O., 1996. The role of basement in volcano deformation, in McGuire, W. J., et al., eds., *Volcano instability on the Earth and other planets: Geological Society [London] Special Publication 110*, p. 95–110
- van Wyk de Vries B., and Francis P.W., 1997. Catastrophic collapse at stratovolcanoes induced by gradual volcano spreading. *Nature* 387: 387–390
- van Wyk de Vries B., and Matela R., 1998. Styles of volcano-induced deformation: numerical models of substratum flexure, spreading and extrusion. *Journal of Volcanology and Geothermal Research*. 81, p 1-18
- van Wyk de Vries B., Kerle N., and Petley D., 2000. Sector collapse forming at Casita volcano, Nicaragua. *Geology*, v. 28; n. 2; p. 167-170
- Vezzoli L., 1988. Island of Ischia. *Quad Ric Sci CNR Rome*, 114, p 10-133
- Vidal N., and Merle O., 2000. Reactivation of basement faults beneath volcanoes: a new model of flank collapse. *Journal of Volcanology and Geothermal Research*, v. 99, p.9-26
- Vinciguerra S., Del Gaudio P., Mariucci M.T., Marra F., Meredith P.G., Montone P., Pierdominici S., Scarlato P., 2009. Physical properties of tuffs from a scientific borehole at Alban hills volcanic. *Tectonophysics*, v. 471, p. 161-169
- Voight B., and Elsworth D., 2000. Instability and collapse of hazardous gas-pressurized lava domes. *Geophysical research letters*, v. 27, n. 1, p. 1-4.
- Voight B., and Elsworth D., 1997. Failure of volcano slopes. *Géotechnique*, v. 47, n. 1, p. 1-31.
- Voight B., and Elsworth D., 1995. Dike intrusion as a trigger for large earthquakes and the failure of volcano flanks. *Journal of Geophysical Research*, v. 100, n. B4, p. 6005-6024.
- Voight B., and Elsworth D., 1992. Theory of Dike Intrusion in a Saturated Porous Solid. *Journal of Geophysical Research*, v. 97, n. B6, p. 9105-9117.
- Voight, B., Janda, R.J., Glicken, H., and Douglass, P.M., 1983, Nature and mechanics of the Mount St. Helens rockslide-avalanche of 18 May 1980: *Geotechnique*, v. 33, p. 243–273.
- Ward S.N., and Day S., 2006. Particulate kinematic simulations of debris avalanches: interpretation of deposits and landslide seismic signals of Mount Saint Helens, 1980 May 18. *Geophys. J. Int.* 167, 991–1004
- Washington, H.S., 1906. The Roman comagmatic region. Carnegie Institution of Washington, publication no. 57, 199 pp.
- Watters, R.J., Delahaut, W.D., 1995. Effect of argillic alteration on rock mass stability. In: Haneberg, W.C., Anderson, S.A. (Eds.), *Clay and Shale Slope Instability. Reviews in Engineering Geology. Geological Society of America, Boulder, CO*, pp. 139–150.
- Watters R.J., Zimbelman D.R., Bowman S.D., and Crowley J.K., 1997. Rock Alteration and Rock Mass Controls on the Stability of the Cascade Range Volcanoes, Abstracts, EOS, Geophysics, Union, F807.
- Watters R.J., Zimbelman D.R., Bowman S.D., and Crowley J.K., 2000. Rock Mass Strength Assessment and Significance to Edifice Stability, Mount Rainer and Mount Hood, Cascade Range Volcanoes. *Pure and applied Geophysics*, n. 157, p. 957-976
- Watt S. F.L., Pyle D. M., Naranjo J. A and Mather T. A. 2008. Landslide and Tsunami hazard at Yale volcano, Chile as an example of edifice destruction on strike-slip fault zones. *Bulletin of Volcanology*, v. 71, n.5 p. 559-574.
- Wong H.C.R., Chau K.T., and Wang P., 1996. Microcracking and grain size effect in Yuen Long Marbles. *International Journal of Rock Mechanics & Mining Sciences*, v. 33, p 479-485
- Wong T.f., Baud P., Klein E., 2001. Localized failure modes in a compactant porous rock. *Geophysical Research Letters* 28, 2521–2524.

- Wooller L.; Murray J.; Rymer H.; van Wyk de Vries B., 2003. Volcano instability and collapse from basement faulting. EGS - AGU - EUG Joint Assembly, Abstracts from the meeting held in Nice, France, 6 - 11 April 2003, abstract n. 304
- Wooller L., van Wyk de Vries B., Murray J.B., Rymer H., Meyer S., 2004. Volcano spreading controlled by dipping substrata. *Geology*; v. 32, no. 7; p 573–576
- Youn H., and Tonon F., 2010. Multi-stage triaxial test on brittle rock. *International Journal of Rock Mechanics & Mining Sciences*, v. 47, p 678–684
- Zimbelman D.R., Watters R.J., Firth I.R., Breit G.N., Carrasco-Nunez G., 2004. Stratovolcano stability assessment methods and results from Citlaltpetl, Mexico. *Bulletin of Volcanology*, v. 66, p. 66-79.

## APPENDIX 1: Standard terminology for description of weathering rock

Table .1. Standard terminology for description of weathering of rock cores, outcrops and material. From Price 2009

Weathering description	Grade	Rock core grade	Rock outcrop grades	Rock material descriptive terms
Fresh	I(A)	No visible sign of weathering	No visible sign of rock material weathering, perhaps slight discolouration on major discontinuity surfaces	Rock material weathering can be described by using terms such as:
Faintly weathered	I(B)	Weathering limited to the surface of major discontinuities		
Slightly weathered	II	Weathering penetrates through most discontinuities, but only slight weathering of rock material	Discolouration indicates weathering of rock material and discontinuity surfaces. All the rock material may be discoloured by weathering	Discoloured: The colour of the original fresh rock material is changed and is evidence of weathering
Moderately weathered	III	Weathering extends throughout the rock mass but the rock material is not friable	Less than half the rock material decomposed or disintegrated to a soil. Fresh or discoloured rock is present as a continuous framework or as corestones	Decomposed: The rock is weathered to the condition of a soil in which the original material fabric is still intact, but some or all of the mineral grains are decomposed
Highly weathered	IV	Weathering through discontinuities and material and the rock material is partly friable	More than half the rock material decomposed or disintegrated to a soil. Fresh or discoloured rock is present as a discontinuous framework or as corestones	Disintegrated: the rock weathered to the condition of a soil in which the original material fabric is still intact. The rock is friable but the mineral grains are not decomposed
Completely weathered	V	Rock is wholly decomposed and in a friable condition but the rock texture and structure are preserved	All rock material is decomposed and/or disintegrated to soil. The original rock mass structure is still largely intact	The stages above may be qualified by using terms such as “partially, slightly, wholly”
Residual soil	VII	A soil material with the original texture, structure, and mineralogy of the rock completely destroyed	All rock material is converted to soil. The mass structure and material fabric are destroyed. There is a large change in volume but the soil has not been significantly transported	

Table .2. Description state of weathering, BS 5930 (1999). From Price 2009

Grade	Classifier	Description
I	Fresh	Unchanged from original state
II	Slightly Weathered	Slight discolouration; slight weakening
III	Moderately weathered	Considerable weakened, penetrative discolouration; large pieces cannot be broken by hand
IV	Highly weathered	Large pieces can be broken by hand; does not readily disintegrated (slake) when dry sample immersed in water
V	Completely weathered	Considerably weakened; slakes in water; original texture apparent soil derived by in-situ weathering but having lost retaining original
VI	Residual soil	texture and fabric

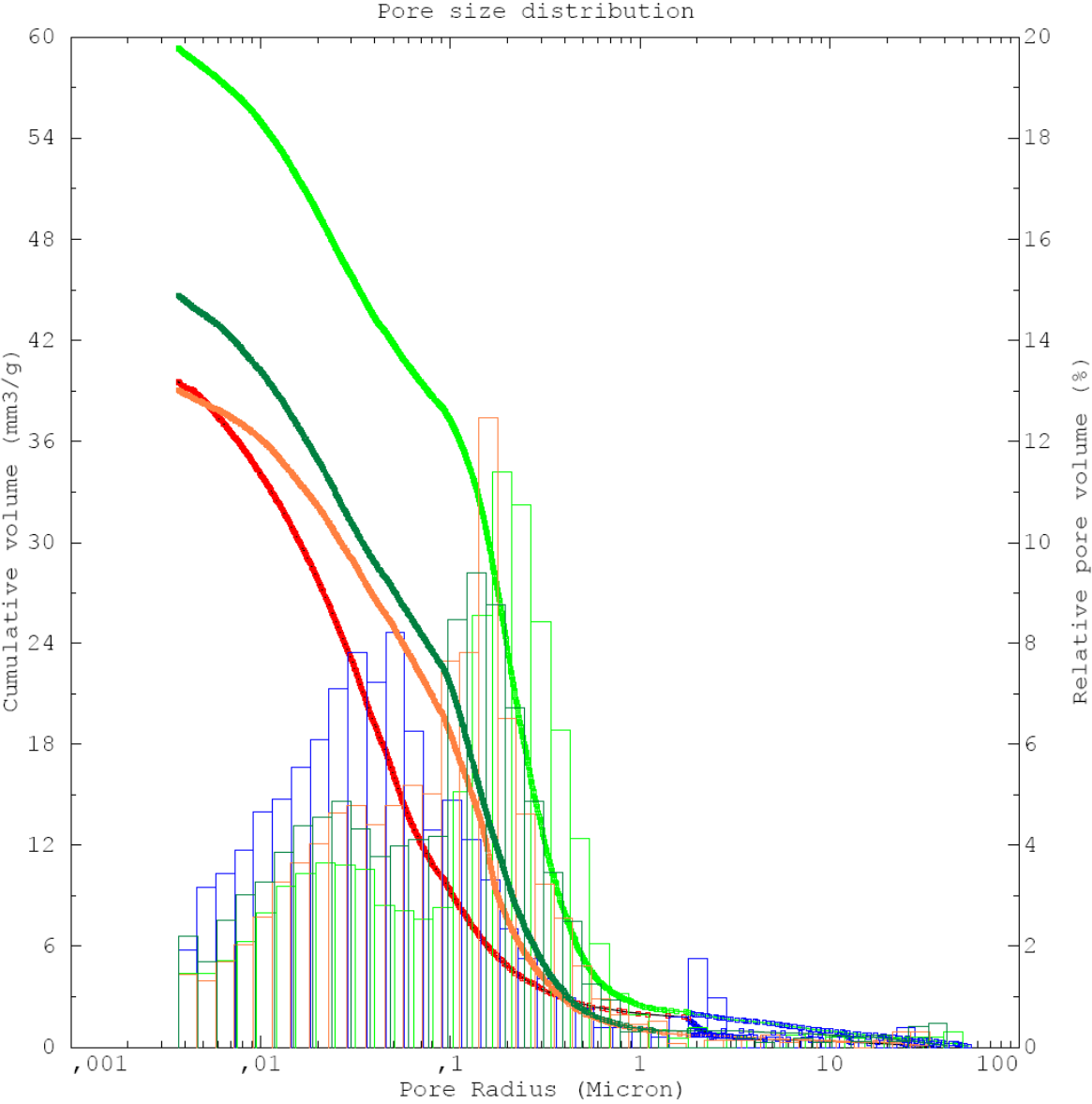
## APPENDIX 2: Properties of samples

Sample ID	mass (g)	Wet mass (g)	Height (mm)	Diameter (mm)	volume (mm <sup>3</sup> )	$\eta$	Bulk density (g/cm <sup>3</sup> )	Unit weight (N/m <sup>3</sup> )
SLA1_2	679.51	695.88	130.04	52.96	0.000286525	0.06	2.37	23264.98
SLA1_3	621.98	638.68	120.25	52.95	0.000264794	0.06	2.35	23042.92
SLA1_4	664.01	682.16	128.78	53.01	0.00028422	0.06	2.34	22918.63
SLA1_5	690.91	703.15	132.5	53.03	0.000292651	0.04	2.36	23160.10
SLA1_6	523.94	541.73	102.34	52.98	0.000225611	0.08	2.32	22781.92
SLA1_7	614.7	629.73	117.79	53.03	0.000260191	0.06	2.36	23176.11
SLA1_8	596.41	605.15	113.14	53.06	0.000250202	0.03	2.38	23384.24
SLA1_9	446.62	456.86	85.71	53.11	0.000189921	0.05	2.35	23069.28
SLA1_10	471.26	479.73	90.5	53.06	0.000200158	0.04	2.35	23097.10
SLA1_11	467.66	481.18	90.6	52.98	0.00019973	0.07	2.34	22969.75
SLA2_1	556.15	567.31	110.05	53.15	0.000244167	0.05	2.28	22344.65
SLA2_2	491.28	501.03	94.77	53.07	0.000209657	0.05	2.34	22987.36
SLA2_3	667.1	681.12	128.69	53.15	0.000285556	0.05	2.34	22917.58
SLA2_4	645.92	664.84	125.82	53.20	0.000279682	0.07	2.31	22656.03
SLA2_5	595.91	611.4	115.26	53.20	0.000256208	0.06	2.33	22816.91
SLA3_1	434.33	481.77	100.03	52.92	0.000220019	0.22	1.97	19365.47
SLA3_2	608.27	655.15	131.35	52.87	0.000288363	0.16	2.11	20693.11
SLA3_3	538.92	606.89	130.61	53.02	0.000288433	0.24	1.87	18329.40
SLA3_5	575.63	640.49	132.1	53.03	0.000291834	0.22	1.97	19349.83
SLA3_6	382.24	438.67	95.04	53.09	0.000210436	0.27	1.82	17819.04
SLA3_7	540.96	614.49	130.19	53.12	0.000288526	0.25	1.87	18392.87
SLA4_1	567.75	630.92	140.09	53.23	0.000311753	0.20	1.82	17865.50
SLA4_2	443.36	486.34	105.69	53.19	0.000234909	0.18	1.89	18515.12
SLA4_4	513.71	582.12	131.02	53.14	0.000290656	0.24	1.77	17338.34
SLA4_5	478.21	533.64	119.64	53.20	0.000265944	0.21	1.80	17639.94
SLA4_6	528.56	581.93	131.43	53.20	0.000292218	0.18	1.81	17744.21
SLA4_7	358.67	390.75	86.84	53.18	0.000192932	0.17	1.86	18237.22
SLA4_8	516.38	581.67	132.32	53.19	0.00029402	0.22	1.76	17229.08
SLA5_1	335.03	379.79	100.17	53.22	0.000222832	0.20	1.50	14749.40
SLA5_2	358.5	404.76	107.27	53.22	0.000238627	0.19	1.50	14738.02
SLA5_3	299.93	343.92	92.5	53.18	0.000205461	0.21	1.46	14320.55
SLA5_4	405.29	455.37	117.74	53.24	0.000262114	0.19	1.55	15168.54
SLA5_5	351.79	390.98	102.06	53.30	0.00022772	0.17	1.54	15154.85
SLA5_6	366.97	410.96	106.62	53.13	0.000236379	0.19	1.55	15229.67
SLA5_7	365.99	413.28	111.29	53.19	0.00024729	0.19	1.48	14518.82
SPRA1_1	450.76	508	131.7	53.01	0.000290665	0.20	1.55	15213.25
SPRA1_2	348.5	406.04	108.67	53.26	0.000242105	0.24	1.44	14121.11
SPRA1_3	328.92	379.09	96	53.21	0.000213476	0.24	1.54	15115.09
SPRA1_4	390.34	497.61	134.42	53.24	0.000299248	0.36	1.30	12796.20
SPRA1_7	334.34	375.75	98.05	53.23	0.000218198	0.19	1.53	15031.62
SPRA1_8	430.99	508.78	132.78	52.93	0.000292164	0.27	1.48	14471.34
SPRA2_1	464.41	526.98	129.44	53.08	0.000286432	0.22	1.62	15905.57

SPRA2_3	488.29	546	133.07	53.12	0.000294908	0.20	1.66	16242.75
SPRA2_4	441.03	511.45	131.02	53.11	0.000290256	0.24	1.52	14905.83
SPRA2_5	438.15	509.04	129.75	52.80	0.000284097	0.25	1.54	15129.54
SPRA2_7	450.63	509.65	130.27	52.96	0.000286967	0.21	1.57	15404.86
SPRA2_8	461	521.09	130.16	53.07	0.000287917	0.21	1.60	15707.36
SPRA2_9	413.14	442.65	104.35	53.13	0.000231347	0.13	1.79	17518.76
SPRA3_1	342.62	412.79	103.16	53.20	0.000229311	0.31	1.49	14657.38
SPRA3_2	365.19	414.05	105.42	53.22	0.000234511	0.21	1.56	15276.51
SPRA3_3	341.22	421.7	110.95	53.05	0.000245239	0.33	1.39	13649.43
SPRA3_4	367.13	459.39	123.09	53.17	0.000273305	0.34	1.34	13177.77
SPRA3_5	345.91	416.49	107.21	53.24	0.000238672	0.30	1.45	14217.72
SPRA3_6	398	490.65	125.74	53.16	0.000279084	0.33	1.43	13990.00
SPRA3_7	271.88	331.26	86.1	53.24	0.000191677	0.31	1.42	13914.77
IGTF_1	447.32	534.69	130.16	52.94	0.000286508	0.30	1.56	15316.20
IGTF_2	334.47	398.17	96.94	53.01	0.000213949	0.30	1.56	15336.16
IGTF_3	329.43	389.91	95.15	53.16	0.000211188	0.29	1.56	15302.50
IGTF_4	435.67	523.62	129.29	52.89	0.000284055	0.31	1.53	15046.09
IGTA_1	541.58	590.89	128.92	53.05	0.000284959	0.17	1.90	18644.45
IGTA_2	284.18	328.02	72.55	53.15	0.000160966	0.27	1.77	17319.19
IGTA_3	319.73	342.36	78.29	53.07	0.000173179	0.13	1.85	18111.61
BoPRA_1	285.96	401.53	129.91	53.20	0.000288773	0.40	0.99	9714.44
BoPRA_2	239.51	383.68	129.32	53.27	0.000288219	0.50	0.83	8152.12
BoPRA_3	273.45	396.68	132.58	53.13	0.000293933	0.42	0.93	9126.38
BoPRA_4	228.2	378.81	129.8	53.28	0.000289397	0.52	0.79	7735.54
BoPRA_5	301.2	394.06	127.61	53.15	0.000283128	0.33	1.06	10436.19
BoPRA_6	267.71	386.28	129.97	53.20	0.000288906	0.41	0.93	9090.26
BoPRA_7	288.9	389.39	129.37	53.20	0.000287573	0.35	1.00	9855.28
BoPRA_8	176.43	256.36	85.84	53.17	0.000190596	0.42	0.93	9080.87
BoPRA_9	199.52	307.88	101.5	53.18	0.000225452	0.48	0.88	8681.64
BoPRA_10	190.02	267.13	86.31	53.30	0.000192578	0.40	0.99	9679.70
BoPRA_11	177.18	257.17	86.52	53.16	0.000192034	0.42	0.92	9051.20
BoPRA_12	205.33	273.44	88.19	53.21	0.000196109	0.35	1.05	10271.28

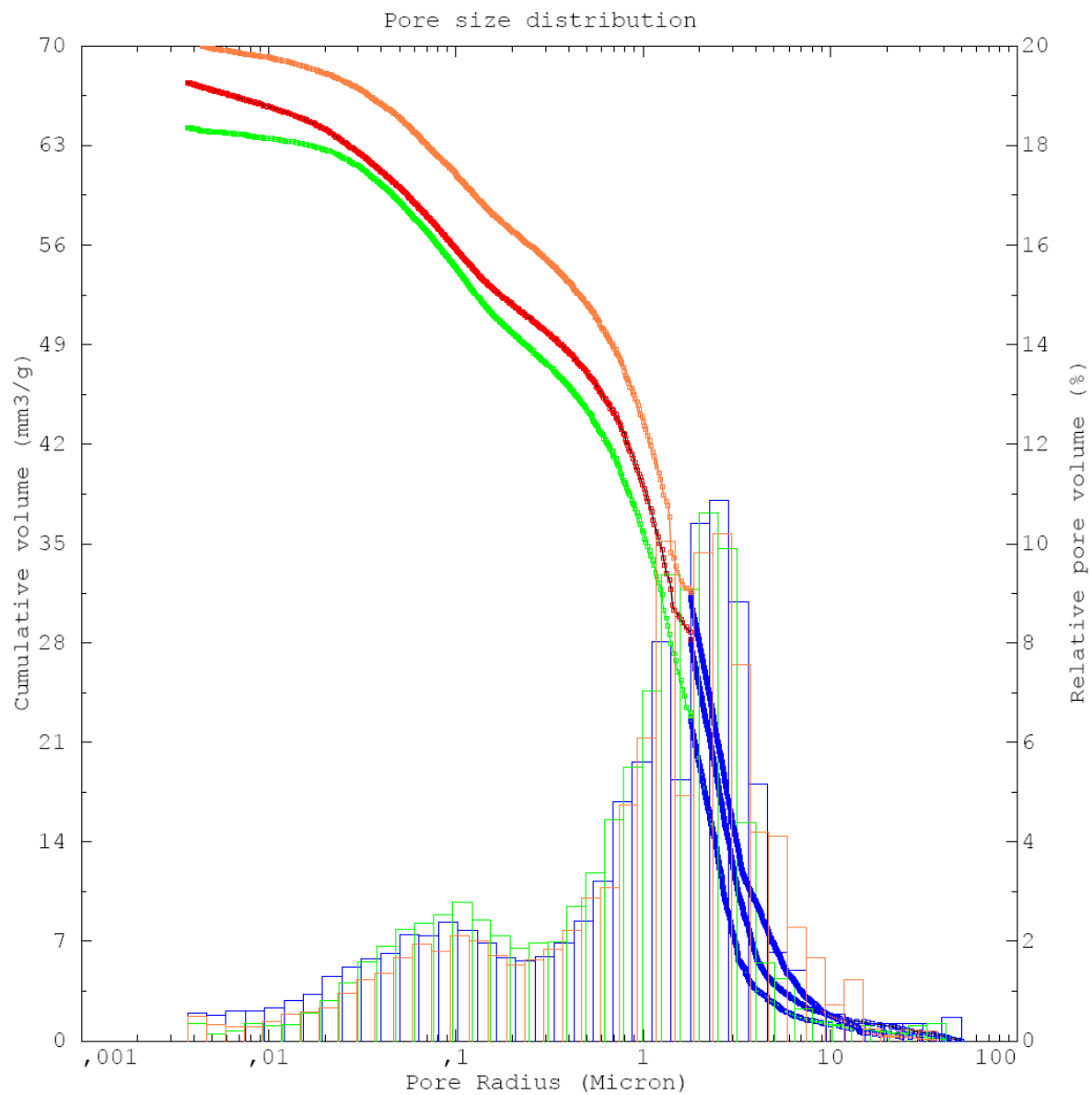
**APPENDIX 3: cumulative pore size distribution from mercury intrusion porosimeter**

SLA1

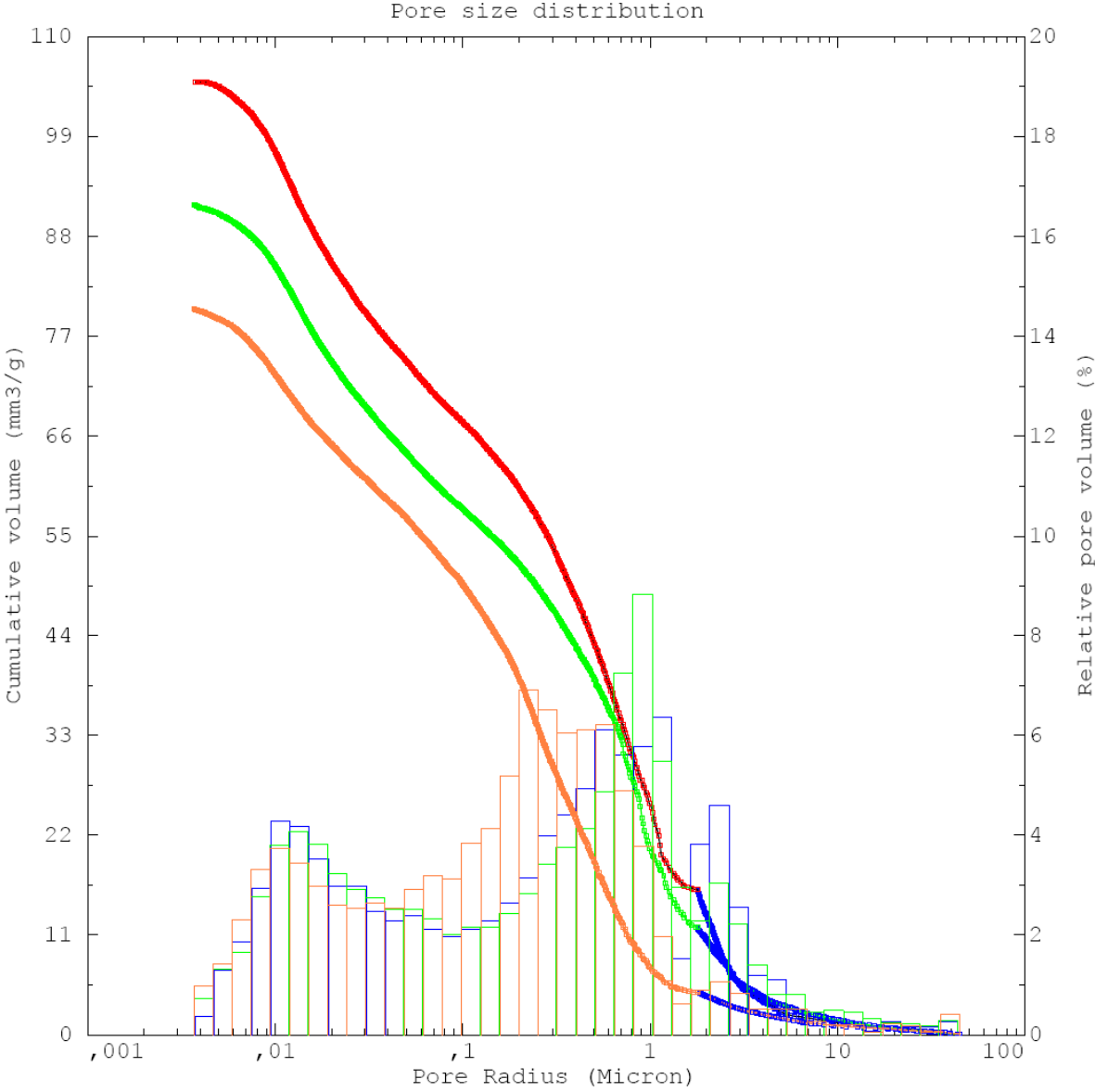




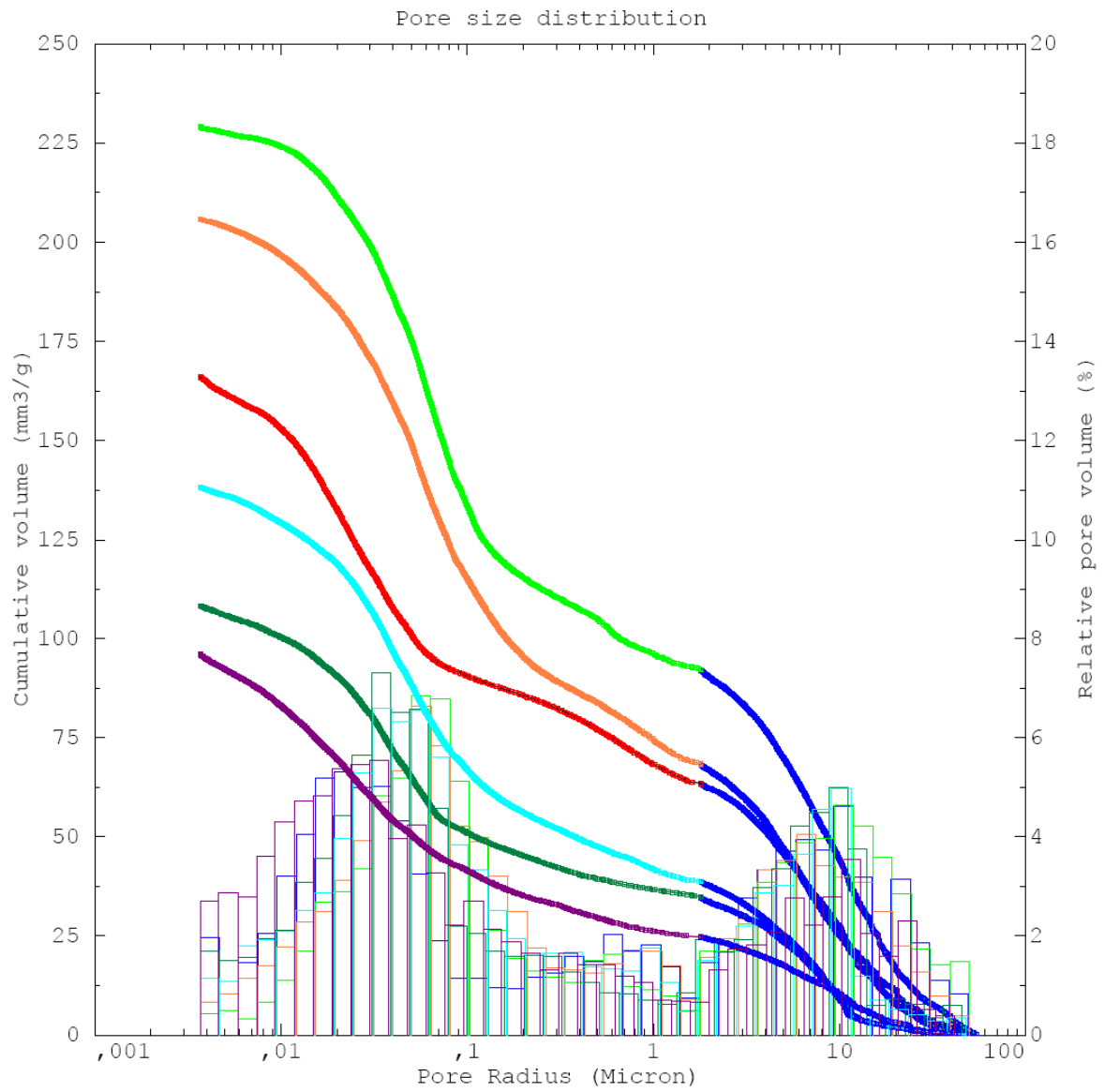
SLA2



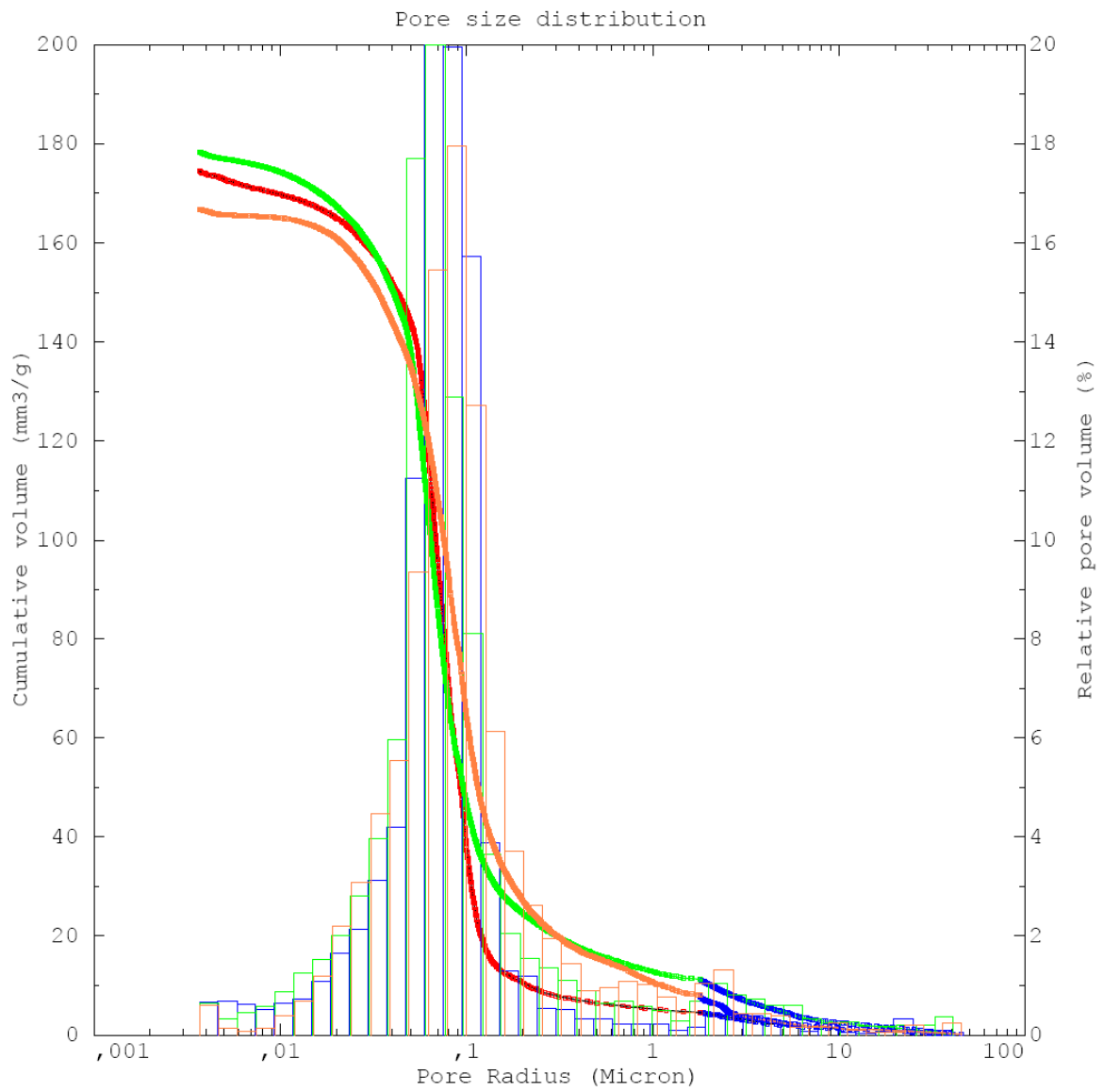
SLA3



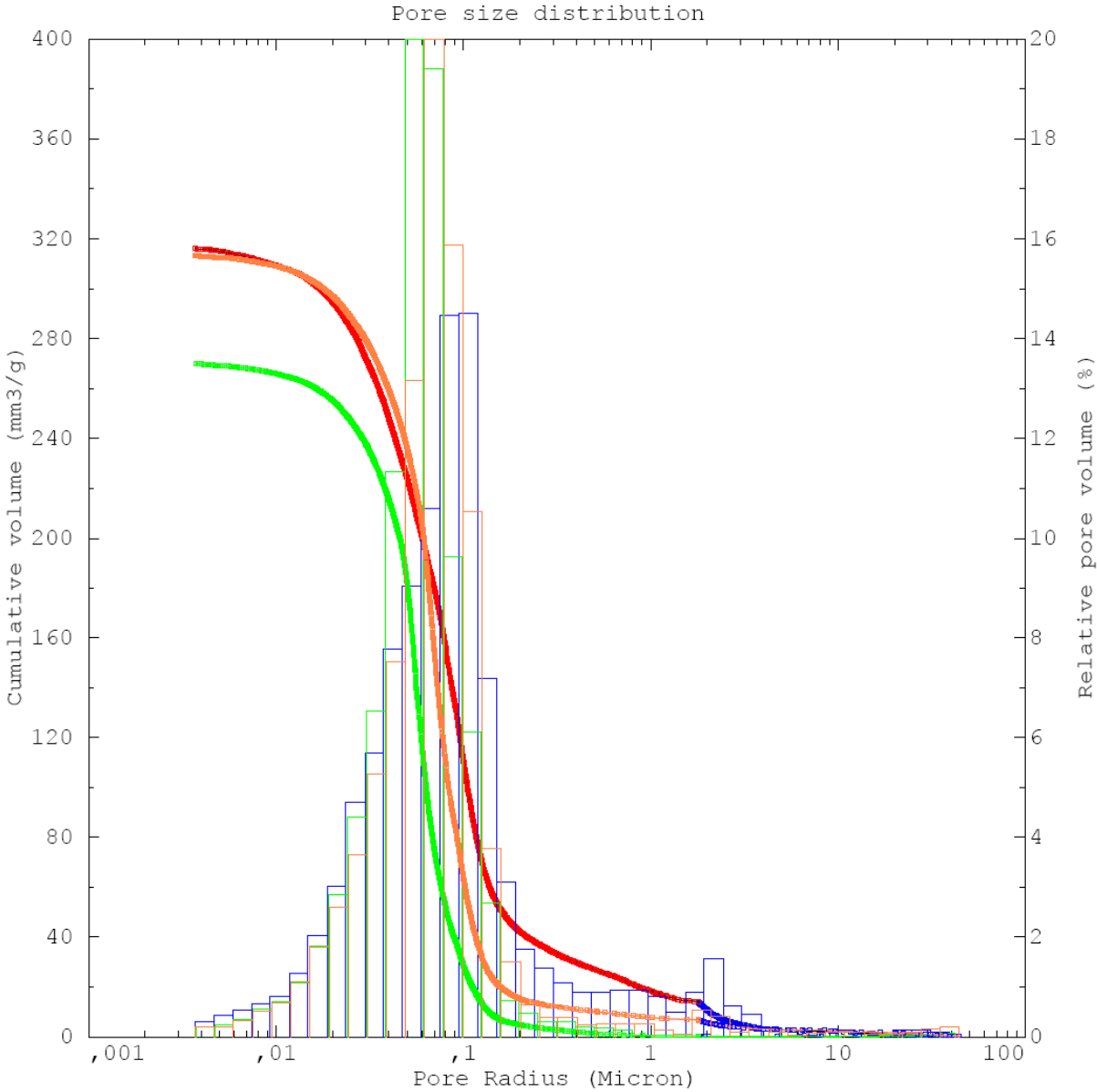
SLA4



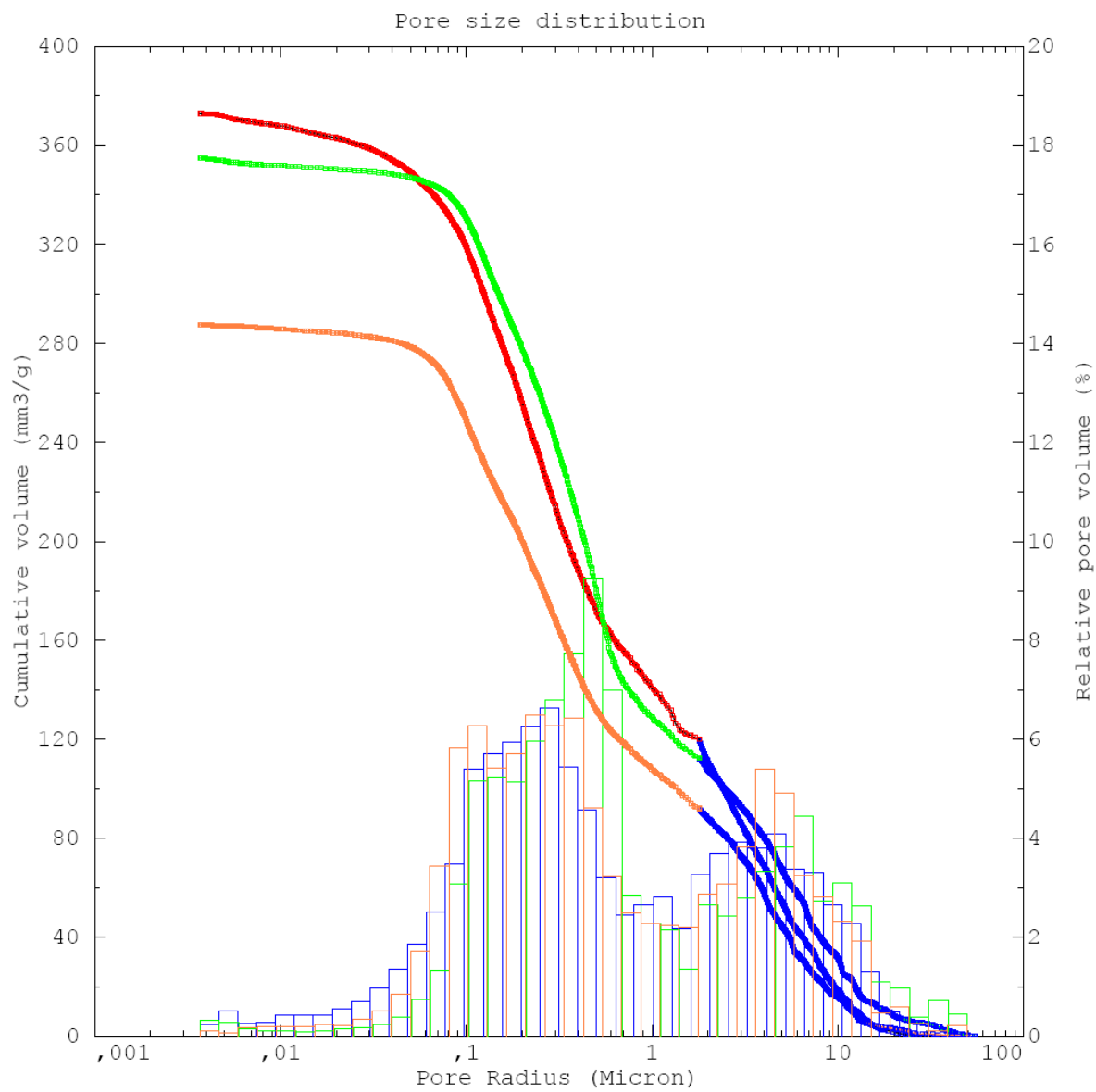
SLA5



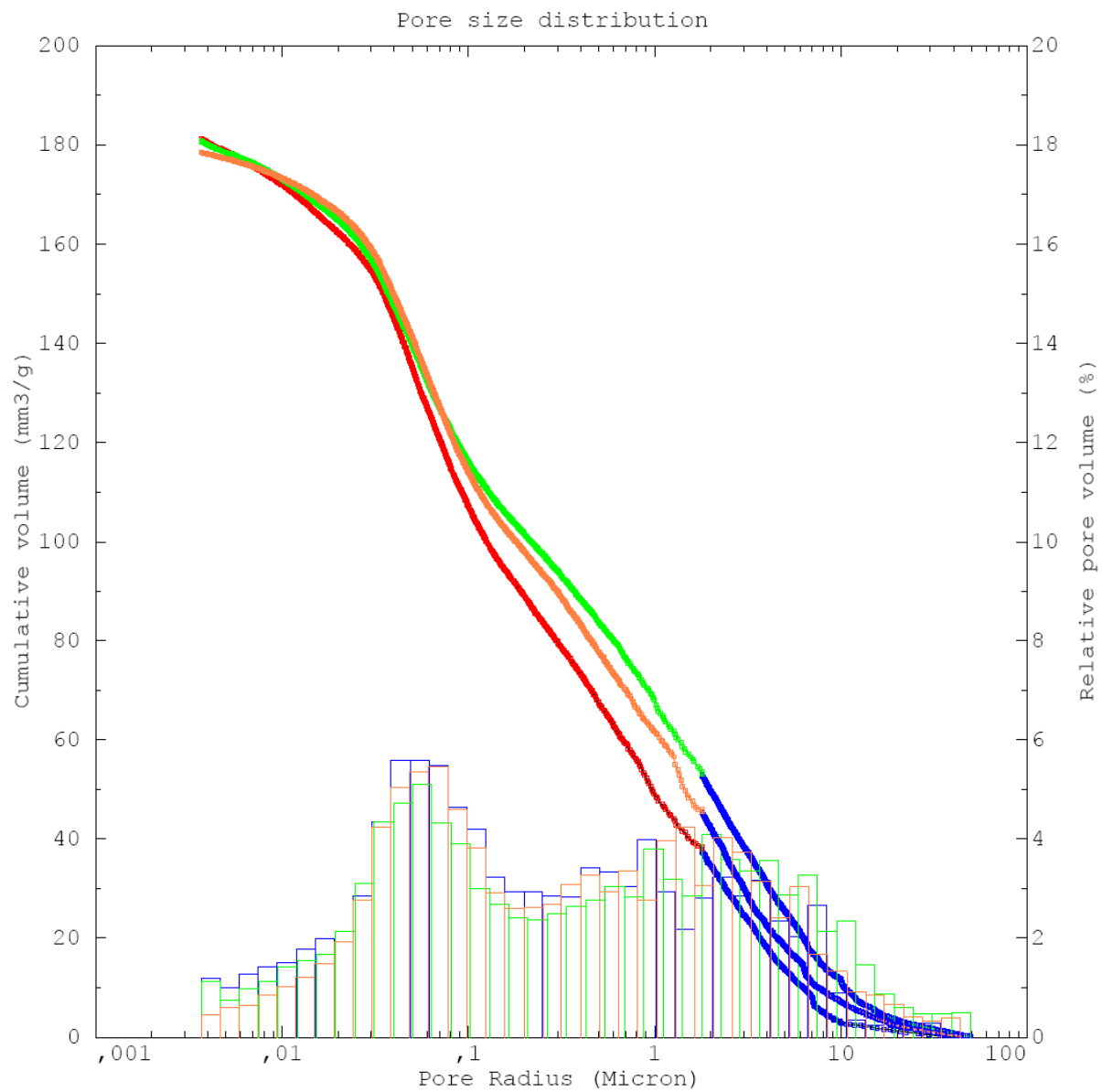
SPRA1



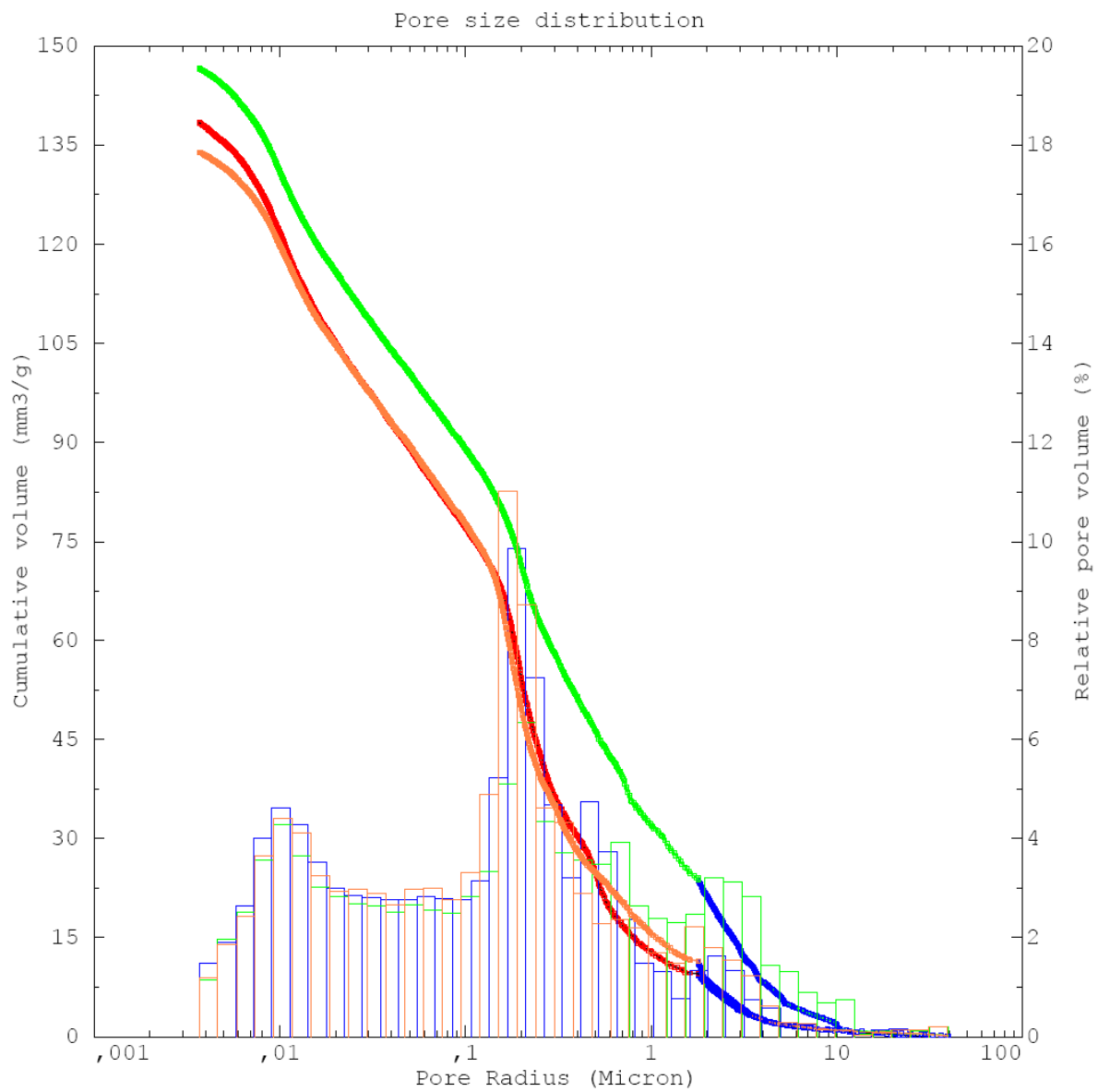
SPRA2



# IGTF

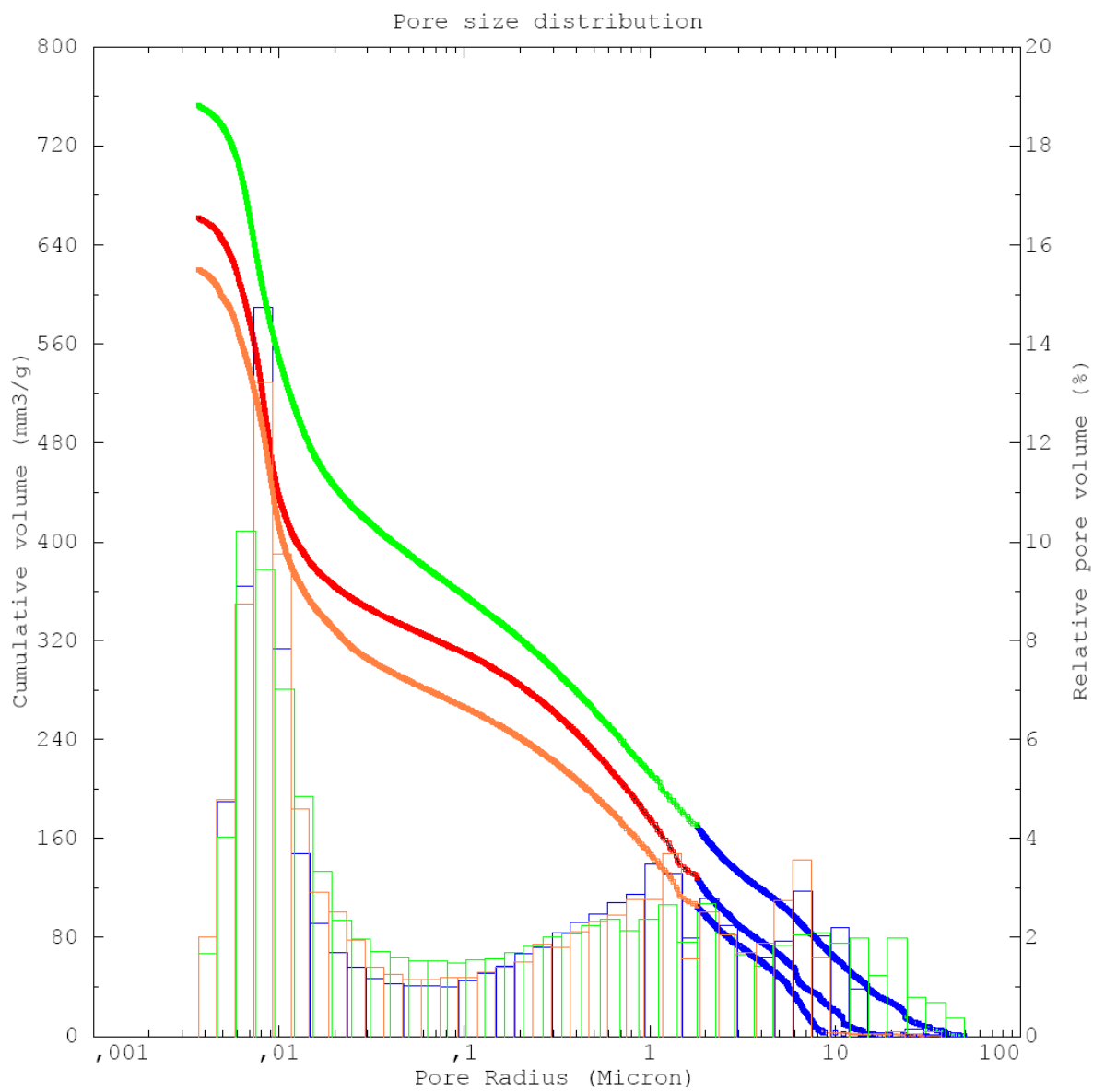


# IGTA





# BoPRA



## APPENDIX 4: Pycnometer

---

<b>SLA-1</b>		
N° picnometro	1.00	4.00
Vol. picnometro	250.00	100.00
Peso picnometro + acqua	341.98	155.47
peso picnometro + acqua + suolo	373.51	168.20
peso lordo suolo secco	309.19	153.82
tara contenitore	260.56	133.69
peso netto suolo secco	48.63	20.13
massa eguale vol acqua	17.10	7.40
Gs	2.84	2.72
<b>MEDIA</b>		<b>2.78</b>

---

---

<b>SLA-2</b>		
N° picnometro	1.00	4.00
Vol. picnometro	250.00	100.00
Peso picnometro + acqua	341.98	155.47
peso picnometro + acqua + suolo	373.12	168.32
peso lordo suolo secco	310.09	182.45
tara contenitore	260.56	162.34
peso netto suolo secco	49.53	20.11
massa eguale vol acqua	18.39	7.26
Gs	2.69	2.77
<b>MEDIA</b>		<b>2.73</b>

---

---

<b>SLA-3</b>		
N° picnometro	1.00	4.00
Vol. picnometro	250.00	100.00
Peso picnometro + acqua	341.98	155.47
peso picnometro + acqua + suolo	373.35	168.59
peso lordo suolo secco	311.70	154.34
tara contenitore	261.65	133.69
peso netto suolo secco	50.05	20.65
massa eguale vol acqua	18.68	7.53
Gs	2.68	2.74
<b>MEDIA</b>		<b>2.71</b>

---

---

<b>SLA-4</b>		
N° picnometro	1.00	4.00
Vol. picnometro	250.00	100.00
Peso picnometro + acqua	341.98	155.47
peso picnometro + acqua + suolo	370.33	167.48
peso lordo suolo secco	310.29	153.51
tara contenitore	261.65	133.69
peso netto suolo secco	48.64	19.82
massa eguale vol acqua	20.29	7.81
Gs	2.40	2.54
<b>MEDIA</b>		<b>2.47</b>

---

<b>SLA-5</b>		
N° picnometro	1.00	4.00
Vol. picnometro	250.00	100.00
Peso picnometro + acqua	341.98	155.47
peso picnometro + acqua + suolo	367.99	165.88
peso lordo suolo secco	309.59	153.80
tara contenitore	260.56	134.63
peso netto suolo secco	49.03	19.17
massa eguale vol acqua	23.02	8.76
Gs	2.13	2.19
<b>MEDIA</b>		<b>2.16</b>

<b>SPRA-1</b>		
N° picnometro	1.00	4.00
Vol. picnometro	250.00	100.00
Peso picnometro + acqua	341.98	155.47
peso picnometro + acqua + suolo	369.90	166.90
peso lordo suolo secco	309.19	181.56
tara contenitore	261.65	162.34
peso netto suolo secco	47.54	19.22
massa eguale vol acqua	19.62	7.79
Gs	2.42	2.47
<b>MEDIA</b>		<b>2.45</b>

<b>SPRA-2</b>		
N° picnometro	1.00	4.00
Vol. picnometro	250.00	100.00
Peso picnometro + acqua	341.98	155.47
peso picnometro + acqua + suolo	370.21	166.95
peso lordo suolo secco	308.56	181.48
tara contenitore	261.65	162.34
peso netto suolo secco	46.91	19.14
massa eguale vol acqua	18.68	7.66
Gs	2.51	2.50
<b>MEDIA</b>		<b>2.50</b>

<b>IGTF</b>		
N° picnometro	1.00	4.00
Vol. picnometro	250.00	100.00
Peso picnometro + acqua	341.98	155.47
peso picnometro + acqua + suolo	369.94	166.97
peso lordo suolo secco	307.96	152.87
tara contenitore	260.56	133.69
peso netto suolo secco	47.40	19.18
massa eguale vol acqua	19.44	7.68
Gs	2.44	2.50
<b>MEDIA</b>		<b>2.47</b>

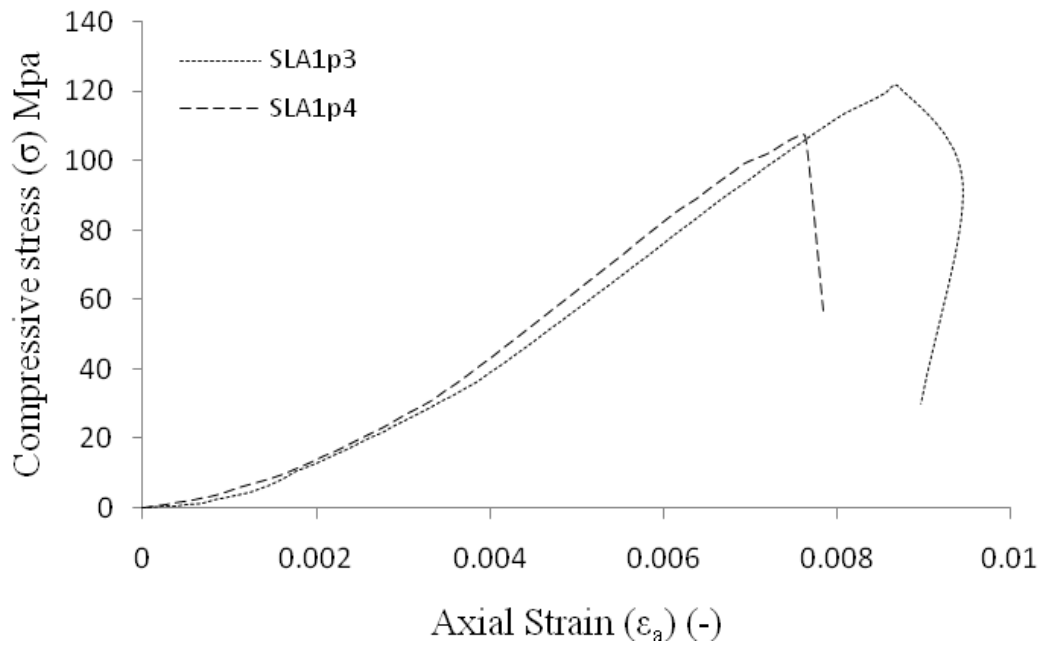
<b>IGTA1</b>		
N° picnometro	1.00	4.00
Vol. picnometro	250.00	100.00
Peso picnometro + acqua	341.98	155.47
peso picnometro + acqua + suolo	368.04	161.94
peso lordo suolo secco	305.53	144.31
tara contenitore	261.65	133.69
peso netto suolo secco	43.88	10.62
massa eguale vol acqua	17.82	4.15
Gs	2.46	2.56
<b>MEDIA</b>		<b>2.51</b>

<b>BOPRA</b>		
N° picnometro	1.00	4.00
Vol. picnometro	250.00	100.00
Peso picnometro + acqua	341.98	155.47
peso picnometro + acqua + suolo	360.47	166.60
peso lordo suolo secco	294.81	155.52
tara contenitore	259.66	134.55
peso netto suolo secco	35.15	20.97
massa eguale vol acqua	16.66	9.84
Gs	2.11	2.13
<b>MEDIA</b>		<b>2.12</b>

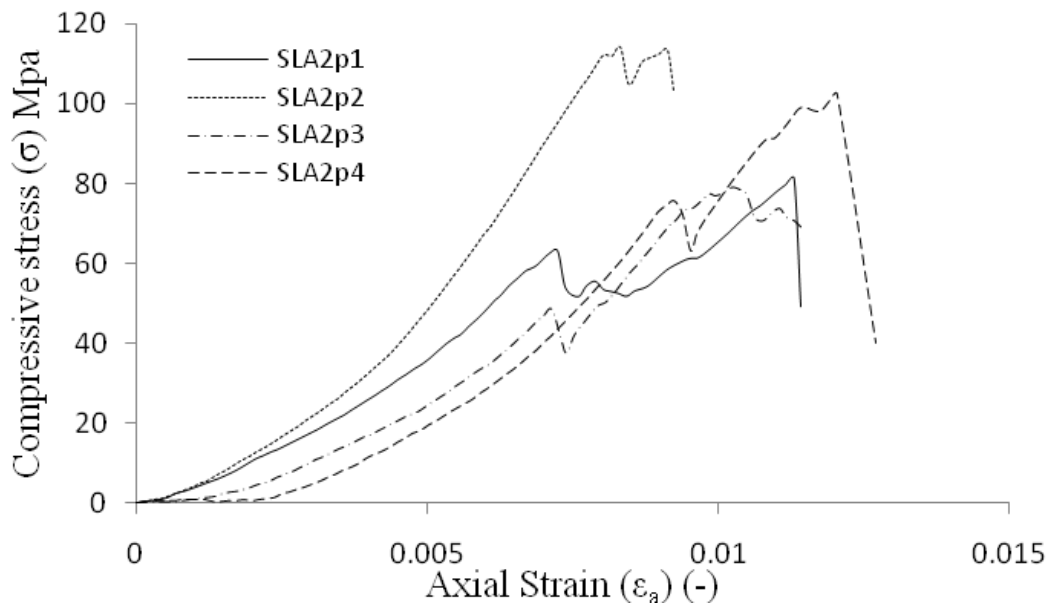
## APPENDIX 5: Preliminary tests of Uniaxial Compressive Strength

ID lithology	ID Sample	Compressive strength Mpa	Young' s Modulus GPa
SLA1	SLA1_3	121.42	18.54
	SLA1_4	112.07	18.32
SLA2	SLA2_1	81.36	25.81
	SLA2_2	114.18	20.04
	SLA2_3	79.00	22.64
	SLA2_4	102.40	14.91
SLA3	SLA3_2	24.58	3.47
	SLA3_3	24.87	3.35
	SLA3_4	25.62	4.32
	SLA3_5	28.20	7.02
SLA4	SLA4_1	24.69	5.67
	SLA4_2	20.21	4.43
	SLA4_4	23.04	2.65
SLA5	SLA5_1	18.24	1.66
	SLA5_2	17.16	2.76
	SLA5_6	14.39	1.63
	SLA5_7	17.36	2.35
SPRA1	SPRA1_1	13.25	1.61
	SPRA1_2	11.31	2.19
	SPRA1_3	13.66	0.73
	SPRA1_4	14.94	1.94
SPRA2	SPRA2_4	8.41	1.45
	SPRA2_5	8.84	2.38
SPRA3	SPRA3_1	7.23	1.43
IGTF	IGTF_3	6.38	0.70
	IGTF_2	5.10	0.71
IGTA	IGTA_	16.26	1.56
BoPRA	BoPRA_1	6.86	1.12
	BoPRA_2	4.82	0.56
	BoPRA_3	6.92	1.19
	BoPRaA_4	4.34	0.45

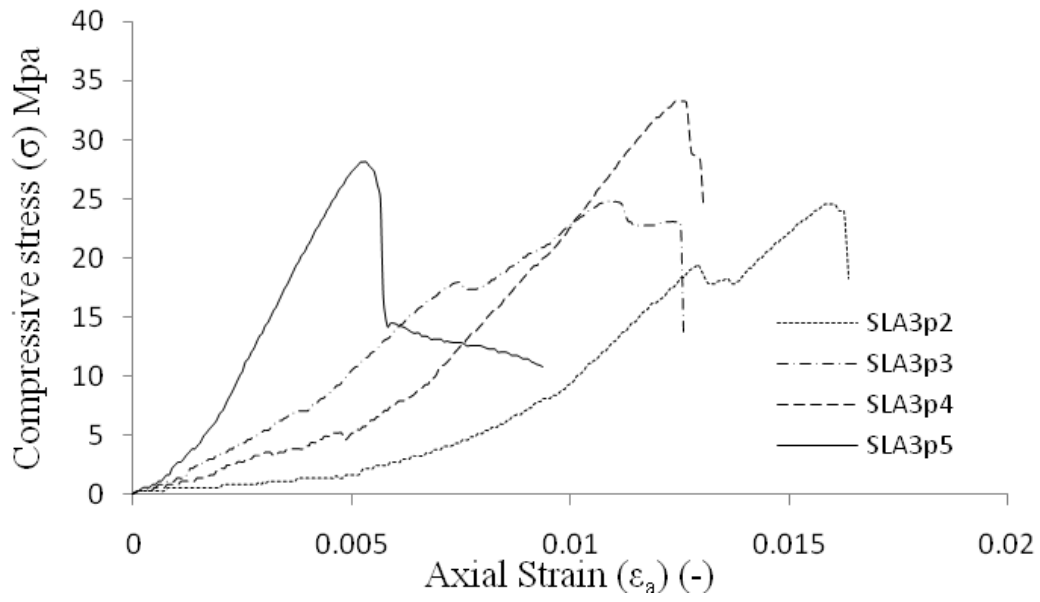
### SLA1



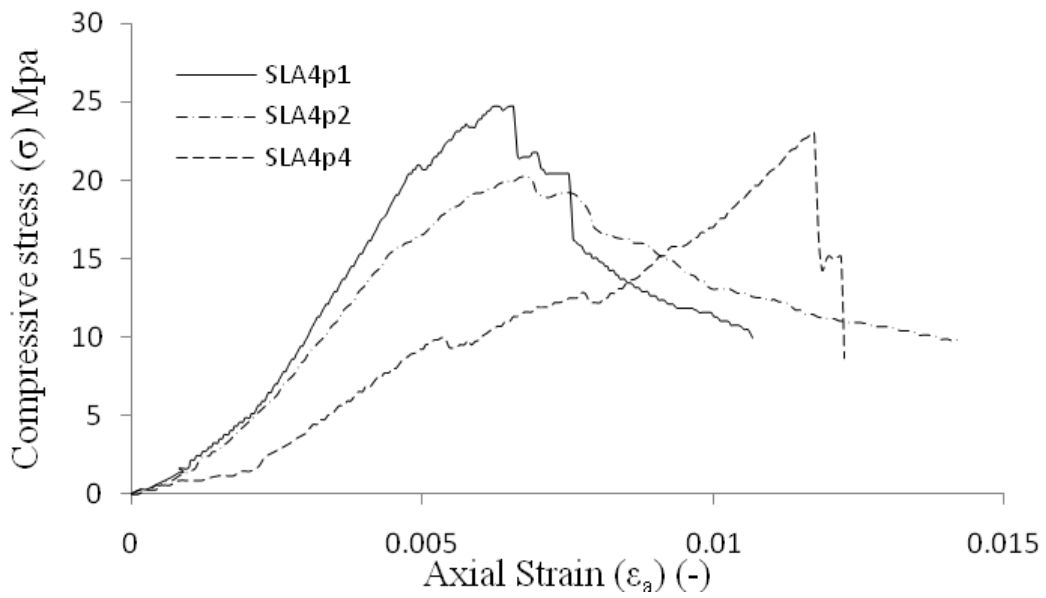
### SLA2



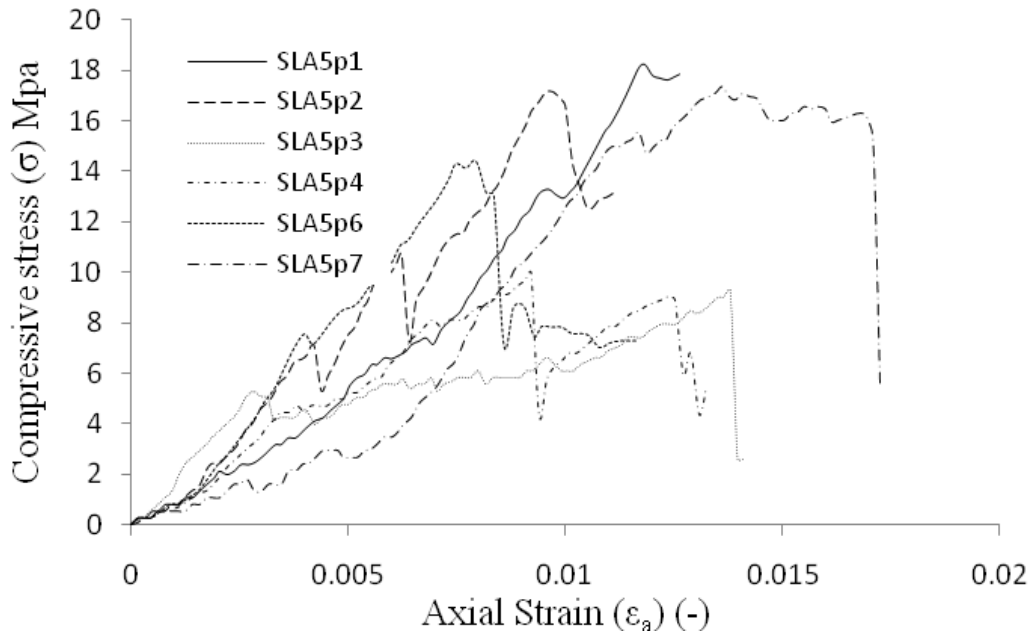
### SLA3



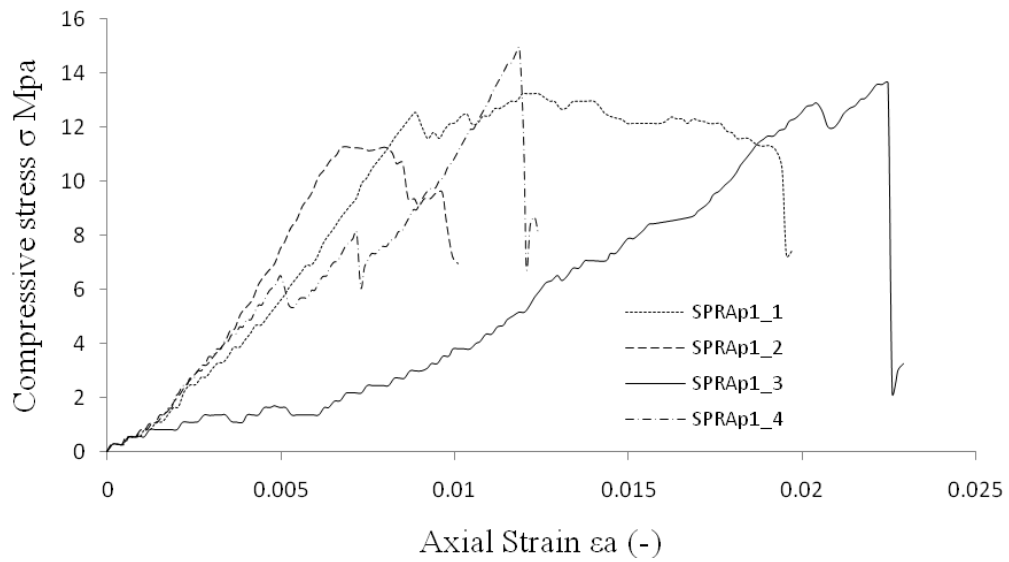
### SLA4



SLA5

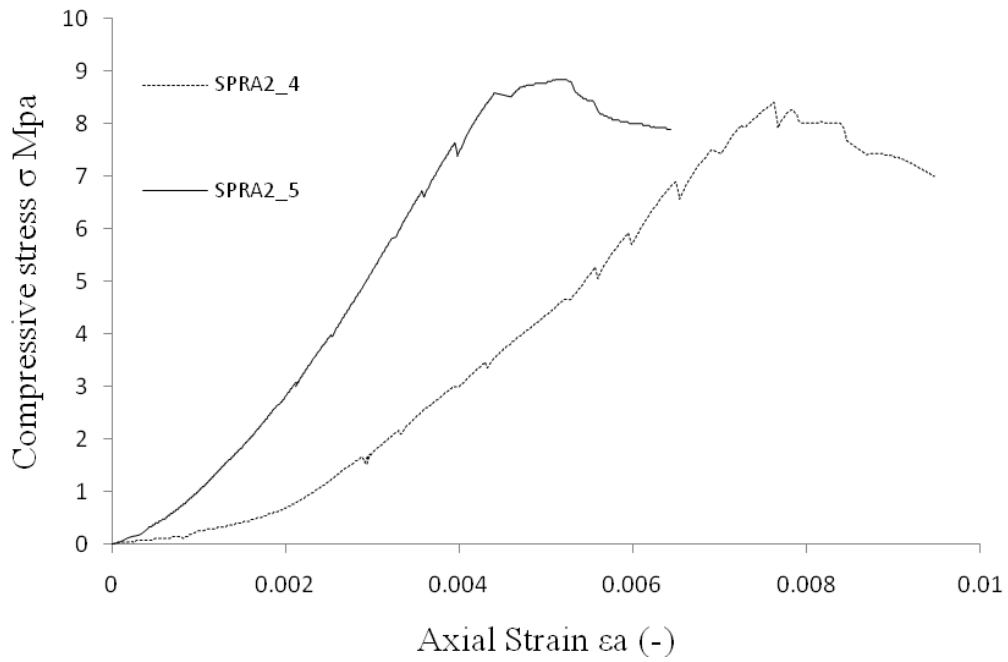


SPRA1

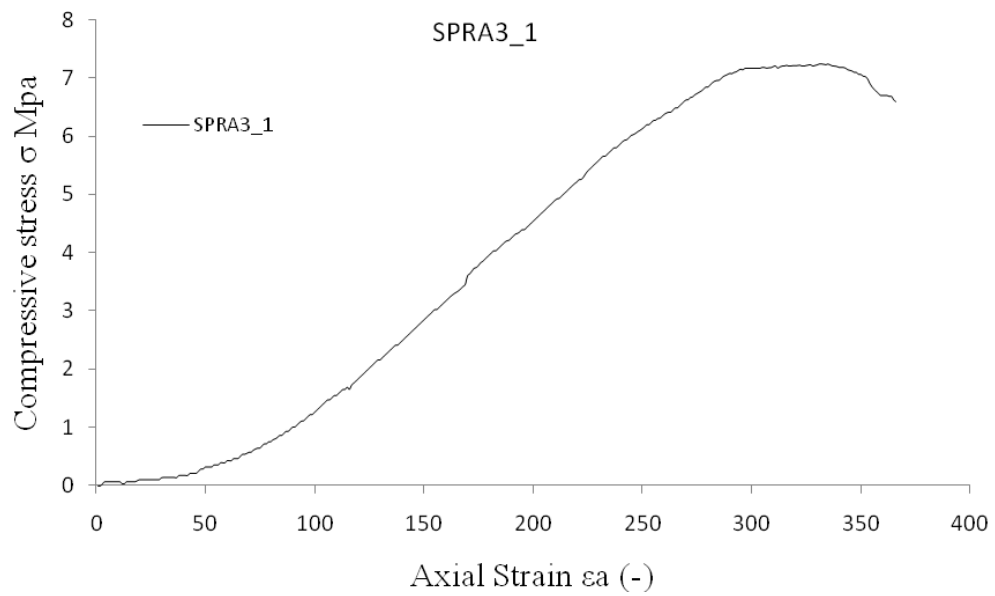




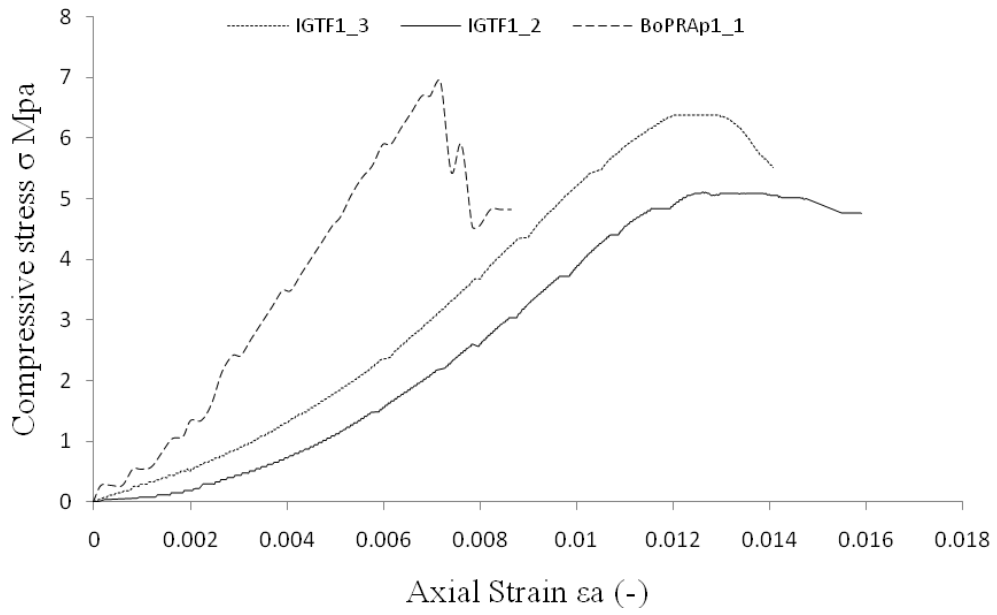
### SPRA2



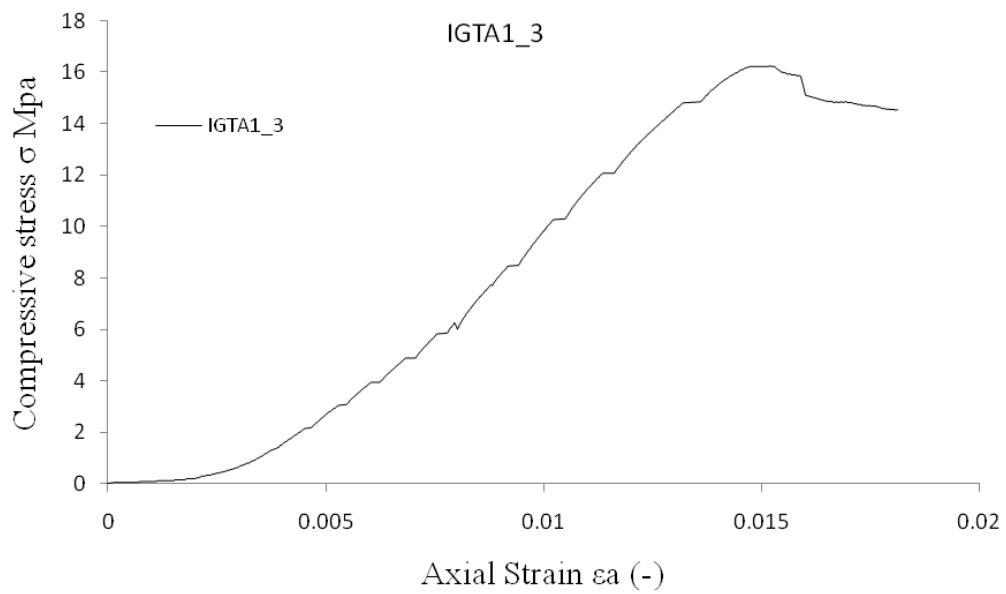
### SPRA3



### IGTF



### IGTA



BoPRA

